Université de Strasbourg

UNIVERSITÉ DE STRASBOURG

École doctorale Mathématiques, sciences de l'information et de l'ingénieur | ED 269 Université de Strasbourg

ED 269 : Mathématiques, Sciences de l'information et de l'Ingénieur

Institut de Recherche Mathématique Avancé

UMR 7501

THÈSE presented by :

Tom Sprunck

soutenue le : **17 décembre 2024**

pour obtenir le grade de :

Docteur de l'Université de Strasbourg

Discipline/Spécialité: Mathématiques

Peut-on entendre la forme d'une pièce ?

Reconstruction de la géométrie d'une salle à partir de mesures acoustiques par super-résolution et optimisation de forme.

THÈSE dirigée par :

Yannick Privat	Professeur, Université de Strasbourg
Antoine Deleforge	Chargé de recherche, Inria Nancy
Cédric Foy	Chargé de recherche, Cerema

RAPPORTEURS :

Hélène Barucq	Directrice de recherche, Inria Bordeaux
Charles Dapogny	Maitre de conférence, Université Grenoble Alpes

AUTRES MEMBRES DU JURY :

Marc Dambrine	Professeur, Université de Pau et des pays de l'Adour
Antoine Laurain	Professeur, Université Duisburg-Essen

Tom Sprunck
Peut-on entendre la forme d'une pièce ?

Résumé

Peut-on entendre la forme d'une pièce ? Cette thèse aborde le problème inverse de la reconstruction de la géométrie d'une pièce à partir de mesures acoustiques. Plus précisément, nous nous concentrons sur les Réponses Impulsionnelles de Salle, qui sont des mesures ponctuelles de la réponse d'une pièce à une source sonore parfaitement impulsionnelle. L'objectif est d'exploiter la réverbération du son dans la pièce pour estimer sa géométrie. Nous développons deux approches distinctes pour résoudre ce problème. La première approche considère des pièces parallélépipédiques avec des murs réfléchissants et repose sur la méthode dite des Sources Images (Image Source Method). Nous proposons un cadre novateur basé sur l'algorithme Frank-Wolfe pour reconstruire les positions 3D des sources images sans utiliser de grille, en résolvant un problème d'optimisation convexe dans l'espace des mesures de Radon. Les positions des sources images sont ensuite utilisées dans un algorithme pour estimer tous les paramètres géométriques de la pièce, y compris l'orientation de l'antenne de microphones. La deuxième approche s'étend à des formes de pièce plus générales et intègre des conditions aux limites d'admittance pour modéliser la réflexion et l'absorption des ondes sonores par les murs. Le problème inverse est formulé comme un problème d'optimisation de forme, où la géométrie de la pièce est optimisée en minimisant les écarts entre des observations dans le domaine fréquentiel et la solution de l'équation de Helmholtz définie sur le domaine de la pièce. Une dérivée de forme est calculée, introduisant des termes tangentiels non standard en raison du manque de régularité des formes polygonales. Enfin, nous implémentons un algorithme de descente de gradient de forme pour reconstruire la géométrie de la pièce.

Mots clés : Forme de salle, Acoustique, Réponse impulsionnelle de salle, Échos, Super-résolution, Optimisation convexe, Frank-Wolfe, Source image, Optimisation de forme, Méthode des solutions fondamentales, Problème inverse

Thèse

INSTITUT DE RECHERCHE MATHÉMATIQUE AVANCÉE

UMR 7501

Strasbourg

présentée pour obtenir le grade de docteur de
l'Université de Strasbourg
Spécialité MATHÉMATIQUES

Tom Sprunck

Can One Hear the Shape of a Room ?

Room Geometry Reconstruction from Acoustic Measurements using Super-Resolution and Shape Optimization

Soutenue le 17 décembre 2024
devant la commission d'examen

Yannick Privat, directeur de thèse
Antoine Deleforge, co-encadrant
Cédric Foy, co-encadrant
Hélène Barucq, rapporteuse
Charles Dapogny, rapporteur
Marc Dambrine, examinateur
Antoine Laurain, examinateur

https://irma.math.unistra.fr

UNIVERSITÉ DE STRASBOURG

École Doctorale Mathématiques, Sciences de l'Information et de l'Ingénieur

Institut de Recherche Mathématique Avancée, UMR 7501

THÈSE présentée par

Tom Sprunck

soutenue le 17 décembre 2024

pour obtenir le grade de Docteur de l'Université de Strasbourg

Spécialité : Mathématiques Appliquées

Can One Hear the Shape of a Room ?

Room Geometry Reconstruction from Acoustic Measurements using Super-Resolution and Shape Optimization

---

THÈSE DIRIGÉE PAR :

Yannick Privat	Directeur de thèse, Université de Lorraine
Antoine Deleforge	co-encadrant, Inria Nancy
Cédric Foy	co-encadrant, Cerema

RAPPORTEURS :

Hélène Barucq	Inria Bordeaux
Charles Dapogny	Université Grenoble Alpes

EXAMINATEURS :

Marc Dambrine	Université de Pau et des Pays de l'Adour
Antoine Laurain	Universität Duisburg-Essen

Remerciements

Je souhaite remercier en premier lieu mes trois encadrants Yannick, Antoine et Cédric, qui ont rendu cette thèse possible. Votre confiance et votre optimisme indéfectibles m'ont porté tout au long de la thèse, et toujours dans une super ambiance (accompagnée d'une bande son de goût).

Je remercie Hélène Barucq et Charles Dapogny d'avoir accepté de rapporter cette thèse, et pour leur relecture attentive du manuscrit. Merci également à Marc Dambrine et Antoine Laurain d'avoir participé au jury. En particulier, merci à Antoine qui a permis de grandement accélérer le développement de la deuxième partie de cette thèse.

Je tiens à remercier tous les (post-)doctorants et (post-)doctorantes de l'IRMA et du Cerema que j'ai croisés de près ou de loin, sans qui ces trois années de thèse auraient paru bien plus longues. Merci aux membres de l'équipe du Click pour toutes ces séances où nous avons communié dans la gloire des poulies. Un merci tout particulier aux membres du comité restreint (qui se reconnaitront) pour des soirées de qualité, vous m'avez chacun et chacune aidé tout ce temps, par votre présence, votre confiance et votre amitié.

Je remercie également en passant tous mes amis non doctorants (pour certains de très longue date) pour avoir continué de me fréquenter toutes ces années.

Merci Mathilde de m'avoir supporté et encouragé ces derniers mois. Tu m'as apporté plus que tu ne le penses, et j'espère que tu continueras à me supporter de nombreuses années.

Enfin, je remercie mes parents et ma soeur pour leur patience et leur soutien constant pendant ces (trop) longues études, qui arrivent finalement à leur terme.

Narcissus, in the hidden fire of passion,
Wanes slowly, with the ruddy color going,
The strength and hardihood and comeliness,
Fading away, and even the very body
Echo had loved. She was sorry for him now,
Though angry still, remembering; you could hear her
Answer “Alas!” in pity, when Narcissus
Cried out “Alas!” You could hear her own hands beating
Her breast when he beat his. “Farewell, dear boy,
Beloved in vain!” were his last words, and Echo
Called the same words to him. His weary head
Sank to the greensward, and death closed the eyes
That once had marveled at their owner’s beauty.

Ovid, Metamorphoses, Book III, translated by Rolfe Humphries

Contents

Symbols

Ω	Room interior	p.26
$\partial\Omega$	Room walls	p.26
$\boldsymbol{n}$	Outward normal vector	p.26
$\partial_{\boldsymbol{n}}$	Normal derivative	p.26
$*$	Convolution operator	p.26
c	Speed of sound	p.26
β	Admittance coefficient	p.26
$\mathfrak{K}$	Wave number	p.27
f	Frequency	p.27
$H_\nu^{(1)}$	Hankel function of the first kind of order ν	p.40
$\odot$	Pointwise Hadamard product of vectors	p.42
$\mathcal{M}(X)$	Space of Radon measures on X	p.44
$\delta_{\boldsymbol{r}}$	Dirac mass at location $\boldsymbol{r}$	p.44
$\Vert\cdot\Vert_{\mathrm{TV}}$	Total variation norm	p.44
Γ^*	Hernitian adjoint of Γ	p.46
$\boldsymbol{r}^{\mathrm{mic}}$	Microphone location	p.54
$\boldsymbol{r}^{\mathrm{src}}$	Source location	p.54
$\Box$	D'Alembert operator	p.54
κ	Microphone filter	p.57
J_ν	Bessel function of the first kind of order ν	p.97
$\otimes$	Outer product of vectors	p.104
$:$	Real inner product of matrices	p.104
D_Γ	Tangential derivative	p.104
div_Γ	Tangential divergence	p.104
∇_Γ	Tangential gradient	p.104
$W^{p,q}$	Sobolev spaces	p.105
$p_{\Omega,\mathfrak{K}}$	Solution of the Helmholtz equation	p.128
$\mathcal{S}_{\mathrm{adm}}$	Set of admissible shapes	p.128

Introduction (Français)

Contexte et objectifs

Cette thèse étudie le problème inverse *d'entendre la forme d'une salle*. Bien que la dénomination fasse référence à *entendre la forme d'un tambour* [86], les deux problèmes diffèrent considérablement. En effet, le célèbre article publié par Kac en 1966 examine l'unicité de la forme d'un tambour par rapport aux fréquences propres de l'opérateur Laplacien-Dirichlet. En pratique, il n'est pas possible d'accéder directement aux fréquences propres ou aux fonctions propres à partir de mesures réelles. Nous examinerons donc le problème inverse, plus réaliste, de la reconstruction de la forme d'une pièce à partir de mesures effectuées en un nombre fini de positions de microphones dans la pièce. De plus, nous examinerons des *réponses impulsionnelles de salle* (RIR), c'est-à-dire les mesures ponctuelles de la réponse de la pièce à une source sonore qui est impulsionnelle à la fois en espace et en temps. Formellement, le champ de pression p résultant d'une source parfaitement impulsionnelle située en $\boldsymbol{r}^{\mathrm{src}}$ est la solution de l'équation des ondes inhomogène suivante à l'intérieur de la pièce Ω [27] :

$$\begin{cases} \frac{1}{c^2}\partial_t^2 p(\boldsymbol{r},t) - \Delta p(\boldsymbol{r},t) = \delta(t)\delta_{\boldsymbol{r}^{\mathrm{src}}}(\boldsymbol{r}) & (\boldsymbol{r},t) \in \Omega \times \mathbb{R} \\ p(\boldsymbol{r},t) = \partial_t p(\boldsymbol{r},t) = 0 & (\boldsymbol{r},t) \in \Omega \times \mathbb{R}_-^* \end{cases} \tag{1}$$

où c désigne la vitesse du son, qui sera prise constante et égale à [1] 343 m.s^{-1} dans nos applications. L'absorption et la réflexion partielles des ondes sonores sur les parois peuvent être modélisées en

[1] 343 m.s^{-1} est la vitesse du son à une température de 20°C et à une pression atmosphérique standard.

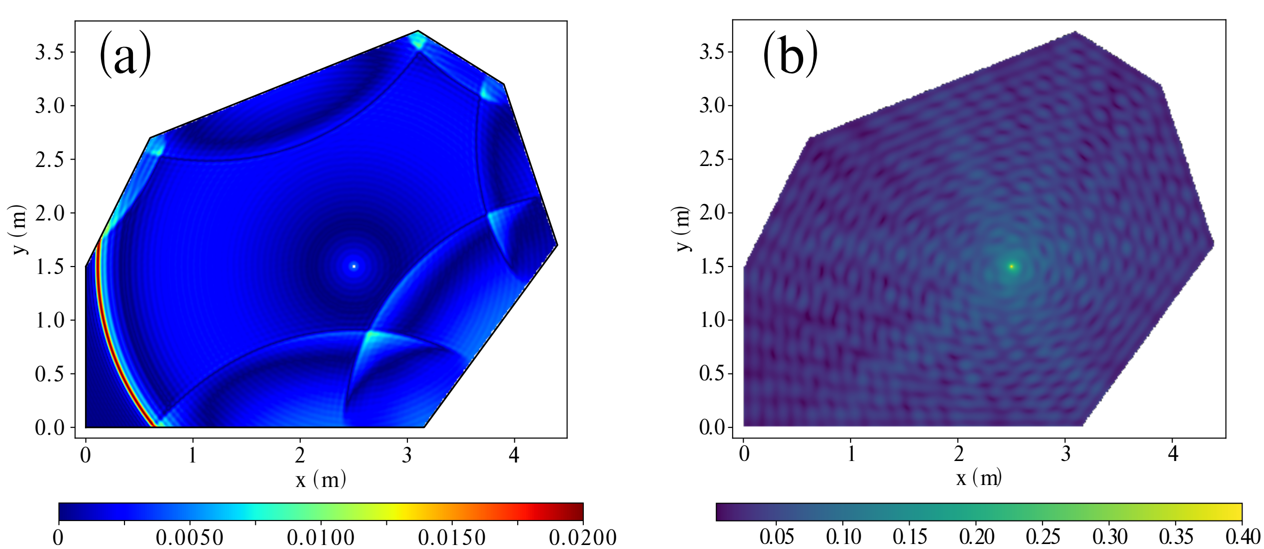

Figure 1: Simulations (a) temporelle ($t = 7$ ms) et (b) fréquentielle ($f = 1500$ Hz) de RIR pour une même position source dans une pièce polygonale 2D.

ajoutant des conditions au bord d'admittance sur la frontière $\partial\Omega$:

$$\partial_{\boldsymbol{n}} p(\boldsymbol{r}, t) + \frac{1}{c}\frac{\partial}{\partial t}\beta(\boldsymbol{r}, \cdot) * p(\boldsymbol{r}, \cdot)(t) = 0 \quad (\boldsymbol{r}, t) \in \partial\Omega \times \mathbb{R} \tag{2}$$

où $\partial_{\boldsymbol{n}}$ est la dérivée normale orientée vers l'extérieur, β est un filtre temporel représentant l'admittance des parois et $*$ désigne une convolution en temps. De manière équivalente, on peut considérer la formulation dans le domaine fréquentiel en appliquant une transformée de Fourier à l'équation des ondes. On obtient alors une équation de Helmholtz à chaque nombre d'onde (ou fréquence) :

$$\Delta\tilde{p}(\boldsymbol{r}, f) + \mathfrak{K}^2\tilde{p}(\boldsymbol{r}, f) = -\delta_{\boldsymbol{r}^{\mathrm{src}}}(\boldsymbol{r}) \quad (\boldsymbol{r}, f) \in \Omega \times \mathbb{R} \tag{3}$$

où $\mathfrak{K} = \frac{2\pi f}{c}$ est le nombre d'onde, f désignant la fréquence, et $\tilde{p}$ est la transformée de Fourier de p, définie par:

$$\tilde{p} : (\boldsymbol{r}, f) \mapsto \int_{-\infty}^{+\infty} p(\boldsymbol{r}, t)e^{-2i\pi f t}dt. \tag{4}$$

La condition au bord d'admittance (2) se transforme alors en une condition de Robin à coefficient complexe :

$$\partial_{\boldsymbol{n}}\tilde{p}(\boldsymbol{r}, f) + i\mathfrak{K}\tilde{\beta}(\boldsymbol{r}, f)\tilde{p}(\boldsymbol{r}, f) = 0 \quad (\boldsymbol{r}, f) \in \partial\Omega \times \mathbb{R}. \tag{5}$$

La figure 1 présente un exemple de réponse impulsionnelle simulée pour une pièce polygonale 2D dans les domaines fréquentiel et temporel.

Lorsque β est nul, les conditions aux limites (2) et (5) deviennent des conditions au bord homogènes de Neumann. Les conditions de Neumann modélisent des murs parfaitement réfléchissants,

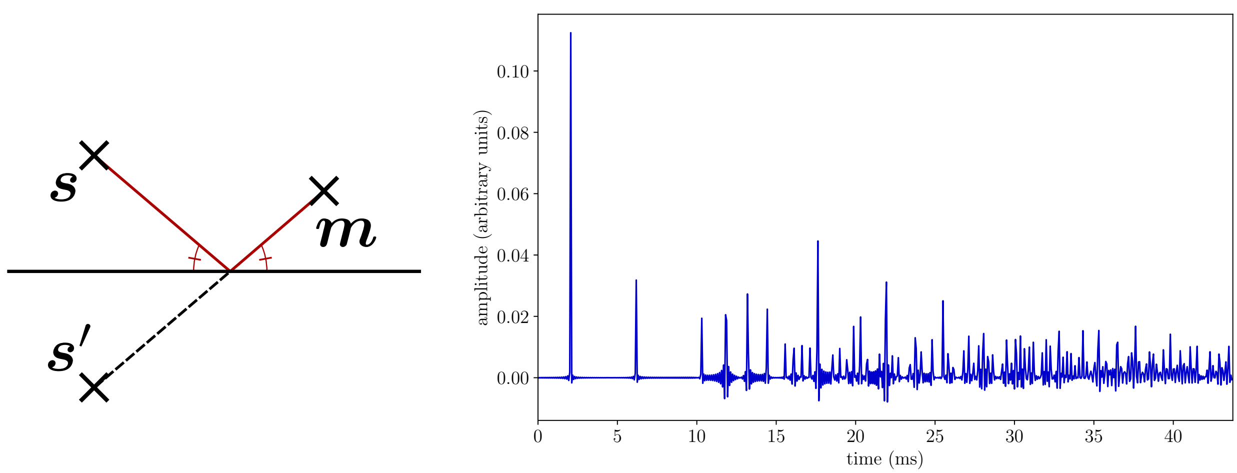

(a) Une source ponctuelle $\boldsymbol{s}$, sa source image $\boldsymbol{s}'$ et la réflexion spéculaire correspondante vers un récepteur $\boldsymbol{m}$.

(b) Réponse impulsionnelle de salle simulée à l'aide de la méthode des sources images à une fréquence d'échantillonnage de 16 kHz.

Figure 2

également appelés *murs rigides*. Dans certaines géométries, le modèle se simplifie considérablement dans ce cas, car on peut alors considérer le *modèle des sources images* (ISM) [5]. En résumé, l'ISM représente les chemins de *réflexions spéculaires* comme des sources virtuelles, les *sources images*. La figure 2a présente un chemin de réflexion spéculaire en 2D ainsi que la source et la source image correspondantes. La source image est construite en prenant le symétrique de la source par rapport à la surface réfléchissante. Il est à noter que la position d'une surface réfléchissante peut être facilement calculée à partir des positions d'une source et de sa source image. La figure 2b présente un exemple de RIR temporelle simulée en une position microphone fixée à l'aide de l'ISM. Le premier pic correspond au champ direct et les pics suivants aux réflexions spéculaires sur les parois. Ce modèle sera introduit plus en détail dans la section 1.1.

Lorsque l'on considère des mesures réelles, il faut tenir compte de certains facteurs limitants :

- Il est impossible d'enregistrer des signaux véritablement continus et il est nécessaire d'appliquer une discrétisation en temps.
- Les microphones ne peuvent pas mesurer des fréquences infiniment élevées et appliquent un effet de filtre sur les observations.

Le filtre appliqué par les microphones est généralement inconnu dans les scénarios réels. En pratique, nous considérerons un cas plus simple où les microphones imposent un filtre passe-bas idéal. Ce filtre est appliqué en convoluant les signaux en temps avec une fonction sinc. Comme la transformée de Fourier de sinc est une fonction porte, cela élimine complètement les effets de toutes les fréquences supérieures à une fréquence de coupure donnée. En outre, en raison de la nature discrète des signaux enregistrés, nous n'avons accès qu'à un nombre fini de mesures en temps t_n, en fréquence f_n ou en nombre d'ondes $\mathfrak{K}_n = \frac{2\pi f_n}{c}$, observées à plusieurs microphones dans la pièce.

À la lumière de ces problèmes et des modèles mentionnés ci-dessus, nous nous posons les questions suivantes :

Q1. Si nous supposons que les réflexions spéculaires sont dominantes et que nous contraignons la forme de la salle à être un parallélépipède rectangle en 3D, pouvons-nous reconstruire la configuration géométrique de la pièce directement à partir des RIR multicanales discrétisées en utilisant la méthode des sources images ?

Q2. Si β est un nombre réel constant et connu, pouvons-nous retrouver la géométrie d'une pièce polygonale en 2D à partir d'un nombre fini de mesures en fréquence de la solution de l'équation (3) grâce à des méthodes d'optimisation de forme ?

L'objectif de cette thèse est de développer un cadre mathématique permettant d'aborder ces questions et de fournir des justifications théoriques et numériques attestant que la réponse est positive dans un contexte assez général. Pour les deux questions, les positions des microphones les unes par rapport aux autres peuvent avoir un impact considérable sur la complexité et résolubilité du problème inverse.

Nous supposerons que la géométrie de l'antenne de microphones est connue, et qu'elle est sphérique (ou circulaire) dans la plupart des expériences, bien que les méthodes utilisées soient applicables à d'autres géométries. La position et l'orientation de l'antenne sont inconnues et devront être évaluées. Il convient de préciser que la restriction au cas 2D et aux polygones convexes dans **Q2** a été adoptée par souci de simplicité. Les méthodes développées dans cette section pourraient, en principe, être étendues au cas 3D et aux formes non convexes.

Structure du manuscrit

La partie I aborde **Q1** en formulant la question comme un problème inverse portant sur les positions des sources images. Le chapitre 1 présente le modèle des sources images de manière plus détaillée, ainsi que le cadre mathématique de la super-résolution qui sera utilisé dans cette partie. La section 1.3 introduit également deux revues de l'état de l'art pour les méthodes de localisation des sources images et d'estimation de la géométrie d'une salle à partir de mesures acoustiques.

Le chapitre 2 porte sur la localisation des sources images à partir de RIR multicanales discrètes. Nous introduisons une nouvelle formulation comme un problème d'optimisation parmi les mesures de Radon, qui est le cadre utilisé dans la reconstruction de sources parcimonieuses et la super-résolution. L'objectif est alors d'inverser un opérateur qui à un terme source dans l'équation d'onde associe les observations correspondantes enregistrées au niveau des microphones. Le problème inverse qui en découle est d'abord formulé dans la section 2.1.2 comme un problème de moindres carrés non convexe en dimension finie portant sur les amplitudes et les positions d'une combinaison linéaire de masses de Dirac. L'opérateur Γ^K prend ses arguments dans $\mathbb{R}_+^K \times \mathbb{R}^{3K}$ et ses valeurs dans $\mathbb{R}^{MN}$, où M est le nombre de microphones et N le nombre d'échantillons temporels. Son expression est donnée par

$$(\Gamma^K(\boldsymbol{a},\boldsymbol{r}))_{m,n} = \sum_{k=1}^{K} a_k \frac{\kappa(n/f_s - \left\|\boldsymbol{r}_k - \boldsymbol{r}_m^{\mathrm{mic}}\right\|_2 /c)}{4\pi \left\|\boldsymbol{r}_k - \boldsymbol{r}_m^{\mathrm{mic}}\right\|_2} \quad \forall (m,n) \in [\![1, M]\!] \times [\![0, N-1]\!] \tag{6}$$

où κ désigne le filtre des microphones, f_s est la fréquence d'échantillonnage et les $\boldsymbol{r}_m^{\mathrm{mic}}$ sont les positions des microphones. On notera que Γ^K est singulier à chaque position de microphone. En désignant par $\boldsymbol{x} \in \mathbb{R}^{MN}$ le vecteur d'observations, le problème des moindres carrés correspondant est alors le suivant :

$$\min_{\boldsymbol{a}\in\mathbb{R}_+^K, \boldsymbol{r}\in\mathscr{C}^K} \frac{1}{2} \left\|\Gamma^K(\boldsymbol{a},\boldsymbol{r}) - \boldsymbol{x}\right\|_2^2 \tag{7}$$

où $\mathscr{C}$ est un ensemble borné qui ne contient pas les emplacements des microphones. Nous étudions le caractère bien posé du problème (7) dans la section 2.2. Le problème est ensuite ramené à un problème d'optimisation convexe dans la section 2.3. En désignant par $\mathbb{R}_\varepsilon^3$ l'espace $\mathbb{R}_3$ privé de l'union des boules de rayon ε centrées sur les microphones, la fonction Γ^K se transforme alors en un opérateur linéaire Γ agissant sur les mesures de Radon $\mathcal{M}(\mathbb{R}^3_\varepsilon)$:

$$(\Gamma\psi)_{m,n} = \int_{\mathbb{R}^3_\varepsilon} \frac{\kappa(n/f_s - \left\|\boldsymbol{r} - \boldsymbol{r}_m^{\mathrm{mic}}\right\|_2/c)}{4\pi \left\|\boldsymbol{r} - \boldsymbol{r}_m^{\mathrm{mic}}\right\|_2} d\psi(\boldsymbol{r}) \quad \forall (m,n) \in [\![1, M]\!] \times [\![0, N-1]\!] \tag{8}$$

et le problème de moindres carrés de dimension finie devient le problème dit de Beurling-Lasso (BLASSO) :

$$\min_{\psi \in \mathcal{M}(\mathbb{R}^3_\varepsilon)} \frac{1}{2} \left\|\Gamma\psi - \boldsymbol{x}\right\|_2^2 + \lambda \|\psi\|_{\mathrm{TV}}. \tag{9}$$

Nous nous appuyons ensuite sur l'algorithme sliding-Frank-Wolfe [53] pour résoudre numériquement (9) et définissons dans la section 2.3.3 une procédure de reconstruction de la mesure composée par les sources images, dans laquelle des modifications spécifiques ont été appliquées afin d'adapter l'algorithme à notre cas. L'algorithme résultant est testé numériquement dans des expériences simulées à la section 2.4. Nous étudions comment la fréquence d'échantillonnage f_s, le nombre de microphones M et le niveau de bruit additif influent sur les résultats numériques.

Le chapitre 3 aborde le problème de la reconstruction de la configuration géométrique complète d'une pièce cubique à partir des positions des sources images. La géométrie de l'antenne est connue, et nous cherchons à estimer les 18 paramètres d'entrée de l'ISM : la position 3D de la source, les dimensions de la pièce, la translation et l'orientation de la pièce, et les coefficients d'absorption attribués à chaque mur. Nous définissons un algorithme en deux étapes qui estime d'abord l'orientation de l'antenne de microphones, puis récupère les dimensions de la pièce et les paramètres restants. En désignant par $\mathcal{G}$ l'ensemble des sources images reconstruites, l'estimation de l'orientation est réalisée en résolvant le problème d'optimisation suivant :

$$\max_{\|\boldsymbol{u}\|_2=1} J_3(\boldsymbol{u}), \quad \text{où} \quad J_3(\boldsymbol{u}) = \sum_{\boldsymbol{s},\boldsymbol{p} \in \mathcal{G}} f_3(\boldsymbol{u}, \boldsymbol{s} - \boldsymbol{p}). \tag{10}$$

Ici, $f_3(\boldsymbol{u}, \boldsymbol{v})$ vaut 1 si $\boldsymbol{u}$ est orthogonal à $\boldsymbol{v}$ et à 0 dans le cas contraire. La fonction objectif J_3 évalue donc le nombre d'orthogonalités entre un vecteur donné et les directions définies par la grille des sources images reconstruites. Nous prouvons dans la section 3.3 que, lorsque $\mathcal{G}$ est un sous-ensemble rectangulaire contigu de la grille des sources images cibles, c'est-à-dire que les sources images sont parfaitement localisées, la solution du problème (21) est un vecteur qui est orthogonal à un mur. L'emplacement de la source peut être facilement identifié à partir de $\mathcal{G}$. Une fois l'orientation récupérée, nous extrayons les sources images de premier ordre en recherchant les points à distance minimale situés dans les cônes définis par la source et les vecteurs normaux aux murs estimés précédemment. Nous utilisons ensuite ces sources de premier ordre pour récupérer les paramètres restants. L'algorithme complet est évalué dans des expériences numériques en section 3.2, en suivant la configuration expérimentale du chapitre 2. Nous comparons aussi favorablement l'algorithme à la méthode basée sur les matrices de distance euclidienne introduite dans [58].

Enfin, le chapitre 4 fournit une preuve alternative à la preuve formelle de la décomposition ISM publiée par Allen et Berkley en 1979 [5]. Contrairement à la preuve d'Allen et Berkley, notre preuve est effectuée dans le domaine temporel, utilise une représentation intermédiaire modale temporelle et traite explicitement la causalité de la solution.

La question **Q2** est traitée dans la partie II. Bien que les méthodes décrites dans cette partie soient applicables en 3D, afin de simplifier l'implémentation et de réduire les coûts de calcul, nous considérerons plutôt le cas simplifié de l'optimisation de polygones 2D. Nous commençons par rappeler des notions générales d'optimisation de formes dans le chapitre 5, ainsi que des outils plus spécifiques utilisés pour les formes polygonales. Nous présentons également la *méthode des solutions fondamentales* (MFS), qui est la méthode de simulation sans maillage utilisée pour résoudre l'équation de Helmholtz dans nos simulations numériques. Le chapitre 6 se concentre sur la résolution numérique du problème direct et présente la mise en œuvre de la MFS. Nous décrivons d'abord une stratégie d'échantillonnage adaptatif utilisée pour simuler efficacement la solution de l'équation de Helmholtz à de multiples fréquences. Dans la section 6.2, nous validons ensuite numériquement la méthode MFS sur quelques cas tests en comparant la solution MFS à des solutions analytiques ou à la solution générée par la méthode des éléments finis. Dans la section 6.3, nous présentons une méthode permettant d'utiliser la MFS pour simuler des RIR dans le domaine temporel en appliquant une transformée de Fourier inverse et un filtre passe-haut.

Le problème inverse est abordé au chapitre 7. La formulation sous forme de problème d'optimisation de forme est décrite dans la section 7.1. Nous considérons le problème d'optimisation suivant :

$$\min_{\Omega \in \mathcal{S}_{\mathrm{adm}}} J(\Omega), \quad J(\Omega) \coloneqq \frac{1}{2LM} \sum_{l=1}^{L} \sum_{m=1}^{M} \left| p_{\Omega,\mathfrak{K}_l}(\boldsymbol{r}_m^{\mathrm{mic}}) - p_{\mathrm{obs},\mathfrak{K}_l}(\boldsymbol{r}_m^{\mathrm{mic}}) \right|^2 \tag{11}$$

où $p_{\Omega,\mathfrak{K}}$ est la solution de l'équation de Helmholtz sur Ω pour le nombre d'onde $\mathfrak{K}$, $p_{\mathrm{obs},\mathfrak{K}}$ est le champ de pression observé et $\mathcal{S}_{\mathrm{adm}}$ est l'ensemble des polygones convexes avec un nombre fixé d'arêtes. La dérivée de forme de la fonction objectif est calculée de manière formelle dans la section 7.2 en utilisant une méthode lagrangienne et des représentations tensorielles. En particulier, nous devons tenir compte de l'irrégularité des polygones, ce qui ajoute des termes tangentiels non standards à la formule finale. La section 7.3 donne une description détaillée du cadre numérique mis en place pour résoudre le problème (11) en utilisant une méthode de descente de gradient et la dérivée de forme calculée dans la section 7.2. Nous discutons du choix de la paramétrisation, calculons le gradient paramétrique correspondant et introduisons un terme de pénalisation qui impose des contraintes d'inclusion pour le microphone et les sources. L'algorithme de descente de gradient lui-même est défini dans la section 7.3.4. Enfin, l'algorithme est évalué expérimentalement dans la section 7.4. Nous considérons deux configurations : l'une sans information préalable sur la forme où nous effectuons des intialisations aléatoires, et une configuration où nous essayons d'affiner une estimation initiale bruitée de la forme.

Contributions

Nous donnons dans cette section un aperçu des principales contributions de cette thèse. Les chapitres 1 et 5 sont omis car ils présentent des notions générales et des outils bien connus dans la littérature.

Chapitre 2. Le problème inverse de localisation des sources images est abordé dans ce chapitre. Nous adoptons une approche différente des méthodes existantes en traitement du signal audio et acoustique en formulant le problème comme un problème d'optimisation sur des mesures de Radon. Nous commençons par étudier le caractère bien posé du problème d'optimisation correspondant en dimension finie dans la section 2.2. En raison de la présence de singularités du noyau de l'opérateur à chaque emplacement de microphone, l'existence de solutions n'est pas garantie lorsque les positions des sources ne sont pas contraintes. En particulier, nous démontrons que tout comportement est possible : la non-existence peut se produire pour certains vecteurs d'observation $\boldsymbol{x}$, et, inversement, nous prouvons que l'existence peut se produire sous certaines hypothèses sur $\boldsymbol{x}$ et sur le filtre des microphones dans le théorème 2.2.1. Nous étudions ensuite numériquement le problème d'optimisation convexe relaxé en dimension infinie (BLASSO). Ce cadre nous permet de tirer parti des outils de super-résolution pour récupérer les sources images sans utiliser de grille. Contrairement aux méthodes proposées précédemment en traitement du signal audio et acoustique, la méthode introduite nécessite peu de connaissances à priori sur la configuration géométrique d'une pièce parallélépipédique. À la connaissance de l'auteur, il s'agit de la première application de techniques de super-résolution pour retrouver les positions de sources images en 3D directement à partir d'une RIR discrétisée. L'opérateur d'onde considéré Γ diffère également des applications usuelles de la super-résolution en imagerie, car son noyau est singulier et présente une décroissance linéaire de l'amplitude avec la distance. Nous présentons un algorithme numérique pour résoudre le BLASSO, et évaluons en détail ses performances dans la section 2.4. L'algorithme est basé sur l'algorithme sliding-Frank-Wolfe [53], qui a été fortement adapté à notre cas d'application spécifique et à la structure de l'opérateur Γ. En particulier, nous modifions l'initialisation de l'étape de localisation des sources pour prendre en compte la nature sphérique des ondes sonores émises. Nous mettons également en place une procédure d'extension qui traite des signaux de plus en plus longs, afin de gérer la croissance quadratique du nombre de sources images à reconstruire. L'algorithme résultant récupère un nombre record de sources images avec une grande précision dans des expériences simulées, avec des taux de rappel supérieurs à 95 % et avec des erreurs euclidiennes inférieures au centimètre dans les conditions les plus favorables. En particulier, les positions des sources images de premier ordre, qui contiennent notamment l'information sur les emplacements des murs, sont reconstruites avec un taux de rappel de 99 % dans les simulations. L'algorithme démontre également une robustesse satisfaisante face au bruit. Le modèle, l'algorithme de reconstruction et certains résultats numériques ont été publiés dans une revue de traitement du signal [136]. L'étude numérique approfondie fournie dans ce chapitre, l'analyse théorique du problème d'optimisation et une présentation plus détaillée de l'algorithme seront soumises à un journal de problèmes inverses.

Chapitre 3. En s'appuyant sur l'algorithme de reconstruction des sources images présenté dans la section 2.3.3, le chapitre 3 introduit un nouvel algorithme de réversion des sources images pour récupérer tous les paramètres géométriques d'une configuration de pièce parallélépipédique. Un écart notable par rapport aux algorithmes existants est l'ajout d'une étape d'estimation de l'orientation de l'antenne de microphones, un facteur souvent négligé dans les algorithmes de reconstruction de la géométrie. Cette étape est en partie rendue possible par les taux de rappel élevés de notre algorithme de localisation des sources images. De plus, l'heuristique utilisée est justifiée théoriquement dans la section 3.3, où nous prouvons que le problème d'optimisation retrouve bien l'orientation lorsque les sources images sont parfaitement estimées.

Une fois la position de la vraie source extraite, les sources images de premier ordre sont identifiées en recherchant les points à distance minimale situés dans des cônes définis par la source et les directions calculées lors de l'étape d'estimation de l'orientation. Prendre en compte l'orientation permet une meilleure identification des sources images de premier ordre en éliminant certaines sources faussement reconstruites (faux positifs) de l'espace de recherche. L'orientation est également utilisée pour améliorer la précision de l'estimation des dimensions de la pièce en effectuant une projection sur les axes de la salle. Lors des tests sur un ensemble de données de pièces parallélépipédique générées aléatoirement, nous obtenons des erreurs remarquablement faibles pour l'estimation des dimensions de la pièce, avec des erreurs absolues moyennes inférieures au millimètre. Nous nous comparons également favorablement à une méthode de référence reposant sur les matrices de distance euclidienne introduite dans [58]. Ce chapitre a été soumis sous forme d'article à un journal de traitement du signal audio [137].

Chapitre 4. Ce chapitre présente une preuve alternative du résultat démontré de manière formelle par Allen et Berkley en 1976 [5], à savoir que la solution de l'équation des ondes avec des conditions aux limites de Neumann peut être décomposée en une somme infinie d'ondes sphériques en 3D (fonctions de Green). Contrairement à la démonstration d'Allen et Berkley, notre preuve reste dans le domaine temporel et une représentation modale intermédiaire temporelle est présentée. Notre preuve impose en hypothèse initiale la causalité des réponses impulsionnelles, tandis que la causalité n'était pas établie et forcée à posteriori dans l'article original.

Chapitre 6. Nous détaillons dans ce chapitre l'implémentation de la MFS sur des domaines polygonaux. En particulier, nous présentons la stratégie d'échantillonnage adaptatif qui sera utilisée pour résoudre l'équation de Helmholtz simultanément à plusieurs fréquences en parallèle. Cette méthode se compare favorablement aux simulations FEM en termes de coût de calcul à haute fréquence. Nous introduisons également une méthode de calcul qui utilise la MFS dans le domaine fréquentiel pour simuler des RIR dans le domaine temporel.

Chapitre 7. Dans ce chapitre, nous abordons enfin l'application de méthodes d'optimisation de forme pour la reconstruction de la géométrie d'une salle. Nous utilisons une méthode lagrangienne en vue de calculer une expression de la dérivée de forme de la fonction coût associée. Un aspect inhabituel de ce problème est que nous considérons des formes peu régulières. Nous appliquons les méthodes décrites dans [103] afin d'obtenir une formulation de la dérivée de forme distribuée sur le bord. Cette formulation contient des termes tangentiels non standards en raison de l'irrégularité des polygones à chaque sommet. Dans la section 7.3, nous détaillons l'algorithme de descente de gradient implémenté pour résoudre le problème inverse. Plutôt que de construire un maillage, nous paramétrisons les polygones en utilisant les sommets ou des demi-plans, et optimisons directement la fonction coût au sein des polygones convexes. Les tests numériques effectués dans la section 7.4 montrent que l'algorithme est capable de retrouver la forme d'une pièce polygonale à partir d'initialisations bruitées et d'une plage de fréquences restreinte, avec une erreur angulaire moyenne sur les murs de $0,26°$ pour les quadrilatères. Nous testons également l'algorithme en exploitant toutes les fréquences jusqu'à une fréquence maximale et des initialisations aléatoires, et obtenons un taux de rappel global pour les murs de 77 % sur un ensemble de polygones aléatoires. Nous obtenons également des erreurs angulaires moyennes satisfaisantes de $3,1°$ pour les quadrilatères correctement estimés et de $3,9°$ pour les pentagones. Les expériences indiquent qu'augmenter le nombre d'initialisations aléatoires et de pas de gradient peut encore améliorer la précision. Le travail mis en route dans ce chapitre fera l'objet d'une future publication dans une revue de mathématiques appliquées.

Communications

Publications

Shape optimization for polygonal room reconstruction from acoustic measurements
Antoine Deleforge, Cédric Foy, Antoine Laurain, Yannick Privat et Tom Sprunck.
Travail en cours.

Can one hear the shape of a cuboid ?
Antoine Deleforge, Cédric Foy, Yannick Privat et Tom Sprunck.
À soumettre à un journal de problèmes inverses.

Fully Reversing the Shoebox Image Source Method: From Impulse Responses to Room Parameters [137]
Tom Sprunck, Antoine Deleforge, Yannick Privat et Cédric Foy, 2024.
Soumis à IEEE Transactions on Audio, Speech, and Language Processing.

Gridless 3D Recovery of Image Sources From Room Impulse Responses [136]
Tom Sprunck, Antoine Deleforge, Yannick Privat and Cédric Foy, 2022.
Publié dans IEEE Signal Processing Letters.

Conférences et séminaires

Exposés scientifiques

- Séminaire d'équipe, *IRMA*, Université de Strasbourg, Novembre 2024
- *46ème Congrès National d'Analyse Numérique*, Le-Bois-Plage-En-Ré, juin 2024
- Séminaire d'équipe, *MaLGa*, University of Genoa, Italie, mai 2024.
- Séminaire d'équipe, *IECL*, Université de Lorraine, Nancy, janvier 2024.
- Séminaire de l'équipe Inria MACARON, Belmont, février 2024.
- Séminaire des doctorants, *Irma*, Université de Strasbourg, décembre 2023.
- GDR de l'ANR Shapo, Sorbonne Université, Paris, avril 2023.
- 24th International Congress on Acoustics, Gyeongju, Corée, novembre 2022.
- 16e Congrès Français d'Acoustique, Marseille, avril 2022.

Sessions poster :

- *IEEE International Conference on Acoustics, Speech, and Signal Processing.*
  Juin 2023. Rhodes, Grèce.
- *45ème Congrès National d'Analyse Numérique.*
  Mai 2022. Evian, France.

Introduction (English)

Context and objectives

This thesis studies the so-called inverse problem of *hearing the shape of a room*. Although the denomination is a reference to *hearing the shape of a drum* [86], the two problems differ considerably. Indeed, Kac's famous 1966 article considers the uniqueness of the shape of a drum relatively to its Dirichlet eigenfrequencies. In practice, one cannot directly access the eigenfrequencies or eigenfunctions from real-life measurements. We will thus consider the more realistic inverse problem of recovering the shape of a room from measurements at a finite number of microphone locations in the room. Moreover, we will consider *Room Impulse Responses*, *i.e.* point measurements of the response of the room to a sound source that is impulsive both in space and time. Formally, the pressure field p resulting from a perfectly impulsive source located at $\boldsymbol{r}^{\mathrm{src}}$ is solution to the following inhomogeneous wave equation inside the room Ω [27]:

$$\begin{cases} \frac{1}{c^2}\partial_t^2 p(\boldsymbol{r},t) - \Delta p(\boldsymbol{r},t) = \delta(t)\delta_{\boldsymbol{r}^{\mathrm{src}}}(\boldsymbol{r}) & (\boldsymbol{r},t) \in \Omega \times \mathbb{R} \\ p(\boldsymbol{r},t) = \partial_t p(\boldsymbol{r},t) = 0 & (\boldsymbol{r},t) \in \Omega \times \mathbb{R}_-^* \end{cases} \tag{12}$$

where c is the speed of sound, which will be constant and equal[2] to 343 m.s^{-1} in our applications. The partial absorption and reflection of the sound waves at the walls can be modeled by adding admittance conditions on the boundary $\partial\Omega$:

$$\partial_{\boldsymbol{n}} p(\boldsymbol{r},t) + \frac{1}{c}\frac{\partial}{\partial t}\beta(\boldsymbol{r},\cdot) * p(\boldsymbol{r},\cdot)(t) = 0 \quad (\boldsymbol{r},t) \in \partial\Omega \times \mathbb{R} \tag{13}$$

[2]343 m.s^{-1} is the speed of sound at a temperature of 20°C and standard atmospheric pressure.

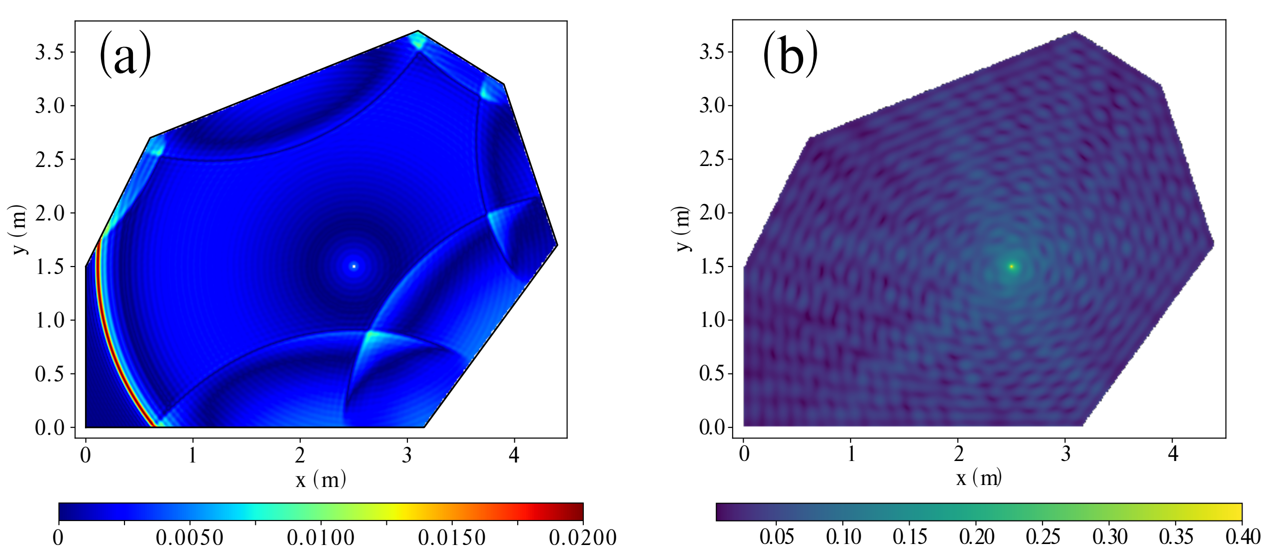

Figure 3: (a) Time ($t = 7$ ms) and (b) frequency domain ($f = 1500$ Hz) simulations of a RIR for the same source location in a 2D polygonal room.

where $\partial_{\boldsymbol{n}}$ is the outward normal derivative, β is the time filter representing the admittance of the walls and $*$ denotes a time-domain convolution. Equivalently, one can consider the frequency-domain formulation by applying a Fourier transform to the wave equation. This yields a Helmholtz equation at each wave number (or frequency):

$$\Delta\tilde{p}(\boldsymbol{r}, f) + \mathfrak{K}^2\tilde{p}(\boldsymbol{r}, f) = -\delta_{\boldsymbol{r}^{\mathrm{src}}}(\boldsymbol{r}) \quad (\boldsymbol{r}, f) \in \Omega \times \mathbb{R} \tag{14}$$

where $\mathfrak{K} = \frac{2\pi f}{c}$ is the wave number, f denoting the frequency, and $\tilde{p}$ is the time Fourier transform of p, *i.e.*:

$$\tilde{p} : (\boldsymbol{r}, f) \mapsto \int_{-\infty}^{+\infty} p(\boldsymbol{r}, t)e^{-2i\pi ft}dt. \tag{15}$$

The admittance boundary condition (13) then turns into a complex Robin condition:

$$\partial_{\boldsymbol{n}}\tilde{p}(\boldsymbol{r}, f) + i\mathfrak{K}\tilde{\beta}(\boldsymbol{r}, f)\tilde{p}(\boldsymbol{r}, f) = 0 \quad (\boldsymbol{r}, f) \in \partial\Omega \times \mathbb{R}. \tag{16}$$

Fig. 3 presents an example of RIR simulation in a 2D polygonal room in time and frequency domain.

When β vanishes to zero, the boundary conditions (13) and (16) become homogeneous Neumann boundary conditions. Neumann conditions model perfectly reflecting walls, also called *rigid walls*. For certain geometries, the model simplifies considerably in that case, as one can then consider the *Image Source Model* (ISM) [5]. In short, the ISM represents *specular reflection* paths as virtual sources, the *image sources*. Fig. 4a presents a specular reflection path in 2D and the corresponding source and image source. The image source is constructed by taking the symmetry of the source

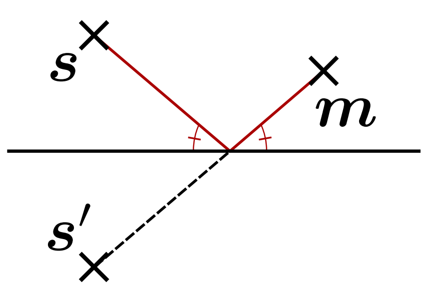

(a) UA point source $\boldsymbol{s}$, its image source $\boldsymbol{s}'$ and the specular reflection path to a receiver $\boldsymbol{m}$.

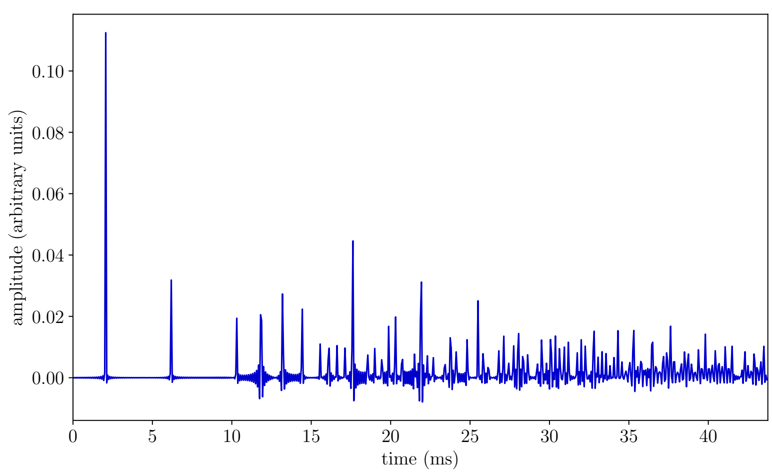

(b) Time-domain RIR simulated using the ISM and a 16 kHz sampling frequency.

Figure 4

with respect to the reflecting surface. Note that the location of a reflecting surface can be calculated from the locations of a source and its image source. An example of time-domain RIR simulated at a given microphone location using the ISM is presented in Fig. 4b, where the first peak corresponds to the direct path and the following peaks to specular reflections. This model will be introduced more in detail in Section 1.1.

When working with actual measurements, one has to take into account some limiting factors:

- We are unable to record truly continuous signals, and a time discretization is applied.
- Microphones cannot measure infinitely high frequencies and have a filtering effect on the observations.

The filter applied by the microphones is usually unknown in real-life scenarios. In practice, we will consider a simpler case where the microphones impose an ideal low-pass filter. This is enforced by convoluting the signals in time with a sinc function. As the Fourier transform of sinc is a rectangular (or gate) function, this completely deletes the effect of all the frequencies above a given cutting frequency. Moreover, due to the discrete nature of recorded signals, we will only have access to a finite number of time t_n, frequencies f_n or equivalently wave number $\mathfrak{K}_n = \frac{2\pi f_n}{c}$ measurements, observed at multiple microphone locations in the room. In light of these issues and the models mentioned above, we consider the following questions:

Q1. If we assume specular reflections are dominant and constrain the room to be a 3D cuboid, can we recover the geometric configuration of the room directly from discretized multichannel RIRs by using the ISM ?

Q2. If β is a known, constant real number, can we recover the shape of a convex, 2D polygonal room from discrete frequency measurements of the solution to Eq. (14) through shape optimization methods ?

The objective of this thesis is to develop a mathematical framework to address these questions and provide both theoretical and numerical evidence that the answer is positive under some broad settings. For both questions, the locations of the microphones relative to each other can have a massive impact on the complexity and solvability of the inverse problem. We will assume the geometry of the microphone array to be known, and to be spherical (or circular) in most experiments, although the underlying methods can be applied to other geometries. The location and orientation of the array are unknown and will need to be evaluated. Note that the restriction to the 2D case and convex polygons in **Q2** is made for simplicity. The methods developed in this section could, in principle, be extended to the 3D case and non-convex shapes.

Structure of the manuscript

Part I tackles **Q1** by formulating the question as an inverse problem on the locations of the image sources. Chapter 1 presents the Image Source Model and the super-resolution framework in more details. We also provide in Section 1.3 two detailed state-of-the-art reviews on image-source localization methods, and room geometry estimation from acoustic measurements.

Chapter 2 focuses on the localization of image sources from discrete multichannel RIRs. We introduce a novel formulation as an optimization problem amongst Radon measures, which is the framework used in sparse source reconstruction and super-resolution. The objective is then to reverse an operator that maps a source term in the wave equation to the recorded observations at the microphones. The ensuing inverse problem is first formulated in Section 2.1.2 as a least-squares, non-convex finite-dimensional problem on the amplitudes and locations of a linear combination of Dirac masses. The operator Γ^K takes its arguments in $\mathbb{R}_+^K \times \mathbb{R}^{3K}$ and its values in $\mathbb{R}^{MN}$, where M is the number of microphones and N the number of time samples. Its expression is given by:

$$(\Gamma^K(\boldsymbol{a}, \boldsymbol{r}))_{m,n} = \sum_{k=1}^{K} a_k \frac{\kappa(n/f_s - \left\|\boldsymbol{r}_k - \boldsymbol{r}_m^{\mathrm{mic}}\right\|_2 / c)}{4\pi \left\|\boldsymbol{r}_k - \boldsymbol{r}_m^{\mathrm{mic}}\right\|_2} \quad \forall (m,n) \in [\![1, M]\!] \times [\![0, N-1]\!] \tag{17}$$

where κ is the microphones' filter, f_s is the sampling frequency and $\boldsymbol{r}_m^{\mathrm{mic}}$ are the microphones' positions. Note that Γ^K is singular at each microphone's location. Denoting by $\boldsymbol{x} \in \mathbb{R}^{MN}$ the vector of observations, the corresponding least-squares problem is then:

$$\min_{\boldsymbol{a} \in \mathbb{R}_+^K, \boldsymbol{r} \in \mathscr{C}^K} \frac{1}{2} \left\|\Gamma^K(\boldsymbol{a}, \boldsymbol{r}) - \boldsymbol{x}\right\|_2^2 \tag{18}$$

where $\mathscr{C}$ is a bounded set from which we exclude the microphones' locations. We proceed to study the well-posedness of Problem (18) in Section 2.2. The problem is then relaxed to a convex optimization problem in Section 2.3. Denoting by $\mathbb{R}_\varepsilon^3$ the space $\mathbb{R}_3$ from which we removed a ball of radius ε around each microphone, the functional Γ^K then translates to a linear operator Γ acting on Radon measures $\mathcal{M}(\mathbb{R}_\varepsilon^3)$:

$$(\Gamma\psi)_{m,n} = \int_{\mathbb{R}_\varepsilon^3} \frac{\kappa(n/f_s - \left\|\boldsymbol{r} - \boldsymbol{r}_m^{\mathrm{mic}}\right\|_2 / c)}{4\pi \left\|\boldsymbol{r} - \boldsymbol{r}_m^{\mathrm{mic}}\right\|_2} d\psi(\boldsymbol{r}) \quad \forall (m,n) \in [\![1, M]\!] \times [\![0, N-1]\!] \tag{19}$$

and the least-squares problem becomes the so-called Beurling-Lasso (BLASSO):

$$\min_{\psi \in \mathcal{M}(\mathbb{R}_\varepsilon^3)} \frac{1}{2} \|\Gamma\psi - \boldsymbol{x}\|_2^2 + \lambda \|\psi\|_{\mathrm{TV}}. \tag{20}$$

We then build on the sliding-Frank-Wolfe algorithm [53] to solve numerically (20) and define in Section 2.3.3 a procedure to reconstruct the measure composed by the image sources, where specific modifications were applied in order to adapt the algorithm to our case. The resulting algorithm is extensively tested in numerical experiments in Section 2.4. We study how the sampling frequency f_s, the number of microphones M and the level of additive noise affect the numerical results.

Chapter 3 addresses the problem of reconstructing the complete geometric configuration of a cuboid room from the locations of the image-sources. The geometry of the antenna is known data, and we seek to estimate the 18 input parameters of the ISM: the 3D source position, the dimensions of the room, the room translation and orientation, and the absorption coefficients attributed to each wall. We define a two-step algorithm that first estimates the orientation of the microphone array and then recovers the room dimensions and the rest of the parameters. Denoting by $\mathcal{G}$ the set of recovered image sources, orientation recovery is achieved by solving the optimization problem:

$$\max_{\|\boldsymbol{u}\|_2=1} J_3(\boldsymbol{u}), \quad \text{where} \quad J_3(\boldsymbol{u}) = \sum_{\boldsymbol{s},\boldsymbol{p}\in\mathcal{G}} f_3(\boldsymbol{u}, \boldsymbol{s}-\boldsymbol{p}). \tag{21}$$

Here, $f_3(\boldsymbol{u}, \boldsymbol{v})$ is equal 1 if $\boldsymbol{u}$ is orthogonal to $\boldsymbol{v}$ and 0 otherwise. The objective function J_3 thus evaluates the number of orthogonalities between a given vector and the directions defined by the recovered image-sources grid. We prove in Section 3.3 that, when $\mathcal{G}$ is a contiguous rectangular subset of the target image-sources grid, *i.e.* we have a perfect localization of image sources, the solution to Problem (21) is a vector that is orthogonal to a wall. The source location can be easily identified from $\mathcal{G}$. Once the orientation is recovered, we extract the first-order image-sources by searching for the closest points that are located in the cones defined by the source and the estimated wall normal vectors. We then use these estimated first-order sources to recover the remaining parameters. The full algorithm is evaluated in numerical experiments in Section 3.2, following the experimental setup of Chapter 2. We also favorably compare the algorithm against the seminal Euclidean distance matrix method introduced in [58].

Finally, Chapter 4 provides an alternative proof to the formal proof of the ISM decomposition given by Allen and Berkley in 1979 [5]. Contrarily to Allen and Berkley's proof, our proof remains in time domain, uses a time-domain modal intermediate representation, and explicitly addresses the causality of the solution.

Question **Q2** is addressed in Part II. Although the methods described in this part are applicable to the 3D case, in order to simplify the implementation and reduce the computational cost we will consider instead the simplified case of optimizing 2D polygons. We begin by recalling general notions of shape optimization in Chapter 5, as well as more specific tools used for polygonal shapes. We also present the *Method of Fundamental Solutions* (MFS), which is the meshless simulation method used to solve the Helmholtz equation in our numerical simulations. Chapter 6 focuses on the numerical resolution of the forward problem and presents our implementation of the MFS. We first describe an adaptive sampling strategy used to efficiently simulate the solution to the Helmholtz equation at numerous frequencies. In Section 6.2, we then validate numerically the MFS method on some test cases by comparing the MFS solution to analytical solutions or to the solution obtained by a finite element method. In Section 6.3, we present a method to use the MFS to simulate time-domain RIRs by applying an inverse Fourier transform and a high-pass filter.

The inverse problem itself is tackled in Chapter 7. The shape optimization formulation is described in Section 7.1. In brief, we consider the following optimization problem:

$$\min_{\Omega \in \mathcal{S}_{\mathrm{adm}}} J(\Omega), \quad J(\Omega) := \frac{1}{2LM} \sum_{l=1}^{L} \sum_{m=1}^{M} \left| p_{\Omega,\mathfrak{K}_l}(\boldsymbol{r}_m^{\mathrm{mic}}) - p_{\mathrm{obs},\mathfrak{K}_l}(\boldsymbol{r}_m^{\mathrm{mic}}) \right|^2 \tag{22}$$

where $p_{\Omega,\mathfrak{K}}$ is the solution to the Helmholtz equation on Ω at wave number $\mathfrak{K}$, $p_{\mathrm{obs},\mathfrak{K}}$ is the observed pressure field and $\mathcal{S}_{\mathrm{adm}}$ is the set of convex polygons with a fixed number of edges S. The shape derivative of the objective function is formally computed in Section 7.2 by using a Lagrangian method and tensor representations. In particular, we have to take into account the non-smooth nature of the polygons, which adds non-standard tangential terms to the final formula. Section 7.3 gives a detailed description of the numerical framework used for solving Problem (22) by using a gradient descent method and the shape derivative that was calculated in Section 7.2. We discuss the choice of parametrization, compute the corresponding parametric gradient and introduce a penalization term that enforces inclusion constraints for the microphone and sources. The gradient descent algorithm itself is defined in Section 7.3.4. Finally, the algorithm is evaluated experimentally in Section 7.4. We consider two setups: one with no prior information on the shape where we use random initializations, and a configuration where we try to refine a noisy initial guess of the shape.

Contributions

We give in this section an overview of the main contributions of this thesis. Chapters 1 and 5 are skipped as they present general notions and tools that are well-known in the literature.

Chapter 2. The problem of image-source localization is tackled in this chapter. We take a different approach from existing methods in audio and acoustic signal processing by formulating the problem as an optimization problem on Radon measures. We begin by studying the well-posedness of the corresponding optimization problem in finite dimension in Section 2.2. Due to the presence of kernel singularities at each microphone location, the existence of solutions is not guaranteed when the locations of the sources are not constrained. In particular, we demonstrate that every behavior is possible: non-existence can happen for certain observation vectors $\boldsymbol{x}$, and conversely we prove that existence can happen under some hypotheses on $\boldsymbol{x}$ and on the microphones' filter in Theorem 2.2.1. We then investigate numerically the relaxed, infinite-dimensional convex optimization problem (BLASSO). This setting allows us to leverage the super-resolution framework to recover the image sources in a gridless manner. Contrarily to prior methods in audio and acoustic signal processing, the proposed method requires little a priori knowledge on the cuboid room's geometric configuration. To the best of the author's knowledge, this is the first application of super-resolution techniques to recover 3D image source locations directly from a multichannel RIR. The considered wave operator Γ also strays from usual applications of super-resolution in imagery, as its kernel is singular in nature and presents a linear decrease in amplitude with distance. We present a numerical algorithm to solve the BLASSO, and extensively evaluate its performance in Section 2.4. The algorithm is based on the sliding-Frank-Wolfe algorithm [53], which was heavily adapted to our specific problem and the structure of the operator Γ. In particular, we tailor the initialization of the source location search step to take into account the spherical nature of incoming sound waves. We also use an extension procedure that deals with increasingly long signals, in order to handle the quadratic growth in the number of image sources to be retrieved. The resulting algorithm retrieves an unprecedented number of image sources with high accuracy in simulated experiments, with global recall rates over 95 % and with Euclidean errors below the centimeter in the most favorable conditions. In particular, first-order image-source locations, that notably contain the information on wall locations, are recovered at a 99 % recall rate in simulations. The algorithm also demonstrates satisfactory robustness to noise. The model, the reconstruction algorithm and some numerical results were published in a signal processing journal [136]. A more extensive numerical study, the theoretical analysis and a more detailed presentation of the algorithm will be submitted to an inverse problems journal.

Chapter 3. Building on the image-source recovery algorithm presented in Section 2.3.3, Chapter 3 introduces a novel image-source reversion algorithm to recover every geometric parameter of a cuboid room configuration. A notable departure from existing algorithms is the incorporation of a microphone array orientation recovery step, which is a factor usually overlooked in geometry recovery algorithms. This step is in part made possible by the high recovery rates of our image-source localization algorithm. Moreover, the heuristic used is theoretically justified in Section 3.3 where we prove that the optimization problem does indeed recover the orientation when the image sources are perfectly estimated.

Once the true source's location has been extracted, the first-order image-sources are identified by searching for the closest points located in cones defined by the source and the directions calculated in the orientation recovery step. Using the orientation allows for a better identification of first order image sources by eliminating false positives from the search space. The orientation is also used to improve the accuracy of room dimension estimation by projecting onto the correct axes. When testing on a dataset of randomly generated cuboid rooms, we achieve remarkably low errors in room dimension estimation, with mean absolute errors falling below a millimeter. We also compare favorably to the baseline method of Euclidean distance matrix introduced in [58].This chapter was submitted in article form to an audio signal processing journal [137].

Chapter 4. This chapter presents an alternative proof to the result proved formally by Allen and Berkley in 1976 [5], that is, that the solution to the wave equation with Neumann boundary conditions can be decomposed by an infinite sum of spherical waves in 3D (Green's functions). Contrarily to Allen and Berkley's proof, our proof remain in time domain and a time-domain modal intermediate representation is presented. Our proof imposes the causality of the RIR as an initial hypothesis, while causality is not established and only enforced a posteriori in Allen and Berkley's article.

Chapter 6. We detail our implementation of the MFS on polygonal domains in this chapter. In particular, we present the adaptive sampling strategy that will be used to solve the Helmholtz equation at multiple frequencies in parallel. The method compares favorably with FEM simulations in terms of computational cost at high frequencies. We also introduce a simulation method that uses the MFS in frequency-domain to simulate time-domain RIRs.

Chapter 7 In this chapter, we finally tackle shape optimization for room reconstruction. We use a Lagrangian method to compute a shape derivative for the associated cost function. An unconventional aspect of this problem is that we consider non-smooth shapes. We apply the methods described in [103] in order to obtain a boundary formulation of the derivative, which involves non-standard tangential terms due to the polygons' irregularity. In Section 7.3, we expand on the gradient descent algorithm used to solve the inverse problem. Rather than constructing a mesh, we parametrize polygons using vertices or half-planes and optimize directly amongst convex polygons. The tests in Section 7.4 show that the algorithm is able to recover the shape of a polygonal room from noisy initializations and limited frequency data, with a mean angular error on walls of 0.26° for quadrilaterals. We also test the algorithm using all frequencies up to a maximum frequency and random initializations, and get an overall wall recall rate of 76 % over a set of random polygons. We also get satisfactory mean angular errors of 3.1° for correctly estimated quadrilaterals and 3.9° for pentagons. Experiments indicate that increasing the number of random initializations and gradient steps can further increase accuracy. The work begun in this chapter will be part of a future publication in an applied mathematics journal.

Communications

Publications

Shape optimization for polygonal room reconstruction from acoustic measurements
Antoine Deleforge, Cédric Foy, Antoine Laurain, Yannick Privat and Tom Sprunck.
Work in progress.

Can one hear the shape of a cuboid ?
Antoine Deleforge, Cédric Foy, Yannick Privat and Tom Sprunck.
To be submitted.

Fully Reversing the Shoebox Image Source Method: From Impulse Responses to Room Parameters [137]
Tom Sprunck, Antoine Deleforge, Yannick Privat and Cédric Foy, 2024.
Submitted to IEEE Transactions on Audio, Speech, and Language Processing.

Gridless 3D Recovery of Image Sources From Room Impulse Responses [136]
Tom Sprunck, Antoine Deleforge, Yannick Privat and Cédric Foy, 2022.
Published in IEEE Signal Processing Letters.

Conferences

Scientific talks

- Team seminar, *IRMA*, University of Strasbourg, November 2024.
- *46ème Congrès National d'Analyse Numérique*, Le-Bois-Plage-En-Ré, June 2024
- Team seminar, *MaLGa*, University of Genoa, Italy, May 2024.
- Team seminar, *IECL*, Université de Lorraine, Nancy, January 2024.
- MACARON Inria team retreat seminar, Belmont, February 2024.
- Phd student seminar, *Irma*, Université de Strasbourg, December 2023.
- ANR Shapo research group, Sorbonne Université, Paris, April 2023.
- 24th International Congress on Acoustics, Gyeongju, Korea, November 2022.
- 16th French Congress on Acoustics, Marseille, April 2022.

Poster sessions

- *IEEE International Conference on Acoustics, Speech, and Signal Processing.*
  June 2023. Rhodes, Greece.
- *45ème Congrès National d'Analyse Numérique.*
  May 2022. Evian, France.

Part I

Rectangular rooms

The aim of this part is to address the problem of estimating the geometrical parameters of a rectangular room from a *room impulse response*. We consider here a rectangular room of volume $V = L_x L_y L_z$ and a sound source located at a location $\boldsymbol{r}^{\mathrm{src}}$ inside the room.

Chapter 1 presents the *image-source method* for rectangular rooms, as well as the *super-resolution* approach for sparse measure recovery. Chapter 2 addresses theoretically and numerically the issue of estimating the image-source locations from filtered room impulse responses. Finally, Chapter 3 introduces an algorithm to recover every geometrical unknown of a rectangular room configuration using the estimated image-source positions.

Chapter 1

Tools for Image-Source localization using super-resolution

This chapter presents the image-source model, which will be used throughout this part. We also provide an introduction to sparse measure reconstruction, and two state-of-the-art reviews.

1.1 Image Source Method

1.1.1 Green's functions

As defined in the introduction, a RIR is the measurement of the response of a room to an impulsive sound source, *i.e.* the measure of a pressure field p resulting from a Dirac source term located at some point $\boldsymbol{r}^{\text{src}} \in \Omega$. Such a solution p is called a Green's function of the wave (respectively Helmholtz) equation for the given boundary conditions. A particular case of Green's functions are the free-field Green's functions, which are solutions to the wave (respectively Helmholtz) equation in free space. The boundary conditions are then replaced by a Sommerfeld radiation condition at infinity:

$$\lim_{r \to \infty} r^{(d-1)/2} \left(\frac{\partial G_{\boldsymbol{r}^{\text{src}}}}{\partial r}(\boldsymbol{r}) - i\mathfrak{K} G_{\boldsymbol{r}^{\text{src}}}(\boldsymbol{r}) \right) = 0. \tag{1.1}$$

Condition (1.1) ensures that the solution is unique and that the waves do not back-propagate. The free-field Green's functions for the wave equation for a point source located at $\boldsymbol{r}^{\text{src}}$ are given by [27]:

$$G_{\boldsymbol{r}^{\text{src}}}(\boldsymbol{r}, t) = \begin{cases} \frac{\delta(t - \|\boldsymbol{r} - \boldsymbol{r}^{\text{src}}\|_2 / c)}{4\pi \|\boldsymbol{r} - \boldsymbol{r}^{\text{src}}\|_2} & \text{if } d = 3 \\ \frac{H(t - \|\boldsymbol{r} - \boldsymbol{r}^{\text{src}}\|_2 / c)}{2\pi \sqrt{t^2 - |\boldsymbol{r} - \boldsymbol{r}^{\text{src}}|^2 / c^2}} & \text{if } d = 2 \end{cases} \quad (\boldsymbol{r}, t) \in \mathbb{R}^d \times \mathbb{R} \tag{1.2}$$

where H is the Heaviside function. The free-field Green's functions for the Helmholtz equation at wave number $\mathfrak{K}$ are given by:

$$G^{\mathfrak{K}}_{\boldsymbol{r}^{\text{src}}}(\boldsymbol{r}) = \begin{cases} \frac{e^{i\mathfrak{K}\|\boldsymbol{r} - \boldsymbol{r}^{\text{src}}\|_2}}{4\pi \|\boldsymbol{r} - \boldsymbol{r}^{\text{src}}\|_2} & \text{if } d = 3 \\ \frac{i}{4} H_0^{(1)}(\mathfrak{K} \|\boldsymbol{r} - \boldsymbol{r}^{\text{src}}\|_2) & \text{if } d = 2 \end{cases} \quad \boldsymbol{r} \in \mathbb{R}^d \tag{1.3}$$

with $H_0^{(1)}$ denoting the Hankel function of the first kind of order 0. Note that we use the convention of equation (14) for the sign, *i.e.* $\Delta G^{\mathfrak{K}}_{\boldsymbol{r}^{\text{src}}} + \mathfrak{K}^2 G^{\mathfrak{K}}_{\boldsymbol{r}^{\text{src}}} = -\delta_{\boldsymbol{r}^{\text{src}}}$.

One notable property of Green's functions is their ability to represent solutions of a particular solution of a given equation by a convolution product. Take for instance $G^{\mathfrak{K}}_{\boldsymbol{r}^{\text{src}}}$ the free-field Green's function for the 3D Helmholtz equation with $\boldsymbol{r}^{\text{src}} = 0$, and consider the inhomogeneous PDE:

$$\Delta p + \mathfrak{K}^2 p = f \tag{1.4}$$

completed with the radiation condition (1.1). Then, as the Dirac distribution is the neutral element for the convolution we get:

$$(\Delta + \mathfrak{K}^2)(-G_{\boldsymbol{r}^{\text{src}}} *_{\boldsymbol{r}} f) = [(\Delta + \mathfrak{K}^2)(-G_{\boldsymbol{r}^{\text{src}}})] *_{\boldsymbol{r}} f = \delta_0 *_{\boldsymbol{r}} f = f \tag{1.5}$$

where $*_{\boldsymbol{r}}$ denotes a spatial convolution. $-G_0 *_{\boldsymbol{r}} f$ is thus a solution for equation (1.4). The same representation holds for the wave equation by applying a double convolution in time and space.

1.1.2 Standard ISM

The *image-source method* (ISM) was formally introduced in room acoustics by Allen and Berkley in 1976 [5] in order to quickly simulate room impulse responses in rectangular rooms. The image-source method is based on the following observation: any specular reflection of an impulse sound source on a wall can be modeled by a virtual source, namely an *image source*, located outside the domain and obtained by taking the symmetry of the original source with respect to the wall. This process can be iterated in order to model reverberation, constructing image sources successively to take into account every reflection of the original sound wave on the walls (see Fig. 1.1 for an illustration of the image-sources up to the second order). In the shoebox case (*i.e.* the room is a cuboid), the image-source coordinates are most easily expressed in a *reference frame* of the room, meaning a frame composed of an orthonormal basis $(\boldsymbol{e}_1, \boldsymbol{e}_2, \boldsymbol{e}_3)$ of normal vectors to the walls along with an origin located at one of the room's corners.

In such a frame, the set of image-source coordinates is given by:

$$I_\Omega := \{\boldsymbol{r}_{\boldsymbol{q},\boldsymbol{\varepsilon}} = \boldsymbol{\varepsilon} \odot \boldsymbol{r}^{\mathrm{src}} + 2\boldsymbol{q} \odot \boldsymbol{v}_L, \quad \boldsymbol{\varepsilon} \in \{-1;1\}^3, \quad \boldsymbol{q} \in \mathbb{Z}^3\} \tag{1.6}$$

where $\boldsymbol{v}_L = \begin{pmatrix} L_x \\ L_y \\ L_z \end{pmatrix}$ is the room size vector, $\boldsymbol{v}_{d^{\mathrm{src}}} = \begin{pmatrix} d_x^{\mathrm{src}} \\ d_y^{\mathrm{src}} \\ d_z^{\mathrm{src}} \end{pmatrix}$ gives the distance of the source to each

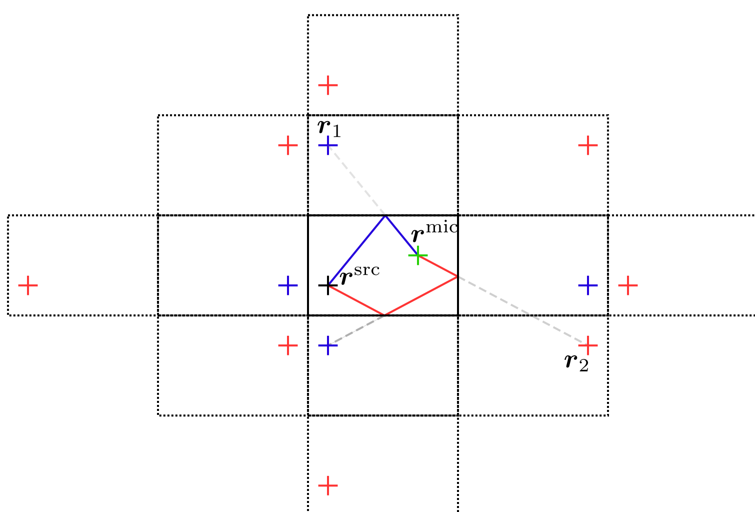

Figure 1.1: Representation of the source in black, the first order image-sources in blue and second order sources in red in 2D. The reflection paths from the source $\boldsymbol{r}^{\mathrm{src}}$ to a microphone $\boldsymbol{r}^{\mathrm{mic}}$ and corresponding to $\boldsymbol{r}_1, \boldsymbol{r}_2$ are drawn in blue and red. Note that the length of these paths is respectively equal to the distances $\boldsymbol{r}_1\boldsymbol{r}^{\mathrm{mic}}$ and $\boldsymbol{r}_2\boldsymbol{r}^{\mathrm{mic}}$.

wall containing the origin and $\odot$ denotes the Hadamard product defined by:

$$\forall \boldsymbol{u}, \boldsymbol{v} \in \mathbb{R}^D,\ \forall i \in [\![1, D]\!], \quad (\boldsymbol{u} \odot \boldsymbol{v})_i = u_i v_i. \tag{1.7}$$

Hence, the image sources lie on eight distinct translated orthogonal lattices of common mesh size $2L_x \times 2L_y \times 2L_z$. The same construction can be done in 2D. For instance, the indices corresponding to the image-sources $\boldsymbol{r}_1, \boldsymbol{r}_2$ of Fig. 1.1 are respectively $\boldsymbol{q} = (0,1), \boldsymbol{\varepsilon} = (1,-1)$ and $\boldsymbol{q} = (1,0), \boldsymbol{\varepsilon} = (-1,-1)$.

Assuming that the walls of the room are perfectly reflecting, the impedance boundary conditions are replaced by homogeneous Neumann boundary conditions on $\partial\Omega$. The pressure field p is then solution to the following system:

$$\begin{cases} \frac{1}{c^2}\partial_t^2 p(\boldsymbol{r},t) - \Delta p(\boldsymbol{r},t) = \delta_0(t)\delta_{\boldsymbol{r}^{\mathrm{src}}}(\boldsymbol{r}) & (\boldsymbol{r},t) \in \Omega \times \mathbb{R} \\ p(\boldsymbol{r},t) = \partial_t p(\boldsymbol{r},t) = 0 & (\boldsymbol{r},t) \in \Omega \times \mathbb{R}_-^* \\ \partial_{\boldsymbol{n}} p(\boldsymbol{r},t) = 0 & (\boldsymbol{r},t) \in \partial\Omega \times \mathbb{R}_+ \end{cases} \tag{N-W}$$

The ISM models the pressure field in a perfectly reflecting room as an infinite sum of spherical waves:

$$p(\boldsymbol{r},t) = \sum_{\boldsymbol{q}\in\mathbb{Z}^3, \boldsymbol{\varepsilon}\in\{-1,1\}^3} p_{\boldsymbol{q},\boldsymbol{\varepsilon}}(\boldsymbol{r},t) = \sum_{\boldsymbol{q}\in\mathbb{Z}^3, \boldsymbol{\varepsilon}\in\{-1,1\}^3} \frac{\delta(t - \|\boldsymbol{r}_{\boldsymbol{q},\boldsymbol{\varepsilon}} - \boldsymbol{r}\|/c)}{4\pi\|\boldsymbol{r}_{\boldsymbol{q},\boldsymbol{\varepsilon}} - \boldsymbol{r}\|}, \quad (\boldsymbol{r},t) \in \mathbb{R}^3 \times \mathbb{R}_+. \tag{1.8}$$

Note that $p_{\boldsymbol{q},\boldsymbol{\varepsilon}}$ is a solution to the free-field wave equation with a point source located at $\boldsymbol{r}_{\boldsymbol{q},\boldsymbol{\varepsilon}}$, *i.e.* a free-field Green function. This representation of the pressure field is thus solution to the following free-field wave equation:

$$\frac{1}{c^2}\partial_t^2 p(\boldsymbol{r},t) - \Delta p(\boldsymbol{r},t) = \delta_0(t) \sum_{\boldsymbol{q}\in\mathbb{Z}^3, \boldsymbol{\varepsilon}\in\{-1,1\}^3} \delta_{\boldsymbol{r}_{\boldsymbol{q},\boldsymbol{\varepsilon}}}(\boldsymbol{r}), \quad (\boldsymbol{r},t) \in \mathbb{R}^3 \times \mathbb{R}_+. \tag{1.9}$$

Allen and Berkley proved in [5] that the pressure field given by formula (1.8) is indeed solution to System (N-W), using a modal decomposition and a frequency-domain formulation. This result is formalized in Section 2.1.1, and a new time-domain proof of this proposition is given in Chapter 4.

1.1.3 Extension to absorbing walls

The most restricting assumption of the standard ISM is that the room is perfectly reflecting. The pressure field appears as a succession of impulses (Dirac masses) in time, and the energy carried by the impulses contained in a sliding time window grows linearly as time increases. Indeed, the number of reflections grows quadratically with the distance to the source whilst the propagation attenuation is only linear with respect to the distance. This leads to a non-physical representation of the pressure field as its energy diverges when time goes to infinity. In their same paper [5], Allen and Berkley proposed to assign an attenuation coefficient to each image source in order to model the absorption of the walls. An absorption coefficient $\alpha_l \in]0,1[,\ 1 \leq l \leq 6$ is associated to each wall, and the amplitude a for an image source of order n is given by :

$$a = \prod_{l=0}^{n} \sqrt{1-\alpha_{n_l}} \tag{1.10}$$

where n_l is the index of the wall corresponding to the l-th reflection. This ensures a geometric decrease of the amplitude of the image sources with the order of reflection. For high orders of reflection the amplitude of the image sources becomes negligible and the pressure field is well approximated by a finite sum of image sources. Denoting by $\boldsymbol{r}_k,\ k \in [\![1, K]\!]$ the locations of the remaining image sources, the pressure field is then given by:

$$p(\boldsymbol{r}, t) = \sum_{k=1}^{K} a_k \frac{\delta\left(t - \|\boldsymbol{r} - \boldsymbol{r}_k\|_2 / c\right)}{4\pi\|\boldsymbol{r} - \boldsymbol{r}_k\|}, \quad (\boldsymbol{r}, t) \in \mathbb{R}^3 \times \mathbb{R}_+ \tag{1.11}$$

which is a solution to the modified free-field wave equation:

$$\frac{1}{c^2}\partial_t^2 p(\boldsymbol{r}, t) - \Delta p(\boldsymbol{r}, t) = \delta_0(t) \sum_{k=1}^{K} a_k \delta_{\boldsymbol{r}_k(\boldsymbol{r})}, \quad (\boldsymbol{r}, t) \in \mathbb{R}^3 \times \mathbb{R}_+. \tag{1.12}$$

Further extensions of this model include considering frequency-dependent coefficients α_l and source directivity, see for instance [138, 54]. We will only consider the case of constant coefficients here. This method falls into the category of *geometric acoustic* methods and provides an accurate approximation of the pressure field at high frequency when the wavelength is sufficiently smaller than the dimensions of the room [96]. This property makes geometric acoustic methods a good substitute to expensive wave-based simulators, such as finite elements, at high frequency.

1.2 Sparse measure reconstruction

We introduce here a mathematical framework for sparse measure recovery from noisy measurements, used, *e.g.*, in [32, 60, 53, 146]. The inverse problem considered in this part will be to recover a sparse measure $\psi_0 = \sum_{k=1}^{K} a_{0,k}\delta_{\boldsymbol{r}_{0,k}}$ from finite, noisy, filtered measurements $\boldsymbol{x}_0$. The measurement process will be modeled by a linear operator Γ on such measures. Formally speaking, we thus want to recover ψ_0 from a vector $\boldsymbol{x}_0 = \Gamma\psi_0 + \boldsymbol{e}$. We will now define each of these terms more rigorously.

1.2.1 The space of Radon measures

Let X be $\mathbb{R}^3$ or a connected compact subset of $\mathbb{R}^3$.

Definition 1.2.1. *We denote by $\mathcal{M}(X)$ the space of bounded Radon measures on X, which is defined as the dual space of $\mathcal{C}_0(X)$, the space of continuous functions on X that vanish at infinity, endowed with $\| \ \|_\infty$.*

In particular, $\mathcal{M}(X)$ contains the weighted sums of Dirac masses. Indeed, a Dirac can be defined as a linear form on $\mathcal{C}_0(X)$ with $\delta_{\boldsymbol{r}} : f \mapsto f(\boldsymbol{r})$. Depending on context, $\delta_{\boldsymbol{r}}$ will either refer to a Dirac mass in the distributional sense or in the sense of the Radon measures.

The dual norm of $\| \ \|_\infty$ is called the total variation norm:

Definition 1.2.2. *The total variation norm of a measure $\psi \in \mathcal{M}(X)$ is:*

$$\|\psi\|_{TV} = \sup \left\{ \int_X f d\psi; \ f \in \mathcal{C}_0(X), \|f\|_\infty \leq 1 \right\}. \tag{1.13}$$

Remark 1.2.1. In particular, if $\psi = \sum_{k=1}^{K} a_k \delta_{\boldsymbol{r}_k}$ takes the same form as the source term in equation (1.12), its total variation norm is the ℓ_1 norm of the corresponding amplitude vector $\boldsymbol{a} \in \mathbb{R}^K$, *i.e.* $\|\psi\|_{\mathrm{TV}} = \sum_{k=1}^{K} |a_k|$. The total variation norm can then be seen as a continuous counterpart of the ℓ_1 norm. Moreover, similarly to the ℓ_1 norm it will act as a sparsity inducing regularizer which favors solutions composed of finite sums of Dirac masses.

$\mathcal{M}(X)$ is then a Banach space when endowed with the total variation norm. The subdifferential of the total variation norm is given in the following proposition:

Proposition 1.2.1. *Let $\psi \in \mathcal{M}(X)$, then the subdifferential of the total variation norm at ψ is:*

$$\partial\|\psi\|_{TV} = \left\{ f \in \mathcal{C}_0(X); \ \|f\|_\infty \leq 1, \ \int_X f d\psi = \|\psi\|_{TV} \right\}. \tag{1.14}$$

In particular, if $\psi = \sum_{k=1}^{K} a_k \delta_{\boldsymbol{r}_k}$, then:

$$\partial\|\psi\|_{TV} = \{ f \in \mathcal{C}_0(X); \ \|f\|_\infty \leq 1, \ \forall k \in [\![1, K]\!], \ f(\boldsymbol{r}_k) = \mathrm{sign}(a_k) \}. \tag{1.15}$$

See [131] for more details on Radon measures.

1.2.2 The BLASSO optimization problem

The observation operator Γ considered here will take the following form:

$$\Gamma : \begin{array}{ccc} \mathcal{M}(X) & \longrightarrow & \mathbb{R}^D \\ \psi & \mapsto & \left(\int_X \varphi_i d\psi \right)_i . \end{array} \tag{1.16}$$

In practice, we consider kernels that verify the following assumptions:

$$\begin{cases} \forall i \in [\![1, D]\!], \quad \varphi_i \in \mathcal{C}^2(X) \\ \forall \boldsymbol{x} \in \mathbb{R}^D, \ \boldsymbol{r} \mapsto \sum_{i=1}^{D} x_i \varphi_i(\boldsymbol{r}) \quad \text{vanishes at infinity} \\ \forall k \in [\![0, 2]\!], \quad \|D^k \varphi_i\|_\infty < +\infty. \end{cases} \tag{1.17}$$

In order to reverse Γ and recover the input measure ψ_0, we minimize an energy composed of a least-squares data compliance term, and a sparsity favoring regularization:

$$\min_{\psi \in \mathcal{M}(X)} \|\boldsymbol{x}_0 - \Gamma\psi\|_2 + \lambda\|\psi\|_{\mathrm{TV}}. \tag{$\mathfrak{B}_\lambda$}$$

Problem ($\mathfrak{B}_\lambda$) is coined Beurling-LASSO [48] or BLASSO in the literature and can be seen as an extension of the finite dimension LASSO to the infinite-dimensional space of Radon measures. The existence of solutions to Problem ($\mathfrak{B}_\lambda$) was proven in [25] for more general operators under a continuity hypothesis on Γ. The addition of the total variation regularization guarantees the existence of at least one sparse solution, *i.e.* a solution that is a finite sum of weighted Dirac masses [151].

Remark 1.2.2. When $\boldsymbol{e} = 0$ and $\lambda = 0$, one considers the following constrained problem:

$$\min_{\psi \in \mathcal{M}(X),\, \Gamma\psi = \boldsymbol{x}_0} \|\psi\|_{\mathrm{TV}}. \tag{1.18}$$

This optimization problem can be seen as a *basis pursuit* [38] problem over the space of Radon measures. In particular, when λ vanishes to zero the solution of ($\mathfrak{B}_\lambda$) converges to a particular solution of (1.18) [60].

By considering the first-order optimality conditions and the subdifferential of the total variation norm given in (1.14), we get a characterization of the sparse, finite solutions to Problem ($\mathfrak{B}_\lambda$):

Proposition 1.2.2. *Let $\psi = \sum_{k=1}^{K} a_k \delta_{\boldsymbol{r}_k}$. Then ψ is a solution to Problem ($\mathfrak{B}_\lambda$) if and only if the function $\eta := \frac{1}{\lambda}\Gamma^*(\boldsymbol{x}_0 - \Gamma\psi)$ verifies:*

$$\|\eta\|_\infty \leq 1 \quad \textit{and} \quad \forall k \in [\![1, K]\!],\ \eta(\boldsymbol{r}_k) = \operatorname{sign}(a_k). \tag{1.19}$$

The function η is called a *dual certificate*. Another powerful notion is the *vanishing derivatives precertificate* η_V introduced in [60]. Under some hypotheses on η_V we can ensure stable recovery of the support of the true measure ψ_0 in the presence of noise. We will now quickly define each of these terms for our application case. More detailed definitions can be found in [60].

Let $\boldsymbol{r} = (\boldsymbol{r}_1, \dots, \boldsymbol{r}_K) \in X^K$. We begin by defining a finite dimensional operator $\Gamma_{\boldsymbol{r}}$ that can be expressed in matrix form by $\Gamma_{\boldsymbol{r}} = \begin{pmatrix} A(\boldsymbol{r}) & B(\boldsymbol{r}) \end{pmatrix}$ where

$$A(\boldsymbol{r}) = \begin{pmatrix} \varphi_1(\boldsymbol{r}_1) & \dots & \varphi_1(\boldsymbol{r}_K) \\ \vdots & & \vdots \\ \varphi_D(\boldsymbol{r}_1) & \dots & \varphi_D(\boldsymbol{r}_K) \end{pmatrix}, \tag{1.20}$$

and

$$B(\boldsymbol{r}) = \begin{pmatrix} \partial_x\varphi_1(\boldsymbol{r}_1) & \dots & \partial_x\varphi_1(\boldsymbol{r}_K) & \partial_y\varphi_1(\boldsymbol{r}_1) & \dots & \partial_y\varphi_1(\boldsymbol{r}_K) & \partial_z\varphi_1(\boldsymbol{r}_1) & \dots & \partial_z\varphi_1(\boldsymbol{r}_K) \\ \vdots & & \vdots & \vdots & & \vdots & \vdots & & \vdots \\ \partial_x\varphi_D(\boldsymbol{r}_1) & \dots & \partial_x\varphi_D(\boldsymbol{r}_K) & \partial_y\varphi_D(\boldsymbol{r}_1) & \dots & \partial_y\varphi_D(\boldsymbol{r}_K) & \partial_z\varphi_D(\boldsymbol{r}_1) & \dots & \partial_z\varphi_D(\boldsymbol{r}_K) \end{pmatrix}. \tag{1.21}$$

In the following we assume that $\boldsymbol{x}_0$ is defined by the amplitude and location vectors $\boldsymbol{a}_0\boldsymbol{r}_0$, *i.e.* $\boldsymbol{x}_0 = \Gamma(\sum_{k=1}^K a_{0,k}\delta_{\boldsymbol{r}_{0,k}})$.

Definition 1.2.3. *Suppose that $\Gamma_{\boldsymbol{r}_0}$ has full rank and let $\boldsymbol{v}^* = (\Gamma_{\boldsymbol{r}_0}^+)^* \begin{pmatrix} \mathrm{sign}(\boldsymbol{a}_0) \\ 0_{\mathbb{R}^{3D}} \end{pmatrix}$, where $\boldsymbol{r}_0 = (\boldsymbol{r}_{0,1}, \dots, \boldsymbol{r}_{0,K})$, $\boldsymbol{a}_0 = (a_{0,1}, \dots, a_{0,K})$, and $(\Gamma_{\boldsymbol{r}_0}^+)^*$ denotes the adjoint of the pseudoinverse of $\Gamma_{\boldsymbol{r}_0}$. We then define the vanishing derivatives precertificate as $\eta_V = \Gamma^*\boldsymbol{v}^*$.*

Proposition 1.2.3. *The vector $\boldsymbol{v}^*$ is the unique solution to:*

$$\min_{\boldsymbol{v}\in\mathbb{R}^{4D}} \|\boldsymbol{v}\|_2 \qquad \textit{such that: } (\Gamma^*\boldsymbol{v})(\boldsymbol{r}_{0,k}) = \mathrm{sign}(a_{0,k}),\ D(\Gamma^*\boldsymbol{v})(\boldsymbol{r}_{0,k}) = 0 \quad \forall k \in [\![1, K]\!]. \tag{1.22}$$

Remark 1.2.3. The precertificate η_V thus interpolates the sign of the true measure at each spike's location, with vanishing derivatives. In the noiseless case, *i.e.* $\boldsymbol{e} = 0$, the condition $\|\eta_V\|_\infty \leq 1$, ensures the uniqueness of the solution to Problem (1.18). In our case Γ^* takes the following expression: an operator on $\mathbb{R}^D$ that takes its values in $\mathcal{C}_0(X)$:

$$\Gamma^* : \begin{array}{ccc} \mathbb{R}^D & \longrightarrow & \mathcal{C}_0(X) \\ \boldsymbol{v} & \mapsto & \boldsymbol{r} \mapsto \sum_{i=1}^D v_i\varphi_i(\boldsymbol{r}). \end{array} \tag{1.23}$$

We now define a criterion on η_V that implies the stable recovery of the support from noisy measurements.

Definition 1.2.4. *We say that η_V is non-degenerate if:*

$$\begin{cases} \det D^2\eta_V(\boldsymbol{r}_{0,k}) \neq 0 & \forall k \in\ [\![1, K]\!] \\ |\eta_V(\boldsymbol{r})| < 1 & \textit{if } \boldsymbol{r} \notin \{\boldsymbol{r}_{0,1}, \dots \boldsymbol{r}_{0,K}\}. \end{cases} \tag{1.24}$$

This condition is hard to prove in practice for our operator, in part because $X \subset \mathbb{R}^3$. However, it can be checked numerically and plotting the precertificate gives some insight on the complexity and behavior of the inverse problem. We finally write one of the main results in [60], which motivates the study of η_V.

Theorem 1.2.1. *Assume that $\Gamma_{\boldsymbol{r}_0}$ has full rank, the kernels φ_i verify (1.17) and η_V is non-degenerate. Then there exist two constants α, $\lambda_0 > 0$ such that for all $\lambda, \boldsymbol{e}$ verifying $0 < \lambda \leq \lambda_0$ and $\frac{\|\boldsymbol{e}\|_2}{\lambda} \leq \alpha$, there exists a unique solution ψ^* to $(\mathfrak{B}_\lambda)$. Moreover, ψ^* takes the form $\psi^* = \sum_{k=1}^{K} a_k^* \delta_{\boldsymbol{r}_k^*}$, and if we take $\lambda = \frac{1}{\alpha}\|\boldsymbol{e}\|_2$ we have:*

$$\|\boldsymbol{a}_0 - \boldsymbol{a}^*\|_\infty = O(\|\boldsymbol{e}\|_2) \text{ and } \|\boldsymbol{r}_0 - \boldsymbol{r}^*\|_\infty = O(\boldsymbol{e}). \tag{1.25}$$

In other words, if the noise level $\|\boldsymbol{e}\|_2$ is low enough and λ is chosen proportionally to $\|\boldsymbol{e}\|_2$, the solution to $(\mathfrak{B}_\lambda)$ is a finite sparse measure that contains as many spikes as the true measure, and it converges to the true measure as λ and $\|\boldsymbol{e}\|_2$ vanish to zero. The idea behind the proof of this theorem and the construction of the precertificate η_V is the following: one can use the implicit function theorem to prove the existence of a discrete measure $\psi_{\lambda,\boldsymbol{e}}$, composed of the correct number of spikes, that interpolates the sign of the true measure at the spike locations with vanishing derivatives. The locations and amplitudes are a function of the noise level and regularization parameter, and one can show that $\eta_\lambda \coloneqq \frac{1}{\lambda}\Gamma^*(\boldsymbol{x}_0 - \Gamma\psi_{\lambda,\boldsymbol{e}})$ converges to η_V when the noise level and λ vanish to zero. The assumptions of the theorem then ensure that $\|\eta_\lambda\|_\infty \leq 1$ in the limit, hence that the corresponding measure verifies the optimality conditions.

1.2.3 Numerical optimization on measures

We describe in this section a method to optimize directly on the space of measure, namely the Frank-Wolfe algorithm [68] or conditional gradient descent. Frank-Wolfe can be applied to constrained optimization problems of the type:

$$\min_{\psi \in C} f(\psi) \tag{1.26}$$

where f is a continuously differentiable function and C is a compact convex subset of a Banach space. In our case, $C = \mathcal{M}(X)$ and $f : \psi \mapsto \|\boldsymbol{x}_0 - \Gamma\psi\|_2 + \lambda\|\psi\|_{\mathrm{TV}}$ is the BLASSO energy functional. The main idea of the algorithm is to consider a linearization of the cost function f at each iteration (see [85] for an illustration).

The condition at line 3 of the algorithm translates the first order optimality condition. The step

Algorithm 1 Frank-Wolfe algorithm

1: **for** $i = 0, \ldots, L$ **do**
2: $\quad\psi_{\mathrm{lin}} \leftarrow \operatorname{argmin}_{\psi \in C} f(\psi^{(i)}) + Df(\psi^{(i)})(\psi - \psi^{(i)})$
3: $\quad$**if** $Df(\psi^{(i)})(\psi_{\mathrm{lin}} - \psi^{(i)}) = 0$ **then**
4: $\quad\quad$Stop.
5: $\quad$**end if**
6: $\quad$Update step $\gamma^{(i)}$
7: $\quad\psi^{(i+1)} \leftarrow \psi^{(i)} + \gamma^{(i)}(\psi_{\mathrm{lin}} - \psi^{(i)})$
8: **end for**

(i) is updated using the rule $\gamma^{(i)} = \frac{2}{i+2}$ or by doing a standard line search. Convergence guarantees can be obtained, with a convergence rate in $O(1/i)$ for convex functions (see for instance [123]). In other words, if ψ^* is optimal for Problem (1.26), there exists a constant C such that:

$$\forall i \in \mathbb{N}^*, \quad f(\psi^{(i)}) - f(\psi^*) \leq \frac{C}{i}. \tag{1.27}$$

The measure $\psi^{(i+1)}$ can be replaced by any other measure $\psi \in C$ such that $f(\psi) \leq f(\psi^{(i+1)})$, without losing the convergence properties. This property is leveraged in [53] by adding a non-convex local search at the end of each iteration in order to refine the results. The algorithm obtained by adding this so-called *sliding* step is guaranteed to converge in a finite number of iterations.

Note that Frank-Wolfe can not be directly applied to the BLASSO as $\mathcal{M}(X)$ is unbounded and the energy T_λ is not differentiable due to the regularization term. This issue is addressed in [53] by solving an equivalent problem on an epigraphical lift, and the usual convergence results apply. Moreover, the linearized problem at line 2 can be resolved by maximizing the 3D function $\eta^{(i)} = \Gamma^*(\boldsymbol{x} - \Gamma\psi^{(i)})$, which can be seen as a numerical dual certificate. More details on this algorithm will be given in Section 2.3.3.

1.3 State of the art

1.3.1 Acoustic source localization

The problem of recovering image sources from measured audio signals can be viewed as a generalization of many tasks that have been independently investigated in the acoustic signal processing literature over the past decade. Estimating the absolute or relative *times of arrival* of image sources at microphones, also known as early *echoes*, is the focus of [91, 45, 55, 134] and can be of independent interest in the context of *echo-aware* signal processing, as reviewed in [33]. Localizing *reflectors* in the room is equivalent to localizing their corresponding first-order image source together with the true source. Most studies on this first estimate echoes and/or directions of arrival of image sources, then label and sort them, and finish by triangulation [141, 8, 139, 106, 58, 84, 126, 61, 105]. Alternatively, [129] proposes a more direct approach based on sparse optimization. Retrieving the coefficients a_k associated to reflectors in frequency bands is studied in [133] and [56], as they relate to their acoustic *impedance*. Finally, recovering image sources within a given range is the focus of recent non-parametric sound-field reconstruction methods [92, 46]. All these tasks can either be performed using RIRs as in [129, 8, 58, 91, 45, 84, 126, 61, 128, 105, 56] or *blindly* using unknown source signals as in [141, 8, 139, 106, 92, 55, 46, 134, 133].

While the above referenced studies developed a rich variety of methodologies, nearly all of them have in common the definition of a *discrete grid* in 1D time [141, 139, 106, 8, 58, 91, 45, 84, 126, 61, 105, 134, 56], in 2D space [139, 106, 128, 92, 46] or in 3D space [129], as well as the use of sparse optimization techniques and/or peak-picking techniques over such grids. This *on-the-grid* paradigm suffers from intrinsic limitations. First, in 3D, the required grid size grows cubically in the desired range and precision. This fundamentally limits the accuracy of current sparse methods under reasonable computational constraints [129, 92, 46], though some works aim at reducing this cost [93]. Second, time-domain peak-picking fails when peaks are overlapping and distorted due to filtering effects such as the application of a low-pass filter. Existing methods address this by using ad-hoc source and microphone placements inside the room [8, 58, 84, 126, 61, 105]. Third, sparse optimization over a discrete grid fundamentally suffers from the so-called *basis-mismatch* problem [39, 53], requiring the use of ad-hoc post-processing steps.

In parallel, recent theoretical and methodological advances on the general problem of gridless spike recovery *off-the-grid* have emerged [48, 32, 60, 115, 53, 146], notably motivated by applications to *super-resolution* in, *e.g.*, fluorescence microscopy [82, 53]. The theoretical gridless spike recovery problem can be approached either by Prony's method and its derivatives, such as MUSIC [132] (MUltiple SIgnal Classification), ESPRIT [130] (Estimation of Signal Parameters by Rotational Invariance Technique), or by variational methods. While some extensions to noisy data [44, 154] and multivariate measures [122, 94] were developed, Prony's type methods are better suited to noiseless, 1D measurements. On the other hand, gridless variational methods aim to resolve optimization problems on a space of measures, without prior knowledge on the number of spikes. These problems can be seen as convex relaxations of similar finite dimension, grid-based problems to infinite dimensional convex optimization problems. We will focus here on these variational methods, which generalize well to any kind of measurement operator and noise. More precisely, we will consider the BLASSO optimization problem ($\mathfrak{B}_\lambda$) as defined in section 1.2.2, which has received considerable attention in recent years, both in theoretical and algorithmic work. A first theoretical issue is to find conditions to ensure exact support recovery of the ground truth measure in the noiseless case. It then follows naturally to study how the solution of ($\mathfrak{B}_\lambda$) with noisy measurements relates to the solution of the noiseless case. The seminal work of Candès and Fernandes-Granda [32] on the 1D low-pass filter vastly contributed to opening the field by proving that exact support recovery could be achieved under a minimum separation constraint between spikes, with latter expansions to noisy measurements [31, 15, 65]. These latter works provide error bounds on the locations of the recovered spikes, but few guarantees on the structure of the reconstructed measure. Duval and Peyré show in [60] that under certain hypotheses on the certificates of the dual problem, λ and the measurement noise, there exists a unique solution to the noisy BLASSO that contains as many spikes as the input measure. Additionally, the recovered measure converges to the exact measure for the weak-$*$ topology when the noise and λ vanish to 0. Note that a particular case of interest focuses on input measures for which the spikes cluster around a set point. Exact noiseless support recovery and stable noisy reconstruction can be achieved when the amplitudes of the spikes are real and positive under some non-degeneracy condition, see for instance [52] in 1D or [124] for higher dimensions, however in our case the spikes will be well-separated in space.

Several successful numerical approaches have been developed over the years in order to solve the super-resolution problem off the grid. We can cite amongst these methods the semi-definite programming (SDP) formulation [32] and its extension to higher dimensions using Lasserre hierarchy [102, 49], optimal transport theory and particle gradient descent [41, 40], over-parametrized projected gradient descent [147, 28] and finally the Frank-Wolfe algorithm (also called the conditional gradient descent) [68, 25, 53, 23]. Except for a small number of recent studies on blind echo estimation [55] and anechoic beamforming [37] or covariance matrix fitting [36], these advances seem not to have received significant attention from the audio and acoustics communities yet. The algorithm for acoustic source localization developed in this thesis is an adaptation of the sliding Frank-Wolfe algorithm [53]. A quick description of Frank-Wolfe was given in section 1.2.3.

Finally, one can also consider deep-learning methods for localizing acoustic sources. These methods are beyond the scope of this thesis, and an extensive review of the vast and recent associated literature can be found in [77].

1.3.2 Room geometry estimation

The key physical phenomenon making room geometry estimation from audio measurements possible at all is that of *early acoustic reflections*. When sound propagates from a source inside a room, it is reflected on surfaces before reaching microphones. This materializes into delayed and filtered copies of the emitted signal inside the measured time-domain signals, that are commonly referred to as *echoes*. The *time of arrival* (TOA) of an echo at a microphone is proportional to the length of the corresponding reflected propagation path, while the *time differences of arrival* (TDOAs) of an echo between two or more microphones are linked to the *direction of arrival* (DOA) of the corresponding reflected propagation path. The core idea of nearly all existing methods in the field is to estimate such quantities from measured signals, to prune, sort and label echoes, and to solve for the acoustic-scene geometry based on the recovered information. A literature review of the works tackling some or all of these steps is proposed in the remainder of this section.

The reflector associated to the TOA of a first-order propagation path from a source to a microphone is known to be tangential to an ellipsoid whose focci are the corresponding source and microphone positions. Assuming the latter are known, a number of early approaches, referred to as *direct localization* in [126], have hence focused on detecting, pruning, clustering and localizing tangent lines to multiple ellipses in the 2D case [9, 67, 29, 30, 66, 8], or tangent planes to multiple ellipsoids in the 3D case [117, 127, 126]. An alternative to this is to combine the TOAs and DOAs of echoes to obtain the 3D locations of their associated image sources. Reflectors can then be localized as the bisecting planes between a true source and its first order image sources, as in [57, 129, 58, 106, 125, 126, 128, 105, 150]. This approach is referred to as *image source reversion* in [126].

Several early works in the field assume that TOAs are trivial to estimate from room impulse responses (RIRs) using peak picking [9, 8] or consider them readily available [57, 117, 58, 114, 108, 84, 125]. This would be the case if microphones, sources and reflectors had perfectly flat responses up to very high frequencies, but this is never true in practice. This band-limitedness results in a significant *smearing* of echoes, blurring the location of their peaks and making them overlap and interfere with each other in the time domain. An analogous phenomenon occurs in the 1D and 2D DOA domains, and is reinforced by the limited diameter of microphone arrays. Interference is all the more present since echoes are, by definition, strongly correlated with each other and with direct-path signals. Due to this, the tasks of TOA, TDOA and DOA estimation of early acoustic reflections has been the focus of significant research effort. The vast majority of existing techniques proceed by some form of peak-picking over a *discretized* time domain [67, 141, 30, 66, 127, 126, 61, 106, 91, 45], DOA domain [29, 139, 127, 105, 134], joint TOA-DOA domain [145, 128, 150], 3D space [129] or ray space [95, 109]. To improve the separation and sharpness of objects inside such discrete grids, some methods leverage sparsity-based techniques [129, 91, 45, 18, 150, 134] or ad-hoc image processing tools [145, 109, 128, 105]. Despite these efforts, operating over discrete time or space suffers from intrinsic limitations, which were mentioned in the last section, namely peak separability, a large grid volume in the 3D case, and basis-mismatch.

There are a few notable exceptions to this discrete grid-search paradigm [108, 158, 142, 55]. In [108], a class of 2D room geometries is selected (rectangle, L-shaped) and the continuous shape dimensions are directly optimized by minimizing a distance between measured and image-source TOAs, using a genetic algorithm. In [158], the wall- and source-to-wall distances in a 1D room are continuously optimized based on resonant frequencies. In [142], non-linear minimization of a likelihood-based cost function in the spherical harmonics domain is utilized to jointly estimate the continuous DOA of a fixed number of reflectors. In [55], the TDOAs of echoes are blindly estimated in the continuous time domain by leveraging an infinite-dimensional convex relaxation of the problem and the *sliding Frank-Wolfe* algorithm [53].

Many of the above-reviewed methods estimate TOAs and/or TDOAs independently across individual channels and/or channel pairs. To leverage these quantities for geometry estimation, they need to be associated to reflectors, a procedure referred to as *echo sorting*. This difficult combinatorial problem is the focus of [57, 58, 84]. The need for echo sorting is bypassed by methods that directly localize image sources from RIRs [129, 106, 142, 126, 128, 105, 150, 134].

Once image sources are localized, a necessary subsequent step is to *label* them, namely, identify their order of reflection. In the literature, labeling is typically performed by ad-hoc algorithms that exploit the geometrical constraints at hands, *e.g.*, [129, 58, 125, 105]. They are often tailored to the specific class of source-microphone-room setup under consideration, and may hence be hard to generalize.

Complementarily to approaches tackling room geometry estimation, a few approaches are focused on estimating surface absorption coefficients or echo amplitudes from recorded signals given the room geometry or image source positions [118, 10, 18, 133, 119, 56]. The approaches in [118, 10, 18, 119] proceed by discretizing the wave equation in both time and space to solve the corresponding sparse inverse problem. The computational burden of discretizing limits these approaches to either frequencies below 500 Hz [118, 10] or 2D rooms [18, 119]. In contrast, the approach in [133] estimate echo amplitudes blindly given their continuous TOAs via least-square optimization. To tackle the high sensitivity of these techniques to geometrical errors, [56] formulates the problem in the magnitude short-time Fourier domain and robustly solves the corresponding non-linear inverse problem with the help of random sampling consensus.

Finally, a relatively recent class of methods replaces some or all of the previously described steps by making use of virtually-supervised deep learning [157, 149, 156, 19]. While promising results have been reported, these approaches are currently restricted to the acoustic setups simulated in their training data. Moreover, the ability of various training simulation strategies to generalize to a broad enough range of real measurements is an open question that calls for further investigation.

We close this section by observing that most of the above-referenced methods are only tested on a restricted set of geometries. For instance, the methods in [95, 9, 67, 141, 117, 57, 29, 30, 66, 139, 108, 109, 145, 106, 58, 127, 134] are tested on less than 3 simulated or real room geometries, and the experimental setups in [129, 66, 139, 106, 126, 61, 128, 105] have in common a favorable positioning of devices, such as a microphone array near the room center, or sources near the reflectors of interest. Combined with the general absence of publicly available code, this makes existing techniques difficult to reproduce or compare.

Chapter 2

Image source estimation

We model in this chapter the cuboid room reconstruction problem as an inverse problem on image-source locations. We provide a theoretical analysis of the finite dimensional formulation of the problem, and present an algorithm to solve its convex relaxation on the space of Radon measures. The numerical performance of the proposed method is then evaluated on synthetic data. This chapter is currently being prepared in article format for submission to an applied mathematics journal.

2.1 Modeling of the inverse problem

2.1.1 The direct problem

Consider a rectangular room Ω with (positive) dimensions L_x, L_y, L_z, and a sound source positioned at $\boldsymbol{r}^{\mathrm{src}}$ within the room. Let $\boldsymbol{r}^{\mathrm{mic}} \neq \boldsymbol{r}^{\mathrm{src}}$ denote a microphone location distinct from the source position. The *Room Impulse Response* (RIR) for this configuration is the signal recorded at microphone $\boldsymbol{r}^{\mathrm{mic}}$ when the source emits an ideal impulse at time $t = 0$. In other words, an RIR represents the measurement at a given microphone location of the Green's function for the wave equation. A *multichannel* RIR refers to a collection of RIRs recorded at various microphone locations for a single source position.

The pressure field p resulting from a *perfectly impulsive source* located at $\boldsymbol{r}^{\mathrm{src}}$ is a solution to the inhomogeneous wave equation (2.1):

$$\begin{cases} \frac{1}{c^2}\partial_t^2 p(\boldsymbol{r},t) - \Delta p(\boldsymbol{r},t) = \delta(t)\delta(\boldsymbol{r}-\boldsymbol{r}^{\mathrm{src}}) & (\boldsymbol{r},t) \in \Omega \times \mathbb{R} \\ p(\boldsymbol{r},t) = \partial_t p(\boldsymbol{r},t) = 0 & (\boldsymbol{r},t) \in \Omega \times \mathbb{R}_-^*, \end{cases} \tag{2.1}$$

where $c > 0$ is the speed of sound.

In the following, we will use the modified image-source model as described in Section 1.1.3. Recall that the ISM models the case of perfectly reflecting walls, which corresponds to setting a time-constant $\beta(\cdot)$ in Eq. (13) *i.e.*, applying Neumann boundary conditions on $\partial\Omega$. The pressure field p is then solution to System (N-W), restated here:

$$\begin{cases} \frac{1}{c^2}\partial_t^2 p(\boldsymbol{r},t) - \Delta p(\boldsymbol{r},t) = \delta(t)\delta(\boldsymbol{r}-\boldsymbol{r}^{\mathrm{src}}) & (\boldsymbol{r},t) \in \Omega \times \mathbb{R} \\ p(\boldsymbol{r},t) = \partial_t p(\boldsymbol{r},t) = 0 & (\boldsymbol{r},t) \in \Omega \times \mathbb{R}_-^* \\ \partial_{\boldsymbol{n}} p(\boldsymbol{r},t) = 0 & (\boldsymbol{r},t) \in \partial\Omega \times \mathbb{R} \end{cases} \tag{N-W}$$

Remark 2.1.1. Let us highlight that p also solves an equivalent formulation. Let us set $\square_c = \frac{1}{c^2}\partial_t^2 - \Delta$, let φ_1 denote a smooth function in Ω, and consider φ the unique solution of the wave equation

$$\begin{cases} \square_c \varphi(\boldsymbol{r},t) = 0 & (\boldsymbol{r},t) \in \Omega \times \mathbb{R}_+ \\ \varphi(\boldsymbol{r},0) = 0, \quad \partial_t \varphi(\boldsymbol{r},0) = \varphi_1(\boldsymbol{r}) & \boldsymbol{r} \in \Omega \\ \partial_{\boldsymbol{n}} \varphi(\boldsymbol{r},t) = 0 & (\boldsymbol{r},t) \in \partial\Omega \times \mathbb{R}_+. \end{cases} \tag{2.2}$$

Let us introduce the function ψ defined by $\psi(\boldsymbol{r},t) = H(t)\varphi(\boldsymbol{r},t)$, where H is the so-called Heaviside function. Then, seeing ψ as a distribution, one gets

$$\square_c \psi(\boldsymbol{r},t) = \delta(t)\varphi_1(\boldsymbol{r}), \qquad (\boldsymbol{r},t) \in \Omega \times \mathbb{R} \tag{2.3}$$

according to the jump rule for distributions [70, Chapter 2]. Let $\widetilde{p}$ be the solution of

$$\begin{cases} \square_c \widetilde{p}(\boldsymbol{r},t) = 0 & (\boldsymbol{r},t) \in \Omega \times \mathbb{R}_+ \\ \widetilde{p}(\boldsymbol{r},0) = 0, \quad \partial_t \widetilde{p}(\boldsymbol{r},0) = \delta(\boldsymbol{r} - \boldsymbol{r}^{\mathrm{src}}) & \boldsymbol{r} \in \Omega \\ \partial_{\boldsymbol{n}} \widetilde{p}(\boldsymbol{r},t) = 0 & (\boldsymbol{r},t) \in \partial\Omega \times \mathbb{R}_+. \end{cases} \tag{2.4}$$

Using the representation formula through Green kernels and denoting by $*_{\boldsymbol{r}}$ the spatial convolution, for any choice of spatial source term φ_1 the equality $p *_{\boldsymbol{r}} \varphi_1 = \widetilde{p} *_{\boldsymbol{r}} \varphi_1$ stands for positive times, thus p is also solution to System (2.4).

It is notable that the analytical solution to the system (N-W) can be explicitly derived using the *image source* method (see Section 1.1). The distributional solution to system (N-W) can then be expressed as a series of functions, with each term corresponding to a virtual source. In [5], a formal proof is provided for expressing the solution to (N-W) using the image-source method, leading to the following result:

Theorem 2.1.1 (Image source method)**.** *The solution p to* (N-W) *in the sense of distributions is given by:*

$$p(\boldsymbol{r},t) = \sum_{\boldsymbol{r}_{\boldsymbol{q},\boldsymbol{\varepsilon}} \in I_\Omega} p_{\boldsymbol{r}_{\boldsymbol{q},\boldsymbol{\varepsilon}}}(\boldsymbol{r},t), \quad \textit{with} \quad p_{\boldsymbol{r}_{\boldsymbol{q},\boldsymbol{\varepsilon}}}(\boldsymbol{r},t) = \frac{\delta(t - \|\boldsymbol{r}_{\boldsymbol{q},\boldsymbol{\varepsilon}} - \boldsymbol{r}\|/c)}{4\pi \|\boldsymbol{r}_{\boldsymbol{q},\boldsymbol{\varepsilon}} - \boldsymbol{r}\|}, \quad (\boldsymbol{r},t) \in \mathbb{R}^3 \times \mathbb{R}_+, \tag{2.5}$$

where I_Ω is defined in (1.6). An alternative proof of Theorem 2.1.1 is given at the end of this part in Chapter 4.

Each $p_{\boldsymbol{r}_{\boldsymbol{q},\boldsymbol{\varepsilon}}}$ is a Green kernel for the 3D wave equation in free-field. The sum can be interpreted as a superposition of sound waves emitted by a set of point sources located at the positions defined in (1.6). Each image source represents a specific path of specular reflections of the original source on the room's walls and is constructed by iteratively reflecting the source across the encountered walls.

It is worth mentioning that the geometric construction of image sources can be generalized to any polyhedral room configuration [22] by incorporating additional source visibility constraints. However, the image source technique provides the sound field solution to system (N-W) only for a very limited number of room geometries, including cuboid rooms, as stated by Theorem 2.1.1.

Remark 2.1.2. The image source technique does not account for general admittance conditions such as (13). In practice, the heuristic defined in Section 1.1.3 is often used, where a reflection coefficient is assigned to each wall based on its material properties and an amplitude coefficient $a_{\boldsymbol{q},\boldsymbol{\varepsilon}}$ is added to each impulse source term in equation (2.5) to model wall absorption. Whilst the resulting sound field solves the free-field wave equation given by (1.12), the addition of these amplitudes breaks the direct connection to the original wave equation (N-W).

2.1.2 A finite dimensional inverse problem

We aim to recover the positions of the image sources based on the pressure field p measured at a finite number of discrete microphones (microphones) in the room.

The pressure field p inside the room. Following the extended ISM model presented in Section 1.1.3, we consider p to be the solution of a free-field wave equation:

$$\frac{1}{c^2}\frac{\partial^2 p}{\partial t^2}(\boldsymbol{r},t) - \Delta p(\boldsymbol{r},t) = \psi(\boldsymbol{r})\delta(t), \qquad (\boldsymbol{r},t) \in \mathbb{R}^3 \times \mathbb{R}_+ \tag{2.6}$$

where $\psi(\boldsymbol{r}) = \sum_{k=1}^{+\infty} a_k \delta_{\boldsymbol{r}_k}(\boldsymbol{r})$, $\boldsymbol{r}_k$ being the locations of the image sources ranging over the set I_Ω defined by (1.6) and the a_k are in $(0,1)$ for every $k \in \mathbb{N}^*$, and are defined according to the heuristic described in Section 1.1.3. Therefore, the pressure field p reads

$$p(\boldsymbol{r},t) = \sum_{k=1}^{+\infty} a_k \frac{\delta(t - \|\boldsymbol{r}_k - \boldsymbol{r}\|_2 / c)}{4\pi \|\boldsymbol{r}_k - \boldsymbol{r}\|_2}, \qquad \boldsymbol{r} \in \mathbb{R}^3. \tag{2.7}$$

Observation of the pressure field at each microphone. Let $M \in \mathbb{N} \setminus \{0\}$ be the number of used microphones and

$$E_M = \{\boldsymbol{r}_m^{\text{mic}},\ m \in [\![1, M]\!]\} \tag{2.8}$$

be the set of microphone positions. In order to avoid the singularity of the Green kernel at each microphone location, we assume that for all $k \in \mathbb{N}^*$, $\boldsymbol{r}_k \notin \{\boldsymbol{r}_m^{\text{mic}}\}_{m\in[\![1,M]\!]}$. In our model, we need to account for three limitations:

- Microphones are unable to measure very high frequencies.
- Microphones cannot measure continuous signals.
- The source amplitudes decrease geometrically with the order of reflection, meaning that if k is large, a_k can be considered negligible. Therefore, we will assume that:

$$\exists K \in \mathbb{N}^* \quad | \quad \forall k \geq K+1, \quad a_k = 0.$$

Let us clarify the first and second limitations. The measured pressure field at each microphone is obtained by convolving p in time with a continuous filter κ that models the microphone's response. In our case we consider a low-pass filter that models the limitation of measuring only low-frequency signals. The resulting signal is then discretized into N time steps according to a fixed sampling frequency f_s, ranging from 0 to $T_{\max} = (N-1)/f_s$. Thus, the microphone m provides a sampled version of the signal in the form of a vector $(x_{m,n})_{0\leq n\leq N-1}$ given by

$$x_{m,n} = \left(\kappa * p(\boldsymbol{r}_m^{\mathrm{mic}}, \cdot)\right)(n/f_s) = \sum_{k=1}^{K} a_k \frac{\kappa(n/f_s - \left\|\boldsymbol{r}_k - \boldsymbol{r}_m^{\mathrm{mic}}\right\|_2 / c)}{4\pi \left\|\boldsymbol{r}_k - \boldsymbol{r}_m^{\mathrm{mic}}\right\|_2}. \tag{2.9}$$

for every $(m,n) \in [\![1, M]\!] \times [\![0, N-1]\!]$.

This leads us to define an observation function mapping a set of K source amplitudes $\boldsymbol{a} = (a_k)_{1\leq k\leq K}$ and positions $\boldsymbol{r} = (\boldsymbol{r}_k)_{1\leq k\leq K}$ to an ideal observation vector:

$$\forall(\boldsymbol{a}, \boldsymbol{r}) \in (\mathbb{R}_+)^K \times (\mathbb{R}^3 \setminus E_M)^K, \qquad \Gamma^K(\boldsymbol{a}, \boldsymbol{r}) = \sum_{k=1}^{K} a_k \gamma(\boldsymbol{r}_k), \tag{2.10}$$

where the function $\gamma : \mathbb{R}^3 \setminus E_M \to \mathbb{R}^{MN}$ is defined component-wise by:

$$\forall(m,n) \in [\![1, M]\!] \times [\![0, N-1]\!],\ \forall \boldsymbol{r} \in \mathbb{R}^3 \setminus E_M, \quad \gamma_{m,n}(\boldsymbol{r}) = \frac{\kappa(n/f_s - \left\|\boldsymbol{r} - \boldsymbol{r}_m^{\mathrm{mic}}\right\|_2 / c)}{4\pi \left\|\boldsymbol{r} - \boldsymbol{r}_m^{\mathrm{mic}}\right\|_2}. \tag{2.11}$$

Remark 2.1.3. In our applications, the amplitudes are contained in $[0, 1]$ (see Section 1.1.3). However, we generalize the problem here with unbounded coefficients.

Let us denote by $B\left(\boldsymbol{r}_m^{\mathrm{mic}}, cT_{\max}\right)$ the open ball of radius $cT_{\max}$ centered at $\boldsymbol{r}_m^{\mathrm{mic}}$. Let

$$\mathscr{C} = \bigcap_{m=1}^{M} \overline{B\left(\boldsymbol{r}_m^{\mathrm{mic}}, cT_{\max}\right)} \setminus E_M \tag{2.12}$$

be the set of spike positions that are observable by every microphone in the time interval, *i.e.* the set of sources for which every time of arrival at the microphones is inferior to the final time $T_{\max}$. Since the number of Dirac measures (or "spikes") to reconstruct is assumed to be lower than K, the reconstruction task can be framed as a least squares optimization problem:

$$\boxed{\inf_{(\boldsymbol{a},\boldsymbol{r})\in\mathcal{O}^K} T(\boldsymbol{a}, \boldsymbol{r}) \quad \text{with} \quad T(\boldsymbol{a}, \boldsymbol{r}) = \frac{1}{2}\left\|\boldsymbol{x} - \sum_{k=1}^{K} a_k \gamma(\boldsymbol{r}_k)\right\|_2^2 \quad \text{and} \quad \mathcal{O}^K = \mathbb{R}_+^K \times \mathscr{C}^K} \tag{$\mathscr{P}^K$}$$

where $\boldsymbol{x} = (x_{mn})_{(m,n)\in[\![1,M]\!]\times[\![0,N-1]\!]}$ is the target observation vector. In the following section, we discuss the well-posedness of this problem. In particular, we will demonstrate that, without further constraints on the problem data, any outcome is possible (existence or non-existence). This will lead us to consider constraining the problem.

2.2 Analysis of Problem $(\mathscr{P}^K)$

2.2.1 Well-posedness issues

In this section, we investigate the existence of solutions for problem $(\mathscr{P}^K)$. We show that, without additional assumptions on the measurements obtained from the microphones, which may include noise in practice, any scenario is possible. In particular, we present two situations: one where problem $(\mathscr{P}^K)$ has a solution, and another where it does not. The answers provided in this section are partial, as the conclusions are derived within frameworks that are not necessarily physical. Notably, two characteristics of the problem can lead to non-existence:

- The function γ is singular at the points where the microphones are placed.
- No regularization term has been added to the least squares function T.

This will lead us to consider a slightly modified version of problem $(\mathscr{P}^K)$.

Choice of the low-pass filter κ. In numerical applications, we will use an ideal low-pass filter given by:

$$\kappa^{\mathrm{lp}} : t \mapsto \mathrm{sinc}(\pi f_s t), \tag{2.13}$$

where f_s is both the sampling frequency and the cutoff frequency of the filter. This filter is designed to pass frequencies up to $f_s/2$, as the Fourier transform of κ^{lp} is a rectangle function of width $\frac{1}{2}$. Another commonly used filter is the Gaussian one, defined by

$$\kappa^{\sigma} : t \mapsto e^{-\frac{t^2}{2\sigma^2}}. \tag{2.14}$$

An example of non-existence. The existence of a solution to Problem $(\mathscr{P}^K)$ is not guaranteed in general. Indeed, the spikes of a minimizing sequence for Problem $(\mathscr{P}^K)$ may converge to microphone positions. In this paragraph, we detail the construction of counterexamples to the existence. Let M, N be two integers larger than 2 and $\boldsymbol{x} = (x_{mn})_{(m,n)\in[\![1,M]\!]\times[\![0,N-1]\!]}$ denote the synthetic observation vector defined by

$$\begin{cases} \forall m \in [\![2, M]\!],\ \forall n \in [\![0, N-1]\!] & x_{m,n} = 0 \\ \forall n \in [\![0, N-1]\!] & x_{1,n} = \alpha\kappa(n/f_s) \end{cases} \tag{2.15}$$

where $\alpha > 0$. Then if κ is continuous and $\kappa(0) > 0$, the optimal value for Problem $(\mathscr{P}^K)$ is zero. Indeed, let $(\boldsymbol{a}^l, \boldsymbol{r}^l)$ denote the sequence defined by

$$\begin{cases} \forall l \in \mathbb{N}^*, & a_1^l = \frac{4\pi\alpha}{l}, \quad \boldsymbol{r}_1^l = \boldsymbol{r}_1^{\mathrm{mic}} + \boldsymbol{u}/l \\ \forall l \in \mathbb{N}^*,\ k \in [\![2, K]\!] & a_k^l = 0, \quad \boldsymbol{r}_k^l = \boldsymbol{r}_1^{\mathrm{mic}} + \boldsymbol{u}/l \end{cases} \tag{2.16}$$

where $\boldsymbol{u}$ is an arbitrary unit vector. For l large enough $\Gamma^K(\boldsymbol{a}^l, \boldsymbol{r}^l)$ is well defined and $\Gamma^K(\boldsymbol{a}^l, \boldsymbol{r}^l)$ converges to $\boldsymbol{x}$ as l goes to infinity. To further simplify this example, assume that $K = 1$, *i.e.* we can place only one spike. Assume by contradiction that there exists a solution $(\boldsymbol{a}, \boldsymbol{r}) = (a_1, \boldsymbol{r}_1)$ to problem ($\mathscr{P}^K$) such that $a_1 > 0$ and $\boldsymbol{r}_1 \neq \boldsymbol{r}_1^{\text{mic}}$. Since the optimal value is 0, $a_1\gamma_{1,n}(\boldsymbol{r}_1) = \alpha\kappa(n/f_s)$ for all n. Let $t_1 = \frac{\|\boldsymbol{r}_1 - \boldsymbol{r}_1^{\text{mic}}\|_2}{c} > 0$ be the source's time of arrival at $\boldsymbol{r}_1^{\text{mic}}$. We get:

$$a_1 \frac{\kappa(n/f_s - t_1)}{4\pi c t_1} = \alpha\kappa(n/f_s), \quad \forall n \in [\![0, N-1]\!]. \tag{2.17}$$

In particular, evaluating this expression at $n = 0$ yields $\frac{a_1}{4\pi c t_1} = \frac{\alpha\kappa(0)}{\kappa(t_1)}$, and (2.17) can therefore be rewritten as:

$$\forall n \in [\![0, N-1]\!], \quad \kappa(n/f_s - t_1) = \kappa(n/f_s)\frac{\kappa(t_1)}{\kappa(0)}. \tag{2.18}$$

Relation (2.18) is not true in general for all values of n, depending on the choice of the filter κ. For instance if $\kappa = \kappa^{\text{lp}}$ as defined in (2.13), then (2.18) yields $\kappa(n/f_s - t_1) = 0$ for every $n \in [\![1, N-1]\!]$, which is false if $f_s t_1$ is not an integer.

If $\kappa = \kappa^\sigma$ (Gaussian filter), we get by definition:

$$\kappa^\sigma(n/f_s - t_1) = \kappa^\sigma(n/f_s)\kappa^\sigma(t_1)e^{\frac{n t_1}{f_s \sigma^2}}. \tag{2.19}$$

As $\kappa^\sigma(0) = 1$, (2.18) leads to $e^{\frac{n t_1}{f_s \sigma^2}} = 1$ and $t_1 = 0$, *i.e.* $\boldsymbol{r}_1 = \boldsymbol{r}_1^{\text{mic}}$. For both filter types we get a contradiction, thus problem ($\mathscr{P}^K$) does not admit a solution in that case.

Existence may arise. We now provide an existence criterion for Problem ($\mathscr{P}^K$) under the assumption that the operator Γ^K is lower bounded in some sense:

Definition 2.2.1. *Γ^K is said to be **amplitude lower-bounded** if there exists a constant $C > 0$ such that:*

$$\forall (\boldsymbol{a}, \boldsymbol{r}) \in \mathcal{O}^K, \quad \left\|\Gamma^K(\boldsymbol{a}, \boldsymbol{r})\right\|_2 \geq C \sum_{k=1}^{K} a_k. \tag{2.20}$$

In what follows, we will make the following general assumption on the kernel κ:

$$\begin{aligned} &(i) \quad \text{The function } \kappa \text{ is continuous on } \mathbb{R}, \text{ such that } \kappa(0) > 0 \\ &(ii) \quad \lim_{|s|\to+\infty} \kappa(s) = 0. \end{aligned} \tag{H_{filter}}$$

Let us now state the main existence result.

Theorem 2.2.1. *Let us assume that κ satisfies (H_{filter}) and that Γ^K is amplitude lower-bounded by a constant $C > 0$. We define the constant :*

$$\phi := \inf_{t \in \mathbb{R}_+^*} \sum_{n=0}^{N-1} \frac{\kappa(n/f_s)\kappa(n/f_s - t)}{4\pi c t} \tag{2.21}$$

and the coefficients

$$\mu_m := \sum_{n=0}^{N-1} x_{m,n}\kappa(n/f_s), \quad m \in [\![1, M]\!]. \tag{2.22}$$

Then Problem ($\mathscr{P}^K$) *has a solution whenever one of the following conditions is satisfied:*

(i) $\phi < 0$ *and for all* $m \in [\![1, M]\!]$, $\mu_m \leq \frac{2}{C}\phi \|\boldsymbol{x}\|_2$

(ii) $\phi \geq 0$ *and for all* $m \in [\![1, M]\!]$, $\mu_m \leq 0$.

The proof of Theorem 2.2.1 is provided in Section 2.2.2. We conclude this section by specifying sufficient conditions on the filter κ that ensure the assumption "Γ^K is amplitude lower-bounded" is satisfied.

On the assumption "Γ^K is amplitude lower-bounded". Intuitively, the assumption that Γ^K is amplitude lower-bounded translates the fact that the positive part of the filter κ is stronger than its negative part, and that two spikes cannot cancel each other out. The following criterion provides a sufficient condition on the filter κ to ensure amplitude lower-boundedness of Γ^K with respect to the number of time samples.

Proposition 2.2.1. *Let* $f_s \in \mathbb{R}_+^*$, $N \in \mathbb{N}^*$. *Let* κ *satisfy* (H_{filter}) *and:*

$$\forall \tau \in \left[0, \frac{N-1}{f_s}\right], \qquad \sum_{n=0}^{N-1} \kappa(n/f_s - \tau) > 0 \tag{2.23}$$

then Γ^K *is amplitude lower-bounded.*

In particular we can apply this result to κ^{lp} defined in (2.13).

Corollary 2.2.1. *Let* $\kappa = \kappa^{lp}$, *then* Γ^K *is amplitude lower-bounded.*

In practice criterion (2.23) can be relaxed to a continuous counterpart which ensures Γ^K is asymptotically amplitude lower-bounded as the number of time samples goes to infinity. The following result encompasses the case of the Gaussian filter κ^σ given by (2.14).

Corollary 2.2.2. *Let* $T_{\max} \in \mathbb{R}_+^*$ *and assume that the filter* κ *verifies:*

$$\forall \tau \in [0, T_{\max}], \quad \int_0^{T_{\max}} \kappa(t-\tau)dt > 0. \tag{2.24}$$

Then there exists $N' \in \mathbb{N}^*$ *such that* Γ^K *is amplitude lower-bounded for all* f_s, N *that verify* $N \geq N'$ *and* $T_{\max} = (N-1)/f_s$.

The proofs for Proposition 2.2.1, and for Corollaries 2.2.1 and 2.2.2 are provided in Section 2.2.3.

2.2.2 Proof of Theorem 2.2.1

We first study the behavior of the spikes of a minimizing sequence for Problem ($\mathscr{P}^K$) (Lemma 2.2.1), and provide an expression of the optimal value (Lemma 2.2.2). From this expression we deduce a simple existence criterion (Lemma 2.2.3) which we then apply to prove Theorem 2.2.1. The following lemma explores the asymptotic behavior of the amplitudes and locations of a minimizing sequence $(\boldsymbol{a}^l, \boldsymbol{r}^l)$.

Lemma 2.2.1. *Consider a minimizing sequence $(\boldsymbol{a}^l, \boldsymbol{r}^l)$ for Problem ($\mathscr{P}^K$), and $k \in [\![1, K]\!]$. Then, up to a subsequence, the sequence of spike positions $(\boldsymbol{r}_k^l)$ satisfies one of the following properties:*

(i) $\exists \boldsymbol{r}_k \in \mathscr{C},\ \exists a_k \in \mathbb{R}_+, \quad \boldsymbol{r}_k^l \xrightarrow[l\to+\infty]{} \boldsymbol{r}_k$ *and* $a_k^l \xrightarrow[l\to+\infty]{} a_k$

(ii) $\exists m_k \in [\![1, M]\!],\ \exists \widetilde{a}_k \in \mathbb{R}_+ \quad \boldsymbol{r}_k^l \xrightarrow[l\to+\infty]{} \boldsymbol{r}_{m_k}^{mic},\ a_k^l \xrightarrow[l\to+\infty]{} 0$ *and* $\frac{a_k^l}{4\pi\left\|\boldsymbol{r}_k^l - \boldsymbol{r}_{m_k}^{mic}\right\|_2} \xrightarrow[l\to+\infty]{} \widetilde{a}_k$.

Proof. Let $k \in [\![1, K]\!]$. $(\boldsymbol{r}^l)$ is bounded by definition of $\mathscr{C}$. The amplitudes $(\boldsymbol{a}^l)$ are also bounded as

$$\left\|\Gamma^K(\boldsymbol{a}^l, \boldsymbol{r}^l) - \boldsymbol{x}\right\|_2 \geq \left|\left\|\Gamma^K(\boldsymbol{a}^l, \boldsymbol{r}^l)\right\|_2 - \|\boldsymbol{x}\|_2\right| \geq C \sum_{k=1}^{K} a_k^l - \|\boldsymbol{x}\|_2 \tag{2.25}$$

by amplitude lower-boundedness of Γ^K. We can thus consider a subsequence (still denoted $(\boldsymbol{a}^l, \boldsymbol{r}^l)$ with a slight abuse of notation) for which the amplitudes $(\boldsymbol{a}^l)$ converge to a certain vector $\boldsymbol{a} \in \mathbb{R}_+^K$ and each position $(\boldsymbol{r}_j^l)$ converges to a location $\boldsymbol{r}_j \in \mathscr{C} \cup E_M$. Case (i) is verified if $\boldsymbol{r}_k \notin E_M$.

Consider now a spike sequence $(\boldsymbol{r}_k^l)$ converging to a microphone position $\boldsymbol{r}_{m_k}^{\mathrm{mic}}$. We define $I_{m_k} \subset [\![1, K]\!]$ as the indices of the spikes locations $\boldsymbol{r}_j^l$ converging towards $\boldsymbol{r}_{m_k}^{\mathrm{mic}}$ as $l \to +\infty$. The residual at the first time sample is given by

$$c_{m_k,0}^l = x_{m_k,0} - \sum_{j \notin I_{m_k}} a_j^l \gamma_{m_k,0}(\boldsymbol{r}_j^l) - \sum_{j \in I_{m_k}} a_j^l \gamma_{m_k,0}(\boldsymbol{r}_j^l) \tag{2.26}$$

By minimality, $(c_{m_k,0}^l)^2$ is necessarily bounded, thus so is $\sum_{j\in I_{m_k}} a_j^l \gamma_{m_k,0}(\boldsymbol{r}_j^l)$. As $\kappa(0) > 0$, each term of the sum is positive if l is large enough, hence these terms are individually bounded. We deduce that

$$a_k^l \gamma_{m_k,0}(\boldsymbol{r}_k^l) = a_k^l \frac{\kappa(\left\|\boldsymbol{r}_k^l - \boldsymbol{r}_{m_k}^{\mathrm{mic}}\right\|_2 / c)}{4\pi \left\|\boldsymbol{r}_k^l - \boldsymbol{r}_{m_k}^{\mathrm{mic}}\right\|_2} \tag{2.27}$$

is bounded. By continuity of κ at 0, $\frac{a_k^l}{\left\|\boldsymbol{r}_k^l - \boldsymbol{r}_{m_k}^{\mathrm{mic}}\right\|_2}$ is bounded, and therefore the case (ii) arises. $\square$

Using Lemma 2.2.1, we now provide a useful expression of the optimal value.

Lemma 2.2.2. *There exists an integer (possibly equal to 0) $K' \leq K$, a pair $(\boldsymbol{a}, \boldsymbol{r}) \in (\mathbb{R}_+)^{K'} \times (\mathbb{R}^3 \setminus E_M)^{K'}$, and $\widetilde{\boldsymbol{a}} \in \mathbb{R}_+^M$ such that, up to a permutation of the indices, the optimal value of problem ($\mathscr{P}^K$) expands as:*

$$\inf_{(\boldsymbol{a},\boldsymbol{r})\in\mathcal{O}^K} T(\boldsymbol{a}, \boldsymbol{r}) = \widetilde{T}(\boldsymbol{a}, \boldsymbol{r}, \widetilde{\boldsymbol{a}}) := \frac{1}{2} \sum_{m=1}^{M} \sum_{n=0}^{N-1} \left(x_{m,n} - \sum_{k=1}^{K'} a_k \gamma_{m,n}(\boldsymbol{r}_k) - \widetilde{a}_m \kappa(n/f_s) \right)^2 \tag{2.28}$$

Moreover, there exists a minimizing sequence $(\boldsymbol{a}^l, \boldsymbol{r}^l)$ for Problem ($\mathscr{P}^K$) such that $(a_k^l, \boldsymbol{r}_k^l)$ converges to $(a_k, \boldsymbol{r}_k)$ for all $k \in [\![1, K']\!]$ and (a_k^l) converges to 0 for $k \in [\![K'+1, K]\!]$.

Proof. Consider an arbitrary minimizing sequence $(\boldsymbol{a}^l, \boldsymbol{r}^l)$ for problem $(\mathscr{P}^K)$. Lemma 2.2.1 shows that, up to extracting a sub-sequence and permuting the indices, we can assume that the first $K' \in [\![0, K]\!]$ spikes positions converge to locations $\boldsymbol{r}_k$ that are distinct from the sensor locations, while the remaining spikes converge to positions in E_M. By continuity of the kernel, $\sum_{k=1}^{K'} a_k^l \gamma_{m,n}(\boldsymbol{r}_k^l)$ converges to $\sum_{k=1}^{K'} a_k \gamma_{m,n}(\boldsymbol{r}_k)$ for all m, n.

Consider now the spikes that converge to some microphone location in E_M. For $m \in [\![1, M]\!]$ we define $I_m \subset [\![1, K]\!]$ as the set of indices k such that $\boldsymbol{r}_k = \boldsymbol{r}_m^{\text{mic}}$. Observe that by Lemma 2.2.1 if several spikes converge to the same microphone m their contributions share the same sign and can then be summed.

$$\forall m, n, \quad \sum_{i \in I_m} a_{k_i}^l \gamma_{m,n}(\boldsymbol{r}_{k_i}^l) \xrightarrow[l \to +\infty]{} \kappa(n/f_s) \sum_{i \in I_m} \widetilde{a}_{k_i} = \kappa(n/f_s)\widetilde{a}_m, \quad \widetilde{a}_m \in \mathbb{R}_+. \tag{2.29}$$

Moreover, if a spike $\boldsymbol{r}_j^l$ converges to a microphone location, the corresponding amplitude a_j^l converges to 0, hence:

$$\forall m \neq m' \in [\![1, M]\!],\ \forall j \in I_{m'}, \quad a_j^l \gamma_{m,n}(\boldsymbol{r}_j^l) \xrightarrow[l \to +\infty]{} 0. \tag{2.30}$$

Thus, a spike that converges to a microphone contributes only to the terms related to that particular microphone in the cost function, which justifies formula (2.28). If none of the spikes converge to a given microphone m, the corresponding coefficient $\widetilde{a}_m$ is zero. □

In the following lemma, we state a numerical condition that guarantees the existence of a minimizer for Problem $(\mathscr{P}^K)$.

Lemma 2.2.3. *Let $K' \leq K$, $(\boldsymbol{a}, \boldsymbol{r}) \in (\mathbb{R}_+)^{K'} \times (\mathbb{R}^3 \backslash E_M)^{K'}$, $\widetilde{\boldsymbol{a}} \in \mathbb{R}_+^M$ such that $\inf_{(\boldsymbol{a},\boldsymbol{r}) \in \mathcal{O}^K} T(\boldsymbol{a}, \boldsymbol{r}) = \widetilde{T}(\boldsymbol{a}, \boldsymbol{r}, \widetilde{\boldsymbol{a}})$. If the pair $(\boldsymbol{a}, \boldsymbol{r})$ is such that*

$$\forall m \in [\![1, M]\!], \quad \sum_{n=0}^{N-1} x_{m,n} \kappa(n/f_s) \leq \sum_{k=1}^{K'} \sum_{n=0}^{N-1} a_k \kappa(n/f_s) \gamma_{m,n}(\boldsymbol{r}_k), \tag{2.31}$$

then $\widetilde{\boldsymbol{a}} = 0$ and Problem $(\mathscr{P}^K)$ has a solution.

Proof. Let $K' < K$, $(\boldsymbol{a}, \boldsymbol{r}, \widetilde{\boldsymbol{a}})$ yielding a decomposition of the optimal value as specified in Lemma 2.2.2 and consider the following quadratic optimization program

$$\inf_{\boldsymbol{b} \in \mathbb{R}^M} \widetilde{T}(\boldsymbol{a}, \boldsymbol{r}, \boldsymbol{b}) = \inf_{\boldsymbol{b} \in \mathbb{R}^M} \sum_{m=1}^{M} \widetilde{T}^m(b_m) \tag{2.32}$$

where $\widetilde{T}^m : t \mapsto \frac{1}{2} \sum_{n=0}^{N-1} \left(x_{m,n} - \sum_{k=1}^{K'} a_k \gamma_{m,n}(\boldsymbol{r}_k) - t\kappa(n/f_s) \right)^2$. Note that $\widetilde{T}^m$ is a positive, convex quadratic polynomial of the real variable t. Denoting by $\widetilde{b}_m^*$ the minimizer of $\widetilde{T}^m$ over $\mathbb{R}$, its minimizer over $\mathbb{R}_+$ is necessarily $\max(\widetilde{b}_k^*, 0)$. We deduce that if every component $\widetilde{b}_m^*$ is negative, then the coefficients $\widetilde{a}_m$ are all zero and consequently there exists a solution to problem ($\mathscr{P}^K$). Indeed, we obtain in this case $T(\boldsymbol{a}', \boldsymbol{r}') = \inf_{(\boldsymbol{a},\boldsymbol{r})\in\mathcal{O}^K} T(\boldsymbol{a}, \boldsymbol{r})$, with

$$(a_k', \boldsymbol{r}_k') = \begin{cases} (a_k, \boldsymbol{r}_k) & \text{if } k \leq K' \\ (0, \boldsymbol{v}) & \text{otherwise} \end{cases} \tag{2.33}$$

where $\boldsymbol{v}$ is an arbitrary location distinct from the microphones. Note that $\widetilde{\boldsymbol{b}}^*$ is given by the first order optimality conditions for each function $\widetilde{T}^m$:

$$\forall m \in [\![1, M]\!], \quad \sum_{n=0}^{N-1} \kappa(n/f_s) \left(x_{m,n} - \sum_{k=1}^{K'} a_k \gamma_{m,n}(\boldsymbol{r}_k) - \widetilde{b}_m^* \kappa(n/f_s) \right) = 0 \tag{2.34}$$

and thus,

$$\forall m \in [\![1, M]\!], \quad \sum_{n=0}^{N-1} \kappa(n/f_s)^2 \widetilde{b}_m^* = \sum_{n=0}^{N-1} \kappa(n/f_s) \left(x_{m,n} - \sum_{k=1}^{K'} a_k \gamma_{m,n}(\boldsymbol{r}_k) \right). \tag{2.35}$$

Since $\sum_{n=0}^{N-1} \kappa(n/f_s)^2 \geq \kappa(0)^2 > 0$, we infer:

$$\forall m \in [\![1, M]\!], \quad \widetilde{b}_m^* \leq 0 \iff \sum_{n=0}^{N-1} \kappa(n/f_s) \left(x_{m,n} - \sum_{k=1}^{K'} a_k \gamma_{m,n}(\boldsymbol{r}_k) \right) \leq 0 \tag{2.36}$$

which is exactly (2.31). □

We can now prove Theorem 2.2.1.

Proof of Theorem 2.2.1. In order to get a global existence criterion on the observation vector $\boldsymbol{x}$ and the operator Γ^K, we only need to compute a uniform lower bound of the right hand side of inequality (2.31). We consider a decomposition of the optimal value as given by Lemma 2.2.2 and keep the same notations.

Consider ϕ as defined in Theorem 2.2.1. Using (H_{filter}), we infer that ϕ is finite by continuity and boundedness of the kernel κ. Let $m \in [\![1, M]\!]$. We distinguish two cases based on the sign of ϕ.

Proof under the assumption (i). Assume $\phi \leq 0$. Consider $(\boldsymbol{a}, \boldsymbol{r}, \widetilde{\boldsymbol{a}})$ a decomposition of the optimal value as given by Lemma 2.2.2, K' the associated truncating integer, and a corresponding minimizing sequence $(\boldsymbol{a}^l, \boldsymbol{r}^l)$. If taking a null vector of amplitudes yields a solution to problem ($\mathscr{P}^K$), then we are done. Otherwise, using the amplitude lower-boundedness hypothesis we obtain the following inequalities for all l large enough:

$$\left\| \boldsymbol{x} - \Gamma^K(0, \boldsymbol{r}^l) \right\|_2 = \|\boldsymbol{x}\|_2 \geq \left\| \boldsymbol{x} - \Gamma^K(\boldsymbol{a}^l, \boldsymbol{r}^l) \right\|_2 \geq \left\| \Gamma^K(\boldsymbol{a}^l, \boldsymbol{r}^l) \right\|_2 - \|\boldsymbol{x}\|_2 \geq C \sum_{k=1}^{K} a_k^l - \|\boldsymbol{x}\|_2 .$$

Letting l go to infinity, we obtain $\frac{2}{C}\|\boldsymbol{x}\|_2 \geq \sum_{k=1}^{K'} a_k$, from which we infer

$$\sum_{n=0}^{N-1}\sum_{k=1}^{K'}\kappa(n/f_s)a_k\gamma_{m,n}(\boldsymbol{r}_k) = \sum_{k=1}^{K'} a_k \sum_{n=0}^{N-1}\frac{\kappa(n/f_s)\kappa(n/f_s - \left\|\boldsymbol{r}_k - \boldsymbol{r}_m^{\text{mic}}\right\|_2/c)}{4\pi\left\|\boldsymbol{r}_k - \boldsymbol{r}_m^{\text{mic}}\right\|_2} \geq \frac{2\phi}{C}\|\boldsymbol{x}\|_2 .$$

By using (i), we finally get that (2.31) is true, whence the result.

Proof under the assumption (ii). Assume $\phi \geq 0$. Then we obviously have:

$$\forall m \in [\![1, M]\!], \quad \sum_{n=0}^{N-1}\sum_{k=1}^{K'}\kappa(n/f_s)a_k\gamma_{m,n}(\boldsymbol{r}_k) \geq 0 \geq \mu_m, \tag{2.37}$$

and (2.31) holds. Applying Lemma 2.2.3 yields the expected conclusion. □

2.2.3 Proofs of Proposition 2.2.1, Corollary 2.2.1 and Corollary 2.2.2

Proof of Proposition 2.2.1. We only need to consider amplitude vectors $\boldsymbol{a}$ such that $\sum_k a_k > 0$. By equivalence of the norms in finite dimension and homogeneity, considering the set of convex weights $H = \{\boldsymbol{\alpha} \in \mathbb{R}_+^K,\ \sum_{k=1}^K \alpha_k = 1\}$, one has to show:

$$\exists C \in \mathbb{R}_+^*,\ \forall r \in \mathscr{C}^K,\ \forall \alpha \in H, \quad \left\|\Gamma^K(\alpha, r)\right\|_1 \geq C. \tag{2.38}$$

Let $J : \boldsymbol{a}, \boldsymbol{r} \mapsto \|\Gamma(\boldsymbol{a}, \boldsymbol{r})\|_1$ and $(\boldsymbol{\alpha}^l, \boldsymbol{r}^l)$ a minimizing sequence for $\inf_\Lambda J$, where $\Lambda = H \times \mathscr{C}^K$. As Λ and $\mathscr{C}$ are bounded, $(\boldsymbol{\alpha}^l, \boldsymbol{r}^l)$ converges up to a subsequence to some $(\boldsymbol{\alpha}^*, \boldsymbol{r}^*)$ where $\boldsymbol{\alpha}^* \in H$ and $\boldsymbol{r}^* \in (\mathscr{C} \cup E_M)^K$. Observe that if a spike $\boldsymbol{r}_k$ converges to a microphone location, the corresponding amplitude converges to 0. Indeed, let $m \in [\![1, M]\!]$ and let $I_m \subset [\![1, K]\!]$ be the set of indices k such that $\boldsymbol{r}_k^* = \boldsymbol{r}_m^{\text{mic}}$. Assume that I_m is non-empty, *i.e.* there exists a spike position converging to microphone $\boldsymbol{r}_m^{\text{mic}}$. We have:

$$\left\|\Gamma^K(\boldsymbol{a}^l, \boldsymbol{r}^l)\right\|_1 \geq \sum_{k=1}^K \alpha_k^l \gamma_{m,0}(\boldsymbol{r}_k^l) \underset{l\to+\infty}{\sim} \sum_{k\in I_m}\alpha_k^l\gamma_{m,0}(\boldsymbol{r}_k^l) + \sum_{k\notin I_m}\alpha_k^*\gamma_{m,0}(\boldsymbol{r}_k^*). \tag{2.39}$$

The sum $\sum_{k\in I_m}\alpha_k^l\gamma_{m,0}(\boldsymbol{r}_k^l)$ is thus bounded. Since $\kappa(0) > 0$ and κ is continuous, each term of the sum is positive for l large enough, and must consequently be bounded:

$$\alpha_k^l\gamma_{m,0}(\boldsymbol{r}_k^l) \underset{l\to+\infty}{\sim} \frac{\alpha_k^l}{4\pi\left\|\boldsymbol{r}_k^l - \boldsymbol{r}_m^{\text{mic}}\right\|_2}\kappa(0) = \mathrm{O}(1) \quad \forall k \in I_m. \tag{2.40}$$

Hence, if $(\boldsymbol{r}_k^l)$ converges to a microphone m for some k, then $\alpha_k^* = 0$ and $\frac{\alpha_k^l}{4\pi \left\|\boldsymbol{r}_k^l - \boldsymbol{r}_m^{\mathrm{mic}}\right\|_2}$ converges up to a subsequence to some nonnegative value c_k^*. Let $0 < K' \leq K'' \leq M$ such that:

$$\begin{cases} \forall k \in [\![1, K']\!],\ \alpha_k^* > 0 \text{ and } \boldsymbol{r}_k^* \in \mathscr{C} \\ \forall k \in [\![K'+1, K'']\!],\ \alpha_k^* = 0 \text{ and } \lim_{l\to+\infty} \boldsymbol{r}_k^l = \boldsymbol{r}_{m_k}^{\mathrm{mic}} \in E_M \\ \forall k \in [\![K''+1, K]\!],\ \alpha_k^* = 0 \text{ and } \boldsymbol{r}_k^* \in \mathscr{C}. \end{cases} \tag{2.41}$$

Note that $K' \neq 0$ as $\alpha^* \in H$. We have:

$$\forall l \in \mathbb{N}, \quad J(\boldsymbol{a}^l, \boldsymbol{r}^l) = \sum_{m=1}^{M} \sum_{n=0}^{N-1} \left| \sum_{k=1}^{K} \alpha_k^l \gamma_{m,n}(\boldsymbol{r}_k^l) \right| \geq \sum_{m=1}^{M} \sum_{n=0}^{N-1} \sum_{k=1}^{K} \alpha_k^l \gamma_{m,n}(\boldsymbol{r}_k^l). \tag{2.42}$$

Letting l go to infinity, we get:

$$\inf_{\Lambda} J \geq \sum_{m=1}^{M} \sum_{k=1}^{K'} \frac{\alpha_k^*}{4\pi \left\|\boldsymbol{r}_k^* - \boldsymbol{r}_m^{\mathrm{mic}}\right\|_2} \sum_{n=0}^{N-1} \kappa\left(\frac{n}{f_s} - \frac{\left\|r_k^* - \boldsymbol{r}_m^{\mathrm{mic}}\right\|_2}{c}\right) + \sum_{k=K'+1}^{K''} c_k^* \sum_{n=0}^{N-1} \kappa(n/f_s). \tag{2.43}$$

By construction of $\mathscr{C}$, $0 \leq \frac{\left\|\boldsymbol{r}_k^* - \boldsymbol{r}_m^{\mathrm{mic}}\right\|_2}{c} \leq (N-1)/f_s$ for $1 \leq k \leq K'$, $1 \leq m \leq M$. Inequality (2.23) then guarantees that the term $\frac{\alpha_k^*}{4\pi \left\|\boldsymbol{r}_k^* - \boldsymbol{r}_m^{\mathrm{mic}}\right\|_2} \sum_{n=0}^{N-1} \kappa\left(\frac{n}{f_s} - \frac{\left\|\boldsymbol{r}_k^* - \boldsymbol{r}_m^{\mathrm{mic}}\right\|_2}{c}\right)$ is positive for all $m \in [\![1, K']\!]$ and $k \in [\![1, K']\!]$. Likewise, the terms $c_k^* \sum_{n=0}^{N-1} \kappa\left(\frac{n}{f_s}\right)$ are nonnegative for $K' < k \leq K''$, thus the right-hand side in (2.43) is positive. □

Proof of Corollary 2.2.1. We call κ^{lp} the continuous extension of κ^{lp} at 0. We will prove that κ^{lp} satisfies (2.23). Let $\tau \in [0, (N-1)/f_s]$, $n^+ \in \mathbb{N}$ the smallest index such that $n^+/f_s \geq \tau$, and n^- the largest index such that $n^-/f_s \leq \tau$, see Fig. 2.1.

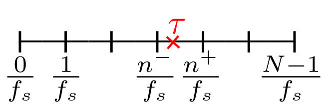

Figure 2.1

Let us set $y_n = \mathrm{sinc}(\pi f_s(n/f_s - \tau))$ for all n. One expands:

$$\sum_{n=0}^{N-1} y_n = \sum_{n=0}^{n^-} y_n + \sum_{n=n^+}^{N-1} y_n - \delta_{n^-,n^+}, \tag{2.44}$$

where δ_{n^-,n^+} denotes here the Kronecker symbol and handles the case where τ is exactly equal to one of the time samples, as $\kappa^{\mathrm{lp}}(0) = 1$.

Let us first assume that $n^- < n^+$. Let $l \in [\![0, N - n^+ - 1]\!]$, we have:

$$y_{n^++l} = \frac{\sin(\pi f_s(n^+/f_s - \tau) + l\pi)}{\pi f_s((n^+ + l)/f_s - \tau)} = (-1)^l \frac{\sin(\pi f_s(n^+/f_s - \tau))}{\pi f_s((n^+ + l)/f_s - \tau)}. \tag{2.45}$$

Note that $\sin(\pi f_s(n^+/f_s - \tau)) > 0$ as $\pi f_s(n^+/f_s - \tau) \in (0, \pi)$, and $y_{n^+} > 0$. By the alternating series theorem, the sum carries the sign of its first term. Indeed, we get the upper bound:

$$\left| \sum_{n=n^++1}^{N-1} y_n \right| \leq |y_{n^++1}| = \frac{\sin(\pi f_s(n^+ f_s - \tau))}{\pi f_s((n^+ + 1)/f_s - \tau)} \tag{2.46}$$

thus $\sum_{n=n^++1}^{N-1} y_n \geq -|y_{n^++1}|$ and

$$\sum_{n=n^+}^{N-1} y_n \geq y_{n^+} - |y_{n^++1}| = \sin(\pi f_s(n^+ f_s - \tau)) \left(\frac{1}{\pi f_s(n^+/f_s - \tau)} - \frac{1}{\pi f_s(n^+ + 1)/f_s - \tau)} \right) > 0.$$

Likewise, the sum $\sum_{n=0}^{n^-} y_n$ is non-zero and shares the sign of $\frac{\sin(\pi f_s(n^-/f_s - \tau))}{\pi f_s(\tau - n^-/f_s)}$, which is also positive.

In the case where $n^- = n^+$, we have $\tau = n^+/f_s$ and $y_{n^+} = 1$ and then,

$$\forall n \in [\![0, N-1]\!], \quad \pi f_s(n/f_s - \tau) = \pi(n - n^+) \in \pi\mathbb{Z}. \tag{2.47}$$

It follows that $y_n = \delta_{n,n^+}$ and $\sum_{n=0}^{N-1} y_n = 1$, which concludes the proof. □

Proof of Corollary 2.2.2. Let $\tau \in [0, T_{\max}]$ be given. Assume that the sampling frequency f_N is chosen such that $T_{\max} = (N-1)/f_N$. Observing that the sum in inequality (2.23) is a Riemann sum

$$S_N(\tau) \coloneqq \sum_{n=0}^{N-1} \kappa(n/f_N - \tau) = \sum_{n=0}^{N-1} \kappa\left(n \frac{T_{\max}}{N-1} - \tau\right), \tag{2.48}$$

it follows that S_N converges uniformly towards $\tau \mapsto \int_0^{T_{\max}} \kappa(t - \tau) dt$ over $[0, T_{\max}]$ as $N \to +\infty$. Thus for N large enough, inequality (2.23) is satisfied and Γ^K is amplitude lower-bounded. □

2.3 A super-resolution-type algorithm

The discussion in Section 2.2 leads us to define a slightly modified version of Problem ($\mathscr{P}^K$) to avoid the potential pathologies described above. In order to avoid non-existence caused by the singularities, we will enforce a small distance $\varepsilon > 0$ to the microphone positions. Let us hence introduce

$$\mathbb{R}^3_\varepsilon = \mathbb{R}^3 \setminus \bigcup_{m \in [\![1,M]\!]} B(\boldsymbol{r}_m^{\mathrm{mic}}, \varepsilon).$$

In our numerical approach, we will reformulate the problem as a BLASSO-type problem. Thus, it is relevant to add a l_1 regularization term to the cost function. We thus consider the problem

$$\inf_{(\boldsymbol{a},\boldsymbol{r})\in\mathcal{O}^K_{0,\varepsilon}} T_\lambda(\boldsymbol{a},\boldsymbol{r}) \quad \text{with} \quad \mathcal{O}^K_{0,\varepsilon} = \mathbb{R}^K_+ \times (\mathbb{R}^3_\varepsilon)^K \text{ and } T_\lambda(\boldsymbol{a},\boldsymbol{r}) = T(\boldsymbol{a},\boldsymbol{r}) + \lambda \sum_{k=1}^{K} a_k. \qquad (\mathscr{P}^K_{\varepsilon,\lambda})$$

2.3.1 Analysis of Problem ($\mathscr{P}^K_{\varepsilon,\lambda}$)

The maximal distance constraint on the spike locations is no longer needed, as the regularization term forces an upper bound on the amplitudes $\boldsymbol{a}$. Any spike vanishing at infinity hence has a null contribution to the objective function. If $\varepsilon > 0$ and $\lambda > 0$, existence is automatically guaranteed. Note that we can also define problem ($\mathscr{P}^K_{\varepsilon,\lambda}$) in the case $\varepsilon = 0$ by optimizing the cost function on $\mathcal{O}^K$.

Proposition 2.3.1. *Let $\varepsilon > 0$, $\lambda \geq 0$. Then, if at least one of the following assumptions holds, problem ($\mathscr{P}^K_{\varepsilon,\lambda}$) has a solution: (i) $\lambda > 0$ (ii) Γ^K is amplitude lower-bounded.*

Proof. Let $(\boldsymbol{a}^l, \boldsymbol{r}^l)$ be a minimizing sequence for problem ($\mathscr{P}^K_{\varepsilon,\lambda}$). If $\lambda > 0$, $(\boldsymbol{a}^l)$ is bounded due to the coercivity of the regularization term. In the case $\lambda = 0$, Γ^K is amplitude lower-bounded, which implies that $(\boldsymbol{a}^l)$ is also bounded. As the amplitudes are bounded and Γ^K is continuous, if a given location $\boldsymbol{r}_k$ diverges to infinity, its contribution $a_k\gamma(\boldsymbol{r}_k)$ vanishes in the limit. We can thus replace each diverging spike location by an arbitrary location $\boldsymbol{v}$ distinct from the microphones to obtain a bounded minimizing sequence. Any closure point of this sequence is a solution to Problem ($\mathscr{P}^K_{\varepsilon,\lambda}$) $\square$

It is notable that Theorem 2.2.1 can be adapted to Problem ($\mathscr{P}^K_{\varepsilon,\lambda}$) if $\lambda > 0$ and $\varepsilon = 0$.

Theorem 2.3.1. *Let $\lambda > 0$ and let us assume that κ is continuous, bounded and $\kappa(0) > 0$. Let ϕ, μ_m be defined as in Theorem 2.2.1. Then if one of the following conditions is met, problem ($\mathscr{P}^K_{\varepsilon,\lambda}$) with $\varepsilon = 0$ has at least one solution:*

(i) $\phi < 0$ *and for all* $m \in [\![1, M]\!]$, $\mu_m \leq \frac{\phi}{2\lambda} \|\boldsymbol{x}\|_2^2$

(ii) $\phi \geq 0$ *and for all* $m \in [\![1, M]\!]$, $\mu_m \leq 0$.

Remark 2.3.1. If Γ^K is amplitude lower-bounded with constant C, the inequality constraint in case (i) can be improved to:

$$\forall m \in [\![1, M]\!], \quad \mu_m \leq \max\left(\frac{\phi}{2\lambda}\|\boldsymbol{x}\|_2^2, \frac{2\phi}{C}\|\boldsymbol{x}\|_2\right). \tag{2.49}$$

Proof. We adapt the proof of Theorem 2.2.1. Observe that because $T_\lambda(\boldsymbol{a}, \boldsymbol{r}) \geq \lambda \sum_k a_k$ the amplitudes of a minimizing sequence $(\boldsymbol{a}^l, \boldsymbol{r}^l)$ are bounded, removing the need for the amplitude lower-boundedness hypothesis in Lemma 2.2.1. Lemma 2.2.1 can then be reproduced, with the added possibility of a spike diverging to infinity. Due to the boundedness of the amplitudes, the contribution of such a spike to the cost function vanishes in the limit. The rest of the proof is identical.

Likewise, the proof of Lemma 2.2.2 is identical in the case $\lambda > 0$, with a different expression of the optimal value:

$$\inf_{(\boldsymbol{a},\boldsymbol{r})\in\mathcal{O}^K} T_\lambda(\boldsymbol{a}, \boldsymbol{r}) = \widetilde{T}_\lambda(\boldsymbol{a}, \boldsymbol{r}, \widetilde{\boldsymbol{a}}) := \widetilde{T}(\boldsymbol{a}, \boldsymbol{r}, \widetilde{\boldsymbol{a}}) + \lambda \sum_{k=1}^{K'} a_k. \tag{2.50}$$

The addition of the regularization term does not affect the argument in Lemma 2.2.3, and the proof is identical as the optimality conditions considered in (2.34) are unchanged. We thus obtain the same existence criterion.

Finally, we only need to adapt the upper bound on the amplitudes given in the proof of Theorem 2.2.1 to handle the case $\phi < 0$. Using the same notations, we have here $T_\lambda(0, \boldsymbol{r}) = \frac{1}{2}\|\boldsymbol{x}\|_2^2 \geq T_\lambda(\boldsymbol{a}, \boldsymbol{r}) \geq \lambda \sum_{k=1}^{K'} a_k$. The same argument as before yields the existence criterion. □

2.3.2 A convex relaxation

Using the integral representation (2.9) we can extend the definition of the observation function Γ^K as a linear operator on the space of Radon measures defined in section 1.2.1. Let us define the linear operator Γ^ε:

$$\begin{aligned} \Gamma^\varepsilon : \mathcal{M}(\mathbb{R}^3_\varepsilon) &\longrightarrow \mathbb{R}^{MN} \\ \psi &\longmapsto \left(\int_{\boldsymbol{r}\in\mathbb{R}^3_\varepsilon} \frac{\kappa(n/f_s - \left\|\boldsymbol{r} - \boldsymbol{r}_m^{\text{mic}}\right\|_2 / c)}{4\pi \left\|\boldsymbol{r} - \boldsymbol{r}_m^{\text{mic}}\right\|_2} d\psi(\boldsymbol{r}) \right)_{\substack{1\leq m\leq M \\ 0\leq n\leq N-1}} \end{aligned} \tag{2.51}$$

which can be interpreted as the mapping of a given source term ψ supported on $\mathbb{R}^3_\varepsilon$ to the measured free-field response at each microphone location. Indeed, the solution to the free-field wave equation with a spatial source term ψ is given by convolving in space with a Green's function. This leads us to the following expression of $p(\boldsymbol{r}, t)$:

$$p(\boldsymbol{r}, t) = \int_{\boldsymbol{r}'\in\mathbb{R}^3_\varepsilon} \frac{\delta(t - \|\boldsymbol{r} - \boldsymbol{r}'\|_2 / c)}{4\pi \|\boldsymbol{r} - \boldsymbol{r}'\|_2} d\psi(\boldsymbol{r}'), \tag{2.52}$$

where the convolution of distributions is denoted with an integral symbol with a slight abuse of notation. We then proceed as in Section 2.1.2. p is convolved in time with the filter κ and discretized at each sample to get the observation vector:

$$x_{m,n} = \left(\kappa * p(\boldsymbol{r}_m^{\mathrm{mic}}, \cdot)\right)(n/f_s) = \int_{\boldsymbol{r}\in\mathbb{R}^3_\varepsilon} \frac{\kappa(n/f_s - \left\|\boldsymbol{r}_m^{\mathrm{mic}} - \boldsymbol{r}\right\|_2/c)}{4\pi\left\|\boldsymbol{r}_m^{\mathrm{mic}} - \boldsymbol{r}\right\|_2} d\psi(\boldsymbol{r}) \quad \forall m \in [\![1, M]\!],\ \forall n \in [\![0, N-1]\!]. \tag{2.53}$$

Whilst (2.52) is not well-defined for a Radon measure ψ, the integral in (2.53) can be seen as the evaluation of ψ at $\boldsymbol{r} \mapsto \frac{\kappa(n/f_s - \left\|\boldsymbol{r}_m^{\mathrm{mic}} - \boldsymbol{r}\right\|_2/c)}{4\pi\left\|\boldsymbol{r}_m^{\mathrm{mic}} - \boldsymbol{r}\right\|_2}$ which is continuous on $\mathbb{R}^3_\varepsilon$.

The convex relaxation of problem ($\mathscr{P}^K_{\varepsilon,\lambda}$) is called Beurling-LASSO or BLASSO (see Section 1.2.2) and can be written as:

$$\inf_{\psi\in\mathcal{M}(\mathbb{R}^3_\varepsilon)} \frac{1}{2}\left\|\boldsymbol{x} - \Gamma^\varepsilon\psi\right\|_2^2 + \lambda\|\psi\|_{\mathrm{TV}}. \tag{$\mathscr{B}_{\lambda,\varepsilon}$}$$

Remark 2.3.2. Problem ($\mathscr{P}^K_{\varepsilon,\lambda}$) is indeed the restriction of problem ($\mathscr{B}_{\lambda,\varepsilon}$) to linear combinations of K Dirac measures, as for $(\boldsymbol{a}, \boldsymbol{r}) \in \mathcal{O}^K_{0,\varepsilon}$, $\Gamma^K(\boldsymbol{a}, \boldsymbol{r}) = \Gamma^\varepsilon(\sum_{k=1}^K a_k\delta_{\boldsymbol{r}_k})$ and $\|\sum_{k=1}^K a_k\delta_{\boldsymbol{r}_k}\|_{\mathrm{TV}} = \sum_{k=1}^K |a_k| = \|\boldsymbol{a}\|_1$. Moreover, Γ^ε is continuous, and for $\lambda > 0$ problem ($\mathscr{B}_{\lambda,\varepsilon}$) admits solutions [25], with at least one MN-sparse solution [24] (meaning a measure composed of at most MN Dirac masses). In particular, for $K \geq MN$, the optimal values for ($\mathscr{P}^K_{\varepsilon,\lambda}$) and ($\mathscr{B}_{\lambda,\varepsilon}$) are the same.

Applying the theory introduced in [60] and summarized in Section 1.2.2 is difficult in our case, as the operator Γ^ε is 3-dimensional and depends on a complex geometric relation between the locations of the sources and the positions of the microphones. However, it is possible to compute numerically the vanishing derivatives pre-certificates η_V (see Definition 1.2.3) to obtain some insights on the operator's behavior. Fig. 2.2 represents the values taken by η_V on a portion of a plane parallel to a wall that contains several image sources, for varying sampling frequencies. The microphone array's geometry is spherical here, and we proceed to increase the radius of the array, as the array size has an impact on the ability to geometrically locate sources (see Section 2.4 for further details on the experimental setup). Note that the mass of η_V is concentrated on spheres that are centered around each microphone, with radii given by the times of arrival of each source to the microphone. Due to the application of the low-pass filter, each sphere is slightly smeared around its true radius, and the location of an image source is given at the intersection of every of its corresponding spheres. As the sampling frequency and the array's radius increase, the mass of η_V becomes more tightly contained around each sphere, ensuring a sharper distribution at the intersection. Recall that stable support recovery is guaranteed by Theorem 1.2.1 under an assumption of non-degeneracy of η_V, *i.e.* $\eta_V(\boldsymbol{r}) < 1$ if $\boldsymbol{r}$ is not a source location. While Fig 2.2 shows that η_V is degenerate at 8 kHz and for the smallest array radius in this case, it seems to be non-degenerate for greater radii and sampling frequencies. More generally, numerical experiments indicate that, for a fixed room and with measurements from a spherical microphone array, η_V is non-degenerate when the sampling frequency and array radius are sufficiently large, and thus that Theorem 1.2.1 applies.

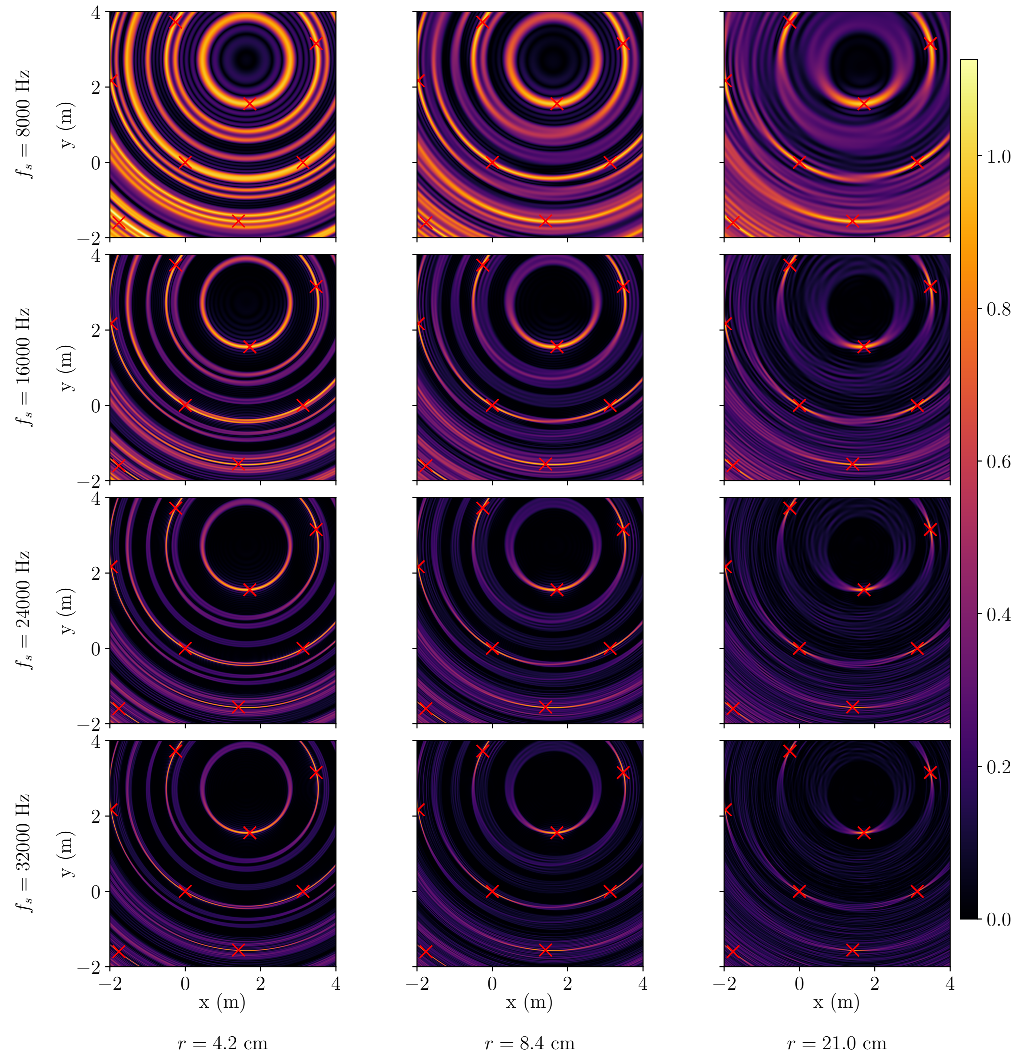

(a) Values taken by $|\eta_V|$ on a section plane

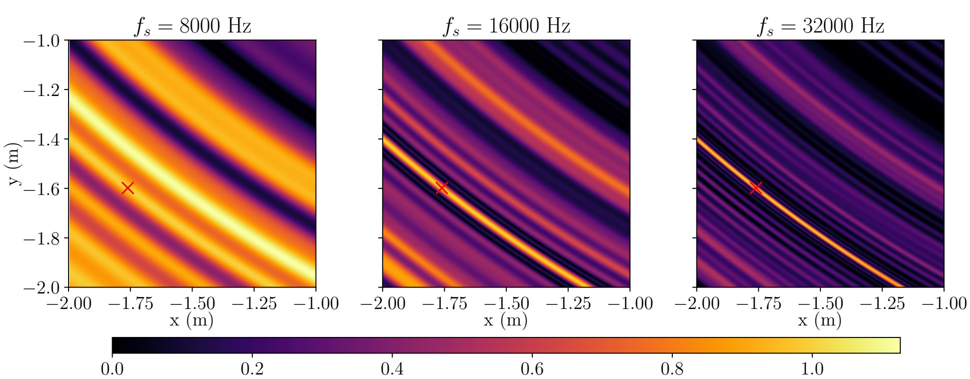

(b) Zoom on the lower left section for $r = 4.2$ cm

Figure 2.2: 2D plot of the absolute value of the vanishing derivative pre-certificate η_V on a section plane parallel to a wall of a room for different sampling frequencies f_s and microphone array radii r. The locations of the image sources that belong to the plane are marked by red crosses.

2.3.3 Numerical algorithm

We implement[1] and adapt the Sliding Frank-Wolfe type algorithm introduced in [53] and initially applied to microscopy in order to find a sparse solution to Problem ($\mathscr{B}_{\lambda,\varepsilon}$) (see Remark 2.3.2). See Section 1.2.3 for a description of the more general Frank-Wolfe algorithm. Let $\psi^{(i)} = \sum_{k=1}^{K^{(i)}} a_k^{(i)} \delta_{\boldsymbol{r}_k^{(i)}}$ be the reconstructed measure at iteration i. The reconstruction algorithm consists of two main steps in each iteration:

1. A new source is located by maximizing the numerical certificate:

$$\begin{array}{rccl} \eta^{(i)}: & \mathbb{R}^3 & \longrightarrow & \mathbb{R} \\ & \boldsymbol{r} & \longmapsto & \left(\Gamma^* \mathbf{res}^{(i)}\right)(\boldsymbol{r}) = \sum_{m,n} \mathbf{res}_{m,n}^{(i)} \gamma_{m,n}(\boldsymbol{r}) \end{array} \tag{2.54}$$

   where $\mathbf{res}^{(i)} := \boldsymbol{x}^{(i)} - \Gamma\psi^{(i)}$ is the residual at iteration i and Γ^* is the adjoint of operator Γ. A stopping criterion can be inferred from the optimality conditions of the BLASSO problem [53]: $\eta^{(i)}(\boldsymbol{r}_*^{(i)}) \leq \lambda$ where $\boldsymbol{r}_*^{(i)}$ is the new candidate location. If this criterion is not met, $\boldsymbol{r}_*^{(i)}$ is added to the list of already reconstructed source positions to form $\boldsymbol{r}^{(i+1)}$.

2. The amplitudes are then updated by solving a non-negative convex LASSO problem:

$$\boldsymbol{a}^{(i+1)} = \underset{\boldsymbol{a} \in \mathbb{R}_+^{\mathrm{len}(\boldsymbol{r}^{(i+1)})}}{\operatorname{argmin}} T_\lambda(\boldsymbol{a}, \boldsymbol{r}^{(i+1)}). \tag{2.55}$$

The full algorithm is defined in the next page in Alg. 2, and the procedure is explained in detail afterwards.

Step 1 is encompassed by the lines 7-9 of Alg. 2. The maximization of $\eta^{(i)}$ is achieved numerically by applying a parallel implementation of the BFGS algorithm [71] to solve the optimization problem. A crucial issue is to provide an accurate guess for initializing BFGS. This becomes especially difficult as the operator's "sharpness" increases with the sampling frequency and the size of the microphone array, as illustrated in the precertificate plots of Fig. 2.2. Due to the spatial extent of the 3D optimization domain, evaluating $\eta^{(i)}$ on a global fine grid would require millions of function evaluations per iteration and is computationally intractable. We consider instead an efficient heuristic to initialize BFGS. As described previously, a true source should be located at the intersection of the spheres centered around each microphone with radii given by the corresponding times of arrival of the source to each microphone. In order to approximate these times of arrival, we apply a moving average over 3 samples to the squared residual signal of each microphone and extract the sample with maximal value. We then consider the 8 microphones with the highest values and build uniform grids with a mean angular spacing of 5° on the corresponding spheres. We also mesh the

[1] The implementation is done in Python and is publicly available at https://github.com/Sprunckt/acoustic-sfw.

Algorithm 2 Adapted Frank-Wolfe

Input: Observation vector $\boldsymbol{x}$, cutting indices $\boldsymbol{j} = (j_1, \ldots, j_L)$
Output: Estimated image-source amplitudes and locations $(\boldsymbol{a}_{\text{fin}}, \boldsymbol{r}_{\text{fin}})$

1: $\psi^{(0)} \leftarrow 0$
2: $\boldsymbol{x}^{(0)} \leftarrow (x_{m,n})_{1 \leq n \leq j_1}^{1 \leq m \leq M}$
3: **while** $i < i_{\max}$ **do**
4:   **if** $\left\|\mathbf{res}^{(i)}\right\|_2$ is sufficiently reduced or i_{ext} iterations have elapsed since last extension **then**
5:     Extend $\boldsymbol{x}^{(i)}$ if possible
6:   **end if**
7:   Create an initialization grid $\mathcal{G}$
8:   Get $\boldsymbol{r}_{\text{ini}} = \operatorname{argmax}_{\boldsymbol{r} \in \mathcal{G}} \eta^{(i)}(\boldsymbol{r})$
9:   Get $\boldsymbol{r}_*^{(i)}$ by applying BFGS to $-\eta^{(i)}$ with initial guess $\boldsymbol{r}_{\text{ini}}$
10:   **if** $\eta^{(i)}(\boldsymbol{r}_*^{(i)}) \leq \lambda$ **then**
11:     **if** $\boldsymbol{x}^{(i)}$ can be extended **then**
12:       Extend $\boldsymbol{x}^{(i)}$ and go to next iteration
13:     **else**
14:       Exit the loop
15:     **end if**
16:   **end if**
17:   Get $\boldsymbol{r}^{(i+1)} = \boldsymbol{r}^{(i)} \cup \{\boldsymbol{r}_*^{(i)}\}$
18:   Get $\boldsymbol{a}^{(i+1)}$ by solving the LASSO problem $\min\limits_{\boldsymbol{a} \in \mathbb{R}_+^{K^{(i+1)}}} T_\lambda(\boldsymbol{a}, \boldsymbol{r}^{(i+1)})$
19:   **if** $a_{K^{(i+1)}}^{(i+1)} < 0.01$ **then**
20:     **if** $\boldsymbol{x}^{(i)}$ can be extended **then**
21:       Extend $\boldsymbol{x}^{(i)}$ and go to next iteration
22:     **else**
23:       Exit the loop
24:     **end if**
25:   **end if**
26:   Delete spikes from $(\boldsymbol{a}^{(i+1)}, \boldsymbol{r}^{(i+1)})$ that have amplitudes below 0.01
27:   $i \leftarrow i + 1$
28: **end while**
29: Delete spikes from $(\boldsymbol{a}^{(i)}, \boldsymbol{r}^{(i)})$ that have amplitudes below 0.01
30: Get $(\boldsymbol{a}_{\text{fin}}, \boldsymbol{r}_{\text{fin}})$ by applying BFGS to T_λ with initial guess $(\boldsymbol{a}^{(i)}, \boldsymbol{r}^{(i)})$
31: Delete spikes from $(\boldsymbol{a}_{\text{fin}}, \boldsymbol{r}_{\text{fin}})$ that have amplitudes below 0.01

surrounding spheres with radii ± 5 cm to obtain a fine grid of approximately 40000 points. The grid point maximizing $\eta^{(i)}$ is picked as the initial position for off-the-grid optimization.

The optimization problem of Step 2 is solved at the line 18 using the Scikit-learn library [120]. We stop the algorithm when the amplitude of the last estimated source is below a threshold $\alpha_{\min} = 0.01$ or the criterion described in Step 1 is met. In order to facilitate the resolution and accelerate the execution, we begin by running the algorithm on a reduced observation vector constructed by limiting the time frame of the signals, *i.e.* only considering the first j_1 samples with $j_1 < N - 1$.

When a stopping criterion is reached at line 10 or 19, we extend the RIR if possible, *i.e.* if the time signals have not yet reached $T_{\max}$. We also increase the number of samples when beginning the iteration at line 5 if 20 iterations have been effected since the last extension, or if the norm of the residual has sufficiently decreased since the last extension (typically a 70 % decrease from the norm computed at the last extension). The indices $j_1 < \ldots < j_L = N - 1$ are chosen in order to have a linear progression of the energy, *i.e.* the norm of the vectors $(x_{m,n})_{j_l \leq n < j_{l+1}}^{1 \leq m \leq M}$ are roughly constant. The first separating indices j_l are well spaced, while the last indices are more clustered together, as the number of reflections arriving at each microphone increases rapidly. This extension procedure has the effect of focusing the resolution at first on the closest sources, for which the time of arrivals are usually well separated in the signals. These low-order sources are also the most valuable, as for instance the whole geometric information on the configuration of a cuboid room is embedded in the locations of the original source and the first order image sources.

Sliding-Frank-Wolfe [53] introduces a so-called "sliding" step at each iteration. The idea is to perform a local descent on both the locations and amplitudes at the end of each iteration i to optimize $T_\lambda(\boldsymbol{a}, \boldsymbol{r})$, using the currently reconstructed measure as initialization. Although this step greatly increases the accuracy of the reconstruction and brings convergence guarantees, the algorithmic complexity explodes for certain rooms in which the number of image sources can reach over a thousand. We thus proceed as in [28] and apply the sliding step only once after the very last step. We also delete low amplitude sources before and after optimization, as described in lines 29-31.

2.4 Numerical experiments

We present here some numerical results obtained by applying the algorithm described in the last section.

2.4.1 Simulation details

The experimental setup is the following: we consider a spherical array of 32 microphones based on the em32 Eigenmike® (radius r=4.2 cm). We generate 200 random cuboid rooms, in which we randomly place the microphone array and sound source, enforcing a minimal separation of 1 m between the array's center and the source. We also constrain the location of the array's center to be located at least 25 cm from each wall in order to ensure that every microphone remains in the room. The room lengths and widths in meters are picked uniformly at random in $[2, 10]$, while the heights are taken in $[2, 5]$. We associate each wall with an absorption coefficient uniformly drawn at random in $[0.01, 0.3]$. The microphone array is randomly rotated, and a multichannel discretized room impulse response is generated by applying the operator described in equation (2.51) to the measure composed of the image sources up to order 20. This amounts to truncating the sum in Proposition 2.1.1 to encompass only the source and the image sources that model reflections of order

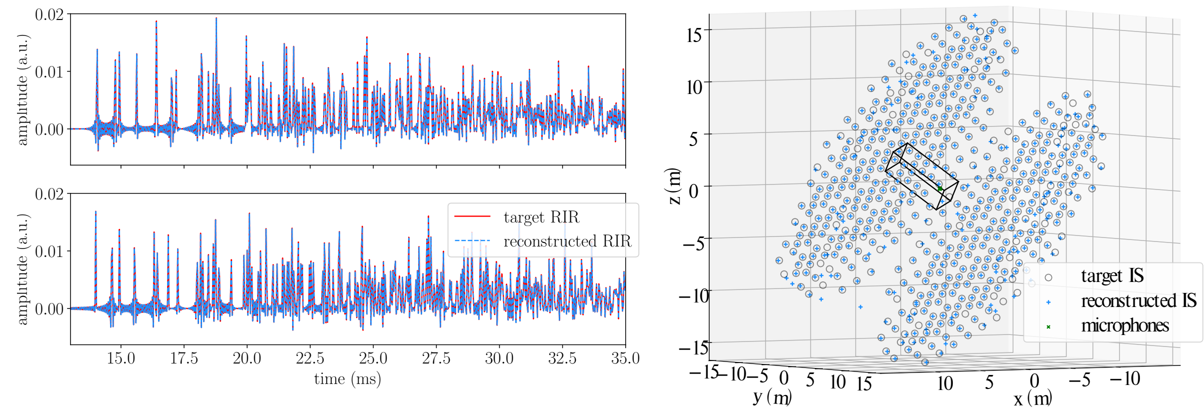

(a) Observed and reconstructed signals for two of the microphones

(b) 3D plot of the room with its associated true and reconstructed sources

Figure 2.3: Reconstruction results for a room of dimensions $6.45 \times 2.51 \times 2.35$ in meters, resulting in 530 target image sources. The recall is 93% for radial and angular thresholds of 1 cm and 2°, and the mean euclidean error for the recovered sources is 6 cm. The sampling frequency and microphone array radius are respectively 32 kHz and 4.2 cm.

lower or equal to 20. We set $\kappa = \kappa^{\mathrm{lp}}$ as defined in (2.13) for all experiments. For each scenario, we choose N as to get signals of duration $T_{\max} = \frac{N-1}{f_s} = 50$ ms. Although we use 11521 image sources to simulate the measurements, only a fraction of these sources has any impact on the first 50 ms of each signal. Note that we will only consider the target sources that are in the set $\mathscr{C}$ (as defined in Section 2.1) in our metrics. In other words, for evaluation we only look at the target image sources that are in range for every microphone and discard the others. The number of image sources considered in the metrics then ranges from less than 100 to over 1500. λ is set to 3.10^{-5} in all experiments based on a preliminary study of its impact on reconstruction accuracy. We also test the robustness to noise by adding Gaussian noise to the signals, with varying Peak Signal-to-Noise Ratio (PSNR) values. We define the Peak Signal to Noise Ratio (PSNR) as $10\log_{10}\left(\frac{\max(\boldsymbol{x})^2}{\|\boldsymbol{e}\|_2^2}\right)$, where $\boldsymbol{x}$ is the noiseless observation vector, and $\boldsymbol{e}$ is the vector of additive noise.

We then proceed to run the algorithm on every resulting measurement vector, and we evaluate the accuracy of the reconstruction. Fig. 2.3 presents 2 of the 32 target and reconstructed time signals for a particular test room, as well as the 3D locations of the sources.

2.4.2 Evaluation metrics

Error metrics

Let $\boldsymbol{r}$ be a target source location, and $\hat{\boldsymbol{r}}$ the estimated source location. We define the Angular Error (AE) as the angle between the unitary vectors defined by the target and estimated source locations:

$$\mathrm{AE}(\boldsymbol{r}, \hat{\boldsymbol{r}}) = \arccos\left(\frac{\boldsymbol{r} \cdot \hat{\boldsymbol{r}}}{\|\boldsymbol{r}\|_2 \, \|\hat{\boldsymbol{r}}\|_2}\right). \tag{2.56}$$

The Radial Error (RE) is the absolute difference between the norms of the target and estimated source locations:

$$\mathrm{RE}(\boldsymbol{r}, \hat{\boldsymbol{r}}) = \left| \|\boldsymbol{r}\|_2 - \|\hat{\boldsymbol{r}}\|_2 \right| . \tag{2.57}$$

We will also consider the Euclidean Error (EE):

$$\mathrm{EE}(\boldsymbol{r}, \hat{\boldsymbol{r}}) = \|\boldsymbol{r} - \hat{\boldsymbol{r}}\|_2 . \tag{2.58}$$

Recall and precision

We set radial and angular thresholds at 1 cm and 2° respectively, and we proceed to compute the recall on the recovered sources, that is the proportion of target image sources that were approximated with an error below the thresholds. We then compute the mean radial, angular and Euclidean errors on the sources that are considered as recovered, as well as the mean error on the corresponding amplitudes. We also consider the precision, *i.e.* the proportion of sources in the reconstructed measures that are counted as truly recovered according to the error thresholds.

Numerical results

Fig. 2.4 presents the influence of the microphone array radius r and sampling frequency f_s on the recall. Each bar's height represents the recall, and the corresponding mean Euclidean error is displayed at the top of each bar. Note that we segmented the room database according to the number of target image-sources, as the number of image-sources varies greatly depending on the size and configuration of the room. In particular, for a limited number of small rooms the number of image sources explodes, increasing the reconstruction's complexity as the echoes become harder to separate in time. We observe that the performance of the algorithm improves as the sampling frequency or the array radius increases, which is expected after the previous observations on the behavior of the certificates (see Fig. 2.2). For the best parameters ($f_s = 32$ kHz and $r = 21$ cm) we get over 99 % recall for the rooms that generate less than 700 image sources, with a mean Euclidean error under 1.5 cm. For these rooms, the precision, *i.e.* the proportion of sources in the reconstructed measures that are counted as truly recovered is over 90 %. Note that if two sources are reconstructed close to a same target source, only the closest one is counted as a true positive. Table 2.1 presents the recall (R), precision (P) and mean radial ($\overline{\mathrm{RE}}$), angular ($\overline{\mathrm{AE}}$), Euclidean ($\overline{\mathrm{EE}}$) and amplitude ($\overline{\mathrm{AmE}}$) errors amongst the recovered sources for every subset of the room database sources, with f_s=24 kHz, r=4.2 cm and no noise. The mean Euclidean errors are of the order of a few centimeters.

Comparatively, the distance of the sources to each microphone ranges from 1 to over 15 meters,

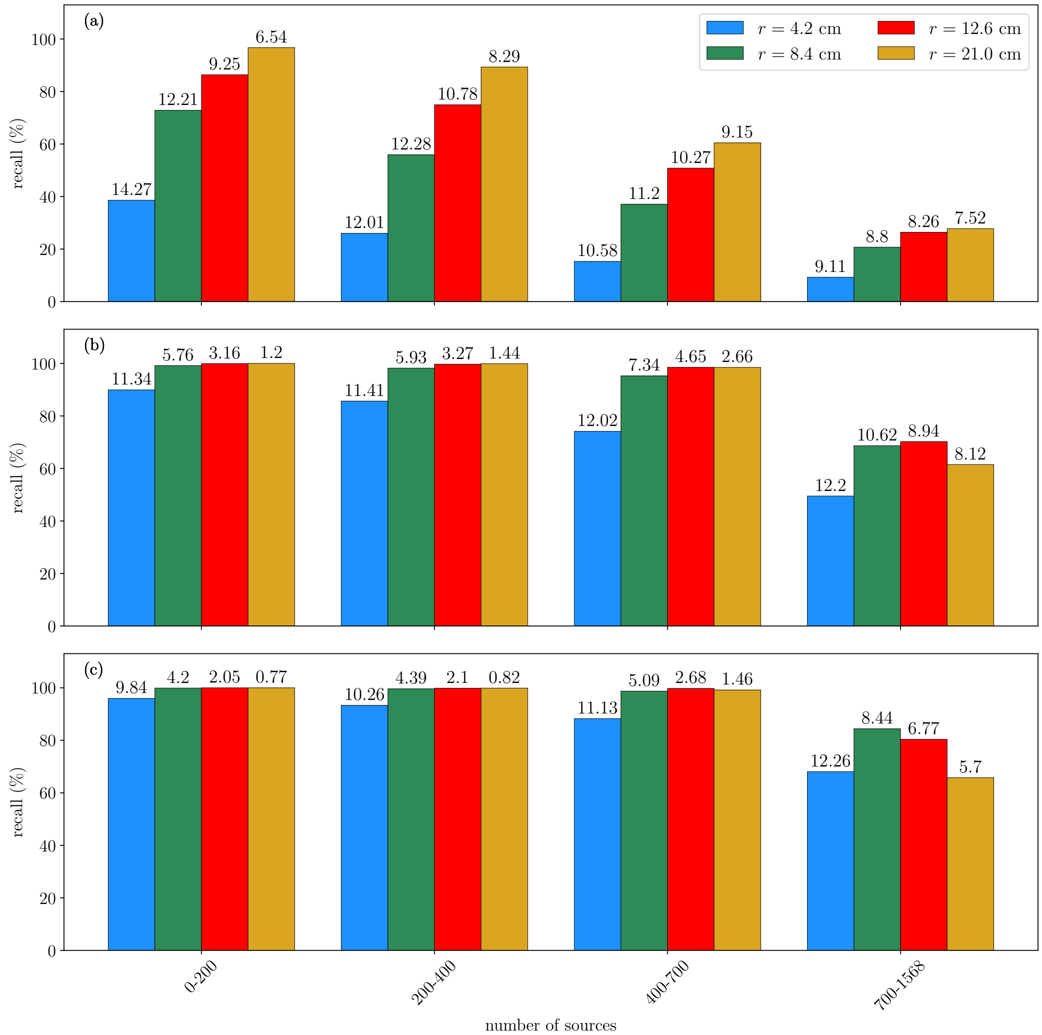

Figure 2.4: Recall for varying microphone array radii r for f_s taking the values 8 kHz (a), 24 kHz (b), 32 kHz (c). The room dataset is segmented in four subsets according to the number of target image sources. The mean Euclidean error for the recovered sources is displayed in cm above each bar.

# of IS	**R(%)**	**P(%)**	$\overline{\mathbf{RE}}$**(mm)**	$\overline{\mathbf{AE}}$**(°)**	$\overline{\mathbf{EE}}$**(mm)**	$\overline{\mathbf{AmE}}$
0-200	89.9	80.5	0.043	0.456	113	0.034
200-400	85.6	78.6	0.062	0.454	114	0.0256
400-700	74.1	67.7	0.097	0.488	120	0.022
700-1568	49.5	43.9	0.166	0.544	122	0.022

Table 2.1: Recall (R), precision (P) and mean radial ($\overline{\mathrm{RE}}$), angular ($\overline{\mathrm{AE}}$), Euclidean ($\overline{\mathrm{EE}}$) and amplitude ($\overline{\mathrm{AmE}}$) errors amongst recovered sources as a function of the number of sources, with $r = 4.2$ cm and $f_s = 24$ kHz.

	Noiseless				30 dB PSNR			
IS order	**R(%)**	**$\overline{\text{RE}}$(mm)**	**$\overline{\text{AE}}$(°)**	**$\overline{\text{EE}}$(mm)**	**R(%)**	**$\overline{\text{RE}}$(mm)**	**$\overline{\text{AE}}$(°)**	**$\overline{\text{EE}}$(mm)**
Source	100	0.00309	0.0163	0.996	100	0.0396	0.149	8.23
Order 1	99.4	0.00717	0.0820	11.7	98.8	0.0875	0.346	37.8
Order 2	98.1	0.0120	0.151	27.0	96.5	0.131	0.513	74.2
Order 3	96.0	0.0207	0.220	44.7	91.7	0.175	0.662	112

Table 2.2: Recall (R), precision (P) and mean radial ($\overline{\text{RE}}$), angular ($\overline{\text{AE}}$) and Euclidean ($\overline{\text{EE}}$) errors amongst recovered sources as a function of the image-source order, with $r = 4.2$ cm and $f_s = 24$ kHz.

and the error increases with distance due to the compact spherical geometry of the microphone array. Table 2.2 presents the recall and mean Euclidean error as a function of image-source order when considering the whole room dataset at once, both for the noiseless case and at 30 dB PSNR.

In particular, we get a satisfactory 99.4 % recall rate for the first order image sources in the noiseless case, with a mean localization error of 1.17 cm. Note that if we increase the sampling frequency to 32 kHz and the array radius to 21 cm, every first order source is recovered, with a mean Euclidean error of 0.773 mm (not displayed in the table).

Fig. 2.5 shows how the parameter λ affects the quality of the reconstruction at two different noise levels. For low noise levels, the curves are practically flat around the chosen value of the parameter. λ could be tuned to increase precision at the cost of recall, especially at high PSNR. However, whilst increasing λ can greatly reduce false positives, it does not only reduce the recall for high order image sources, but also for first order sources. For some applications, such as room geometry reconstruction, the locations of first order sources are crucial, which justifies using a low regularization parameter at the expense of additional false positives.

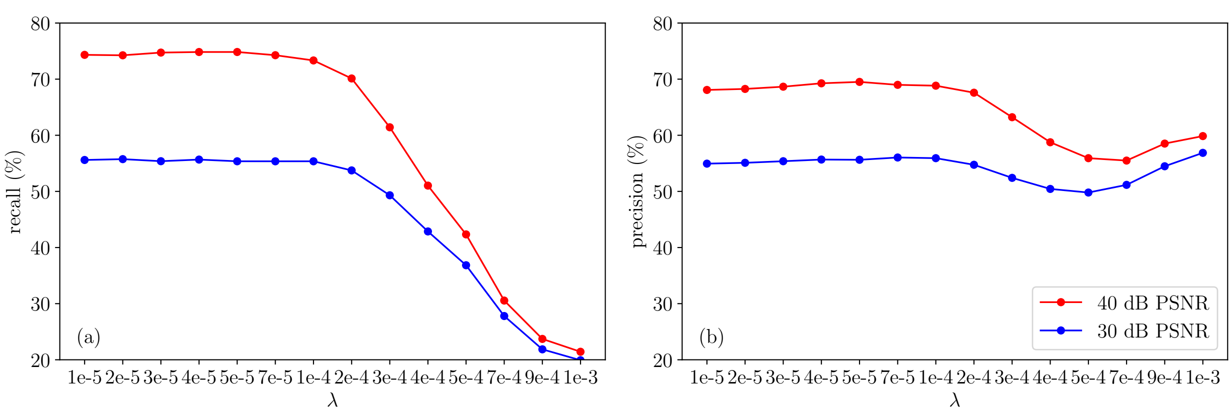

Figure 2.5: (a) Recall and (b) precision as a function of λ at two different PSNRs.

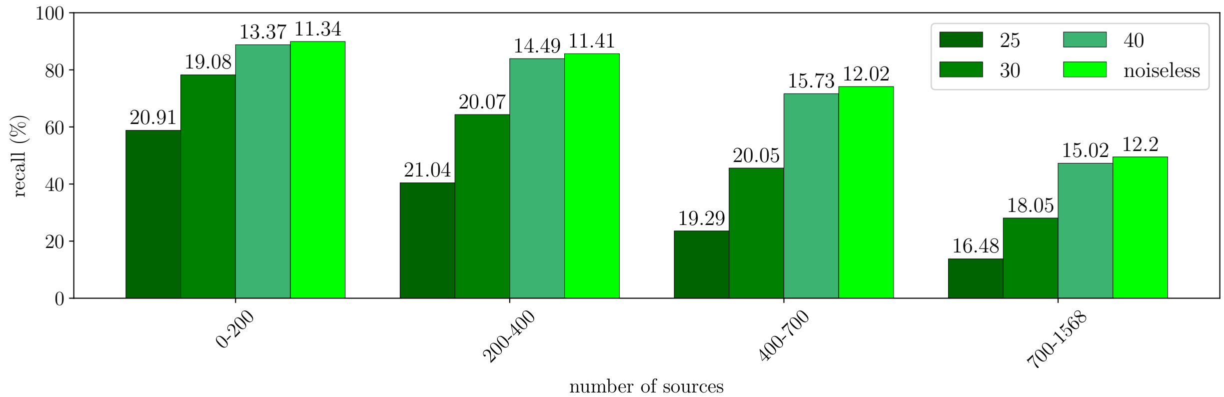

Figure 2.6: Recall for varying PSNR with a microphone array radii $r = 4.2$ cm and $f_s = 24$ kHz.

Finally, Fig. 2.6 presents the recall obtained for different Peak to Signal Noise Ratios (PSNR). At 40 PSNR we see little impact on the recall and errors, while the Euclidean errors tend to increase quickly at 30 PSNR. However, this damages mainly the high order sources, for which the heights of the time-signals peaks are close to the standard deviation of the noise. Indeed, as highlighted in Table 2.2 even at 30 PSNR we have a 98.8 % recall rate for the first order sources, with an associated mean Euclidean error of 3.78 cm. These results were obtained for $f_s = 24$ kHz and $r = 4.2$ cm and might be further improved by increasing the resolution.

2.5 Conclusion

We have introduced a new formulation for the inverse problem of locating image sources from discretized multichannel RIRs. The study of the finite dimensional, non-convex optimization problem on the amplitudes and locations of the sources highlights the complexity of the problem. In particular, the singularities of the kernel require a minimum distance to be enforced, as, depending on the observation vector $\boldsymbol{x}$, the problem can be ill-posed. We have proposed a numerical method based on the Frank-Wolfe algorithm to solve the relaxation of the optimization problem to the space of Radon measures, effectively locating the image sources in 3D space directly from discretized measurements. The algorithm presents a very high recall rate when the diameter of the microphone array and its sampling frequency are sufficiently large, with vanishingly small errors. Moreover, the high accuracy and recall rates obtained for the first order image sources suggest a good adequacy of the method for room geometry reconstruction.

Chapter 3

Cuboid room reconstruction

This chapter finally tackles the problem of room shape estimation by leveraging the image-source reconstruction algorithm introduced in the last chapter. We present an image-source reversion algorithm that is able to infer the complete geometric configuration of a cuboid room from a set of estimated image sources. We proceed to evaluate the performance of the algorithm on simulated data.

3.1 Room geometry recovery

This section presents an ISM reversion algorithm for cuboid rooms, which is able to reliably recover the 18 input parameters: these are the 3D source position, the 3 dimensions of the room, the 6-degrees-of-freedom room translation and orientation, and an absorption coefficient for each of the 6 room boundaries. The algorithm consists in three steps which are detailed in the following subsections. The first step is estimating the orientation, *i.e.* finding a rotation to transform the array vector basis to a room referential basis. The second step is to extract the order 1 image sources from the image-source point cloud. The third and final step consists in inferring the remaining parameters, *i.e.* the distance of the source relative to each wall and the room dimensions.

3.1.1 Orientation

Let us first consider the task of recovering the room orientation from an unlabeled image source point cloud, such as the one obtained by the algorithm presented in Section 2.3.3. The key idea is to estimate its underlying orthogonal grid structure, which is apparent in the examples of Fig. 3.1**(a)** and 3.2. The task amounts to finding a rotation matrix that transforms the microphone array's reference frame to the room's reference frame, up to a permutation of directions. By Eq. (1.6), the projected coordinates of image sources onto a normal vector to a wall will form clusters, each cluster containing the coordinates of a plane of image sources parallel to this wall. Conversely, projecting image sources onto a randomly chosen vector will, intuitively, not form clusters but instead spread out over the entire range of possible values. In other words, the room basis vectors are orthogonal to the image-source planes generated by the corresponding walls and are expected to maximize the number of orthogonalities. Our method seeks to exploit this structure by scoring basis vector candidates according to their orthogonality to the directions generated by image-source pairs. Formally, let us define f_D as follows:

$$\forall \boldsymbol{u}, \boldsymbol{v} \in \mathbb{R}^D, \quad f_D(\boldsymbol{u}, \boldsymbol{v}) = \begin{cases} 1 & \text{if } \boldsymbol{u} \perp \boldsymbol{v} \\ 0 & \text{otherwise.} \end{cases} \tag{3.1}$$

Let $\mathcal{G} \subset \mathbb{R}^3$ be a finite set of image source locations. Let us consider the following optimization problem:

$$\max_{\|\boldsymbol{u}\|_2 = 1} J_3(\boldsymbol{u}), \quad \text{where} \quad J_3(\boldsymbol{u}) = \sum_{\boldsymbol{s}, \boldsymbol{p} \in \mathcal{G}} f_3(\boldsymbol{u}, \boldsymbol{s} - \boldsymbol{p}). \tag{3.2}$$

It can be shown that in the noiseless case, for a complete finite cuboid grid $\mathcal{G}$ of image sources, the solution to this problem is indeed a wall normal:

Proposition 3.1.1. *Let N_1, N_2, N_3 be non-zero even integers. Consider the following subset of image sources: $\mathcal{G} = \{\boldsymbol{r}_{\boldsymbol{q},\boldsymbol{\varepsilon}},\ \boldsymbol{q} \in [\![0, N_1/2 - 1]\!] \times [\![0, N_2/2 - 1]\!] \times [\![0, N_3/2 - 1]\!],\ \boldsymbol{\varepsilon} \in \{-1, 1\}^3\}$ with $\boldsymbol{r}_{\boldsymbol{q},\boldsymbol{\varepsilon}}$ defined as in (1.6). Then, any solution $\boldsymbol{u}^*$ to problem (3.2) is a wall normal,* i.e, *$\boldsymbol{u}^* = \pm \boldsymbol{e}_i$ for some $i \in [\![1, 3]\!]$.*

Proof. See Section 3.3. $\square$

Note that in Proposition 3.1.1, the coordinates are expressed using Eq. (1.6), *i.e.*, in the unknown reference frame of the room. However, the definition of the cost function J_3 is independent of the coordinate system, so that the result remains true in any coordinate frame. Note also that adversarial cases could be built by carefully removing sources from the image-source point cloud in order to have the score function bear its maximum in a wrong direction. However, assuming the reconstruction algorithm of Section 2.3.3 misses image sources at random, the probability of encountering such an adversarial situation is vanishingly small, and Proposition 3.1.1 is expected to hold for generic subsets, as will be confirmed by our experiments.

In practice, the image-source reconstruction is noisy and the function f_D defined in (3.1) cannot be computed exactly. f_D is instead approximated using a Gaussian kernel

$$f_D^\sigma(\boldsymbol{u}, \boldsymbol{v}) = \exp\left(-\frac{1}{2\sigma^2}\left(\frac{\boldsymbol{u}.\boldsymbol{v}}{\|\boldsymbol{u}\|_2\,\|\boldsymbol{v}\|_2}\right)^2\right), \tag{3.3}$$

such that $\lim_{\sigma\to 0} f_D^\sigma = f_D$ in the pointwise sense. The scale parameter σ controls the tightness of the approximation and plays a regularizing role with respect to the error committed in the localization of image sources. A small σ will yield a noisy loss function if the source localization error is high. Conversely, a large σ means poor precision on room orientation recovery. As we are searching for an optimal *unit* vector, the regularized score function J_3^σ can be re-parameterized in spherical coordinates by two angles $(\theta, \phi) \in [0, 2\pi[\times[0, \pi[$:

$$J_3^\sigma(\theta, \phi) = \sum_{\boldsymbol{s},\boldsymbol{p}\in\mathcal{G}} f_3^\sigma(\boldsymbol{u}(\theta, \phi), \boldsymbol{s} - \boldsymbol{p}) \tag{3.4}$$

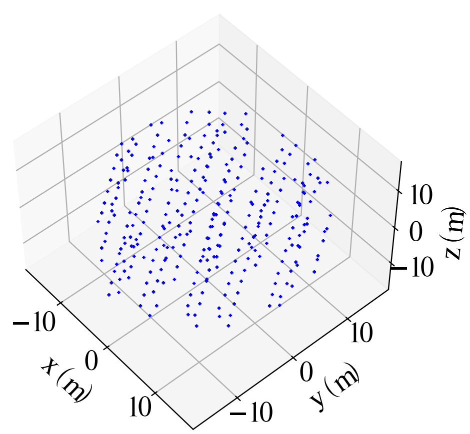

(a)

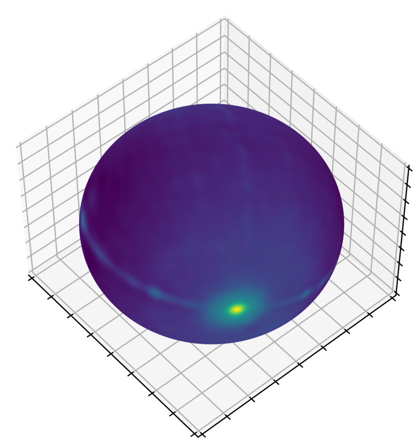

(b)

Figure 3.1: (a) Reconstructed image-source point cloud using Alg. 2 (b) Associated J_3^σ score plotted on the sphere (brighter is higher). A sharp peak is observed in the direction of a wall normal.

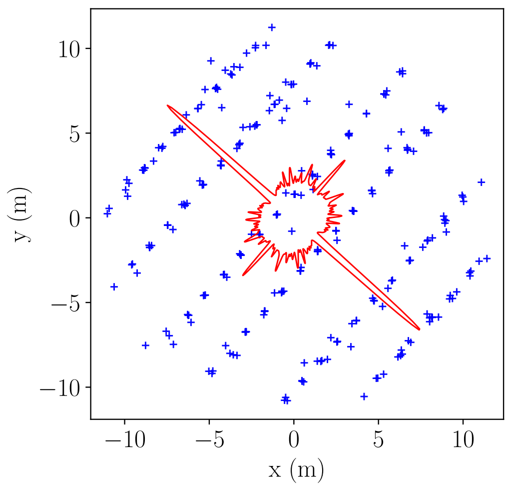

Figure 3.2: Projection of the estimated sources on $\hat{\boldsymbol{e}}_1$ (blue) and the associated 2D $J^\sigma_{2,\hat{\boldsymbol{e}}_1}$ score (red). We observe maximal values in the directions of the wall normals.

Algorithm 3 Orientation estimation

Input: Image sources $(\boldsymbol{r}_k)_{k=1}^K$
Output: Estimated room orthonormal basis $\hat{\boldsymbol{e}}_1, \hat{\boldsymbol{e}}_2, \hat{\boldsymbol{e}}_3$
1: $\hat{\boldsymbol{e}}_1 \leftarrow \operatorname{argmin}_{\boldsymbol{u}\in\mathcal{S}^2_{\text{discr}}} J_3^{0.01}$
2: **for** $\sigma \in [0.01, 0.005, 0.0005]$ **do**
3: $\quad \hat{\boldsymbol{e}}_1 \leftarrow \text{local\_descent}(\hat{\boldsymbol{e}}_1, J_3^\sigma)$
4: **end for**
5: $\hat{\boldsymbol{e}}_2 \leftarrow \operatorname{argmin}_{\boldsymbol{u}\in\mathcal{S}^1_{\text{discr}}} J_{2,\hat{\boldsymbol{e}}_1}^{0.01}$
6: **for** $\sigma \in [0.01, 0.005, 0.0005]$ **do**
7: $\quad \hat{\boldsymbol{e}}_2 \leftarrow \text{local\_descent}(\hat{\boldsymbol{e}}_2, J_{2,\hat{\boldsymbol{e}}_1}^\sigma)$
8: **end for**
9: $\hat{\boldsymbol{e}}_3 = \hat{\boldsymbol{e}}_1 \times \hat{\boldsymbol{e}}_2$

---

where $\boldsymbol{u}(\theta,\phi)$ is the unit vector defined by spherical coordinates (θ,ϕ). Once a first basis vector $\boldsymbol{u}$ maximizing J_3^σ has been found, we can proceed in a greedy manner by projecting $\mathcal{G}$ onto $\boldsymbol{u}^\perp$:

$$J^\sigma_{2,\boldsymbol{u}}(\theta) = \sum_{\boldsymbol{s},\boldsymbol{p}\in\mathcal{G}} f_2^\sigma(\boldsymbol{v}(\theta), \mathcal{P}_{\boldsymbol{u}^\perp}(\boldsymbol{s}-\boldsymbol{p})) \quad \forall\theta\in[0,2\pi[, \tag{3.5}$$

where $\mathcal{P}_{\boldsymbol{u}^\perp}$ is the orthogonal projection onto the plane orthogonal to $\boldsymbol{u}$, and $\boldsymbol{v}(\theta)$ is the unit vector contained in this plane and defined by the polar angle θ. As can be seen in the examples of Fig. 3.1 and 3.2, both score functions J_3^σ and $J^\sigma_{2,\boldsymbol{u}}$ feature maxima along the room axes.

We use the *Scipy* implementation of the *BFGS* algorithm [153] to maximize J_3^σ. Due to the non-convexity of the problem we initialize the optimization algorithm on a finely meshed half-sphere $\mathcal{S}^2_{\text{discr}}$. In order to reduce even more the chance of the algorithm stopping at a local minimum, we begin with a high value of the scale parameter σ and perform the optimization with gradually decreasing values. This process yields an accurate, gridless reconstruction of a first basis vector $\hat{\boldsymbol{e}}_1$, given a sufficiently accurate image-source reconstruction. The sources are then projected onto the plane orthogonal to $\hat{\boldsymbol{e}}_1$ and the process is repeated to recover a second vector $\hat{\boldsymbol{e}}_2$ by optimizing $J^{\sigma}_{2,\hat{\boldsymbol{e}}_1}$. The third vector is then obtained by taking the cross product $\hat{\boldsymbol{e}}_1 \times \hat{\boldsymbol{e}}_2$. The full process is summarized in Algorithm 3. The same values of σ will be used in all experiments, without any specific tuning.

3.1.2 First order identification and geometry inference

Once the room orientation has been estimated, we seek to identify which of the estimated image sources are of first order. We leverage the fact that the zeroth order image source, *i.e.*, the true source, can be straightforwardly identified (it is the closest one to the microphone array's center). It is also very accurately localized, since the direct path is usually well separated from reflections in all RIRs. We then cast a cone from the true source in each reconstructed direction $\hat{\boldsymbol{e}}_d$ and their opposite $-\hat{\boldsymbol{e}}_d$. The image source closest to the source in each cone is picked as a first order source candidate. If the cone is empty (implying that source localization errors are too great) we progressively extend the cone's width until it contains at least one source. As the reconstruction algorithm sometimes produces clusters of sources around the true image-source location, we assume that any source close to an estimated first order source is a reconstruction artifact. We thus proceed to merge the closest estimated sources. Let $\boldsymbol{r}^*$ be a candidate first order source, $\mu \in \mathbb{R}^*_+$ a threshold and $\{\boldsymbol{r}^*_1, \ldots \boldsymbol{r}^*_P\}$ the set of reconstructed sources such that $\left\|\boldsymbol{r}^*_p - \boldsymbol{r}^*\right\|_2 < \mu \;\forall p \in [\![1, P]\!]$. We use a heuristic inspired by [147] to merge the corresponding Diracs and their amplitudes:

$$\begin{aligned} \hat{a} =& \quad \textstyle\sum_{p=1}^{P} a^*_p \\ \hat{\boldsymbol{r}} =& \quad \textstyle\sum_{p=1}^{P} \frac{a^*_p}{\hat{a}} \boldsymbol{r}^*_p. \end{aligned} \tag{3.6}$$

This procedure gives us estimates for the six first-order image sources $\hat{\boldsymbol{r}}_k$ and their associated reflection coefficients $\hat{a}_k$. The distances of the true source to each wall are then recovered by computing the projections on each estimated wall normal. Let $\hat{\boldsymbol{r}}_{t-}, \hat{\boldsymbol{r}}_{t+}$ be the first order image

Algorithm 4 Source-wall distances, first order amplitudes

Input: Image sources and amplitudes $(\boldsymbol{r}_k)_{k=1}^K, (a_k)_{k=1}^K$; directions $\hat{\boldsymbol{e}}_1, \hat{\boldsymbol{e}}_2, \hat{\boldsymbol{e}}_3$; threshold μ
Output: Corrected amplitudes up to order 1 $\hat{a}_0, \ldots, \hat{a}_6$, source-walls distances $\hat{d}_1, \ldots, \hat{d}_6$

```
1: r̂_0 ← fusion(r_{k_0}, (a_k)_k, (r_k)_k, μ),  k_0 = argmin_k ‖r_k‖_2
2: for t = 1, ..., 3 do
3:     (r_left, r_right) ← closest_in_cone(r̂_0, ê_t, (r_k)_k)
4:     (â_{t,−}, r̂_{t,−}) ← fusion(r_left, (a_k)_k, (r_k)_k, μ)
5:     (â_{t,+}, r̂_{t,+}) ← fusion(r_right, (a_k)_k, (r_k)_k, μ)
6: end for
```

sources corresponding to $\hat{\boldsymbol{e}}_t$ such that $\hat{\boldsymbol{r}}_{t+}$ is in the cone emitted from $\hat{\boldsymbol{r}}_0$ with direction $\hat{\boldsymbol{e}}_t$, and $\hat{\boldsymbol{r}}_{t-}$ is contained in the opposite cone. We summarize the procedure in Alg. 4. The room length in a given direction is given by the following formula:

$$\hat{L}_t = \frac{1}{2}\left(\hat{\boldsymbol{e}}_t.(\hat{\boldsymbol{r}}_0 - \hat{\boldsymbol{r}}_{t-}) + \hat{\boldsymbol{e}}_t.(\hat{\boldsymbol{r}}_{t+} - \hat{\boldsymbol{r}}_0)\right) \tag{3.7}$$

$$= \frac{1}{2}\hat{\boldsymbol{e}}_t.(\hat{\boldsymbol{r}}_{t+} - \hat{\boldsymbol{r}}_{t-}). \tag{3.8}$$

Setting the intersection of the walls corresponding to $\hat{\boldsymbol{r}}_{1-}, \hat{\boldsymbol{r}}_{2-}, \hat{\boldsymbol{r}}_{3-}$ as a reference vertex of the room, the translation vector of the room with respect to the source is:

$$\hat{\tau}_{\text{room}} = \frac{1}{2}\begin{pmatrix} \hat{\boldsymbol{e}}_1.(\hat{\boldsymbol{r}}_0 - \hat{\boldsymbol{r}}_{1-}) \\ \hat{\boldsymbol{e}}_2.(\hat{\boldsymbol{r}}_0 - \hat{\boldsymbol{r}}_{2-}) \\ \hat{\boldsymbol{e}}_3.(\hat{\boldsymbol{r}}_0 - \hat{\boldsymbol{r}}_{3-}) \end{pmatrix} \tag{3.9}$$

Given the coordinates $\boldsymbol{r}$ of a point in the frame of the microphones, we can then compute the corresponding coordinates in the recovered room frame:

$$\hat{\boldsymbol{r}}_{\text{room}} = \begin{pmatrix} \hat{\boldsymbol{e}}_1^T \\ \hat{\boldsymbol{e}}_2^T \\ \hat{\boldsymbol{e}}_3^T \end{pmatrix} (\boldsymbol{r} - \hat{\boldsymbol{r}}_0) + \hat{\tau}_{\text{room}}. \tag{3.10}$$

We now have recovered all 18 input parameters that were used to generate the multichannel RIR:

- the room orientation vectors $\hat{\boldsymbol{e}}_1, \hat{\boldsymbol{e}}_2, \hat{\boldsymbol{e}}_3$
- the 3D source position $\hat{\boldsymbol{r}}_0$
- the room translation with respect to the source $\hat{\tau}_{\text{room}}$
- the room dimensions $\hat{L}_1, \hat{L}_2, \hat{L}_3$
- the 6 wall absorption coefficients $\hat{\alpha}_k = 1 - \hat{a}_k^2$ for $k = 1, \ldots, 6$ (see Eq. (1.10)).

3.2 Numerical Experiments

We proceed in this section to evaluate the effectiveness of the proposed inverse algorithm, which can be decomposed into two major steps: first estimating an image source point cloud from a multichannel RIR and then inferring the room parameters from it. We focus here on the estimation of the 18 room parameters given an image-source point cloud estimated using the algorithm described in Sec. 2.3.3. All the following tests are based on RIRs simulated using the shoebox ISM, *i.e.*, Eq. (2.9). As in Sec. 2.4, the RIRs are simulated using image sources up to order 20 and are cut after 50 ms, so that all audible reflections are present in the signals.

3.2.1 Simulation Details

We test the full reconstruction procedure on a set of 200 randomly generated rooms containing an omnidirectional impulse sound source and a microphone array. We use two distinct array geometries that are detailed in the following subsections. The rooms' lengths and widths in meters are picked uniformly at random in $[2, 10]$ while the heights are picked in $[2, 5]$. The array's center and the source are randomly placed in each room with a minimal separation distance of one meter to each other and the array is randomly rotated. We also enforce a distance constraint of 25 cm of the array center to each wall to avoid having any microphone placed beyond the room's boundary. Each wall's absorption coefficient is drawn uniformly at random in $[0.01, 0.3]$.

3.2.2 Evaluation Metrics

Orientation and dimensions

In order to match each recovered direction with the corresponding ground truth wall normal, we apply the ground truth inverse rotation to $(\hat{\boldsymbol{e}}_1, \hat{\boldsymbol{e}}_2, \hat{\boldsymbol{e}}_3)$. Each resulting vector should contain two zero coefficients, the last coefficient being -1 or 1. The indices of the non-zero coefficients allow us to re-order the vectors of the rotation matrix to match the recovered directions. We then compute the mean angular errors between the recovered directions $\hat{e}_d$ and the associated wall normals by taking the arccosine of the dot products. We also compute the mean absolute errors on recovered room dimensions.

Wall absorptions

Having matched recovered first-order sources to walls, we compute the mean absolute errors on estimated absorption coefficients: $\hat{\alpha}_k = 1 - \hat{a}_k^2$.

Room translation

In order to evaluate the room translation estimation, we calculate the room's center in the array's reference frame from estimated parameters. This is done by inserting $\hat{\boldsymbol{r}}_{\text{room}} = [\hat{L}_1/2, \hat{L}_2/2, \hat{L}_3/2]^\top$ in (3.10) and solving for $\boldsymbol{r}$. We then calculate the mean of Euclidean distances to the ground truth.

RIR extrapolation

Lastly, we evaluate the global accuracy of the method by re-simulating a RIR $\hat{\boldsymbol{x}}$ corresponding to a new random source-array placement in the room using the image-source method (2.9) with estimated parameters as input. Using the same sampling rate, we compute the signal-to-error ratio to the true RIR $\boldsymbol{x}$ at the new location:

$$\text{SER}(\hat{\boldsymbol{x}}, \boldsymbol{x}) = 10 \log_{10} \left(\frac{\sum_{i=1}^{NM} (\hat{x}_i - x_i)^2}{\sum_{i=1}^{NM} x_i^2} \right). \tag{3.11}$$

3.2.3 Experimental Results and Analysis

We first consider a 32-element spherical microphone array based on the geometry of the em32 Eigenmike® (radius R=4.2 cm) and scaled by various factors. Figure 3.3 presents the algorithm's performance on the geometry estimation task for varying sampling frequencies and microphone array radii. In accordance with the image source localization results reported in Section 2.3.3, the accuracy of the estimation improves as the radius or the sampling frequency grow. The lowest resolution ($R = 4.2$ cm and $f_s = 8$ kHz) presents some catastrophic reconstruction failures that heavily impact the mean errors. These catastrophic cases seem to vanish when the array size and sampling rate increase, the mean error steadily converging towards zero for all three metrics. This empirically supports our main claim that the shoebox image-source method is indeed fully algorithmically reversible for large enough arrays and frequencies of sampling. For a frequency of sampling of 24 kHz and the lowest radius, the mean room dimension estimation error is around 3 mm. This number goes down to 0.15 mm when dilating the array by a factor of 5. Meanwhile, the mean error on room orientation (Figure 3.3.c) remains under 0.06° in all experiments, except for the very lowest resolution. The errors on room center localization are somewhat higher. For the smallest array we get a mean error of 0.42 cm at 24 kHz which diminishes to 0.022 cm after dilation. This is expected because estimating the room center couples errors on orientation estimation and source-wall distance estimation.

We then evaluate the estimation of wall absorption coefficients. We observed some rare failures of absorption recovery even for relatively high array resolutions and frequency of sampling. In order

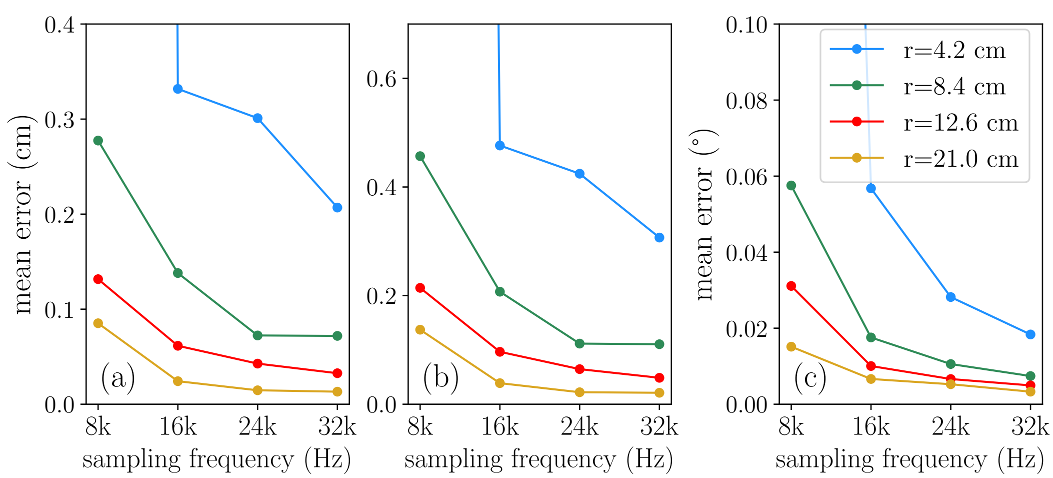

Figure 3.3: Mean absolute errors on room dimensions (a), mean Euclidean errors on room center (b) and mean angular error on room orientation (c) in function of the sampling frequency for varying array radii and frequency of sampling.

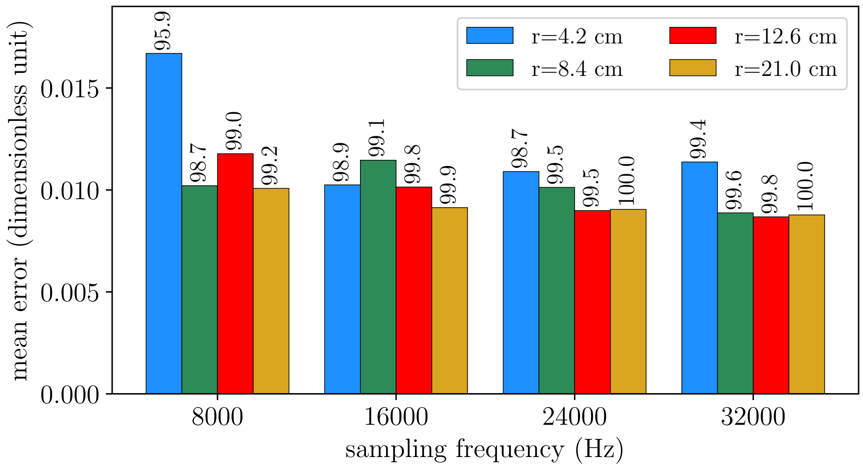

Figure 3.4: Mean absolute error on absorption coefficients recovered below a 0.3 threshold for varying array radii and frequency of sampling. The recall for this threshold is indicated above each bar in percent.

to get a more meaningful picture of the error committed, we only compute the mean errors over coefficients estimated with an error below 0.3, and consider the rest as outliers. Recall that in our simulations, the coefficients take values in $[0.01, 0.3]$, thus outliers correspond to overestimated absorptions between 0.31 and 1. We also computed the recall rates for this threshold. Both metrics are displayed in Fig. 3.4. The obtained mean errors are around 0.01, and 100% recall rates are obtained with the largest array sampling at 24 kHz or above. While these are low errors, we do not observe the same convergence towards zero as on geometrical errors. One possible explanation is that we kept the spike estimation algorithm described in Section 2.3.3 untouched, including two spike pruning steps that discard low amplitude Diracs before and after the final gradient descent.

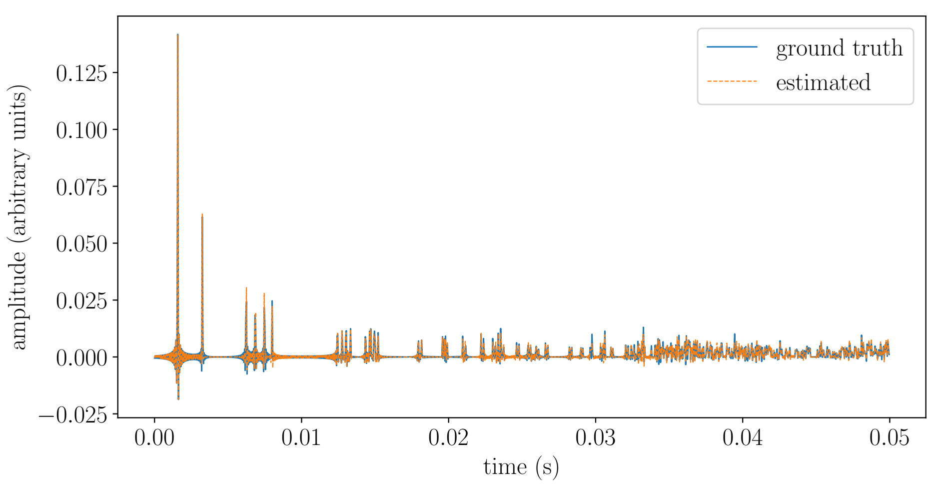

Figure 3.5: Example of RIR extrapolation inside the room of Fig. 3.2 (4.2 cm array radius, 24 kHz frequency of sampling).

While the first pruning step does seem to help the optimization algorithm, the second step, which is aimed at reducing false positives, might cause an issue on amplitude estimation. Rather than deleting the spikes and losing the corresponding amplitudes, a lead for improvement would be to merge the spikes by, *e.g*, adapting the heuristic presented in [147].

We now proceed with evaluating the ability of the method to extrapolate RIRs to arbitrary source-array placements in the same room. The results are shown in Fig. 3.5. Despite the slight absorption errors, we again observe a strong convergence of RIR extrapolation errors towards zero as the array size increases, bringing further support to the claim that the shoebox image-source method has been successfully reversed. Note that we did not observe such convergence as a function of the frequency of sampling. This is expected, since the RIR extrapolation task itself, as assessed by the proposed metric, becomes harder as the frequency of sampling increases. An example of RIR extrapolation result is presented in Fig. 3.5. As can be seen, the extrapolated RIR very closely matches the ground truth.

We finally study the impact of noise on geometry estimation. Figure 3.6 presents the recall curves for the recovery of each individual room dimension L_i, for different thresholds. The sampling frequency and array radius are respectively set to 24 kHz and 4.2 cm, and we proceed to varying the peak signal-to-noise ratio (PSNR) of input signals using additive white Gaussian noise. As expected, the algorithm's performance deteriorates when the noise increases and a severe drop appears at 25 dB PSNR. Nevertheless, the algorithm still manages to recover 95.5% of all room dimensions with an error below 5 cm under such noise level, suggesting a reasonable robustness of the overall approach.

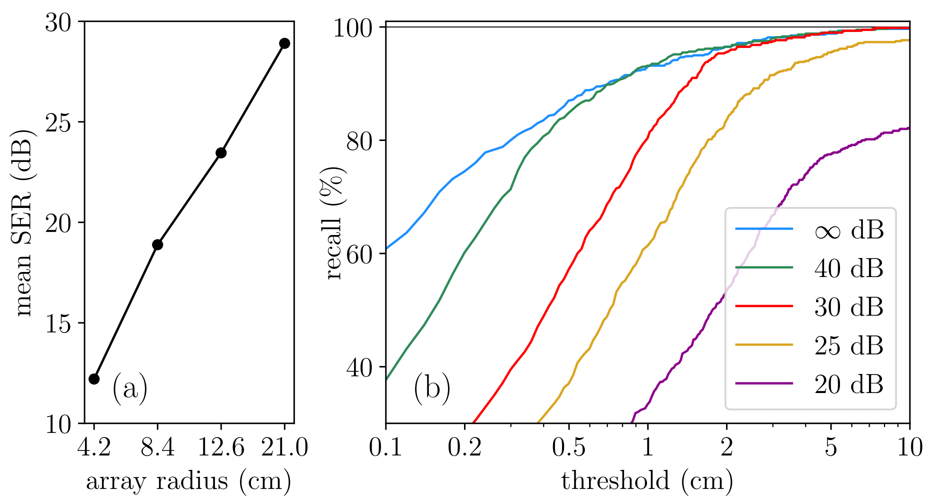

Figure 3.6: (a) Mean signal-to-error-ratio of RIR extrapolation for varying array radii at $f_s = 24$ kHz (b) Recall on room dimension recovery as a function of threshold for varying PSNRs for an array radius $r = 4.2$ cm and a frequency of sampling $f_s = 24$ kHz.

3.2.4 Baseline Comparison

We now compare the accuracy of the proposed algorithm with the landmark Euclidean distance matrix (EDM)-based method introduced by Dokmanic et al. [58], using the code provided by the authors[1]. This method takes as input a set of unlabeled times of arrival (TOAs) on multiple RIRs, and returns the 3D locations of first order image sources. Given a set of TOAs, one for each microphone, the algorithm estimates whether the combination could correspond to an image source in 3D space. This estimation is performed by checking the rank of the corresponding EDM. Direct comparison on the synthetic dataset defined in Section 3.2.1 turned out to be unfeasible. Indeed, the algorithmic complexity of the EDM-based method explodes when the number of reflections increases. Moreover, the method makes the strong assumption that only TOAs from image sources of orders lower than or equal to two are provided. Even when only considering these low-order sources, the number of considered combinations can become very high if the reflections are tightly clustered together due to the room's configuration, which frequently happens in our dataset. Finally, the method was designed for and tested with arrays of typically 5 microphones, since the complexity also drastically increases with the number of channels.

To produce a meaningful comparison, we configure the experiments to be favorable to the EDM-based method. To demonstrate that our approach is agnostic to the array geometry and number of elements, we consider a non-spherical microphone array of 8 microphones composed of two squares stacked on top of each other, the top square being rotated by an angle $\pi/4$. The corresponding array diameter is 37.5 cm. In order to avoid choosing a peak picking method to process the input of the EDM-based method, we place it in an oracle setting. Namely, we provide it with the true times of arrival of all image sources up to order 2 that are in recording range (partial oracle labeling), rounded to the nearest discrete-time sample at 32 kHz. Note that working in discrete time is a fundamental limit of such approaches. We run the two algorithms on the same room configurations as before, only altering the array's geometry but retaining the same location for its center.

For each method, we compute the precision and recall for a 20 cm error threshold on the source and first-order image sources localization and labelling. While the proposed algorithm always returns exactly 6 first-order sources, the EDM-based method can wrongfully label second-order reflections as first-order reflections, causing a loss in precision. The results for these experiments are listed in

[1] https://infoscience.epfl.ch/record/186657/

	O_1 Rec.	O_1 Prec.	O_1 MEE	O_0 MEE
[58]	84.4%	59.7%	65.7± 41.3 mm	35.1± 26.0 mm
Ours	97.2%	97.2%	2.41± 5.71 mm	0.289± 0.584 mm

Table 3.1: Recall, precision and mean Euclidean errors (MEE) for first-order image sources (O_1) and MEE for the true source (O_0) using [58] or the proposed method.

Table 3.1. The localization errors committed by the EDM-based method are an order of magnitude larger than with the proposed approach. This highlights that, even using oracle information, the considered task is far from trivial when considering fully randomized room parameters. The proposed algorithm obtains a mean Euclidean error below 3 mm, which is below $\frac{343}{2\times 32000} \approx 5.1$ mm, the theoretically lowest achievable radial error by any discrete-time method at this frequency of sampling, indicating that super-resolution is achieved. The number of rooms for which all 6 first-order sources were retrieved without spurious second-order ones was 25.5% for the EDM-based method. Hence, the method could not be used to recover the full geometry of most of the rooms. In contrast, this ratio reached 95.5% of the rooms using the proposed method. For those rooms, the mean geometrical reconstruction errors obtained by it, following the metrics presented in Section 3.2.2, were respectively 0.34 ± 0.6 mm for the room dimensions, 0.61 ± 0.6 mm for the room translation and $0.016 \pm 0.05°$ mm for the room orientation. These are in line with those obtained with the 32-element spherical microphone array of comparable radius and sampling frequency. This seems to indicate that when the array resolution is sufficient, adding microphones does not significantly improve the accuracy of correctly recovered sources. However, adding microphones does seem to reduce some of the geometrical ambiguities and hence to increase the number of correctly identified sources.

3.3 Proof of Proposition 3.1.1

Proof. Note that, by construction, $|\mathcal{G}| = N_1 N_2 N_3$. Let $\boldsymbol{u} \in \mathbb{R}^3$ and denote by $\mathcal{P}_{\boldsymbol{s}}^{\boldsymbol{u}}$ the affine plane passing by $\boldsymbol{s} \in \mathcal{G}$ with normal vector $\boldsymbol{u}$. J_3 can be reinterpreted as the total number of intersections of all planes $\{\mathcal{P}_{\boldsymbol{s}}^{\boldsymbol{u}}\}_{\boldsymbol{s}\in\mathcal{G}}$ with $\mathcal{G}$:

$$J_3(\boldsymbol{u}) = \sum_{\boldsymbol{s}\in\mathcal{G}} |\mathcal{G} \cap \mathcal{P}_{\boldsymbol{s}}^{\boldsymbol{u}}|. \tag{3.12}$$

Indeed, for all $\boldsymbol{s}, \boldsymbol{p} \in \mathcal{G}$, $\boldsymbol{s} - \boldsymbol{p}$ is orthogonal to $\boldsymbol{u}$ if and only if $\boldsymbol{p} \in \mathcal{P}_{\boldsymbol{s}}^{\boldsymbol{u}}$. Note that for $1 \leq i \leq 3$ the set $\mathcal{G}$ is partitioned by the disjoint union of N_i parallel planes $\mathcal{Q}_j^i := \mathcal{P}_{\boldsymbol{s}_j^i}^{\boldsymbol{e}_i}$, $1 \leq j \leq N_i$ where $\{\boldsymbol{s}_j^i, 1 \leq j \leq N_i\} = \{\boldsymbol{r}_{\boldsymbol{q},\boldsymbol{\varepsilon}} \in \mathcal{G}, (q_l, \varepsilon_l) = (0,1) \text{ if } l \neq i\}$. Then:

$$J_3(\boldsymbol{u}) = \sum_{\boldsymbol{s}\in\mathcal{G}} \sum_{j=1}^{N_i} |\mathcal{Q}_j^i \cap \mathcal{P}_{\boldsymbol{s}}^{\boldsymbol{u}} \cap \mathcal{G}| \quad \forall i \in [\![1,3]\!]. \tag{3.13}$$

Assume in the following that $\boldsymbol{u}$ is not colinear to any of the vectors $\boldsymbol{e}_i$. Then there exists a direction $\boldsymbol{e}_i$ such that every line $\mathcal{Q}_j^i \cap \mathcal{P}_{\boldsymbol{s}}^{\boldsymbol{u}}$, $1 \leq j \leq N_i$ is diagonal, in the sense that the direction of the line is not given by any of the basis vectors $\boldsymbol{e}_j$. Indeed, consider the converse proposition by contradiction: assume that for each $i \in [\![1,3]\!]$ there exists an image source $\boldsymbol{s} \in \mathcal{G}$ and a plane $\mathcal{Q}_j^i$ such that the line $\mathcal{Q}_j^i \cap \mathcal{P}_{\boldsymbol{s}}^{\boldsymbol{u}}$ is generated by a basis vector $\boldsymbol{e}_{k_i}$, $k_i \neq i$. In particular, $\boldsymbol{u}$ is orthogonal to $\boldsymbol{e}_{k_1}$ by definition as $\mathcal{P}_{\boldsymbol{s}}^{\boldsymbol{u}}$ contains the direction $\boldsymbol{e}_{k_1}$. Similarly, $\boldsymbol{e}_{k_{k_1}}$ is orthogonal to $\boldsymbol{u}$. Moreover, as the direction $\boldsymbol{e}_{k_{k_1}}$ is contained in $\mathcal{Q}_j^{k_1}$ which is orthogonal to $\boldsymbol{e}_{k_1}$, then $\boldsymbol{e}_{k_1}$ and $\boldsymbol{e}_{k_{k_1}}$ are distinct.

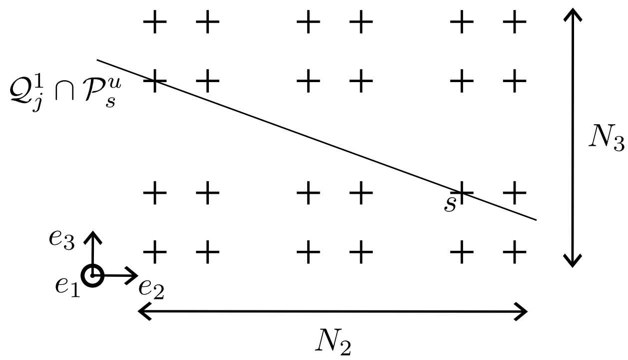

Figure 3.7: Intersection of $\mathcal{Q}_j^1$ and $\mathcal{P}_{\boldsymbol{s}}$ when $\boldsymbol{u}$ and $\boldsymbol{e}_1$ are not orthogonal

Hence $\boldsymbol{u}$ would be colinear to the last basis vector, raising a contradiction.

We can assume without any loss of generality that direction $\boldsymbol{e}_1$ verifies this property (see Figure 3.7 for a depiction in that case), *i.e* every line $\mathcal{Q}_j^1 \cap \mathcal{P}_{\boldsymbol{s}}^{\boldsymbol{u}}$, $1 \leq j \leq N_1$ is not generated by $\boldsymbol{e}_2$ or $\boldsymbol{e}_3$. Then, the line $\mathcal{Q}_j^1 \cap \mathcal{P}_{\boldsymbol{s}}^{\boldsymbol{u}}$ intersects $\mathcal{G}$ at at most $\min(N_2, N_3)$ image sources. Moreover, as $\boldsymbol{u}$ is not colinear to $\boldsymbol{e}_2$ and $\boldsymbol{e}_3$, this upper bound can only be reached for the sources $\boldsymbol{s}$ located on the diagonal. Indeed, we need only consider the worst-case scenario, in which the straight line passes through all the nodes on the diagonal. These nodes are at most $\min(N_2, N_3)$. Hence:

$$\begin{aligned} J_3(\boldsymbol{u}) = \sum_{\boldsymbol{s}\in\mathcal{G}}\sum_{j=1}^{N_1} |\mathcal{Q}_j^1 \cap \mathcal{P}_{\boldsymbol{s}}^{\boldsymbol{u}} \cap \mathcal{G}| < \sum_{\boldsymbol{s}\in\mathcal{G}} N_1 \min(N_2, N_3) \\ = N_1^2 N_2 N_3 \min(N_2, N_3). \end{aligned} \tag{3.14}$$

Now by replacing $\boldsymbol{u}$ with $\boldsymbol{e}_1$, formula (3.13) becomes :

$$J_3(\boldsymbol{e}_1) = \sum_{j=1}^{N_1} \sum_{\boldsymbol{s}\in\mathcal{G}} |\mathcal{Q}_1^1 \cap \mathcal{G}| \mathbb{1}_{\boldsymbol{s}\in\mathcal{Q}_j^1} = N_1 |\mathcal{Q}_1^1 \cap \mathcal{G}|^2. \tag{3.15}$$

Thus, $J_3(\boldsymbol{e}_1) = N_1 N_2^2 N_3^2$. We obtain similar formulas for $\boldsymbol{e}_2$ and $\boldsymbol{e}_3$, hence:

$$J_3(\boldsymbol{u}) < \max_{1\leq i\leq 3} J_3(\boldsymbol{e}_i) = N_1 N_2 N_3 \max_{1\leq i<j\leq 3} N_i N_j \tag{3.16}$$

and the maximum is reached for a vector $\boldsymbol{e}^*$ colinear to $\boldsymbol{e}_1$, $\boldsymbol{e}_2$ or $\boldsymbol{e}_3$. Note that this proof extends to 2D by considering the projection of $\mathcal{G}$ on $\boldsymbol{e}^{*\perp}$ in order to obtain a second basis vector. □

3.4 Conclusion

A new algorithm that leverages the gridless image-source localization method introduced in Section 2.3.3 to achieve full image-source reversion from a discrete, low-passed, multichannel, shoebox RIR was presented. In contrast to previous methods, we introduce a novel optimization step to recover the microphone array's orientation, which improves the accuracy of dimension estimation, and decreases the sensitivity to the false positives appearing in the image-source localization step. Extensive numerical experiments on simulated RIRs from randomized input parameters reveal that near-exact recovery of all input parameters is achieved by the method, for large enough array sizes and sampling rates. This constitutes, to our knowledge, the first empirical evidence that the historical image-source method of Allen and Berkley [5] is algorithmically reversible, for a wide range of configurations.

Chapter 4

Proof of the ISM decomposition

We provide in this chapter an alternative proof of the ISM decomposition introduced by Allen and Berkley for the solution of the wave equation with Neumann boundary conditions in a cuboid.

4.1 Modal decomposition

Let us introduce the eigenfunctions $\Psi_{\boldsymbol{w}}$ of the Neumann Laplacian in Ω, with associated eigenvalues $k_{\boldsymbol{w}}^2 \in \mathbb{R}_+$, defined by (see for instance [96]):

$$\begin{cases} \Psi_{\boldsymbol{w}}(\boldsymbol{r}) = \frac{2\sqrt{2}}{\sqrt{V}} \cos(\frac{\pi w_1}{L_x} r_1) \cos(\frac{\pi w_2}{L_y} r_2) \cos(\frac{\pi w_3}{L_z} r_3) \\ k_{\boldsymbol{w}} = \|v_{\boldsymbol{w}}\|_2 \,, \quad v_{\boldsymbol{w}} = (\frac{\pi w_1}{L_x}, \frac{\pi w_2}{L_y}, \frac{\pi w_3}{L_z}) \end{cases} \tag{4.1}$$

where $V = L_x L_y L_z$ is the volume of Ω, and $\boldsymbol{w} = (w_1, w_2, w_3) \in \mathbb{N}^3$. Recall that the family $\{\Psi_{\boldsymbol{w}}\}_{\boldsymbol{w} \in \mathbb{N}^3}$ forms a Hilbert basis of $L^2(\Omega)$. In the following, the duality pairings are defined with respect to the $L^2(\Omega)$ dot product. In order to solve analytically system (N-W), we introduce the eigenmode decomposition of the solution p:

$$\begin{cases} p(\boldsymbol{r}, t) = \sum_{\boldsymbol{w} \in \mathbb{N}^3} a_{\boldsymbol{w}}(t) \Psi_{\boldsymbol{w}}(\boldsymbol{r}) & (\boldsymbol{r}, t) \in \Omega \times \mathbb{R} \\ \Delta \Psi_{\boldsymbol{w}}(\boldsymbol{r}) = -k_{\boldsymbol{w}}^2 \Psi_{\boldsymbol{w}}(\boldsymbol{r}) & \boldsymbol{w} \in \mathbb{N}^3, \boldsymbol{r} \in \Omega \\ \partial_{\boldsymbol{n}} \Psi_{\boldsymbol{w}}(\boldsymbol{r}) = 0 & \boldsymbol{r} \in \partial\Omega, \end{cases} \tag{4.2}$$

this expansion being understood in a distributional sense. The time-dependent coefficients $a_{\boldsymbol{w}}$ can be obtained explicitly. This yields the following *modal decomposition* of the sound field in the time domain.

Proposition 4.1.1. *Let $\Omega = [0, L_x] \times [0, L_y] \times [0, L_z]$ be a 3-dimensional orthotope. The solution to System (N-W) can be written as:*

$$\forall (\boldsymbol{r}, t) \in \Omega \times \mathbb{R}, \quad p(\boldsymbol{r}, t) = \sum_{\boldsymbol{w} \in \mathbb{N}^3} c^2 t H(t) \operatorname{sinc}(ct k_{\boldsymbol{w}}) \Psi_{\boldsymbol{w}}(\boldsymbol{r}^{src}) \Psi_{\boldsymbol{w}}(\boldsymbol{r}) \tag{4.3}$$

where H denotes the Heaviside function. Such an expression makes sense in a distributional sense.

Proof. Let $\varphi \in \mathcal{C}_c^\infty(\Omega \times \mathbb{R})$ be a test function. Plugging (4.2) and (4.1) into (N-W), we get

$$\begin{aligned} \left\langle (\frac{1}{c^2}\partial_t^2 - \Delta) p \,,\, \varphi \right\rangle &= \int_{t \in \mathbb{R}} \int_{\boldsymbol{r} \in \Omega} \left(\sum_{\boldsymbol{w} \in \mathbb{N}^3} \frac{1}{c^2} a''_{\boldsymbol{w}}(t) + k_{\boldsymbol{w}}^2 a_{\boldsymbol{w}}(t) \right) \Psi_{\boldsymbol{w}}(\boldsymbol{r}) \varphi(\boldsymbol{r}, t) d\boldsymbol{r} dt & (4.4) \\ &= \int_{t \in \mathbb{R}} \sum_{\boldsymbol{w} \in \mathbb{N}^3} \int_{\boldsymbol{r} \in \Omega} \left(\frac{1}{c^2} a''_{\boldsymbol{w}}(t) + k_{\boldsymbol{w}}^2 a_{\boldsymbol{w}}(t) \right) \Psi_{\boldsymbol{w}}(\boldsymbol{r}) \varphi(\boldsymbol{r}, t) d\boldsymbol{r} dt & (4.5) \\ &= \varphi(\boldsymbol{r}^{\text{src}}, 0). & (4.6) \end{aligned}$$

Now, for $t \in \mathbb{R}$, $\varphi(t,\cdot)$ is in $L^2(\Omega)$. Hence, we can also write:

$$\begin{aligned} \varphi(\boldsymbol{r}^{\mathrm{src}},0) &= \left\langle \delta_0 \,,\, \sum_{\boldsymbol{w}\in\mathbb{N}^3} \left(\int_{\boldsymbol{r}\in\Omega} \varphi(\cdot,\boldsymbol{r})\Psi_{\boldsymbol{w}}(\boldsymbol{r})d\boldsymbol{r} \right) \Psi_{\boldsymbol{w}}(\boldsymbol{r}^{\mathrm{src}}) \right\rangle & (4.7)\\ &= \left\langle \delta_0 \,,\, \int_{\boldsymbol{r}\in\Omega} \sum_{\boldsymbol{w}\in\mathbb{N}^3} \Psi_{\boldsymbol{w}}(\boldsymbol{r})\Psi_{\boldsymbol{w}}(\boldsymbol{r}^{\mathrm{src}})\varphi(\cdot,\boldsymbol{r})d\boldsymbol{r} \right\rangle . & (4.8)\end{aligned}$$

By identifying the distributions, we deduce that $a_{\boldsymbol{w}}$ satisfies the ODE

$$a''_{\boldsymbol{w}}(t) + c^2k^2_{\boldsymbol{w}}a_{\boldsymbol{w}}(t) = c^2\Psi_{\boldsymbol{w}}(\boldsymbol{r}^{\mathrm{src}})\delta_0(t). \tag{4.9}$$

Since $a_{\boldsymbol{w}}$ is a causal function, let us write $a_{\boldsymbol{w}}(t) = H(t)\alpha_{\boldsymbol{w}}$ with $\alpha_{\boldsymbol{w}} \in H^1_{loc}(\mathbb{R})$. It follows from the jump rule [70, Chapter 2] that

$$a'_{\boldsymbol{w}}(t) = \alpha'_{\boldsymbol{w}}H(t) + [\alpha_{\boldsymbol{w}}](0)\delta_0(t) \quad \text{and} \quad a''_{\boldsymbol{w}}(t) = \alpha''_{\boldsymbol{w}}H(t) + [\alpha'_{\boldsymbol{w}}](0)\delta_0(t) + [\alpha_{\boldsymbol{w}}](0)\delta'_0(t)$$

where the notation $[f](0)$ stands for the jump of f at 0. We are thus led to identify $\alpha_{\boldsymbol{w}}$ solving the ODE

$$\begin{cases} \alpha''_{\boldsymbol{w}}(t) + c^2k^2_{\boldsymbol{w}}\alpha_{\boldsymbol{w}} = 0 & t > 0 \\ \alpha_{\boldsymbol{w}}(0) = 0, \quad \alpha'_{\boldsymbol{w}}(0) = c^2\Psi_{\boldsymbol{w}}(\boldsymbol{r}^{\mathrm{src}}) \end{cases} \tag{4.10}$$

and by solving this simple equation, we get

$$a_{\boldsymbol{w}}(t) = \frac{c}{k_{\boldsymbol{w}}}H(t)\Psi_{\boldsymbol{w}}(\boldsymbol{r}^{\mathrm{src}})\sin(ctk_{\boldsymbol{w}}) = tc^2H(t)\Psi_{\boldsymbol{w}}(\boldsymbol{r}^{\mathrm{src}})\operatorname{sinc}(ctk_{\boldsymbol{w}}), \qquad \boldsymbol{w} \in (\mathbb{N}^*)^3, t \in \mathbb{R}. \tag{4.11}$$

Recall that this solution is unique. Likewise, solving (4.10) in the case $\boldsymbol{w} = (0,0,0)$ yields:

$$a_{(0,0,0)}(t) = tc^2H(t)\Psi_{(0,0,0)}(\boldsymbol{r}^{\mathrm{src}}) = tc^2H(t)\Psi_{(0,0,0)}(\boldsymbol{r}^{\mathrm{src}})\operatorname{sinc}(ctk_{(0,0,0)}). \tag{4.12}$$

We finally obtain the expected expression of p. □

Note that applying a Fourier transform in time to the expression in Prop. 4.1.1 yields the frequency-domain modal decomposition in a cuboid:

Corollary 4.1.1. *The solution to the Helmholtz equation at wave number $\mathfrak{K}$ on Ω with Neumann boundary conditions is given by:*

$$p(\boldsymbol{r},\mathfrak{K}) = \sum_{\boldsymbol{w}\in\mathbb{N}^3} \left(\frac{1}{k^2_{\boldsymbol{w}} - \mathfrak{K}^2} + i\frac{\pi}{2k_{\boldsymbol{w}}}\left(\delta(ck_{\boldsymbol{w}} + \mathfrak{K}) - \delta(ck_{\boldsymbol{w}} - \mathfrak{K})\right) \right) \Psi_{\boldsymbol{w}}(\boldsymbol{r}^{src})\Psi_{\boldsymbol{w}}(\boldsymbol{r}) \quad (\boldsymbol{r},\mathfrak{K}) \in \Omega\times\mathbb{R}. \tag{4.13}$$

Proof. Using the convolution theorem and standard Fourier pair tables, we have:

$$\mathcal{F}\left[H(\cdot)\sin(\cdot(k_{\boldsymbol{w}}c))\right] = \frac{1}{2\pi}\mathcal{F}[H] * \mathcal{F}[\sin(\cdot(k_{\boldsymbol{w}}c))] = \frac{i\pi^2}{2\pi}\left[\frac{1}{i\pi\cdot+\delta(\cdot)}\right] * \left[\delta(\cdot+k_{\boldsymbol{w}}c) - \delta(\cdot-k_{\boldsymbol{w}}c)\right], \tag{4.14}$$

thus

$$\mathcal{F}\left[H(\cdot)\sin(\cdot(k_{\boldsymbol{w}}c))\right](\omega) = \frac{i\pi}{2}\left[\frac{1}{i\pi(\omega+k_{\boldsymbol{w}})} - \frac{1}{i\pi(\omega-k_{\boldsymbol{w}})} + \delta(\omega/c+k_{\boldsymbol{w}}) - \delta(\omega/c-k_{\boldsymbol{w}})\right], \tag{4.15}$$

where $\omega = 2\pi f$ is the angular speed. Multiplying by $\frac{c}{k_{\boldsymbol{w}}}\Psi_{\boldsymbol{w}}(\boldsymbol{r}^{\text{src}})\Psi_{\boldsymbol{w}}(\boldsymbol{r})$ and refactoring yields the expression in Cor. 4.1.1, using $\mathfrak{K} = \frac{\omega}{c}$. $\square$

4.2 Image source expansion

We now modify the modal decomposition of the solution p provided by Proposition 4.1.1 to obtain the desired image source expansion. Let $\boldsymbol{w} \in \mathbb{N}^3$, $\boldsymbol{w} \neq (0,0,0)$. Using Euler's formula and the notations introduced in (4.1), we can expand the products $\Psi_{\boldsymbol{w}}(\boldsymbol{r})\Psi_{\boldsymbol{w}}(\boldsymbol{r}^{\text{src}})$ into a sum of complex exponentials:

$$\Psi_{\boldsymbol{w}}(\boldsymbol{r})\Psi_{\boldsymbol{w}}(\boldsymbol{r}^{\text{src}}) = \frac{8}{64V}\sum_{\boldsymbol{\xi}_1,\boldsymbol{\xi}_2\in\{-1,1\}^3} e^{iv_{\boldsymbol{w}}.(\boldsymbol{\xi}_1\odot\boldsymbol{r}+\boldsymbol{\xi}_2\odot\boldsymbol{r}^{\text{src}})} = \frac{1}{8V}\sum_{\boldsymbol{\xi}_1,\boldsymbol{\xi}_2\in\{-1,1\}^3} e^{i\boldsymbol{\xi}_1\odot v_{\boldsymbol{w}}.(\boldsymbol{r}+\boldsymbol{\xi}_2\odot\boldsymbol{r}^{\text{src}})}. \tag{4.16}$$

The application $(\xi, m) \mapsto \xi \odot m$ is a bijection from $\{-1,1\}^3 \times \left(\mathbb{N}^3 \setminus \{(0,0,0)\}\right)$ into $\mathbb{Z}^3 \setminus \{(0,0,0)\}$. Thus, by injecting identity (4.16) in formula (4.3) we get:

$$\begin{aligned} p(\boldsymbol{r},t) &= \frac{1}{8V}\sum_{\boldsymbol{w}\in\mathbb{N}^3}\sum_{\boldsymbol{\xi}_1,\boldsymbol{\xi}_2\in\{-1,1\}^3} c^2tH(t)\,\mathrm{sinc}(ct\,\|\boldsymbol{v}_{\boldsymbol{w}}\|_2)e^{i\boldsymbol{\xi}_1\odot\boldsymbol{v}_{\boldsymbol{w}}.(\boldsymbol{r}+\boldsymbol{\xi}_2\odot\boldsymbol{r}^{\text{src}})} && (4.17)\\ &= \frac{1}{8V}\sum_{\boldsymbol{w}\in\mathbb{Z}^3}\sum_{\boldsymbol{\xi}\in\{-1,1\}^3} c^2tH(t)\,\mathrm{sinc}(ct\,\|\boldsymbol{v}_{\boldsymbol{w}}\|_2)e^{i\boldsymbol{v}_{\boldsymbol{w}}.(\boldsymbol{r}+\boldsymbol{\xi}\odot\boldsymbol{r}^{\text{src}})} && (4.18)\end{aligned}$$

where we define $\boldsymbol{v}_{\boldsymbol{w}}$ and $k_{\boldsymbol{w}}$ similarly to (4.2) for $\boldsymbol{w} \in \mathbb{Z}^3$. If we express each term of the sum as an integral against a Dirac delta distribution this expands to:

$$p(\boldsymbol{r},t) = \frac{1}{8V}\sum_{\boldsymbol{w}\in\mathbb{Z}^3}\sum_{\boldsymbol{\xi}\in\{-1,1\}^3}\int_{\boldsymbol{u}\in\mathbb{R}^3} c^2tH(t)\,\mathrm{sinc}(ct\,\|\boldsymbol{u}\|_2)e^{i\boldsymbol{u}.(\boldsymbol{r}+\boldsymbol{\xi}\odot\boldsymbol{r}^{\text{src}})}\delta_{\boldsymbol{v}_{\boldsymbol{w}}}(\boldsymbol{u})d\boldsymbol{u}. \tag{4.19}$$

The following calculations are presented formally, so as not to make the notations too cumbersome, and additional justifications will be provided at the end of the proof. The one dimensional Dirac comb Fourier series decomposition is given by:

$$\frac{1}{\alpha}\sum_{n=-\infty}^{+\infty} e^{\frac{2i\pi nx}{\alpha}} = \sum_{n=-\infty}^{+\infty}\delta_{n\alpha}(x) \quad \forall\alpha\in\mathbb{R}^*. \tag{4.20}$$

Decomposing the Dirac along each dimension, $\delta_{\boldsymbol{v_w}}$ can be seen as product of 1D Dirac distributions:

$$\delta_{\boldsymbol{v_w}}(\boldsymbol{u}) = \delta_{\frac{\pi}{L_x}k_x}(\boldsymbol{u}_x)\delta_{\frac{\pi}{L_y}k_y}(\boldsymbol{u}_y)\delta_{\frac{\pi}{L_z}k_z}(\boldsymbol{u}_z), \quad \text{where } \boldsymbol{v_w} = (\frac{\pi}{L_x}k_x, \frac{\pi}{L_y}k_y \frac{\pi}{L_z}k_z) \text{ and } (k_x, k_y, k_z) \in \mathbb{Z}^3. \tag{4.21}$$

This product is rigorously defined as a tensor product of distributions [70, Chapter 4]. We can then apply the decomposition (4.20) on each dimension in equation (4.19) to get:

$$p(\boldsymbol{r}, t) = \frac{1}{8\pi^3} \sum_{\boldsymbol{w}\in\mathbb{Z}^3} \sum_{\boldsymbol{\xi}\in\{-1,1\}^3} \int_{\boldsymbol{u}\in\mathbb{R}^3} c^2 t H(t) \operatorname{sinc}(ct \|\boldsymbol{u}\|_2) e^{i\boldsymbol{u}.(\boldsymbol{r}+\boldsymbol{\xi}\odot\boldsymbol{r}^{\text{src}}+2\boldsymbol{w}\odot\boldsymbol{v}_L)} d\boldsymbol{u}. \tag{4.22}$$

The last step is to compute the integral $\int_{\boldsymbol{u}\in\mathbb{R}^3} \frac{c\sin(\|\boldsymbol{u}\|_2 ct)}{\|\boldsymbol{u}\|_2} e^{i\boldsymbol{u}.\boldsymbol{v}} d\boldsymbol{u}$ where $\boldsymbol{v}$ is an arbitrary vector in $\mathbb{R}^3$.

Lemma 4.2.1. *Let $\boldsymbol{v} \in \mathbb{R}^3$. We have the following identity:*

$$\int_{\boldsymbol{u}\in\mathbb{R}^3} \frac{c\sin(\|\boldsymbol{u}\|_2 ct)}{\|\boldsymbol{u}\|_2} e^{i\boldsymbol{u}.\boldsymbol{v}} d\boldsymbol{u} = \frac{2\pi^2}{\|\boldsymbol{v}\|_2}(\delta(\|\boldsymbol{v}\|_2/c - t)) - \delta(\|\boldsymbol{v}\|_2/c + t)). \tag{4.23}$$

Proof. This integral can be seen as the Fourier transform of the 3D spherically symmetric function $f : \boldsymbol{u} \mapsto \frac{c\sin(\|\boldsymbol{u}\|_2 ct)}{\|\boldsymbol{u}\|_2}$. Denoting by $\boldsymbol{v}$ the Fourier variable, one has

$$\int_{\boldsymbol{u}\in\mathbb{R}^3} c\frac{\sin(\|\boldsymbol{u}\|_2 ct)}{\|\boldsymbol{u}\|_2} e^{i\boldsymbol{u}\cdot\boldsymbol{v}} d\boldsymbol{u} = \frac{1}{c}\int_{c\boldsymbol{u}\in\mathbb{R}^3} \frac{\sin(\|c\boldsymbol{u}\|_2 t)}{\|c\boldsymbol{u}\|_2} e^{i(c\boldsymbol{u})\cdot(\boldsymbol{v}/c)} d(c\boldsymbol{u}) = \frac{1}{c}\int_{\boldsymbol{u}\in\mathbb{R}^3} \frac{\sin(\|\boldsymbol{u}\|_2 t)}{\|\boldsymbol{u}\|_2} e^{i\boldsymbol{u}\cdot(\boldsymbol{v}/c)} d\boldsymbol{u}$$

The unnormalized Fourier transform $\hat{f}$ of a function f of d arguments with radial symmetry is only radius-dependent, and is given by the following identity [74]:

$$\hat{f}(\boldsymbol{u}) = \frac{(2\pi)^{d/2}}{\|\boldsymbol{u}\|_2^{d/2-1}} \int_0^{+\infty} r^{d/2} f(r) J_{d/2-1}(\|\boldsymbol{u}\|_2 r) dr \tag{4.24}$$

where we denote by J_k the Bessel function of the first kind of order k. In particular in the case $d = 3$, $J_{1/2}$ is given explicitly by:

$$J_{1/2}(t) = \sqrt{\frac{2}{\pi}} \frac{\sin(t)}{\sqrt{t}} \quad \forall t \in \mathbb{R}_+. \tag{4.25}$$

Applying formula (4.24) to the integral of interest yields:

$$\int_{\boldsymbol{u}\in\mathbb{R}^3} \frac{\sin(\|\boldsymbol{u}\|_2 t)}{\|\boldsymbol{u}\|_2} e^{i\boldsymbol{u}\cdot(\boldsymbol{v}/c)} d\boldsymbol{u} = \frac{4\pi}{\|\boldsymbol{v}\|_2} \int_0^{+\infty} \sin(rt) \sin\left(r\frac{\|\boldsymbol{v}\|_2}{c}\right) dr \tag{4.26}$$

$$= \frac{2\pi}{\|\boldsymbol{v}\|_2} \int_{-\infty}^{+\infty} \sin(rt) \sin\left(r\frac{\|\boldsymbol{v}\|_2}{c}\right) dr. \tag{4.27}$$

Using both the Euler formula and the fact that the Fourier transform with oscillatory factor -1 of the distribution e^{iax} is $2\pi\delta(\xi - a)$, for $a \in \mathbb{R}$, we get

$$\frac{1}{c}\int_{u\in\mathbb{R}^3} \frac{\sin(\|\boldsymbol{u}\|_2\, t)}{\|\boldsymbol{u}\|_2} e^{i\boldsymbol{u}\cdot(\boldsymbol{v}/c)} d\boldsymbol{u} = \frac{2\pi^2}{\|\boldsymbol{v}\|_2}\left(\delta\left(\frac{\|\boldsymbol{v}\|_2}{c} - t\right) - \delta\left(\frac{\|\boldsymbol{v}\|_2}{c} + t\right)\right), \tag{4.28}$$

which is the desired formula. $\square$

Injecting this last identity in (4.22), we get:

$$p(r,t) = \sum_{\boldsymbol{w}\in\mathbb{Z}^3}\sum_{\boldsymbol{\xi}\in\{-1,1\}^3} \frac{\delta(t - \|\boldsymbol{r} + \boldsymbol{\xi}\odot\boldsymbol{r}^{\text{src}} + 2\boldsymbol{w}\odot\boldsymbol{v}_L\|_2 / c)}{4\pi\,\|\boldsymbol{r} + \boldsymbol{\xi}\odot\boldsymbol{r}^{\text{src}} + 2\boldsymbol{w}\odot\boldsymbol{v}_L\|_2}, \tag{4.29}$$

which concludes the proof.

The transition from Eq. (4.19) to Eq. (4.22) can be made rigorous by performing a truncation of $\operatorname{sinc}(ct\,\|\cdot\|_2)$ using a smooth, compactly supported function χ_μ, where χ_μ equals 1 on the ball of radius μ centered at the origin, and vanishes outside the ball of radius 2μ. Indeed, the equality between both expressions hold for the truncation, and we can let μ go to infinity in Eq (4.23) to obtain the desired result.

Remark 4.2.1. In the case $d = 2$, integral (4.24) translates to:

$$\begin{aligned}
\int_{u\in\mathbb{R}^2} c\frac{\sin(\|\boldsymbol{u}\|_2\, ct)}{\|\boldsymbol{u}\|_2} e^{i\boldsymbol{u}.\boldsymbol{v}} d\boldsymbol{u} &= \int_{u\in\mathbb{R}^2} \frac{\sin(\|\boldsymbol{u}\|_2\, t)}{\|\boldsymbol{u}\|_2} e^{i\boldsymbol{u}\cdot(\boldsymbol{v}/c)} d\boldsymbol{u} \\
&= 2\pi\int_0^{+\infty} \sin(rt) J_0(r\,\|\boldsymbol{v}/c\|_2) dr \\
&= \frac{2\pi}{\|\boldsymbol{v}_c\|_2^{1/2}} \int_0^{+\infty} r^{-1/2}\sin(rt) J_0(r\,\|\boldsymbol{v}_c\|_2)(\|\boldsymbol{v}_c\|_2\, r)^{1/2} dr
\end{aligned}$$

where $\boldsymbol{v}_c = \boldsymbol{v}/c$. According to formula 8.2.32 in [17], this last Hankel transform becomes:

$$\int_{u\in\mathbb{R}^2} c\frac{\sin(\|\boldsymbol{u}\|_2\, ct)}{\|\boldsymbol{u}\|_2} e^{i\boldsymbol{u}\cdot\boldsymbol{v}} d\boldsymbol{u} = 2\pi\frac{H(t - \|\boldsymbol{v}_c\|_2)}{\sqrt{t^2 - \|\boldsymbol{v}_c\|_2^2}} \tag{4.30}$$

which is proportional to the 2D causal Green function for the wave equation. Similarly to the 3D case, the pressure field can then be expressed as a sum of Green functions:

$$p(\boldsymbol{r},t) = \sum_{\boldsymbol{w}\in\mathbb{Z}^2}\sum_{\boldsymbol{\xi}\in\{-1,1\}^2} \frac{H(t - \|\boldsymbol{r} + \boldsymbol{\xi}\odot\boldsymbol{r}^{\text{src}} + 2\boldsymbol{w}\odot v_L\|_2 / c)}{2\pi\sqrt{t^2 - \|\boldsymbol{r} + \boldsymbol{\xi}\odot\boldsymbol{r}^{\text{src}} + 2\boldsymbol{w}\odot v_L\|_2^2 / c^2}}. \tag{4.31}$$

Part II

General approach

We consider in this part the more general case of a polyhedral room. To simplify the problem, we place ourselves in 2D and consider a convex room Ω with a polygonal boundary $\partial\Omega$. Chapter 5 introduces useful notations and formulas, as well as general notions on shape optimization and simulation of the Helmholtz equation. The application of the method of fundamental solutions (MFS) to the simulation of the 2D Helmholtz equation in a closed polygonal domain is presented in details in Chapter 6. We then address the problem of reconstructing the shape of Ω from a set of measurements in Chapter 7 by using a shape-optimization approach.

Chapter 5

Tools for shape-optimization on polygons

We introduce in this chapter some notations and useful identities, as well as some basic notions of shape optimization. We also provide a short overview of numerical methods for the resolution of the Helmholtz equation, and present the Method of Fundamental Solutions.

5.1 Shape optimization on polygons

5.1.1 Notations and useful identities

We begin by introducing some notations and useful elementary properties for vector calculus. We denote by $\otimes$ the *outer product of vectors*:

$$\forall \boldsymbol{x}, \boldsymbol{y} \in \mathbb{C}^D, \quad (\boldsymbol{x} \otimes \boldsymbol{y}) = (x_i y_j)_{1 \leq i,j \leq D}. \tag{5.1}$$

The *Frobenius inner product* : of real matrices is defined by:

$$\forall A, B \in \mathfrak{M}_{D,D}(\mathbb{R}), \quad A : B \coloneqq \sum_{i=1}^{D} \sum_{j=1}^{D} A_{i,j} B_{i,j} = \operatorname{tr}(A^T B). \tag{5.2}$$

Note that we will apply Formula (5.2) to complex valued matrices, but we do not consider the complex Frobenius inner product, in which case the transpose would become a conjugate transpose. The divergence of a matrix $Z : \mathbb{R}^D \to \mathfrak{M}_{D,D}(\mathbb{R})$ is the vector of the divergences of its rows:

$$\operatorname{div} Z \coloneqq (\operatorname{div} Z_i)_{1 \leq i \leq D} = (\sum_{j=1}^{D} \partial_j Z_{i,j})_{1 \leq i \leq D}. \tag{5.3}$$

The *tangential derivative* of a vector field $V : \mathbb{R}^D \to \mathbb{R}^D$ on $\partial\Omega$ writes:

$$D_\Gamma V = DV - (DV)\boldsymbol{n} \otimes \boldsymbol{n} = DV - (DV.\boldsymbol{n}) \otimes \boldsymbol{n}, \tag{5.4}$$

the *tangential divergence* of V is defined as:

$$\operatorname{div}_\Gamma(V) = \operatorname{div} V - (DV.\boldsymbol{n}) \cdot \boldsymbol{n} = \operatorname{tr}(D_\Gamma V), \tag{5.5}$$

and the *tangential gradient* of a scalar field $f : \mathbb{R}^D \to \mathbb{R}$ is:

$$\nabla_\Gamma f = \nabla f - (\nabla f \cdot \boldsymbol{n})\boldsymbol{n}. \tag{5.6}$$

Recall Green's first and second identities [62], stated here for regular domains and functions:

Theorem 5.1.1 (Green's first and second identities)**.** *Assume that Ω is open, bounded with a $\mathcal{C}^1$ boundary. Let $\varphi_1, \varphi_2 \in \mathcal{C}^2(\Omega, \mathbb{R})$. We have the identities:*

$$\int_\Omega \varphi_1 \Delta\varphi_2 - \varphi_2 \Delta\varphi_1 = \int_{\partial\Omega} \varphi_1 \partial_{\boldsymbol{n}} \varphi_2 - \varphi_2 \partial_{\boldsymbol{n}} \varphi_1 \tag{5.7}$$

and

$$\int_\Omega \varphi_1 \Delta\varphi_2 + \nabla\varphi_1 \cdot \nabla\varphi_2 = \int_{\partial\Omega} \varphi_1 \partial_{\boldsymbol{n}} \varphi_2. \tag{5.8}$$

The following identities will be useful in the next sections.

Lemma 5.1.1. *Let $V_1, V_2, V_3 : \mathbb{R}^D \to \mathbb{R}^D$, $f : \mathbb{R}^D \to \mathbb{R}$, and $Z : \mathbb{R}^D \to \mathfrak{M}_{D,D}(\mathbb{C})$. If V_1, V_2, V_3, f, Z are sufficiently regular, we have the following expressions:*

$$Z : DV_1 + V_1 \cdot \operatorname{div} Z = \operatorname{div}(Z^T V_1) \tag{5.9}$$

$$Z : \mathrm{I} = \operatorname{tr}(Z) \tag{5.10}$$

$$(V_1 \otimes V_2) : Z = V_1 \cdot (Z V_2). \tag{5.11}$$

$$\operatorname{div}_\Gamma(f V_1) = \nabla_\Gamma(f) \cdot V_1 + f \operatorname{div}_\Gamma(V_1) \tag{5.12}$$

$$\nabla(V_1 \cdot V_2) = DV_1^T V_2 + DV_2^T V_1. \tag{5.13}$$

$$(V_1 \otimes V_2).V_3 = (V_2 \cdot V_3) V_1. \tag{5.14}$$

5.1.2 Shape derivative

We wish to minimize an objective function J that depends on the domain Ω, and on the solution p_Ω of a PDE system defined on Ω and its boundary $\partial\Omega$. We will focus here on an "optimize-then-discretize" approach, meaning that we will begin by computing the continuous derivative of J with respect to the shape Ω, and then discretize the resulting expression for numerical optimization. This section provides a short presentation of shape derivatives.

Let $V \in W^{1,\infty}(\mathbb{R}^2, \mathbb{R}^2)$ a deformation vector field operating on a domain Ω chosen in such a way that $\Omega + \varepsilon V$ belongs to the set of admissible shapes $\mathcal{S}_{\mathrm{adm}}$ whenever $\varepsilon > 0$ is small enough. For $\varepsilon > 0$, we define the transformation $T_\varepsilon \coloneqq \mathrm{Id} + \varepsilon V$ and the deformed domain $\Omega_\varepsilon \coloneqq T_\varepsilon(\Omega)$. The shape derivative of the cost function J in direction V, when it exists, is defined by:

$$DJ(\Omega) \cdot V = \lim_{\varepsilon \to 0^+} \frac{J(\Omega_\varepsilon) - J(\Omega)}{\varepsilon}. \tag{5.15}$$

It is standard to introduce the so-called Eulerian derivative p'_Ω of p_Ω in direction V given by

$$p'_\Omega \coloneqq \dot{p}_\Omega - \nabla p_\Omega \cdot V, \tag{5.16}$$

where $\dot{p}_\Omega$ denotes the Lagrangian derivative of p_Ω in direction V, defined as the derivative at $\varepsilon = 0$

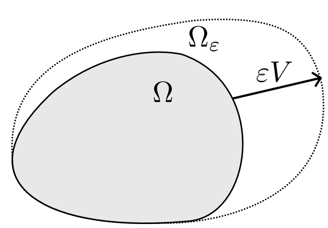

Figure 5.1: Effect of T_ε on Ω

of the mapping $\varepsilon \mapsto p_{\Omega_\varepsilon} \circ (\mathrm{Id} + \varepsilon V)$. Formally and intuitively, p'_Ω verifies the expression

$$p'_\Omega = \lim_{\varepsilon \to 0^+} \frac{p_{\Omega_\varepsilon} - p_\Omega}{\varepsilon}, \tag{5.17}$$

which is ill-defined on the boundary.

In our case, we will derive formal calculations for the shape derivative that will be utilized in a gradient descent algorithm. In practice, we will seek a boundary expression of the type:

$$DJ(\Omega) \cdot V = \int_{\partial\Omega} F_{\partial\Omega}.(V \cdot \boldsymbol{n}), \tag{5.18}$$

where $F_{\partial\Omega}$ is a scalar function to be determined. Under some regularity assumptions, the existence of an expression of the type (5.18) is guaranteed by a structure theorem, see [50, Theorem 3.6]. Further details and more rigorous definitions of shape derivatives can be found for instance in [81, 80, 50, 79, 4].

5.1.3 Shape derivative on polygons

We will consider in our case a polygonal domain Ω, defined by S vertices $\boldsymbol{v}_1, \dots, \boldsymbol{v}_S$ indexed in trigonometric ordering, with the convention $\boldsymbol{v}_{S+1} = \boldsymbol{v}_1$. We denote by $\boldsymbol{\tau}_s$ the s-th unitary tangential vector $\boldsymbol{\tau}_s = \frac{\boldsymbol{v}_{s+1} - \boldsymbol{v}_s}{\|\boldsymbol{v}_{s+1} - \boldsymbol{v}_s\|_2}$, and Γ_s the corresponding edge, *i.e.* $\partial\Omega = \bigcup_{s=1}^{S} \overline{\Gamma_s}$. Fig. 7.1 will give an overview of these notations.

We will use a similar framework to [104, 103], based on a Lagrangian formulation, to compute the shape derivative. We will require an adaptation of the tangential divergence theorem in order to transform some boundary integrals used to compute the derivative. We will thus make use of an adaptation of the theorem for polygons, introduced in the more general context of $\mathcal{C}^k$ curvilinear polygons in [103].

Theorem 5.1.2. *Let Ω a 2D polygonal domain with S edges, and $\partial\Omega = \bigcup_{s=1}^{S} \overline{\Gamma_s}$ its boundary. Let $V \in W^{1,1}(\Gamma_s, \mathbb{R}^2) \cap \mathcal{C}^0(\overline{\Gamma_s}, \mathbb{R}^2)$. Then, for every $1 \leq s \leq S$, we have:*

$$\int_{\Gamma_s} \mathrm{div}_\Gamma(V) = (V(\boldsymbol{v}_{s+1}) - V(\boldsymbol{v}_s)) \cdot \boldsymbol{\tau}_s, \tag{5.19}$$

with the convention $\boldsymbol{v}_{S+1} = \boldsymbol{v}_1$.

Remark 5.1.1. An additional term containing the mean curvature of the polygon has to be computed for general $\mathcal{C}^k$ curvilinear polygons. This term vanishes in our case, as the curvature is null on each edge.

The final form of the shape derivative will be the sum of a boundary integral of the type (5.18), and a finite linear combination of functions evaluated at each vertex of the polygon.

5.1.4 State of the art

Whilst shape optimization problems on smooth domains are well studied in the literature, the case of non-smooth domains remains less explored. However, some works on the existence, structure and regularity of shape derivatives for non-smooth domains have been published. For instance, [51] provides results on the structure of shape derivatives for general non-smooth domains, whilst [69, 90] focus on domains with cracks and [135] considers discrete singularities. The regularity of shape derivatives around irregular domains is studied in [99], and the structure of derivatives for domains with finite perimeters is investigated in [100]. In our case, we will concentrate on polygonal domains, and prioritize numerical applications. The shape derivative of our objective function will be computed using a Lagrangian method [34]. In order to obtain a boundary integral formulation, we will use a strategy based on tensor representations, described in [103] in for more general classes of irregular domains. Finally, several works provide numerical frameworks for shape optimization amongst convex shapes. For instance, [98] defines a numerical method to optimize functions with a convexity constraint by using the half-space (or half-plane) parametrization for convex shapes. However, this method is designed to be used with many half-spaces discretizing the domain. In particular, half-spaces may become inactive during the optimization process, leading to the vanishing of some faces of the domain, where in our case we wish to keep a constant number of edges. In [21], the author proposes to use the support function for the optimization of convex shapes. The convexity constraints are enforced by discretizing the support function. Again, keeping a fixed number of edges would be problematic in this context. We will thus use one of the natural parametrizations of polygons in our method.

5.2 Numerical resolution of the Helmholtz equation

5.2.1 A short overview of Helmholtz simulation methods

In order to implement a shape optimization algorithm we will require an efficient simulation method. Indeed, at each gradient step we will solve two Helmholtz equations: one to compute the pressure field on the current shape, and another to calculate an adjoint state, which is necessary to update the gradient. The chosen resolution method has to offer a decent accuracy to get a good approximation of the cost function and gradient at each step, with a low computational cost. Moreover, the source terms considered are singular, and the resolution method has to be able to handle a finite combination of point sources. We can divide simulation methods into two categories: mesh-based methods and meshless methods. Amongst mesh-based methods, the Finite Element Method (FEM) is widely used in acoustics, see for instance [144, 121, 59, 116]. We give here a short description of the Galerkin method applied to the Helmholtz equation. By multiplying the Helmholtz equation by a test function φ, integrating over the whole domain and applying Green's second identity (5.8), we get the following weak formulation for equation (14) with Robin boundary conditions (16):

$$\int_\Omega \nabla p \cdot \nabla \overline{\varphi} - \mathfrak{K}^2 \int_\Omega p\overline{\varphi} + i\mathfrak{K}\beta \int_{\partial\Omega} p\overline{\varphi} = \overline{\varphi}(\boldsymbol{r}^{\mathrm{src}}), \quad \forall \varphi \in \mathcal{C}^1(\Omega). \tag{5.20}$$

The domain Ω is discretized in a number of subdomains $\Omega_j, j \in [\![1, N]\!]$, typically triangles, called *finite elements*. We then choose a basis of local interpolating functions $\varphi_j^{(k)}, k \in [\![1, K]\!]$ over Ω_j, for instance Lagrange polynomials. The basis functions $\varphi_j^{(k)}$ are chosen such that they are globally continuous across the domain, with piecewise definitions on individual elements Ω_j. The approximated solution on Ω_j then writes $\hat{p}_j = \sum_{k=1}^{K} \alpha_j^{(k)} \varphi_j^{(k)}$. Applying Equation (5.20) with $\varphi = \varphi_j^{(k)}, k = 1, \ldots, K$ yields a local system of integral equations over Ω_j with unknowns $\alpha_j^{(k)}$, that can be discretized using a numerical quadrature formula. Each system of equations is then assembled into a global equation matrix taking into account the connectivity constraints between elements.

Although the FEM produces accurate results, it is known to be computationally expensive, especially as the frequency increases. Indeed, the number of elements necessary to accurately represent the solution highly depends on the wavelength [2]. Several methods were developed to counteract this issue, such as enrichment methods [64], Galerkin least-squares [78] or adaptive methods using *a posteriori* error estimates [3, 83]. [143] provides a review of FE methods for the Helmholtz equation.

Managing the mesh can become a burden in shape optimization problems as it has to be updated at each optimization step, adding a significant computational cost. Meshless methods, however, do not require a spatial discretization of the interior of the domain. Only the boundary of the domain is meshed, effectively reducing the dimension of the problem by one. This especially reduces the computational and implementation complexity in 2D, as the boundary is one-dimensional and consequently no triangulation is necessary. This offers a significant advantage for shape optimization algorithms as it is easier and less costly to handle the resulting boundary mesh between gradient steps. Amongst meshless methods, the Boundary Element Method (BEM) is the most prominent method in acoustics [107, 16, 35, 101]. Let p be the solution of the homogeneous Helmholtz equation with inhomogeneous Robin boundary conditions. Applying Green's first identity (5.7) yields:

$$\int_{\partial\Omega} \partial_{\boldsymbol{n}} G_{\boldsymbol{r}}^{\mathfrak{K}}(\boldsymbol{r}') p(\boldsymbol{r}') d\boldsymbol{r}' + p(\boldsymbol{r}) = \int_{\partial\Omega} \partial_{\boldsymbol{n}} p(\boldsymbol{r}) G_{\boldsymbol{r}}^{\mathfrak{K}}(\boldsymbol{r}') d\boldsymbol{r}', \quad \boldsymbol{r} \in \Omega \tag{5.21}$$

where $G_{\boldsymbol{r}}^{\mathfrak{K}}$ denotes a free field Green's function for the Helmholtz equation at wave number $\mathfrak{K}$ (see Section 1.1.1). The values of p inside Ω can thus be inferred from the values taken on the boundary. Assuming Ω is sufficiently regular and letting $\boldsymbol{r}$ approach $\partial\Omega$ yields a singular boundary integral formulation [89]:

$$\int_{\partial\Omega} \partial_{\boldsymbol{n}} G_{\boldsymbol{r}}^{\mathfrak{K}}(\boldsymbol{r}') p(\boldsymbol{r}') d\boldsymbol{r}' + \frac{1}{2} p(\boldsymbol{r}) = \int_{\partial\Omega} \partial_{\boldsymbol{n}} p(\boldsymbol{r}) G_{\boldsymbol{r}}^{\mathfrak{K}}(\boldsymbol{r}') d\boldsymbol{r}', \quad \boldsymbol{r} \in \partial\Omega. \tag{5.22}$$

Equation (5.22) is used to construct a linear system of equations for which the unknowns are the values taken by the solution p at a finite number of elements on the boundary $\partial\Omega$. The numerical solution can then be evaluated at any point inside the domain by using formula (5.21). See [42, 155, 89] for more details on BEM.

The method implemented in this thesis is the Method of Fundamental Solutions (MFS). It carries common traits with the BEM: it makes use of the free-field Green's functions, and it is a meshless method for which the solution of the approximated field can be computed at any location inside the domain. The MFS has seen various applications in acoustics, such as the simulation of horns [72], acoustic scattering [97, 88], vibro-acoustics [43], wave propagation [11] or eigenfrequencies computation [148, 6]. The MFS was favorably compared to the BEM in [73] for the simulation of the Helmholtz equation with impedance boundary conditions in 3D. Due to its simplicity, the MFS has also been used in the context of shape optimization, with applications to eigenproblems [7, 13, 12], source [110, 1], obstacle [111, 87] or cavity [140] reconstruction from boundary measurements. In the next section we provide a detailed description of the MFS applied to the Helmholtz equation in a closed domain.

5.2.2 The Method of Fundamental Solutions

General description

The Method of Fundamental Solutions (MFS) is a meshless numerical resolution method that consists in approximating the solution of a PDE with boundary conditions by a linear combination of free-field Green's functions:

$$p(\boldsymbol{r}) \approx \sum_{j=1}^{K} \alpha_j G^{\mathfrak{K}}_{\boldsymbol{r}_j}(\boldsymbol{r}), \quad \boldsymbol{r} \in \Omega. \tag{5.23}$$

The $\boldsymbol{r}_j$ are set virtual source locations that are located outside Ω. Consider a homogeneous Helmholtz equation with inhomogeneous Robin boundary conditions:

$$\begin{cases} \Delta p + \mathfrak{K}^2 p = 0 & \text{in } \Omega \\ \partial_{\boldsymbol{n}} p + i\mathfrak{K}\beta p = g & \text{on } \partial\Omega. \end{cases} \tag{5.24}$$

Let $(\alpha_j, \boldsymbol{r}_j) \in \mathbb{C} \times \mathbb{R}^d,\ j \in [\![1, K]\!]$ where the $\boldsymbol{r}_j$ are located outside $\bar{\Omega}$. Then, it follows from the definition of Green's functions that $\widehat{p} = \sum_{j=1}^{K} \alpha_j G^{\mathfrak{K}}_{\boldsymbol{r}_j}$ solves the interior equation of System (5.24) regardless of the values of the weights α_j. We then adjust the weights α_j in order to meet the boundary condition. Setting a collection of collocations points $\boldsymbol{b}_i \in \partial\Omega,\ i \in [\![1, N_c]\!]$ where $N_c \geq K$, we solve the following linear system:

$$\begin{pmatrix} (\partial_{\boldsymbol{n}} + i\mathfrak{K}\beta)G^{\mathfrak{K}}_{\boldsymbol{r}_1}(\boldsymbol{b}_1) & \cdots & (\partial_{\boldsymbol{n}} + i\mathfrak{K}\beta)G^{\mathfrak{K}}_{\boldsymbol{r}_K}(\boldsymbol{b}_1) \\ \vdots & & \vdots \\ (\partial_{\boldsymbol{n}} + i\mathfrak{K}\beta)G^{\mathfrak{K}}_{\boldsymbol{r}_1}(\boldsymbol{b}_{N_c}) & \cdots & (\partial_{\boldsymbol{n}} + i\mathfrak{K}\beta)G^{\mathfrak{K}}_{\boldsymbol{r}_K}(\boldsymbol{b}_{N_c}) \end{pmatrix} \begin{pmatrix} \alpha_1 \\ \vdots \\ \alpha_K \end{pmatrix} = \begin{pmatrix} g(\boldsymbol{b}_1) \\ \vdots \\ g(\boldsymbol{b}_{N_c}) \end{pmatrix}. \tag{5.25}$$

Now, in order to simulate room impulse responses, we consider instead an inhomogeneous Helmholtz equation with homogeneous Robin boundary conditions:

$$\begin{cases} \Delta p + \mathfrak{K}^2 p = -\delta_{\boldsymbol{r}^{\mathrm{src}}}(\boldsymbol{r}) & \text{in } \Omega \\ \partial_{\boldsymbol{n}} p + i\mathfrak{K}\beta p = 0 & \text{on } \partial\Omega. \end{cases} \tag{5.26}$$

This can be achieved by the previous method by setting $g(\boldsymbol{r}) = -(\partial_{\boldsymbol{n}} + i\mathfrak{K}\beta)G_{\boldsymbol{r}^{\mathrm{src}}}(\boldsymbol{r})$ in (5.25), and considering the approximated solution $\widehat{p} = \sum_{j=1}^{K} \alpha_j G_{\boldsymbol{r}_j} + G_{\boldsymbol{r}^{\mathrm{src}}}$. Note that by linearity we can also solve the equation similarly in the case of a weighted sum of point sources. Moreover, the method adapts easily to Neumann, Dirichlet or more complex boundary conditions as we need only to modify the boundary conditions applied to the Green's functions in (5.25).

Remark 5.2.1. This method is the strong formulation of the MFS. It is also possible to use the same principle to compute a weak formulation of the MFS, which requires integrating the fundamental solutions over the boundary. Note however that, contrarily to the boundary integrals used in the BEM, the singularities of the Green's functions involved are not directly located on the boundary.

Adaptation to polygons

The case of polygonal domains introduces some difficulties in the computation of the MFS. Indeed, the fundamental solutions fail to replicate the behavior of the solution near the vertices of the boundary in the case of singular corners. A corner is called regular if its inner angle is of the form π/ω with $\omega \in \mathbb{N}$. If $\omega \notin \mathbb{N}$, the corner is said to be irregular and can cause convergence issues in the MFS, which will be addressed in the numerical experiments of Section 6.2. Antunes and Valtchev proposed in [14] an enrichment of the basis of fundamental solutions in order to take into account the irregularity of the solution at the singular corners. The idea is to add particular solutions of the homogeneous Helmholtz equation that can compensate the asymptotic behavior of the solution of the boundary problem near the corners. The functions considered are of the form:

$$\psi_l(r, \theta) = J_{l\omega}(kr)\cos(l\omega\theta), \quad l \in \mathbb{N} \tag{5.27}$$

where $J_{l\omega}$ denotes the Bessel function of the first kind of order $l\omega$ and r, θ are the polar coordinates with the origin located at the corner and the x-axis aligned with an edge, as represented on Fig. 5.2. The functions ψ_l are Neumann corner eigenfunctions for the Helmholtz equation and are adapted to counteract the asymptotic behavior for a Neumann boundary problem. However, numerical experiments have shown that these functions also perform satisfactorily for Robin boundary conditions (see Section 6.2). More details on the implementation are given in Section 6.1.

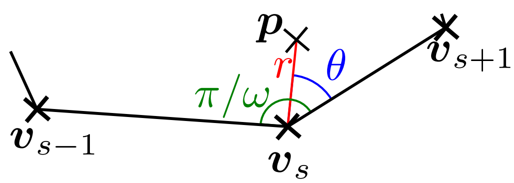

Figure 5.2: Polar system of coordinates for a corner function at vertex s and a given location $\boldsymbol{p}$.

Chapter 6

Method of fundamental solutions

In this chapter, we describe more precisely the implementation of the MFS in the context of our problem, and assess its numerical efficiency for the resolution of the 2D Helmholtz equation with a point source inside a polygonal domain. We also present an approach to compute a time-domain RIR using the MFS.

6.1 Implementation details

6.1.1 Virtual source locations

A first crucial issue to ensure the accurate execution of the MFS is the choice of the virtual source locations outside the domain. It is possible to optimize on the locations of the sources in order to maximize accuracy [112]. However, to reduce computational costs, we sample the sources on the polygon and simply shift them in the direction of the outgoing normal vector by a distance dx (see Fig. 6.1). As we will only consider convex polygons, this guarantees that every virtual source is located at the same distance to the boundary. The choice of the distance dx between $\partial\Omega$ and the virtual boundary is discussed in Section 6.2. Given a desired number of virtual sources K, we assign to each edge a number of sources proportional to its length and uniformly spread the locations on the edge. The choice of K is addressed in the next section.

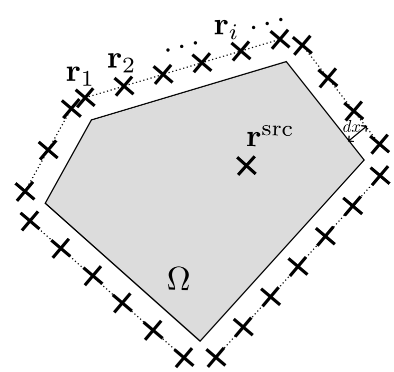

Figure 6.1: Resolution domain Ω and associated sampling boundary for the virtual sources.

6.1.2 Adaptive sampling strategy

A sufficient number of basis functions must be used to approximate the solution in order to have an accurate representation. The choice of the number of fundamental solutions is far from obvious, as it depends both on the geometry and the wave number. In particular, when solving the Helmholtz equation at different wave numbers, we can adapt the number of virtual sources accordingly. We then choose the number of collocation points on the boundary to be superior or equal to the number of virtual sources. Moreover, we can check the adequacy of the approximated solution by evaluating the corresponding boundary conditions, and increase the number of virtual sources if necessary. In order to reduce the memory usage and computational cost when computing the solution at numerous frequencies, we only check the solution at certain reference frequencies in order to set the number of sources. The same virtual boundary mesh is then used for a whole frequency range. Alg. 5 gives a description of the setup procedure given a sequence of increasing reference wave numbers, and two sequences of initial spacing parameters for the collocation points and virtual sources. For

Algorithm 5 Setting up of a simulation

Input: Reference wave numbers $\mathfrak{K}_1^{\text{ref}} < \ldots < \mathfrak{K}_L^{\text{ref}}$, virtual source spacing σ_l, collocation points spacing μ_l, error threshold ε

Output: Virtual source locations $(\boldsymbol{r}_k^l)_{1\le k\le K_l}$, collocation points $(\boldsymbol{b}_k^l)_{1\le k\le K_l'}$ and corresponding normal vectors $(\boldsymbol{n}_k^l)_{1\le k\le K_l'}$ for each reference wave number $\mathfrak{K}_l^{\text{ref}}$

for $l = 1, \ldots, L$ **do**
  $e \leftarrow +\infty$
  while $e > \varepsilon$ **do**
    if $\sigma_l > \sigma_{l-1}$ **then**
      $\sigma_{l-1} \leftarrow \sigma_l$
    end if
    if $\mu_l > \sigma_l$ **then**
      $\mu_l \leftarrow 0.95\mu_l$
    end if
    $(\boldsymbol{r}_k^l)_{1\le k\le K_l}, (\boldsymbol{b}_k^l)_{1\le k\le K_l'}, (\boldsymbol{n}_k^l)_{1\le k\le K_l'} \leftarrow \text{sample}(\partial\Omega, dx, \sigma_l, \mu_l)$
    $(\alpha_k^l)_{1\le k\le K_l} \leftarrow \text{solve}(\mathfrak{K}_l^{\text{ref}}, (\boldsymbol{r}_k^l), (\boldsymbol{b}_k^l), (\boldsymbol{n}_k^l))$
    $e \leftarrow \text{evaluate\_error}(\mathfrak{K}_l^{\text{ref}}, \partial\Omega, (\alpha_k^l), (\boldsymbol{r}_k^l), 0.8\mu_l)$
  end while
end for

each wave number we proceed to sample the real and virtual boundary to get the source locations, the collocation points, and the corresponding normal vectors. We then evaluate the error on the boundary conditions, and we reduce the spacings until the error reaches a certain threshold. For Robin boundary conditions, we consider the following relative error for the $l-$th reference frequency:

$$e_l = \frac{\sqrt{\sum_{j=1}^{N^{\text{err}}} \left| (\partial_{\boldsymbol{n}} + i\mathfrak{K}_l^{\text{ref}}\beta) \left(G_{\boldsymbol{r}^{\text{src}}}^{\mathfrak{K}_l^{\text{ref}}}(\boldsymbol{b}_j^{\text{err}}) + \sum_{k=1}^{K_l} \alpha_k^l G_{\boldsymbol{r}_k^l}^{\mathfrak{K}_l^{\text{ref}}}(\boldsymbol{b}_j^{\text{err}}) \right) \right|^2}}{\sqrt{\sum_{j=1}^{N^{\text{err}}} \left| (\partial_{\boldsymbol{n}} + i\mathfrak{K}_l^{\text{ref}}\beta) G_{\boldsymbol{r}^{\text{src}}}^{\mathfrak{K}_l^{\text{ref}}}(\boldsymbol{b}_j^{\text{err}}) \right|^2}}, \tag{6.1}$$

where the $\boldsymbol{b}_j^{\text{err}}$ are located on the boundary and are distinct from the collocation points, and the α_k^l are the coefficients in the MFS approximation for the reference wave number $\mathfrak{K}_l^{\text{ref}}$. In practice, to reduce the number of parameters, only one collocation spacing μ is used and is chosen to be lower than the last source spacing σ_L. The initial source spacings σ_l, $1 \le l \le L$ and error threshold ε can be set depending on the accuracy required.

For a given wave number $\mathfrak{K}$ such that $\mathfrak{K}_l^{\text{ref}} < \mathfrak{K} \le \mathfrak{K}_{l+1}^{\text{ref}}$, we then use the reference collocation points $(\boldsymbol{b}_k^{l+1})_{1\le k\le K_{l+1}}$ and source locations $(\boldsymbol{r}_k^{l+1})_{1\le k\le K_{l+1}}$ to solve the Helmholtz equation at that particular frequency. We use the *NumPy* least-squares function to solve the system. Moreover, the solutions for different wave numbers are computed in parallel using the *multiprocessing* package.

The number of corner particular solutions in the enriched basis (see Section 5.2.2) is easier to set. Indeed, numerical experiments (supported by the claims in [14]) showed that only a handful of corner

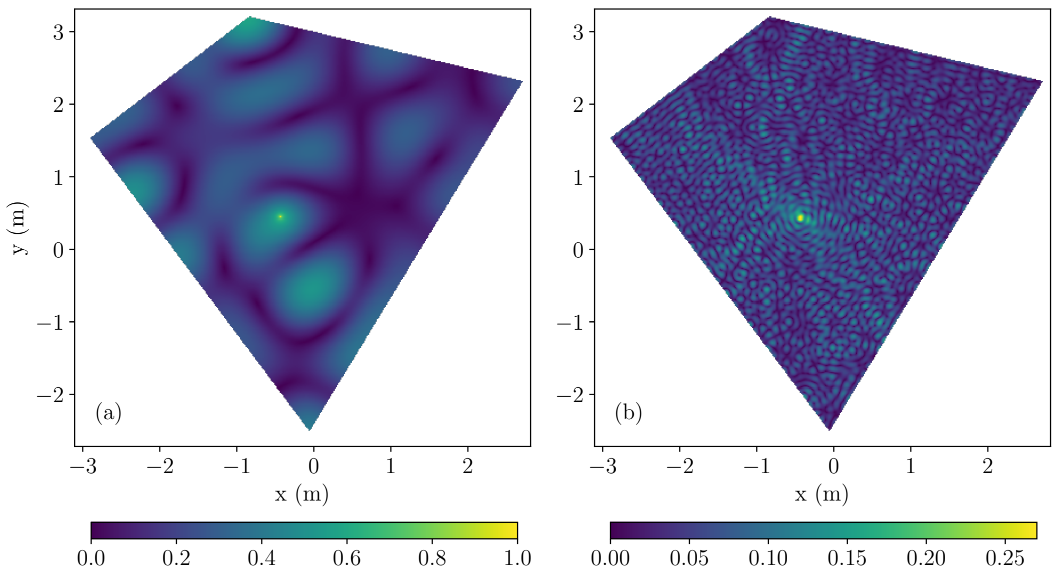

Figure 6.2: Numerical solution of the Helmholtz equation at frequencies 200 Hz (a) and 2000 Hz (b) obtained using respectively 51 and 492 virtual sources, and 1034 collocation points on the boundary.

functions per vertex were necessary to dampen the numerical instabilities. As the number of corner functions usually remains well under the number of virtual sources, adding a few basis functions has a relatively low cost. Hence, we use 20 particular solutions per corner in all experiments. Fig. 6.2 gives an example of resolution for $f = 200$ Hz and $f = 2000$ Hz using respectively 51 and 492 virtual sources, and 20 corner functions per vertex. The perimeter of the polygon is approximately 16.84 m, which corresponds to sampling around 6 sources per wavelength on the virtual boundary. This yields relative errors of the order of 10^{-6}.

6.2 Numerical validation of the MFS implementation

6.2.1 Rectangular domain

We first test the implementation on a rectangular domain $\Omega = [0, L_x] \times [0, L_y]$ which only contains regular corners, where $L_x = 5.2$ m and $L_y = 3.3$ m. In the case of Neumann boundary conditions, the analytical solution is given by its eigenmode decomposition as expressed in Corollary 4.1.1. We estimate this sum numerically by doing a truncation, and compare the result with the MFS simulations. We compute the relative L^2 error between the MFS approximation and the truncation of the exact series, which is defined as the L^2 norm of the difference between the two solutions divided by the L^2 norm of the reference solution. Fig. 6.3 gives the convergence of the approximated solution to the exact solution in L^2 norm when the number of virtual sources increases for different simulated frequencies. The series defining the analytical solution was truncated up to order $N = 10,000$ for

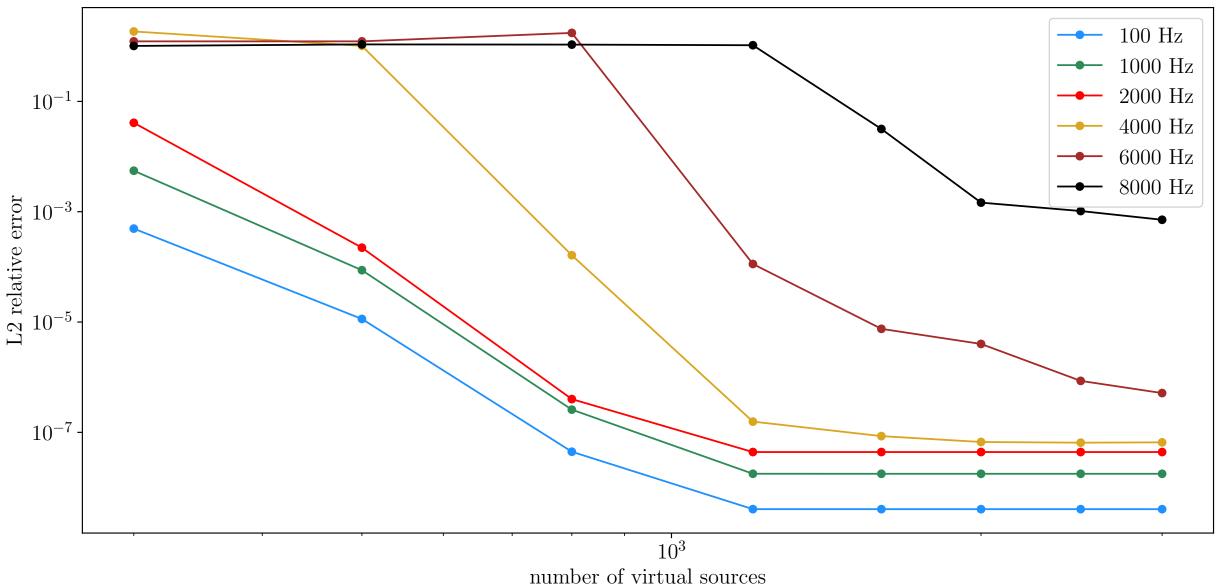

Figure 6.3: Relative L^2 error between the MFS approximation and the truncation of the exact modal decomposition series as a function of the number of virtual sources for a rectangular domain. The series is truncated at order $N = 10,000$, and we consider a square system in the MFS.

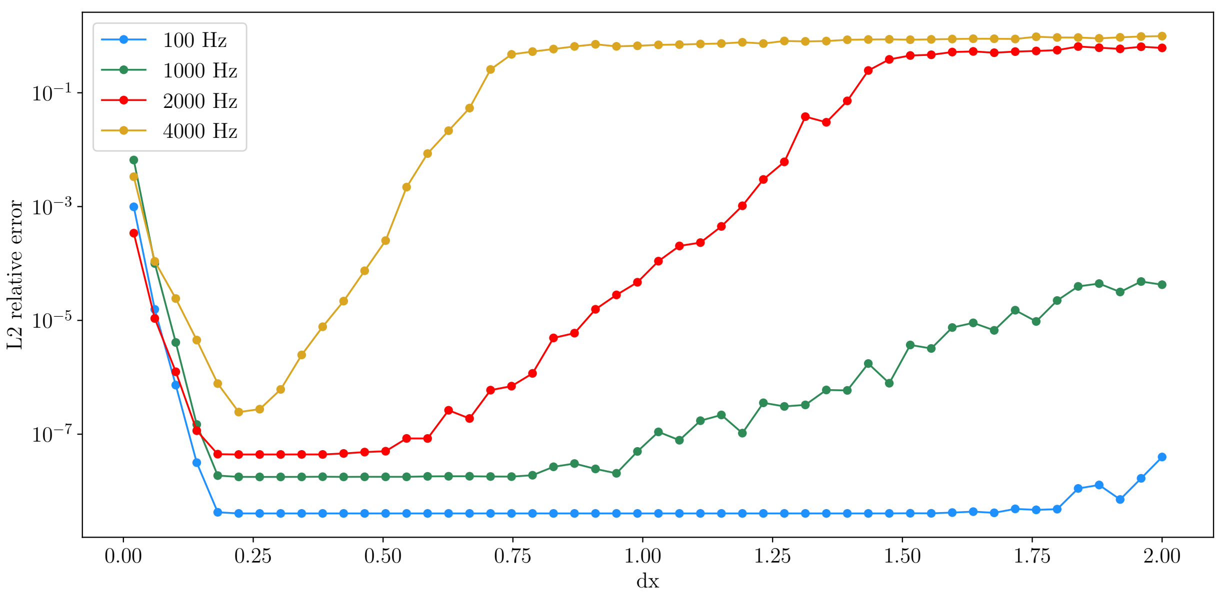

Figure 6.4: Relative L^2 error between the MFS approximation and the truncation of the exact modal decomposition series as a function of the shift dx between the real and virtual boundary for a rectangular domain (1000 virtual sources, 1200 boundary points)

the numerical solution. The MFS approximation seems to converge quickly to the exact solution for lower frequencies, higher frequencies requiring more virtual sources in order to have an accurate numerical solution. Note that at low frequencies the error reaches a plateau and remains stable when the number of sources is high. This can be explained by a predominance of the truncation error of the series, whilst the MFS approximation continues to converge towards the exact solution. The number of virtual sources exactly matches the number of boundary points in that figure, however in practice we will often consider over-determined systems, *i.e.* more boundary points than sources.

As mentioned previously, the choice of the distance parameter dx has an impact on the quality of the resolution. Fig. 6.4 shows the dependence on this parameter for this particular geometry. The optimal shift depends on the frequency, lower frequencies being more permissive in the range of adequate shifts. It would be possible to adapt this shift for every simulated frequency and geometry, however in practice we will empirically set $dx = 0.3$ in all experiments unless mentioned otherwise.

6.2.2 Polygonal domain

We then test the MFS on an arbitrary polygonal domain containing singular corners with complex Robin boundary conditions. We compare the results with FEM simulations as no analytical solution is available in this case. Fig. 6.5 shows an example of Helmholtz resolution using FreeFem++ and the MFS on the polygonal test case.

In order to reduce the computational cost of the FEM resolution we limit the maximal testing frequency to 1000 Hz. Fig. 6.6 presents the L^2 error between the FreeFem++ and MFS numerical solutions. We see a steady decline of the error as the number of virtual sources increases, followed

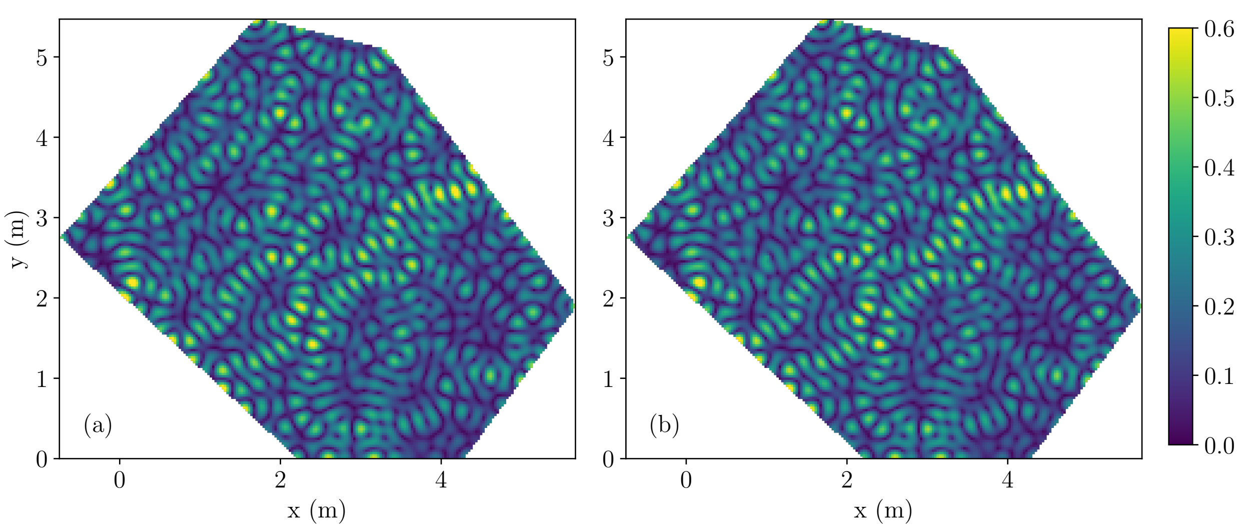

Figure 6.5: (a) FreeFem++ approximation (b) MFS approximation (300 virtual sources and boundary points, 20 corner functions per vertex) at 1000 Hz for Robin boundary conditions ($\beta = 0.01$).

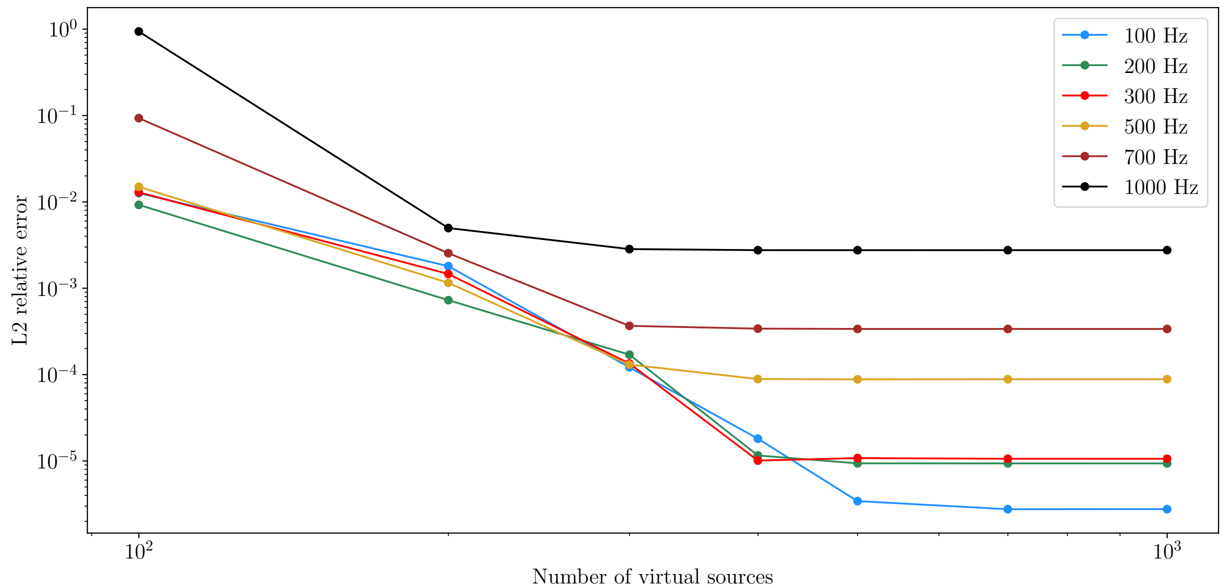

Figure 6.6: Relative L^2 error between the MFS and FreeFem++ approximations as a function of the number of virtual sources for the polygonal domain depicted in Fig. 6.5.

by a plateau. Once again, the plateau is likely due to the approximation error of the FEM solution. Note that the plateau is reached sooner for high frequencies, as the number of elements in the FEM mesh is fixed and more elements are needed for an accurate resolution at higher frequencies.

Fig. 6.7 highlights the numerical instabilities that appear in the presence of singular corners. The blue curve represents the Robin boundary condition induced by the virtual sources on each edge, *i.e.* $(\partial_{\boldsymbol{n}} + i\mathfrak{K}\beta)\sum_{j=1}^{K}\alpha_j G^{\mathfrak{K}}_{\boldsymbol{r}_j}$ using the notations of Section 5.2.2. The orange curve depicts the source contribution $-(\partial_{\boldsymbol{n}} + i\mathfrak{K}\beta)G^{\mathfrak{K}}_{\boldsymbol{r}_{\mathrm{src}}}$. Significantly increasing the number of boundary points or virtual sources does not reduce the oscillations, however adding a few corner eigenfunctions to the approximation counteracts these issues, as illustrated in Fig. 6.8. Note that, as the quality of the resolution only depends on the approximation of the boundary conditions, a near-perfect approximation as represented in Fig. 6.8 ensures an accurate numerical solution inside the domain.

Remark 6.2.1. The appearance of the plateau in the error curves could be delayed by improving the accuracy of the reference solution, either by increasing the number of modal terms in the expansion in the previous section, or by refining the FEM mesh here. Such improvements would enable a more precise assessment of the convergence rate of the MFS but at a significantly higher computational cost, particularly for high-frequency FEM simulations. Since the aim of these experiments is only to validate the MFS implementation, we will not pursue this direction further.

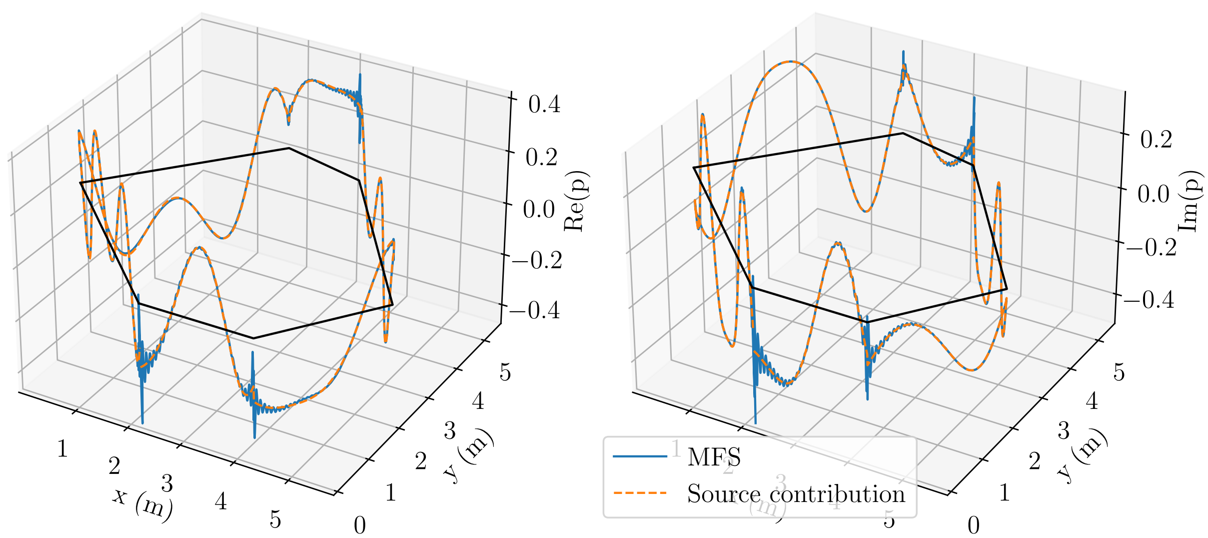

Figure 6.7: Real and imaginary parts of the MFS approximation of the boundary conditions without corner eigenfunctions (500 virtual sources, 700 boundary points, $f = 375$ Hz)

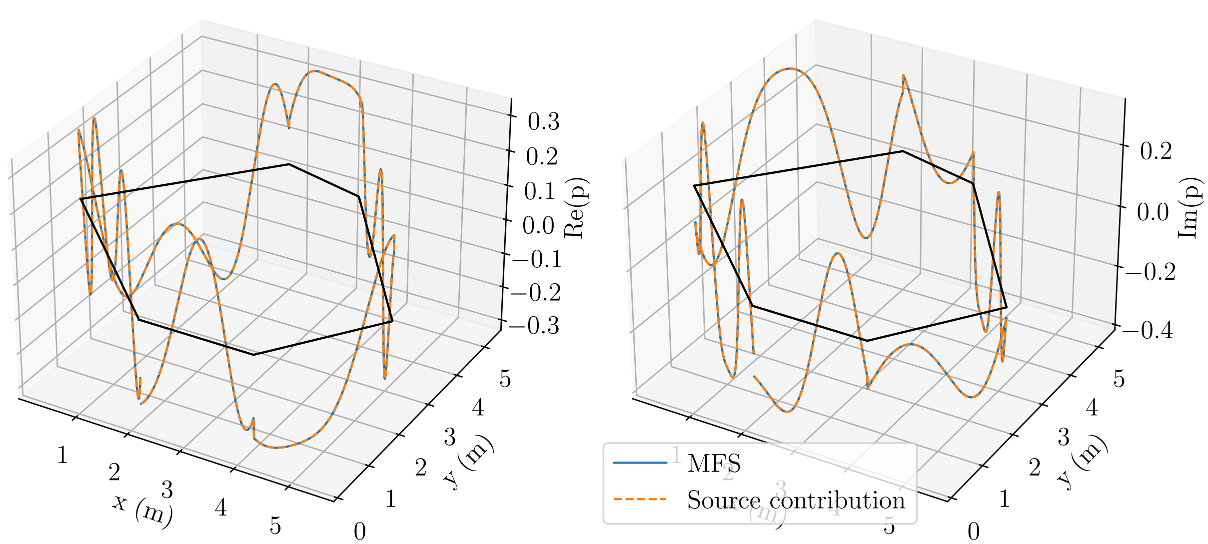

Figure 6.8: Real and imaginary parts of the MFS approximation of the boundary conditions with 20 corner eigenfunctions per vertex (500 virtual sources, 700 boundary points, $f = 375$ Hz)

6.2.3 Eigenvalues of the Laplacian

This section addresses the resolution issues caused by the eigenvalues of the Laplacian, also called resonant frequencies or eigenfrequencies in acoustics. Recall that an eigenvalue of the Laplacian is a frequency for which there exists a non-zero solution of the associated homogeneous Helmholtz equation for given boundary conditions. The resonant frequencies and corresponding eigenmodes for a rectangular domain with Neumann boundary conditions are given by (4.1), but are usually unknown for general domains. Fig. 6.9 highlights the ill-conditioning of the MFS system on a rectangular domain with Neumann boundary conditions by plotting the smallest singular value of the MFS system matrix as a function of the frequency.

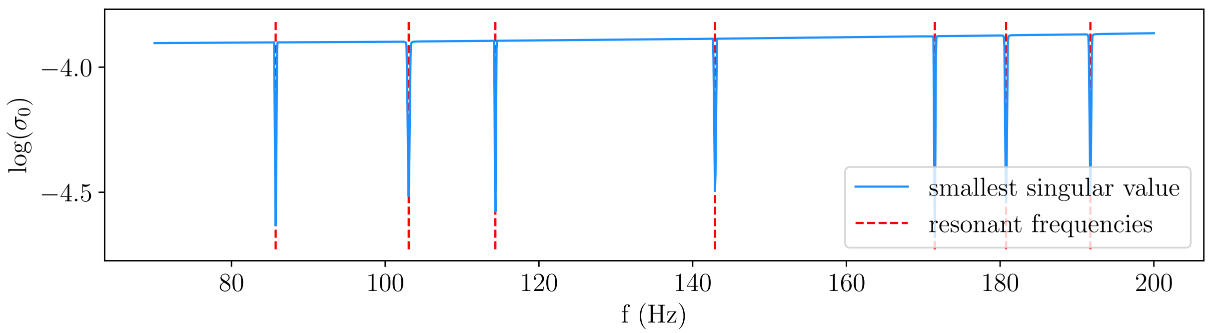

Figure 6.9: Exact resonant frequencies for the Neumann boundary conditions against the smallest singular value σ_0 of the MFS system for a 3×2 rectangle, 150 virtual sources and 200 collocation points.

Consider the resolvent of the Neumann-Laplacian, *i.e.* the linear operator $T : L^2(\Omega) \to \{u \in H^1(\Omega),\ \int_\Omega u = 0\}$ that maps a source term f to the solution u of $-\Delta u = f$ with zero mean satisfying Neumann boundary conditions. T is self-adjoint and compact [47], and its eigenvalues μ_l are the inverses of the Laplacian eigenvalues λ_l. Indeed, let $\mu > 0$ be an eigenvalue for T. We have:

$$u \coloneqq Tf = \mu f = -\mu \Delta u \iff -\Delta u = \frac{1}{\mu} u. \tag{6.2}$$

We can then apply the Fredholm alternative [26]. Let $\widetilde{T} = \frac{1}{\mu} T$, the equation $f - \widetilde{T} f = g$ is solvable if and only if $g \in \operatorname{Ker}\left(\operatorname{Id} - \widetilde{T}\right)^{\perp}$. This kernel is finite-dimensional, and its dimension is the multiplicity of the associated eigenvalue $\lambda = \frac{1}{\mu}$. Formally, in our case $g = -\delta_{r^{\mathrm{src}}}$, and the orthogonality constraints become: $u(\boldsymbol{r}^{\mathrm{src}}) = 0$ for every λ-eigenfunction u. In other words, if $\mathfrak{K}$ corresponds to an eigenfrequency, the associated Helmholtz equation with a Dirac source term located at $\boldsymbol{r}^{\mathrm{src}}$ is ill-posed if $\boldsymbol{r}^{\mathrm{src}}$ is not located on the nodal set for this wave number. In practice, numerical instabilities are observed when the simulated frequency is chosen too close to an eigenfrequency. For the case of Neumann boundary conditions, the resonant frequencies are real and positive, and have a distribution that makes computing the MFS solution on a large frequency range intractable. Indeed, if we denote by $N(\mathfrak{K})$ the number of eigenvalues of the Neumann-Laplacian that are less than $\mathfrak{K}$, we have the asymptotics [152]:

$$N(\mathfrak{K}) \underset{\mathfrak{K}\to\infty}{=} \mathcal{O}(\mathfrak{K}^{d/2}) \tag{6.3}$$

in the case of a $d-$dimensional smooth boundary, which implies a linear growth in the number of eigenfrequencies with regard to the frequency in $2D$. See also [75] for an overview of the properties of Laplace eigenvalues.

Remark 6.2.2. These issues render the MFS impractical for shape optimization, as the resonant frequencies of the domain are unknown at each optimization step. However, Neumann boundary conditions are never encountered in the real world, as surfaces absorb and transmit some of the sound energy. We will consider admittance boundary conditions in numerical applications, *i.e.* complex Robin boundary conditions. These issues do not arise in that case as long as the admittance coefficient has a non-zero real part, because the corresponding resonant frequencies are not located on the real line.

6.3 Wave equation simulations using the MFS

We describe here how we can simulate time-domain room impulse responses with impedance boundary conditions using the frequency-domain MFS. Recall that the Helmholtz equation can be obtained by applying a Fourier transform to the wave equation and the associated boundary conditions. We then have a simple framework to compute solutions of the wave equation at a given location $\boldsymbol{r}^{\text{mic}}$:

1. Pick a maximum frequency $f_{\max}$ and a number of frequencies n_f. Let $\mathfrak{K}_n = \frac{2\pi n f_{\max}}{c n_f}$, $0 \leq n \leq n_f$.

2. Solve the Helmholtz equation with Robin boundary conditions at location $\boldsymbol{r}^{\text{mic}}$ for every $\mathfrak{K}_n$, $0 < n \leq n_f$ and store the results in a vector $\tilde{\boldsymbol{u}}$ with $\tilde{u}_0 = 0$.

3. Apply a high-pass filter to $\tilde{\boldsymbol{u}}$.

4. Apply a real inverse Discrete Fourier Transform (DFT) to $\tilde{\boldsymbol{u}}$ to get the discrete time signal $\boldsymbol{u}$.

The resulting vector $\boldsymbol{u}$ contains an approximation of the time response between $t_0 = 0$ and $t_{\max} = \frac{n_f}{f_{\max}}$. Note that $t_{\max}$ must be high enough, so that $p(\boldsymbol{r}^{\text{mic}}, t_{\max}) \approx 0$, *i.e.* the time signal has a finite duration. Setting $\tilde{u}_0$ amounts to choosing a normalization for the RIR, as it equals the mean value of the signal. In the absence of a high-pass filter, low-frequency effects are visible in the signals and the obtained RIR are non-physical. Common impedance models, such as the Delany-Bazley-Miki model for porous media [113] are not valid for low frequencies. Intuitively, this limitation arises because certain assumptions in such models become invalid when the wave length is large relative to the dimensions of the room, thus motivating the need for a high-pass filter.

To get an estimate of the computational cost, we consider the following test case: we solve the Helmholtz equation on a 4.5×2.3m rectangle at 3000 frequencies uniformly sampled between 0 and 4 kHz, using 478 virtual sources and 1352 collocation points. With a simple parallel implementation, the simulation takes around 11 minutes using 64 cores split in 16 batches of 4 cores. A single frequency simulation takes between 1 and 2 seconds on 4 cores, meaning that a significant amount of time is lost on the parallelization overhead. This could be improved upon, as each frequency simulation is independent of the others. Once the coefficients are computed, evaluating the time signal at a single location takes less than 1 second. Note that Step 2 can be further sped up by using the adaptive sampling strategy described in Alg. 5.

Remark 6.3.1. A major advantage of working in the frequency domain is to avoid handling the time convolution in the boundary condition (13), as it transforms into a frequency-wise product after applying the Fourier transform.

We perform two time simulations on a polygon by solving the Helmholtz equation at $n_f = 4000$ frequencies up to $f_{\max} = 4$ kHz, which corresponds to a total simulation time $t_{\max} = 1$ s. We also apply a fourth-order Butterworth high-pass filter at 50 Hz. Figure 6.10 represents two RIRs simulated at a fixed location $\boldsymbol{r}^{\text{mic}}$ on a polygonal domain, respectively by applying the Delany-Bazley-Miki

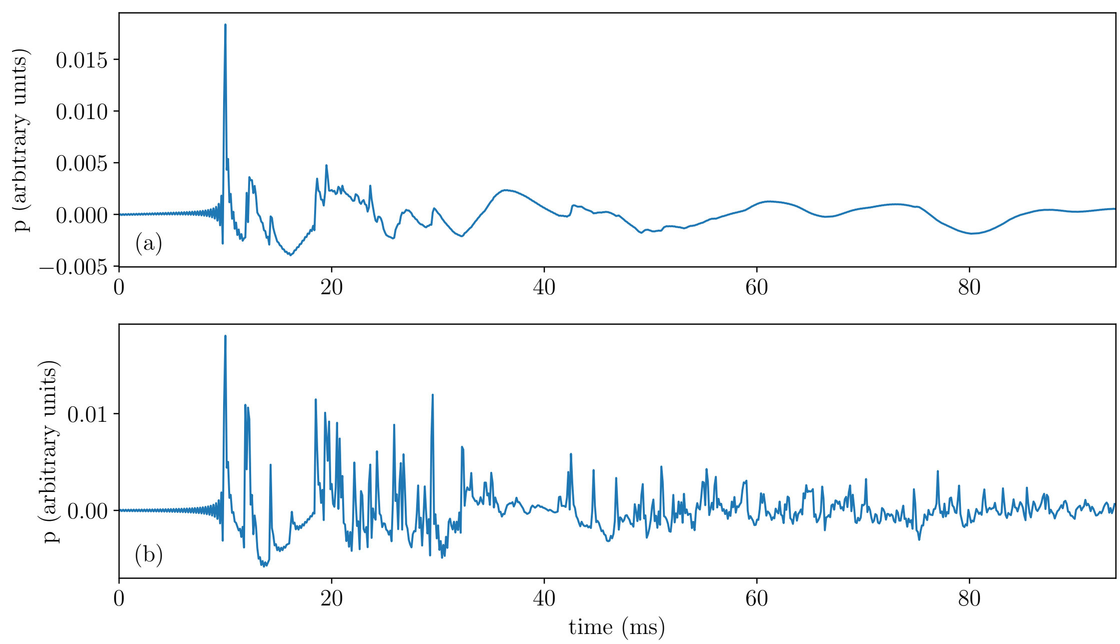

Figure 6.10: RIRs computed at location $\boldsymbol{r}^{\text{mic}} = (3.75, 0.5)$ using the MFS on the polygonal domain represented in Fig. 6.11 and 6.12. (a) uses Delany-Bazley-Miki to model β with the static air flow resistivity $\sigma = 20000$ N.s.m^{-4} and the thickness $h = 10$ cm, whilst (b) uses a constant coefficient $\beta = 0.1$.

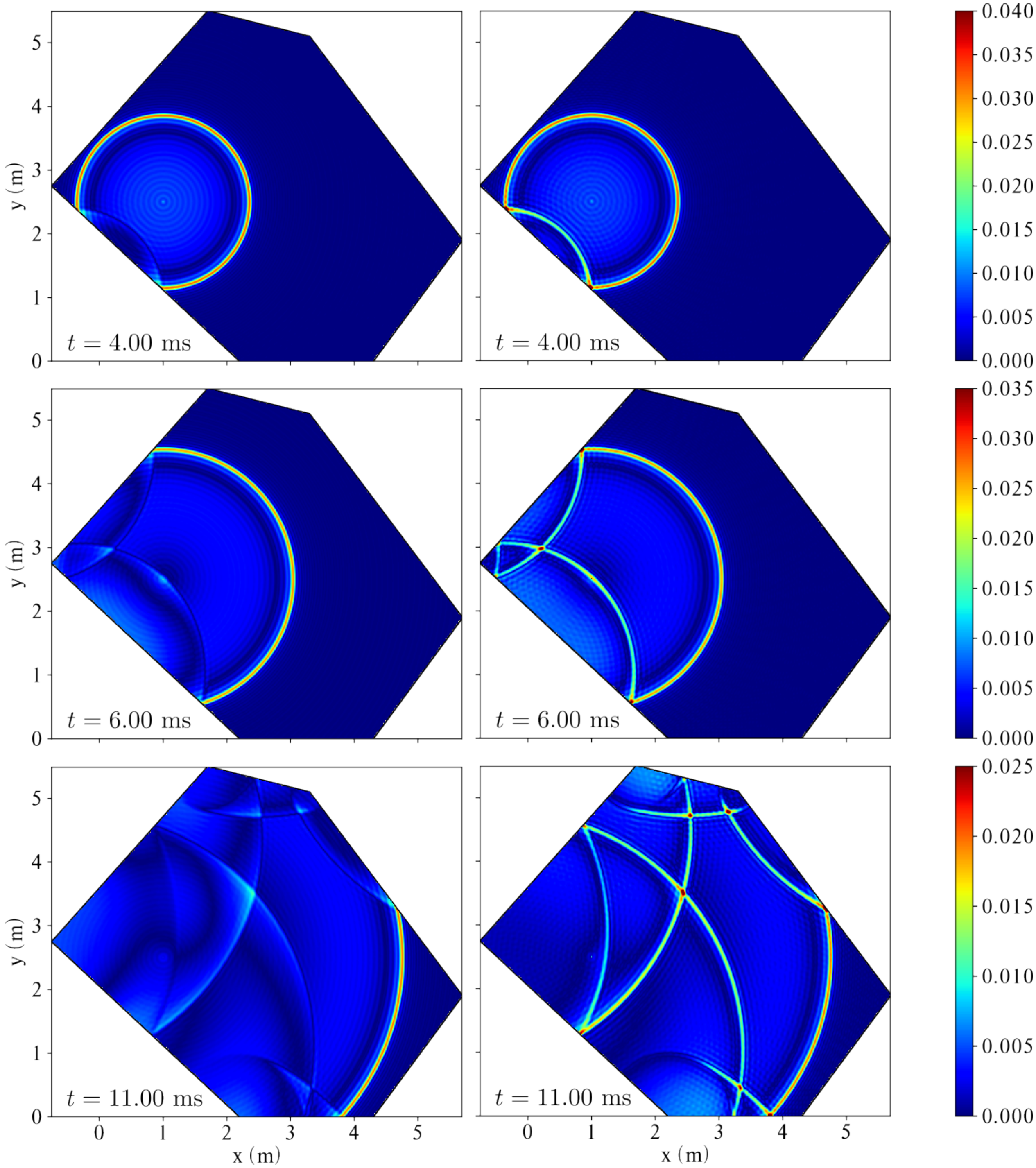

Figure 6.11: Absolute value of the pressure field in arbitrary units computed using the MFS. On the left we use the Delany-Bazley-Miki model for β with the static air flow resistivity $\sigma = 20000$ N.s.m^{-4} and the thickness $h = 10$ cm, and on the right $\beta = 0.1$ is constant.

model to compute the impedance and by taking a constant value for β. Fig. 6.11 gives some snapshots of the associated wave propagation

The early specular reflections are clearly visible in the time signals, however the echoes are considerably damped in the case of the porous model. In both cases the simulated RIRs are very different from those produced by the image source model, such as those presented in Fig. 4b. This is partially caused by the fact that we consider 2-dimensional simulations here, rather than the 3D model of the first part.

However, we can also observe phenomena that would not be represented by the basic extensions of the ISM to non-rectangular domains as the one presented in [22]. In particular, Fig. 6.12 illustrates that in the case of an occlusion, *i.e.* an image-source that would not be observable from a given measurement point, a reflection is still visible. On this figure, the first order image-source $\boldsymbol{r}_1$ is not visible above the red line, as the corresponding specular reflection would occur outside the room, but a perturbed wavefront still propagates in the occlusion zone. Note that this wavefront is circular with its center located at the vertex delimiting two walls, as if an image-source was emitting a wave from the corner. Such a phenomenon cannot be accounted for by the image-source method. Although the damping effect of the frequency-dependent model used for β is particularly visible on the left figures, the specular reflections are still noticeable. We can also observe some resolution artifacts. These artifacts are probably caused by the application of the inverse DFT. Increasing the

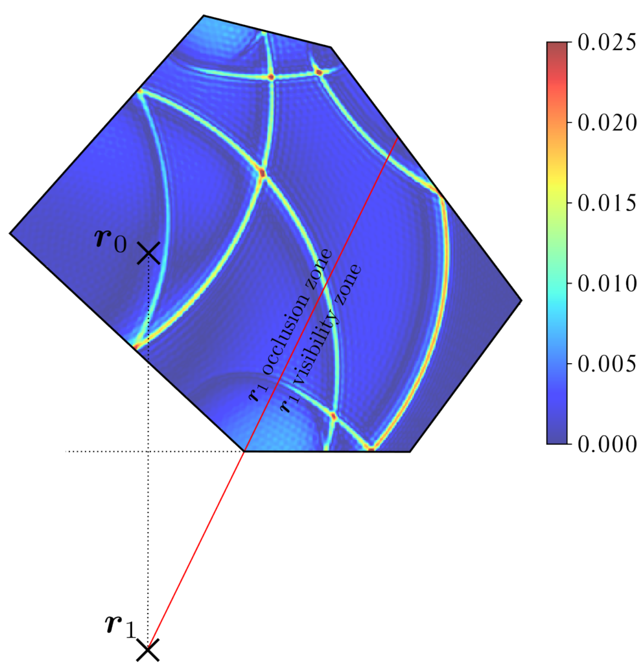

Figure 6.12: Absolute value of the pressure field after 11 ms for $\beta = 0.1$ (see Fig. 6.11). $\boldsymbol{r}_0$ is the source location, $\boldsymbol{r}_1$ is the first order image-source location corresponding to the bottom wall. The occlusion boundary for $\boldsymbol{r}_1$ is represented in red.

maximum simulated frequency and the maximum time can contribute to reduce the errors linked to the Fourier transform. Besides, the impact of the accuracy of the frequency-domain solutions on the resulting time-domain signals has not been studied extensively, and increasing the number of virtual sources and boundary points could improve the results.

6.4 Conclusion

We have described our implementation of the MFS for the resolution of the Helmholtz equation with a Dirac source term on a polygonal domain. The method demonstrates a good computational efficiency when compared to the FEM simulations, and is able to handle higher frequencies. This ability to simulate high frequencies is then leveraged to compute time-domain RIRs, revealing a more complex behavior than the one predicted by the image-source model.

Chapter 7

2D Shape optimization for room reconstruction

We introduce in this chapter a formulation of the room shape recovery inverse problem in 2D as a shape optimization problem on polygons. We compute the corresponding shape derivative, and define a shape gradient descent algorithm. Finally, we evaluate the algorithm on a set of randomly generated polygons.

7.1 Shape optimization formulation

We consider in this part a bounded, convex, polygonal domain $\Omega \subset \mathbb{R}^2$. Similarly to Part I, we will consider low-pass filtered, discrete measurements of the pressure field in order to reconstruct the geometry. Unlike in Part I, we place ourselves in the frequency-domain, and formalize the problem as an optimization problem on the shape Ω. We thus consider the following optimization problem:

$$\min_{\Omega \in \mathcal{S}_{\text{adm}}} J(\Omega), \quad J(\Omega) \coloneqq \frac{1}{2LM} \sum_{l=1}^{L} \sum_{m=1}^{M} \left| p_{\Omega,\mathfrak{K}_l}(\boldsymbol{r}_m^{\text{mic}}) - p_{\text{obs},\mathfrak{K}_l}(\boldsymbol{r}_m^{\text{mic}}) \right|^2 \tag{7.1}$$

where $\mathcal{S}_{\text{adm}}$ is the set of admissible shapes defined below, $p_{\text{obs},\mathfrak{K}}$ is the observed pressure field at wave number $\mathfrak{K}$, and $p_{\Omega,\mathfrak{K}}$ is a compact notation for the solution of the Helmholtz equation on Ω with Robin boundary conditions:

$$\begin{cases} \Delta p + \mathfrak{K}^2 p = -\delta_{\boldsymbol{r}^{\text{src}}} & \text{in } \Omega \\ \partial_{\boldsymbol{n}} p + i\mathfrak{K}\beta p = 0 & \text{on } \partial\Omega, \end{cases} \tag{7.2}$$

which admits the following variational formulation:

$$\int_{\Omega} \nabla p_{\Omega,\mathfrak{K}} \cdot \nabla \overline{\varphi} - \mathfrak{K}^2 p_{\Omega,\mathfrak{K}} \overline{\varphi} + i\mathfrak{K}\beta \int_{\partial\Omega} p_{\Omega,\mathfrak{K}} \overline{\varphi} = \overline{\varphi(\boldsymbol{r}^{\text{src}})} \quad \forall \varphi \in H^1(\Omega). \tag{7.3}$$

We consider here that β is constant on each wall, and real valued. The source location $\boldsymbol{r}^{\text{src}}$ and the microphone positions are assumed to be known and contained inside Ω. $\mathcal{S}_{\text{adm}}$ is the set of convex polygons that contain the microphone positions $\boldsymbol{r}_m^{\text{mic}}$ and the source location $\boldsymbol{r}^{\text{src}}$, with a fixed number of vertices S.

Remark 7.1.1. In practical on-site acoustic measurements, the range of available frequencies is limited. In particular, the very-low frequencies (typically < 50 Hz) cannot be accurately recorded, and similarly high frequencies are inaccessible. Moreover, the impedance model becomes invalid as the frequency drops and the wave length grows larger relative to the size of the room. This issue will be addressed in the numerical section.

7.2 Shape derivative

7.2.1 Introduction

In the following, we will consider a single wave number $\mathfrak{K}$ in the expression of the objective function J defined in (7.1). The full expression can be obtained by linearity by adding the derivative for each wave number. Using the notations of Section 5.1.2, it is straightforward to compute formally an expression of the shape derivative:

$$DJ(\Omega)\cdot V = \frac{1}{M}\sum_{m=1}^{M} p'_{\Omega,\mathfrak{K}}(\boldsymbol{r}_m^{\mathrm{mic}})\left(p_{\Omega,\mathfrak{K}}(\boldsymbol{r}_m^{\mathrm{mic}}) - p_{\mathrm{obs},\mathfrak{K}}(\boldsymbol{r}_m^{\mathrm{mic}})\right). \tag{7.4}$$

However, this formula is not usable in practice, as we cannot access the values of the Eulerian derivative of the pressure field $p'_{\Omega,\mathfrak{K}}$. We will instead use the boundary formulation given in the following theorem.

Theorem 7.2.1. *Let $\Omega \in \mathcal{S}_{adm}$ be a convex polygon, and $V \in W^{1,\infty}(\mathbb{R}^2,\mathbb{R}^2)$ be a vector field such that V vanishes in a neighborhood of $\boldsymbol{r}^{src}$ and $\boldsymbol{r}_m^{mic}$, $1 \le m \le M$. Let $p_{\Omega,\mathfrak{K}}$ be the solution of the Helmholtz equation (7.2) on Ω, and $q_{\Omega,\mathfrak{K}}$ be the solution of the adjoint system:*

$$\begin{cases} \Delta q_{\Omega,\mathfrak{K}} + \mathfrak{K}^2 q_{\Omega,\mathfrak{K}} = \frac{1}{M}\sum_{m=1}^{M}\left(p_{\Omega,\mathfrak{K}}(\boldsymbol{r}_m^{mic}) - p_{obs,\mathfrak{K}}(\boldsymbol{r}_m^{mic})\right)\delta_{\boldsymbol{r}_m^{mic}} & \text{in } \Omega \\ \partial_{\boldsymbol{n}} q_{\Omega,\mathfrak{K}} - i\mathfrak{K}\beta q_{\Omega,\mathfrak{K}} = 0 & \text{on } \partial\Omega. \end{cases} \tag{7.5}$$

Then the shape derivative of the cost function J in direction V satisfies:

$$DJ(\Omega)\cdot V = \int_{\partial\Omega}(V\cdot\boldsymbol{n})\,\mathrm{Re}\left[\nabla p_{\Omega,\mathfrak{K}}\cdot\nabla\overline{q_{\Omega,\mathfrak{K}}} + \mathfrak{K}^2(2\beta^2-1)p_{\Omega,\mathfrak{K}}\overline{q_{\Omega,\mathfrak{K}}}\right] \tag{7.6}$$

$$+\sum_{s=1}^{S}(\boldsymbol{\tau}_{s-1}-\boldsymbol{\tau}_s)\cdot V(\boldsymbol{v}_s)\,\mathrm{Re}[i\mathfrak{K}\beta\, \mathrm{p}_{\Omega,\mathfrak{K}}(\boldsymbol{v}_s)\overline{q_{\Omega,\mathfrak{K}}(\boldsymbol{v}_s)}] \tag{7.7}$$

where $\boldsymbol{\tau}_s$ denotes the unit vector tangent to the edge $\boldsymbol{v}_s\boldsymbol{v}_{s+1}$, and $\boldsymbol{\tau}_0 = \boldsymbol{\tau}_S$.

Remark 7.2.1. Note that we can remove the singularities from the source term of the PDE by considering an equivalent system. Indeed, writing $\widetilde{p}_{\Omega,\mathfrak{K}} = p_{\Omega,\mathfrak{K}} - G^{\mathfrak{K}}_{\boldsymbol{r}^{\mathrm{src}}}$ where $G^{\mathfrak{K}}_{\boldsymbol{r}^{\mathrm{src}}}$ is a free-field Green's function located at the source, $\widetilde{p}_{\Omega,\mathfrak{K}}$ satisfies a homogeneous Helmholtz equation with non-homogeneous boundary conditions:

$$\begin{cases} \Delta\widetilde{p}_{\Omega,\mathfrak{K}} + \mathfrak{K}^2\widetilde{p}_{\Omega,\mathfrak{K}} = 0 & \text{in } \Omega \\ \partial_{\boldsymbol{n}}\widetilde{p}_{\Omega,\mathfrak{K}} + i\mathfrak{K}\beta\widetilde{p}_{\Omega,\mathfrak{K}} = -(\partial_{\boldsymbol{n}} G^{\mathfrak{K}}_{\boldsymbol{r}^{\mathrm{src}}} + i\mathfrak{K}\beta G^{\mathfrak{K}}_{\boldsymbol{r}^{\mathrm{src}}}) & \text{on } \partial\Omega \end{cases} \tag{7.8}$$

where $G^{\mathfrak{K}}_{\boldsymbol{r}^{\mathrm{src}}}$ is singular at the source location, but regular elsewhere (and in particular at the boundary). The same reasoning can be applied to $q_{\Omega,\mathfrak{K}}$ by considering a combination of Green's functions located at the microphones' positions. For Neumann boundary conditions and a convex domain, *i.e.* $\beta = 0$, $\widetilde{p}_{\Omega,\mathfrak{K}}$ belongs to $H^2(\Omega)$ by elliptic regularity [76]. We will assume in the following that the same regularity holds in the case of complex Robin boundary conditions. $p_{\Omega,\mathfrak{K}}$ and $q_{\Omega,\mathfrak{K}}$ are then the sum of a regular function, and a function containing discrete singularities located inside Ω.

We will use the Cea formal differentiation approach introduced originally in [34] and a tensor representation as described in [103] to obtain a usable expression of the shape derivative $DJ(\Omega)\cdot V$.

To this aim, let us introduce the Lagrangian functional $\mathcal{L}$ defined by

$$\mathcal{L}(\widetilde{\Omega}, \varphi, \psi) = \frac{1}{2M} \sum_{m=1}^{M} |\varphi(\boldsymbol{r}_m^{\text{mic}}) - p_{\text{obs}}(\boldsymbol{r}_m^{\text{mic}})|^2 + \text{Re}\left(-\overline{\psi(\boldsymbol{r}^{\text{src}})} + \int_{\widetilde{\Omega}} (\nabla\varphi \cdot \nabla\overline{\psi} - \mathfrak{K}^2 \varphi\overline{\psi}) \right) \tag{7.9}$$

$$+ \text{Re}\left(i\mathfrak{K}\beta \int_{\partial\widetilde{\Omega}} \varphi\overline{\psi} \right). \tag{7.10}$$

$\mathcal{L}$ is obtained by summing the objective function and the weak formulation of the PDE verified by $p_{\Omega,\mathfrak{K}}$.

The strategy used to compute the shape derivative is the following:

1. Establish the equation verified by the adjoint state $q_{\Omega,\mathfrak{K}}$, which is defined by:

$$\partial_\varphi \mathcal{L}(\Omega, p_{\Omega,\mathfrak{K}}, q_{\Omega,\mathfrak{K}})(\widetilde{\varphi}) = 0, \quad \forall \widetilde{\varphi} \in H^1(\Omega). \tag{7.11}$$

2. Apply a change of variable to express the integrals on Ω instead of Ω_ε and consider:

$$\mathcal{G}(\varepsilon, p_{\Omega,\mathfrak{K}}, q_{\Omega,\mathfrak{K}}) := \mathcal{L}(\Omega_\varepsilon, p_{\Omega,\mathfrak{K}} \circ T_\varepsilon^{-1}, q_{\Omega,\mathfrak{K}} \circ T_\varepsilon^{-1}), \tag{7.12}$$

   where $T_\varepsilon := \text{Id} + \varepsilon V$.

3. Find a volumetric expression of the shape derivative by using the relation

$$DJ(\Omega) \cdot V = \partial_\varepsilon \mathcal{G}(0, p_{\Omega,\mathfrak{K}}, q_{\Omega,\mathfrak{K}}). \tag{7.13}$$

4. Transform this formula using Theorem 5.1.2 to get a boundary expression depending on $p_{\Omega,\mathfrak{K}}$, $q_{\Omega,\mathfrak{K}}$, and $V \cdot \boldsymbol{n}$.

We now proceed with formal calculations using the so-called "Céa method". It is standard in this approach to assume that the expression for the shape derivative is valid under certain regularity assumptions on the functions $\widetilde{p}_{\Omega,\mathfrak{K}}$ and $\widetilde{q}_{\Omega,\mathfrak{K}}$, as described in Remark 7.2.1. A rigorous proof that these regularity assumptions hold in our case will be provided in a forthcoming article. Notably, by ensuring the perturbation field V vanishes near the source and microphone positions, multiplying $p_{\Omega,\mathfrak{K}}$ and $q_{\Omega,\mathfrak{K}}$ by V effectively eliminates the singularities in the computations.

7.2.2 Adjoint state

Equation (7.11) translates to:

$$\text{Re}\left[\int_\Omega (\nabla\widetilde{\varphi} \cdot \nabla\overline{q_{\Omega,\mathfrak{K}}} - \mathfrak{K}^2 \widetilde{\varphi}\overline{q_{\Omega,\mathfrak{K}}})) + i\mathfrak{K}\beta \int_{\partial\Omega} \widetilde{\varphi}\overline{q_{\Omega,\mathfrak{K}}} + \frac{1}{M} \sum_{m=1}^{M} \widetilde{\varphi}(\boldsymbol{r}_m^{\text{mic}})(\overline{p_{\Omega,\mathfrak{K}}(\boldsymbol{r}_m^{\text{mic}}) - p_{\text{obs},\mathfrak{K}}(\boldsymbol{r}_m^{\text{mic}})}) \right] = 0 \tag{7.14}$$

for any $\widetilde{\varphi} \in H^1(\Omega)$. Let $q_{\Omega,\mathfrak{K}} = q_1 + iq_2$, $p_{\Omega,\mathfrak{K}} - p_{\text{obs},\mathfrak{K}} = g_1 + ig_2$, and take $\widetilde{\varphi} = \widetilde{\varphi}_1 + i\widetilde{\varphi}_2$ with $q_1, q_2, g_1, g_2, \widetilde{\varphi}_1, \widetilde{\varphi}_2$ real-valued. Equation (7.14) yields:

$$\int_\Omega (\nabla\widetilde{\varphi}_1 \cdot \nabla q_1 + \nabla\widetilde{\varphi}_2 \cdot \nabla q_2 - \mathfrak{K}^2(\widetilde{\varphi}_1 q_1 + \widetilde{\varphi}_2 q_2)) + \mathfrak{K}\beta \int_{\partial\Omega} (\widetilde{\varphi}_1 q_2 - \widetilde{\varphi}_2 q_1) + \frac{1}{M}\sum_{m=1}^{M} (\widetilde{\varphi}_1 g_1 + \widetilde{\varphi}_2 g_2)(\boldsymbol{r}_m^{\text{mic}}) = 0. \tag{7.15}$$

Setting now $\widetilde{\varphi} = \widetilde{\varphi}_2 - i\widetilde{\varphi}_1$ we get:

$$\int_\Omega (\nabla\widetilde{\varphi}_2 \cdot \nabla q_1 - \nabla\widetilde{\varphi}_1 \cdot \nabla q_2 - \mathfrak{K}^2(\widetilde{\varphi}_2 q_1 - \widetilde{\varphi}_1 q_2)) + \mathfrak{K}\beta \int_{\partial\Omega} (\widetilde{\varphi}_1 q_1 + \widetilde{\varphi}_2 q_2) + \frac{1}{M}\sum_{m=1}^{M} (\widetilde{\varphi}_2 g_1 - \widetilde{\varphi}_1 g_2)(\boldsymbol{r}_m^{\text{mic}}) = 0. \tag{7.16}$$

By considering the combination (7.15) $- i$(7.16), we thus obtain the variational formulation of the complex adjoint equation:

$$\int_\Omega (\nabla q_{\Omega,\mathfrak{K}} \cdot \nabla\overline{\varphi} - \mathfrak{K}^2 q_{\Omega,\mathfrak{K}}\overline{\varphi})) - i\mathfrak{K}\beta \int_{\partial\Omega} q_{\Omega,\mathfrak{K}}\overline{\varphi} + \frac{1}{M}\sum_{m=1}^{M} (p_{\Omega,\mathfrak{K}}(\boldsymbol{r}_m^{\text{mic}}) - p_{\text{obs},\mathfrak{K}}(\boldsymbol{r}_m^{\text{mic}}))\overline{\varphi(\boldsymbol{r}_m^{\text{mic}})} = 0, \quad \forall\varphi. \tag{7.17}$$

In other words, $q_{\Omega,\mathfrak{K}}$ satisfies

$$\begin{cases} \Delta q_{\Omega,\mathfrak{K}} + \mathfrak{K}^2 q_{\Omega,\mathfrak{K}} = \frac{1}{M}\sum_{m=1}^{M} (p_{\Omega,\mathfrak{K}}(\boldsymbol{r}_m^{\text{mic}}) - p_{\text{obs},\mathfrak{K}}(\boldsymbol{r}_m^{\text{mic}}))\delta_{\boldsymbol{r}_m^{\text{mic}}} & \Omega \\ \partial_{\boldsymbol{n}} q_{\Omega,\mathfrak{K}} - i\mathfrak{K}\beta q_{\Omega,\mathfrak{K}} = 0 & \partial\Omega \end{cases} \tag{7.18}$$

Remark 7.2.2. Note that the state $p_{\Omega,\mathfrak{K}}$ satisfies

$$\partial_\psi \mathcal{L}(\Omega, p_{\Omega,\mathfrak{K}}, \psi)(\widetilde{\psi}) = 0, \ \forall\widetilde{\psi} \in H^1(\Omega), \tag{7.19}$$

i.e.

$$\text{Re}\left[\int_\Omega (\nabla p_{\Omega,\mathfrak{K}} \cdot \nabla\overline{\widetilde{\psi}} - \mathfrak{K}^2 p_{\Omega,\mathfrak{K}}\overline{\widetilde{\psi}}) - \overline{\widetilde{\psi}(\boldsymbol{r}^{\text{src}})} + i\mathfrak{K}\beta \int_{\partial\Omega} p_{\Omega,\mathfrak{K}}\overline{\widetilde{\psi}}\right] = 0, \ \forall\widetilde{\psi} \in H^1(\Omega). \tag{7.20}$$

By doing similar computations we can obtain the PDE system (7.2) for $p_{\Omega,\mathfrak{K}}$ by applying relation (7.19).

7.2.3 Volumetric shape derivative

Note that T_ε leaves $\boldsymbol{r}^{\text{src}}$ and $\boldsymbol{r}_m^{\text{mic}}$ invariant, as V is equal 0 in the neighborhood of each of these locations. Using the notations of Section 5.1.2, we apply a change of variable and define:

$$\begin{aligned} \mathcal{G}(\varepsilon, \varphi, \psi) &= \mathcal{L}(\Omega_\varepsilon, \varphi \circ T_\varepsilon^{-1}, \psi \circ T_\varepsilon^{-1}) && (7.21) \\ &= \text{Re}\left[\int_\Omega (\nabla\varphi \cdot A_\varepsilon.\nabla\overline{\psi} - \mathfrak{K}^2\varphi\overline{\psi}\xi_\varepsilon) + i\mathfrak{K}\beta \int_{\partial\Omega} \varphi\overline{\psi}\xi_\varepsilon^\Gamma\right. && (7.22) \\ &\qquad \left. -\overline{\psi(\boldsymbol{r}^{\text{src}})} + \frac{1}{2M}\sum_{m=1}^{M} |\varphi(\boldsymbol{r}_m^{\text{mic}}) - p_{\text{obs},\mathfrak{K}}(\boldsymbol{r}_m^{\text{mic}})|^2\right] && (7.23) \end{aligned}$$

where ξ_ε denotes the Jacobian of T_ε, namely $\xi_\varepsilon = |\det DT_\varepsilon|$, A_ε is given by

$$A_\varepsilon = \xi_\varepsilon DT_\varepsilon^{-1} DT_\varepsilon^{-T},$$

and ξ_ε^Γ is the tangential Jacobian of T_ε:

$$\xi_\varepsilon^\Gamma = |\det DT_\varepsilon| \|DT_\varepsilon^{-T} \boldsymbol{n}\|.$$

Note that $\det DT_\varepsilon > 0$ for ε small enough. We now compute the derivative of each term in expression (7.23) with respect to ε and consider the evaluation at $\varepsilon = 0$. Using the differentials of the matrix determinant and inversion operators, we get:

$$\frac{d}{d\varepsilon}\xi_\varepsilon\big|_{\varepsilon=0} = \operatorname{tr}\left(\operatorname{Com}(\mathrm{Id})^T DV\right) = \operatorname{div} V, \tag{7.24}$$

and, if M, H are in $\mathfrak{M}_D(\mathbb{R})$:

$$\frac{d}{d\varepsilon}(M+\varepsilon H)^{-1} = -(M+\varepsilon H)^{-1} H (M+\varepsilon H)^{-1}. \tag{7.25}$$

Applying (7.25) yields:

$$\frac{d}{d\varepsilon}\big|_{\varepsilon=0} DT_\varepsilon^{-1} = -DV. \tag{7.26}$$

Combining every term in the derivative, we hence get:

$$\frac{d}{d\varepsilon}A_\varepsilon\big|_{\varepsilon=0} = \operatorname{div} V.\,\mathrm{Id} - (DV + DV^T). \tag{7.27}$$

Similarly, we have:

$$\frac{d}{d\varepsilon}\xi_\varepsilon^\Gamma\big|_{\varepsilon=0} = \operatorname{div} V - DV.\boldsymbol{n}\cdot\boldsymbol{n} = \operatorname{div}_\Gamma(V). \tag{7.28}$$

We thus get a volumetric form for the shape derivative by using (5.10) and (5.11):

$$\begin{aligned}
\partial_\varepsilon \mathcal{G}(0, p_{\Omega,\mathfrak{K}}, q_{\Omega,\mathfrak{K}}) &= \operatorname{Re}\left[\int_\Omega \nabla p_{\Omega,\mathfrak{K}} \cdot (\operatorname{div} V.\mathrm{I} - DV - DV^T).\nabla\overline{q_{\Omega,\mathfrak{K}}} - \operatorname{div} V \mathfrak{K}^2 p_{\Omega,\mathfrak{K}}\overline{q_{\Omega,\mathfrak{K}}}\right. && (7.29)\\
&\qquad \left. + i\mathfrak{K}\beta\int_{\partial\Omega} \operatorname{div}_\Gamma(V) p_{\Omega,\mathfrak{K}}\overline{q_{\Omega,\mathfrak{K}}}\right] && (7.30)\\
&= \int_\Omega Z : DV + \int_{\partial\Omega} Z_\Gamma : D_\Gamma V && (7.31)
\end{aligned}$$

where

$$Z = \operatorname{Re}\left[(\nabla p_{\Omega,\mathfrak{K}}\cdot\nabla\overline{q_{\Omega,\mathfrak{K}}} - \mathfrak{K}^2 p_{\Omega,\mathfrak{K}}\overline{q_{\Omega,\mathfrak{K}}})\mathrm{I} - \nabla p_{\Omega,\mathfrak{K}} \otimes \nabla\overline{q_{\Omega,\mathfrak{K}}} - \nabla\overline{q_{\Omega,\mathfrak{K}}} \otimes \nabla p_{\Omega,\mathfrak{K}}\right], \tag{7.32}$$

and

$$Z_\Gamma = \operatorname{Re}\left[i\mathfrak{K}\beta p_{\Omega,\mathfrak{K}}\overline{q_{\Omega,\mathfrak{K}}}\right]\mathrm{I}. \tag{7.33}$$

7.2.4 Boundary formulation

Let $\omega = \bigcup_{m=1}^{M} B(\boldsymbol{r}_m^{\text{mic}}, t) \bigcup B(\boldsymbol{r}^{\text{src}}, t)$, with $t > 0$ chosen such that V vanishes on ω. Assuming elliptic regularity for $p_{\Omega,\mathfrak{K}}$ and $q_{\Omega,\mathfrak{K}}$ as in Remark 7.2.1, we have $Z|_{\Omega\setminus\omega} \in W^{1,1}(\Omega \setminus \omega)$, and $\operatorname{div}(Z^T V)$ is well-defined. Moreover, a quick calculation shows that $\operatorname{div} Z|_{\Omega\setminus\omega}$ is null as the source terms for $p_{\Omega,\mathfrak{K}}$ and $q_{\Omega,\mathfrak{K}}$ are contained in ω. We can then apply (5.9) to get:

$$Z|_{\Omega\setminus\omega} : DV = Z|_{\Omega\setminus\omega} : DV + \operatorname{div} Z|_{\Omega\setminus\omega} \cdot V = \operatorname{div}(Z|_{\Omega\setminus\omega}^T V). \tag{7.34}$$

Note also that the identity (5.14) gives $(\nabla p_{\Omega,\mathfrak{K}} \otimes \nabla\overline{q_{\Omega,\mathfrak{K}}}).\boldsymbol{n} = (\nabla\overline{q_{\Omega,\mathfrak{K}}} \cdot \boldsymbol{n})\nabla p_{\Omega,\mathfrak{K}} = \partial_{\boldsymbol{n}}\overline{q_{\Omega,\mathfrak{K}}}\nabla p_{\Omega,\mathfrak{K}}$, and $(\nabla\overline{q_{\Omega,\mathfrak{K}}} \otimes \nabla p_{\Omega,\mathfrak{K}}).\boldsymbol{n} = \partial_{\boldsymbol{n}} p_{\Omega,\mathfrak{K}}\nabla\overline{q_{\Omega,\mathfrak{K}}}$. We can then apply the divergence theorem for a Lipschitz domain (see for instance the generalized Gauss-Green theorem in [63]) to obtain:

$$\begin{aligned}
\int_\Omega Z : DV &= \int_{\partial\Omega} Z^T V \cdot \boldsymbol{n} = \int_{\partial\Omega} V \cdot Z\boldsymbol{n} && (7.35)\\
&= \int_{\partial\Omega} \operatorname{Re}\Big[(V\cdot\boldsymbol{n})(\nabla p_{\Omega,\mathfrak{K}} \cdot \nabla\overline{q_{\Omega,\mathfrak{K}}} - \mathfrak{K}^2 p_{\Omega,\mathfrak{K}}\overline{q_{\Omega,\mathfrak{K}}}) && (7.36)\\
&\qquad - (\partial_{\boldsymbol{n}}\overline{q_{\Omega,\mathfrak{K}}}\nabla p_{\Omega,\mathfrak{K}} + \partial_{\boldsymbol{n}} p_{\Omega,\mathfrak{K}}\nabla\overline{q_{\Omega,\mathfrak{K}}}) \cdot V\Big]. && (7.37)
\end{aligned}$$

By using Formula (5.12), we can also write on each edge Γ_s:

$$\begin{aligned}
\int_{\Gamma_s} Z_\Gamma : D_\Gamma V &= \int_{\Gamma_s} \operatorname{div}_\Gamma(\operatorname{Re}[i\mathfrak{K}\beta\, p_{\Omega,\mathfrak{K}}\,\overline{q_{\Omega,\mathfrak{K}}}]V) - V \cdot \nabla_\Gamma \operatorname{Re}[i\mathfrak{K}\beta p_{\Omega,\mathfrak{K}}\overline{q_{\Omega,\mathfrak{K}}}] && (7.38)\\
&= \int_{\Gamma_s} \operatorname{div}_\Gamma(\operatorname{Re}[i\mathfrak{K}\beta\, p_{\Omega,\mathfrak{K}}\,\overline{q_{\Omega,\mathfrak{K}}}]V) - V \cdot \operatorname{Re}\Big[i\mathfrak{K}\beta\Big(\overline{q_{\Omega,\mathfrak{K}}}\nabla p_{\Omega,\mathfrak{K}} + p_{\Omega,\mathfrak{K}}\nabla\overline{q_{\Omega,\mathfrak{K}}} && (7.39)\\
&\qquad -(\partial_{\boldsymbol{n}} p_{\Omega,\mathfrak{K}}\overline{q_{\Omega,\mathfrak{K}}} + p_{\Omega,\mathfrak{K}}\partial_{\boldsymbol{n}}\overline{q_{\Omega,\mathfrak{K}}})\boldsymbol{n}\Big)\Big]. && (7.40)
\end{aligned}$$

As $\partial_{\boldsymbol{n}} p_{\Omega,\mathfrak{K}}\overline{q_{\Omega,\mathfrak{K}}} = p_{\Omega,\mathfrak{K}}\partial_{\boldsymbol{n}}\overline{q_{\Omega,\mathfrak{K}}} = -i\mathfrak{K}\beta p_{\Omega,\mathfrak{K}}\overline{q_{\Omega,\mathfrak{K}}}$ on $\partial\Omega$, the terms in (7.37) cancel out with some of the terms in (7.39), and we get by adding both integrals:

$$\begin{aligned}
\partial_\varepsilon \mathcal{G}(0, p_{\Omega,\mathfrak{K}}, q_{\Omega,\mathfrak{K}}) &= \int_{\partial\Omega} (V\cdot\boldsymbol{n}) \operatorname{Re}\Big[\nabla p_{\Omega,\mathfrak{K}} \cdot \nabla\overline{q_{\Omega,\mathfrak{K}}} - \mathfrak{K}^2 p_{\Omega,\mathfrak{K}}\overline{q_{\Omega,\mathfrak{K}}} + 2\mathfrak{K}^2\beta^2 p_{\Omega,\mathfrak{K}}\overline{q_{\Omega,\mathfrak{K}}}\Big] && (7.41)\\
&\quad + \sum_{s=1}^{S} \int_{\Gamma_s} \operatorname{div}_\Gamma(\operatorname{Re}[i\mathfrak{K}\beta\, p_{\Omega,\mathfrak{K}}\,\overline{q_{\Omega,\mathfrak{K}}}]V). && (7.42)
\end{aligned}$$

By applying the tangential divergence theorem 5.1.2 on each edge Γ_s, we get:

$$\begin{aligned}
\int_{\Gamma_s} \operatorname{div}_\Gamma(\operatorname{Re}[i\mathfrak{K}\beta\, p_{\Omega,\mathfrak{K}}\,\overline{q_{\Omega,\mathfrak{K}}}]V) &= \boldsymbol{\tau}_s \cdot \Big(\operatorname{Re}[i\mathfrak{K}\beta\, p_{\Omega,\mathfrak{K}}(\boldsymbol{v}_{s+1})\overline{q_{\Omega,\mathfrak{K}}(\boldsymbol{v}_{s+1})}]V(\boldsymbol{v}_{s+1}) && (7.43)\\
&\qquad - \operatorname{Re}[i\mathfrak{K}\beta\, p_{\Omega,\mathfrak{K}}(\boldsymbol{v}_s)\overline{q_{\Omega,\mathfrak{K}}(\boldsymbol{v}_s)}]V(\boldsymbol{v}_s)\Big). && (7.44)
\end{aligned}$$

Summing over s finally yields a boundary formulation of the shape derivative in direction V:

$$DJ(\Omega) \cdot V = \int_{\partial\Omega} (V \cdot \boldsymbol{n}) \operatorname{Re}\left[\nabla p_{\Omega,\mathfrak{K}} \cdot \nabla \overline{q_{\Omega,\mathfrak{K}}} + \mathfrak{K}^2(2\beta^2 - 1) p_{\Omega,\mathfrak{K}} \overline{q_{\Omega,\mathfrak{K}}}\right] \tag{7.45}$$

$$+ \sum_{s=1}^{S} (\boldsymbol{\tau}_{s-1} - \boldsymbol{\tau}_s) \cdot V(\boldsymbol{v}_s) \operatorname{Re}[i\mathfrak{K}\beta \, \mathrm{p}_{\Omega,\mathfrak{K}}(\boldsymbol{v}_s) \overline{q_{\Omega,\mathfrak{K}}(\boldsymbol{v}_s)}] \tag{7.46}$$

where $\tau_0 = \tau_S$.

7.3 Shape optimization algorithm

In order to implement a numerical optimization algorithm, we begin by choosing a parametrization for the geometry. As we work with convex polygons, we have two natural parametrizations available: the polygon's vertices, or the half-planes defining the edges of the polygon. Vertex parametrization is the easiest to implement, and the resulting formula for the shape derivative is also less complex. On the other hand, the half-planes parametrization has the advantage, by definition, of constraining the shape to be convex, the algorithm will have to keep track of line intersections, *i.e.* vertices, as the shape evolves.

Half-planes parametrization can be implemented in a number of ways. Let $\boldsymbol{o}$ be a reference location inside Ω. The polygon can then be parametrized by the orthogonal projections $\boldsymbol{p}_s$ of $\boldsymbol{o}$ on the lines defining each edge. Regardless of the choice of the parametrization used for the descent, the projections $\boldsymbol{p}_s$ can be used to check if a given point is located inside or outside the polygon. Indeed, a location $\boldsymbol{r}$ is inside the polygon if and only if $\boldsymbol{r}$ is on the same side of each of the lines defined by the polygon's edges. This can be checked by evaluating some scalar products and comparing their values to the distance of the origin $\boldsymbol{o}$ to the corresponding edge:

$$\boldsymbol{r} \in \mathring{\Omega} \iff \Big((\boldsymbol{p}_s - \boldsymbol{o}) \cdot (\boldsymbol{r} - \boldsymbol{o}) < \|\boldsymbol{p}_s - \boldsymbol{o}\|_2^2 \quad \forall s \in [\![1, S]\!] \Big) \tag{7.47}$$

$$\iff \left((\boldsymbol{p}_s - \boldsymbol{o}) \cdot (\boldsymbol{r} - \boldsymbol{p}_s) < 0 \quad \forall s \in [\![1, S]\!] \right). \tag{7.48}$$

Fig 7.1 illustrates the parametrization. The projections $\boldsymbol{p}_s$ and origin $\boldsymbol{o}$ are represented in (a), and (b) shows the situation in the case of a point $\boldsymbol{r}$ located outside the polygon. Here $\boldsymbol{r}$ is on the wrong side of the edge $\boldsymbol{v}_4\boldsymbol{v}_5$, and denoting by $\boldsymbol{p}'$ the intersection $(\boldsymbol{ro}) \cap (\boldsymbol{v}_4\boldsymbol{v}_5)$, we have:

$$(\boldsymbol{p}_4 - \boldsymbol{o}) \cdot (\boldsymbol{r} - \boldsymbol{o}) > (\boldsymbol{p}_4 - \boldsymbol{o}) \cdot (\boldsymbol{p}' - \boldsymbol{o}) = (\boldsymbol{p}_4 - \boldsymbol{o}) \cdot (\boldsymbol{p}_4 - \boldsymbol{o}) = \|\boldsymbol{p}_4 - \boldsymbol{o}\|_2^2 . \tag{7.49}$$

In particular, this condition will be used to enforce an inclusion constraint on the microphones. Finally, we can express $\boldsymbol{p}_s$ as a function of the vertices:

$$\boldsymbol{p}_s = \boldsymbol{v}_s + \frac{(\boldsymbol{o} - \boldsymbol{v}_s) \cdot (\boldsymbol{v}_{s+1} - \boldsymbol{v}_s)}{\|\boldsymbol{v}_{s+1} - \boldsymbol{v}_s\|_2^2} (\boldsymbol{v}_{s+1} - \boldsymbol{v}_s). \tag{7.50}$$

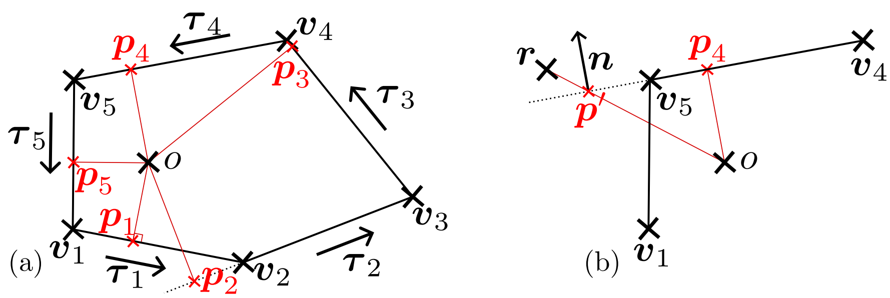

Figure 7.1: (a) Vertices $\boldsymbol{v}_s$ and projections $\boldsymbol{p}_s$ parametrizations for the polygon. (b) Illustration of inclusion checking for the edge $\boldsymbol{v}_4\boldsymbol{v}_5$.

7.3.1 Parametrization

7.3.2 Parametric gradient

We recall here the method described in [21] to compute the parametric gradient of the cost function J. Assume that the shape derivative for the cost function J exists and is well-defined, and denote one of the two mentioned parametrizations by $\boldsymbol{c} = (c_1, \dots, c_N)$. Denote by $\Omega(\boldsymbol{c})$ the shape defined by a given parameter vector $\boldsymbol{c}$. Let $\boldsymbol{\delta c} \in \mathbb{R}^N$ be a small, admissible perturbation of the parameters. Then, there exists a vector field $V_{\boldsymbol{c}}(\boldsymbol{\delta c}) \in W^{1,\infty}(\mathbb{R}^2, \mathbb{R}^2)$ such that $V_{\boldsymbol{c}}(0) = (0,0)$ and $\Omega(\boldsymbol{c}+\boldsymbol{\delta c}) = (\mathrm{Id} + V_{\boldsymbol{c}}(\boldsymbol{\delta c}))\Omega(\boldsymbol{c})$. We then apply the chain rule:

$$\frac{d}{d\boldsymbol{\delta c}} J(\Omega(\boldsymbol{c}+\boldsymbol{\delta c}))\big|_{\boldsymbol{\delta c}=0} = DJ(\Omega(\boldsymbol{c})) \cdot \frac{d}{d\boldsymbol{\delta c}} V_{\boldsymbol{c}}(d\boldsymbol{\delta c})\big|_{\boldsymbol{\delta c}=0}. \tag{7.51}$$

In practice, we thus only have to compute the vector field $V_{\boldsymbol{c}}$ corresponding to a perturbation of the parameters, derivate this vector field with respect to the parameters, and calculate the scalar product with the normal vector to apply the shape derivative formula. In the next paragraphs we compute the derivative of J for both of the previously introduced parametrizations. $V(\boldsymbol{\delta})$ will denote in each case the vector field resulting from a small perturbation $\boldsymbol{\delta} \in \mathbb{R}^2$, which is applied either to a vertex $\boldsymbol{v}_s$ or a projection $\boldsymbol{p}_s$.

Derivatives with respect to vertices

Moving the s-th vertex $\boldsymbol{v}_s$ only affects the neighboring edges of indices $s-1$ and s. Hence, the consequent perturbation field $V(\boldsymbol{\delta})$ is null on every other edge. If $\boldsymbol{r} \in \partial\Omega$, we denote by $\boldsymbol{r}'$ the corresponding point on the new shape, *i.e.* $\boldsymbol{r}' = \boldsymbol{r} + V(\boldsymbol{\delta})(\boldsymbol{r})$. We parametrize the $(s-1)$-th edge linearly. If $\boldsymbol{r} = (1-\alpha)\boldsymbol{v}_{s-1} + \alpha \boldsymbol{v}_s,\ \alpha \in [0,1]$, we take:

$$V(\boldsymbol{\delta})(\boldsymbol{r}) = \boldsymbol{r}' - \boldsymbol{r} = \alpha \boldsymbol{\delta}. \tag{7.52}$$

Derivating V with respect to $\boldsymbol{\delta}$ and applying the dot product with the normal vector yields:

$$DV(0)(\boldsymbol{r}) \cdot \boldsymbol{n} = \alpha \boldsymbol{n} \tag{7.53}$$

We can apply the same calculation to the s-th edge. In particular, $DV(0)(\boldsymbol{v}_k)$ is equal to $(1,1)$ if $k = s$ and 0 otherwise. We thus get the partial derivative with respect to both coordinates of the s-th vertex.

Derivatives with respect to projections

As can be seen on Fig. 7.2, moving p_s only affect the $s - th$ edge. To simplify the notations, we begin by considering a perturbation on the first coordinate of $\boldsymbol{p_s}$. Hence, every component of $\boldsymbol{\delta}$ is zero, except for the component that corresponds to the x coordinate of $\boldsymbol{p_s}$, which we take equal to δ. As before, $\boldsymbol{r'}$ denotes the mapping of the point $\boldsymbol{r} \in \partial\Omega$ on the new boundary. Using once again a linear parametrization, we can write for $\boldsymbol{r} = (1-\alpha)\boldsymbol{v}_s + \alpha \boldsymbol{v}_{s+1}$:

$$V(\boldsymbol{\delta})(\boldsymbol{r}) = (1-\alpha)(\boldsymbol{v}'_s - \boldsymbol{v}_s) + \alpha(\boldsymbol{v}'_{s+1} - \boldsymbol{v}_{s+1}) = (1-\alpha)\varepsilon_s(\delta)\boldsymbol{\tau}_{s-1} + \alpha\varepsilon_{s+1}(\delta)\boldsymbol{\tau}_{s+1} \tag{7.54}$$

where $\varepsilon_s(\delta), \varepsilon_{s+1}(\delta)$ are respectively the signed distances from $\boldsymbol{v}_s$ to $\boldsymbol{v}'_s$ and $\boldsymbol{v}_{s+1}$ to $\boldsymbol{v}'_{s+1}$. Let $\boldsymbol{p}_s = (x, y)$, $\boldsymbol{o} = (x_{\boldsymbol{o}}, y_{\boldsymbol{o}})$, and $\boldsymbol{\tau}_{s-1} = (x_{\boldsymbol{\tau}_{s-1}}, y_{\boldsymbol{\tau}_{s-1}})$. By using $(\boldsymbol{p}'_s - \boldsymbol{o}) \perp (\boldsymbol{v}'_s - \boldsymbol{p}'_s)$ and writing $\boldsymbol{v}'_s - \boldsymbol{p}'_s = \boldsymbol{v}_s - \boldsymbol{p}'_s + \varepsilon_s(\delta)\boldsymbol{\tau}_{s-1}$, we get:

$$\varepsilon_s(\delta) = \frac{(x + \delta - x_{\boldsymbol{o}})(x + \delta - x_{\boldsymbol{v}_s}) + (y - y_{\boldsymbol{o}})(y - y_{\boldsymbol{v}_s})}{x_{\boldsymbol{\tau}_{s-1}}(x + \delta - x_{\boldsymbol{o}}) + y_{\boldsymbol{\tau}_{s-1}}(y - y_{\boldsymbol{o}})}, \tag{7.55}$$

with the associated derivative in 0:

$$\varepsilon'_s(0) = \frac{(2x - x_{\boldsymbol{o}} - x_{\boldsymbol{v}_s})\boldsymbol{\tau}_{s-1} \cdot (\boldsymbol{p}_s - \boldsymbol{o}) - x_{\boldsymbol{\tau}_{s-1}}(\boldsymbol{p}_s - \boldsymbol{o}) \cdot (\boldsymbol{p}_s - \boldsymbol{v}_s)}{(\boldsymbol{\tau}_{s-1} \cdot (\boldsymbol{p}_s - \boldsymbol{o}))^2}. \tag{7.56}$$

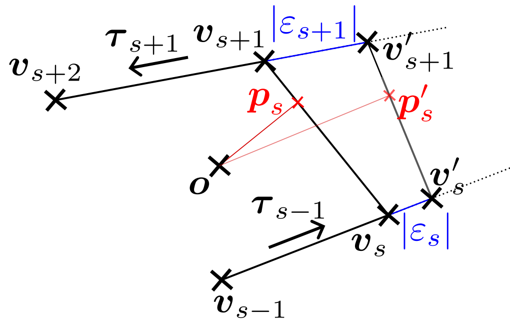

Figure 7.2: Geometric configuration when adding a perturbation to $\boldsymbol{p}_s$

Switching the indices $s-1$ and $s+1$ yields a similar formula for $\varepsilon'_{s+1}(0)$. We then get, on edge s:

$$DV(0)(\boldsymbol{r}) = (1-\alpha)\varepsilon'_s(0)\boldsymbol{\tau}_{s-1} + \alpha\varepsilon'_{s+1}(0)\boldsymbol{\tau}_{s+1}. \tag{7.57}$$

The partial derivative with respect to the x coordinate of $\boldsymbol{p}_s$ is then obtained by applying the shape derivative formula to the vector field defined by (7.57) on edge s. The same process can be used to get the y derivative.

7.3.3 Penalization of inclusion constraints

We describe here the penalization method applied to constrain the microphones locations to remain inside the polygon. We use the inequality (7.48) to check inclusion, and define the penalization functional:

$$P_\varepsilon(\Omega) = \frac{1}{2\varepsilon}\sum_{m=1}^{M}\sum_{s=1}^{S}\max[0, (\boldsymbol{p}_s - \boldsymbol{o})\cdot(\boldsymbol{r}_m^{\mathrm{mic}} - \boldsymbol{p}_s)]^2. \tag{7.58}$$

The cost function J then becomes:

$$J_\varepsilon(\Omega) = \frac{1}{2LM}\sum_{l=1}^{L}\sum_{m=1}^{M}\left|p_{\Omega,\mathfrak{K}_l}(\boldsymbol{r}_m^{\mathrm{mic}}) - p_{\mathrm{obs},\mathfrak{K}_l}(\boldsymbol{r}_m^{\mathrm{mic}})\right|^2 + P_\varepsilon(\Omega). \tag{7.59}$$

Again, we compute the derivative of P_ε with respect to the projections $\boldsymbol{p}_s$ and vertices $\boldsymbol{v}_s$.

Derivative with respect to projections

The derivative with respect to the s-th projection is straightforward to compute:

$$\nabla_{\boldsymbol{p}_s} P_\varepsilon(\Omega) = \frac{1}{\varepsilon}\sum_{m=1}^{M}\max\left[0, (\boldsymbol{p}_s - \boldsymbol{o})\cdot(\boldsymbol{r}_m^{\mathrm{mic}} - \boldsymbol{p}_s)\right](\boldsymbol{r}_m^{\mathrm{mic}} + \boldsymbol{o} - 2\boldsymbol{p}_s). \tag{7.60}$$

Derivative with respect to vertices

The derivative with respect to the s-th vertex is given by:

$$\nabla_{\boldsymbol{v}_s} P_\varepsilon(\Omega) = \frac{1}{\varepsilon}\sum_{m=1}^{M}\sum_{l=1}^{S}\max\left[0, (\boldsymbol{p}_l - \boldsymbol{o})\cdot(\boldsymbol{r}_m^{\mathrm{mic}} - \boldsymbol{p}_l)\right]\nabla_{\boldsymbol{v}_s}[(\boldsymbol{p}_l - \boldsymbol{o})\cdot(\boldsymbol{r}_m^{\mathrm{mic}} - \boldsymbol{p}_l)]. \tag{7.61}$$

In practice only the terms of indices s and $s-1$ (mod S) can be non-zero, as the other projections do not depend on $\boldsymbol{v}_s$. Let $t_s = \frac{(\boldsymbol{o}-\boldsymbol{v}_s)\cdot(\boldsymbol{v}_{s+1}-\boldsymbol{v}_s)}{\|\boldsymbol{v}_{s+1}-\boldsymbol{v}_s\|_2^2}$. We have:

$$\nabla_{\boldsymbol{v}_s} t_s = \frac{2\boldsymbol{v}_s - \boldsymbol{o} - \boldsymbol{v}_{s+1}}{\|\boldsymbol{v}_{s+1} - \boldsymbol{v}_s\|_2^2} - 2\frac{(\boldsymbol{o} - \boldsymbol{v}_s)\cdot(\boldsymbol{v}_{s+1} - \boldsymbol{v}_s)}{\|\boldsymbol{v}_{s+1} - \boldsymbol{v}_s\|_2^4}(\boldsymbol{v}_s - \boldsymbol{v}_{s+1}) = \frac{2\boldsymbol{v}_s - \boldsymbol{o} - \boldsymbol{v}_{s+1} + 2t_s(\boldsymbol{v}_{s+1} - \boldsymbol{v}_s)}{\|\boldsymbol{v}_{s+1} - \boldsymbol{v}_s\|_2^2} \tag{7.62}$$

and

$$\nabla_{\boldsymbol{v}_s} t_{s-1} = \frac{\boldsymbol{o} - \boldsymbol{v}_{s-1} - 2t_{s-1}(\boldsymbol{v}_s - \boldsymbol{v}_{s-1})}{\|\boldsymbol{v}_s - \boldsymbol{v}_{s-1}\|_2^2}. \tag{7.63}$$

Using (7.50), we get the following jacobian matrices for the derivatives of $\boldsymbol{p}_s$ and $\boldsymbol{p}_{s-1}$ with respect to $\boldsymbol{v}_s$:

$$D_{\boldsymbol{v}_s}\boldsymbol{p}_s = \begin{pmatrix} 1-t_s \\ 1-t_s \end{pmatrix} \mathrm{I} + \begin{pmatrix} \partial_x t_s.(\boldsymbol{v}_{s+1} - \boldsymbol{v}_s) & \partial_y t_s.(\boldsymbol{v}_{s+1} - \boldsymbol{v}_s) \end{pmatrix} = \begin{pmatrix} 1-t_s \\ 1-t_s \end{pmatrix} \mathrm{I} + (\boldsymbol{v}_{s+1} - \boldsymbol{v}_s) \otimes \nabla_{\boldsymbol{v}_s} t_s, \tag{7.64}$$

and

$$D_{\boldsymbol{v}_s}\boldsymbol{p}_{s-1} = \begin{pmatrix} t_{s-1} \\ t_{s-1} \end{pmatrix} \mathrm{I} + \begin{pmatrix} \partial_x t_{s-1}.(\boldsymbol{v}_s - \boldsymbol{v}_{s-1}) & \partial_y t_{s-1}.(\boldsymbol{v}_s - \boldsymbol{v}_{s-1}) \end{pmatrix} = \begin{pmatrix} t_{s-1} \\ t_{s-1} \end{pmatrix} \mathrm{I} + (\boldsymbol{v}_s - \boldsymbol{v}_{s-1}) \otimes \nabla_{\boldsymbol{v}_s} t_{s-1}. \tag{7.65}$$

We can then apply (5.13) to get

$$\nabla_{\boldsymbol{v}_s}[(\boldsymbol{p}_s - \boldsymbol{o}) \cdot (\boldsymbol{r}_m^{\mathrm{mic}} - \boldsymbol{p}_s)] = D_{\boldsymbol{v}_s}\boldsymbol{p}_s^T(\boldsymbol{r}_m^{\mathrm{mic}} - 2\boldsymbol{p}_s + \boldsymbol{o}), \tag{7.66}$$

hence

$$\nabla_{\boldsymbol{v}_s}[(\boldsymbol{p}_s - \boldsymbol{o}) \cdot (\boldsymbol{r}_m^{\mathrm{mic}} - \boldsymbol{p}_s)] = (1-t_s)(\boldsymbol{r}_m^{\mathrm{mic}} - 2\boldsymbol{p}_s + \boldsymbol{o}) + [\nabla_{\boldsymbol{v}_s} t_s \otimes (\boldsymbol{v}_{s+1} - \boldsymbol{v}_s)].(\boldsymbol{r}_m^{\mathrm{mic}} - 2\boldsymbol{p}_s + \boldsymbol{o}) \tag{7.67}$$

and by (5.14) we have:

$$\nabla_{\boldsymbol{v}_s}[(\boldsymbol{p}_s - \boldsymbol{o}) \cdot (\boldsymbol{r}_m^{\mathrm{mic}} - \boldsymbol{p}_s)] = (1-t_s)(\boldsymbol{r}_m^{\mathrm{mic}} - 2\boldsymbol{p}_s + \boldsymbol{o}) + (\boldsymbol{r}_m^{\mathrm{mic}} - 2\boldsymbol{p}_s + \boldsymbol{o}) \cdot (\boldsymbol{v}_{s+1} - \boldsymbol{v}_s)\nabla_{\boldsymbol{v}_s} t_s. \tag{7.68}$$

Similarly, we can write:

$$\nabla_{\boldsymbol{v}_s}[(\boldsymbol{p}_{s-1} - \boldsymbol{o}) \cdot (\boldsymbol{r}_m^{\mathrm{mic}} - \boldsymbol{p}_{s-1})] = t_{s-1}(\boldsymbol{r}_m^{\mathrm{mic}} - 2\boldsymbol{p}_{s-1} + \boldsymbol{o}) + (\boldsymbol{r}_m^{\mathrm{mic}} - 2\boldsymbol{p}_{s-1} + \boldsymbol{o}) \cdot (\boldsymbol{v}_s - \boldsymbol{v}_{s-1})\nabla_{\boldsymbol{v}_s} t_{s-1}. \tag{7.69}$$

We finally get:

$$\nabla_{\boldsymbol{v}_s} P_\varepsilon(\Omega) = \frac{1}{\varepsilon} \sum_{m=1}^{M} c_{s,m} + c_{s-1,m} \tag{7.70}$$

where $s-1$ is taken modulo S, and

$$\left\{ \begin{array}{rcl} c_{s,m} & = & \max[0, (\boldsymbol{p}_s - \boldsymbol{o}) \cdot (\boldsymbol{r}_m^{\mathrm{mic}} - \boldsymbol{p}_s)]\big[(1-t_s)(\boldsymbol{r}_m^{\mathrm{mic}} - 2\boldsymbol{p}_s + \boldsymbol{o}) + \\ & & \qquad (\boldsymbol{r}_m^{\mathrm{mic}} - 2\boldsymbol{p}_s + \boldsymbol{o}) \cdot (\boldsymbol{v}_{s+1} - \boldsymbol{v}_s)\nabla_{\boldsymbol{v}_s} t_s\big] \\ c_{s-1,m} & = & \max[0, (\boldsymbol{p}_{s-1} - \boldsymbol{o}) \cdot (\boldsymbol{r}_m^{\mathrm{mic}} - \boldsymbol{p}_{s-1})]\big[t_{s-1}(\boldsymbol{r}_m^{\mathrm{mic}} - 2\boldsymbol{p}_{s-1} + \boldsymbol{o}) + \\ & & \qquad (\boldsymbol{r}_m^{\mathrm{mic}} - 2\boldsymbol{p}_{s-1} + \boldsymbol{o}) \cdot (\boldsymbol{v}_s - \boldsymbol{v}_{s-1})\nabla_{\boldsymbol{v}_s} t_{s-1}\big] \end{array} \right. \tag{7.71}$$

7.3.4 Gradient descent

The implementation of the shape gradient descent is described in Alg. 6. We apply a line search at each iteration by translating the vertices in the direction of the gradient, and stopping when the objective function J_ε has decreased or a maximal number of steps have been applied. We apply the penalization P_ε on the inclusion constraints as described in Section 7.3.3, using $\varepsilon = 1$. The shape gradient is computed by applying the formulas given in Theorem 7.2.1 and Equation (7.70). The boundary integrals are evaluated numerically using Simpson's rule. The step γ is updated dynamically on lines 7-12, depending on if the line search requires more than one step to stop. The frequency range is modified during the execution of the algorithm. We set a minimal accessible frequency $f_{\min}$, a global maximum frequency $f_{\max}$, and one or several intermediate maximal frequencies $f_{\min} < f_{\max}^{(l)} \leq f_{\max}$. We consider only the frequencies between $f_{\min}$ and the current

---

Algorithm 6 Gradient descent algorithm

Input: Global maximum number of iterations $\mathrm{it}_{\max}$, initial vertices $\boldsymbol{v}_{\mathrm{ini}}$, initial step γ, intermediate maximal frequencies $f_{\max}^{(l)}$, minimal and maximal number of iterations per frequency $\mathrm{it}_{\min}^{(l)}$ and $\mathrm{it}_{\max}^{(l)}$

Output: Estimated vertices $\boldsymbol{v}_{\mathrm{fin}}$

1: $\boldsymbol{v}_{\mathrm{curr}} \leftarrow \boldsymbol{v}_{\mathrm{ini}}$
2: $k \leftarrow 0$
3: $k_{\mathrm{freq}} \leftarrow 0$
4: **while** $k < \mathrm{it}_{\max}$ **do**
5:     $\boldsymbol{g}_{\mathrm{curr}} \leftarrow \partial_{\boldsymbol{v}} J(\boldsymbol{v}_{\mathrm{curr}})$
6:     Get updated $\boldsymbol{v}_{\mathrm{curr}}$ by applying a line search in direction $\boldsymbol{g}_{\mathrm{curr}}$
7:     **if** line search stopped after 1 iteration 3 times in a row **then**
8:         $\gamma \leftarrow 1.2\gamma$
9:     **end if**
10:     **if** line search took more than 1 iteration 3 times in a row **then**
11:         $\gamma \leftarrow 0.8\gamma$
12:     **end if**
13:     **if** no vertex has moved more than 0.5 mm in the last 50 iterations **then**
14:         Set patience flag to **true**
15:     **end if**
16:     **if** ($\mathrm{cost}_{\mathrm{curr}} < \mathrm{cost}_{\min}$ **or** $k_{\mathrm{freq}} \geq \mathrm{it}_{\max}^{(l)}$ **or** patience is **true**) **and** $k_{\mathrm{freq}} \geq \mathrm{it}_{\min}^{(l)}$ **then**
17:         **if** $f_{\max}^{(l)} < f_{\max}$ **then**
18:             Increase l, reset patience and k_{freq}
19:         **else**
20:             Break the loop and stop.
21:         **end if**
22:     **end if**
23:     Increment k and k_{freq}
24: **end while**

---

maximal frequency when computing the cost and the gradient. When a stopping criterion is reached, we first check if the current frequency has already reached $f_{\max}$. In that case we stop the algorithm. Otherwise, we reset the relevant counters and increase f to the next frequency. A first criterion is based on a patience heuristic which is checked at line 13: we consider that the criterion is achieved if the maximal Euclidean distance covered by the vertices of the polygon over 50 iterations is less than 0.5 mm. This condition should trigger when the algorithm has stalled and the error plateaued. We also check the value of the cost (7.59), stopping if it goes below the threshold 10^{-6}. Finally, we track the number of iterations executed at the current maximal frequency f using a counter k_{freq}. We set a maximal and a minimal number of iterations for each $f^{(l)}_{\max}$, denoted by $\text{it}^{(l)}_{\min}$ and $\text{it}^{(l)}_{\max}$. The aim of these bounds is to enforce a minimal and maximal computing budget for each frequency range, ensuring for instance that the whole descent is not spent only on lower frequencies.

Note that the hyperparameters described in this section, such as the threshold for the cost, are arbitrary and were set as such based on prior numerical experiments but not on an extensive study. These hyperparameters could be further fine-tuned to improve results.

7.4 Numerical experiments

7.4.1 Experimental setup

Room datasets

We test the gradient descent algorithm on two datasets of 50 convex rooms each, one containing quadrilaterals and the other pentagons. The rooms are generated randomly by taking the convex hull of 4 (respectively 5) vertices picked uniformly at random in the disk centered at $(0, 0)$ and of radius 4 m. If the number of vertices was decreased, we reject the room and try again in order to get a convex polygon with the correct number of vertices. We also reject the room if any of the walls' lengths is less than 2 m, or if any of the inner angles of the polygon is less than $\frac{\pi}{4}$ or greater than $\frac{3\pi}{4}$, in order to get non-degenerate rooms. Finally, we consider an array of 8 microphones regularly spaced on the circle centered at the origin and of radius 50 cm. We only keep rooms for which the measure points are at least at a 50 cm distance from the walls. The source is located at the center of the microphone array. See Fig. 7.3 for a graphical representation of some rooms sampled from the datasets.

Experiments and parameters

We will consider two types of experiments. The first experiments will evaluate the task of reconstructing the shape with minimal geometric knowledge, using 128 frequencies ranging from 0 to 256 Hz. We test 25 random initializations using the same procedure used to generate the datasets. For each polygon, we apply 30 gradient steps, considering only the frequencies below 100 Hz. Initializations

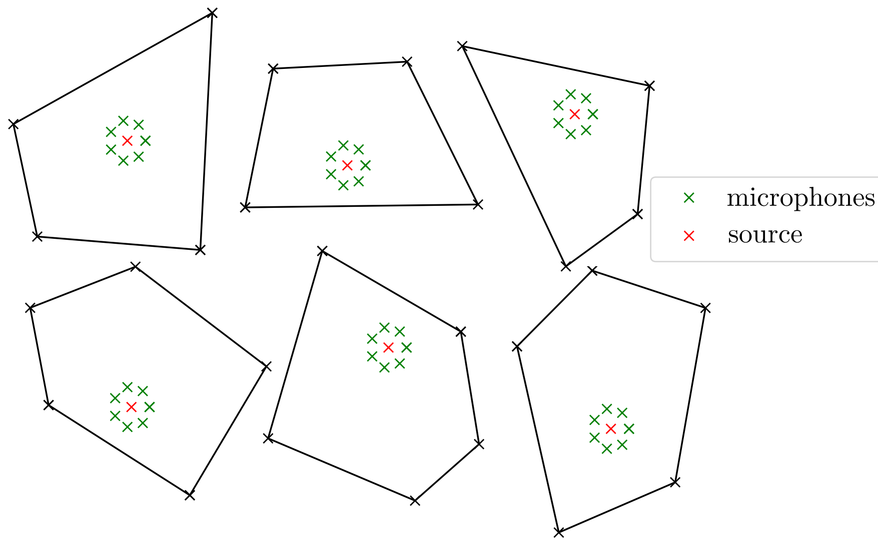

Figure 7.3: Some examples of random rooms generated for the experiments.

that degenerate to a non-convex polygon are restarted with a new random polygon. We then consider the polygon that achieved the lowest cost, and launch a full gradient descent with a maximal number of iterations of 2000. See Tab. 7.1 for the parameters used for the final gradient descent, following the notations of Section 7.3.4. As mentioned in Section 7.1, on-site measurements cannot capture low frequencies. We will run the same experiments, removing every frequency below 50 Hz. This means only 103 frequencies are used when considering a maximal frequency of 256 Hz.

$f_{\max}^{(l)}$ (Hz)	100	256
$\mathrm{it}_{\min}^{(l)}$	50	1000
$\mathrm{it}_{\max}^{(l)}$	500	-

Table 7.1: Parameters used for the experiments.

In practical cases, one could have access to a first estimate of the shape, obtained for instance by applying another method or from in-situ measurements. We are then interested in the ability of the algorithm to refine this estimation by using acoustic measurements. In the second type of experiments, we thus consider that an initial guess for the shape is available, and that we cannot access low frequencies. Once again, we remove the frequencies below 50 Hz and try to refine the initial guess with the remaining 103 frequencies in the $50 - 256$ Hz range. The initial guesses are chosen by considering the target polygons and applying Gaussian, zero-mean additive noise. We apply an angular noise $e_\theta \sim \mathcal{N}(0, \sigma_\theta)$ to the normal vectors of the polygon, and a metric noise $e_d \sim \mathcal{N}(0, \sigma_d)$ to the corresponding distance of the origin to each edge. The wall distance and angular noise standard deviations are respectively set to $\sigma_d = 10$ cm, and $\sigma_\theta = 5°$.

7.4.2 Evaluation metrics

In order to evaluate the ability of our proposed shape descent method to reconstruct rooms, we will compute a number of error metrics. Let us consider the half-plane parametrization of convex polygons described in Fig. 7.1, with $\boldsymbol{o}$ set at the origin $(0, 0)$. Let $\boldsymbol{p}_s$, $\hat{\boldsymbol{p}}_s$ be the respective projections of $\boldsymbol{o}$ on the s-th wall of the target and the estimated rooms.

Shape metrics

The wall distance error measures the radial error committed on wall locations and is defined by:

$$e_d^{(s)} = \big|\, \|\boldsymbol{p}_s\|_2 - \|\hat{\boldsymbol{p}}_s\|_2 \,\big|. \tag{7.72}$$

The angular error is defined by the angle formed by the target and the estimated walls:

$$e_\theta^{(s)} = \min(|\theta|, 2\pi - |\theta|), \quad \theta = \arccos(\boldsymbol{p}_s \cdot \hat{\boldsymbol{p}}_s)|. \tag{7.73}$$

We will also measure the Euclidean error on vertices, which is easily defined but slightly less interpretable than other metrics:

$$e_{\boldsymbol{v}}^{(s)} = \|\boldsymbol{v}_s - \hat{\boldsymbol{v}}_s\|_2\,. \tag{7.74}$$

Another value of interest is the absolute error on the volume of the rooms, denoted by e_V.

Error reduction for noisy initializations

For the type 2 experiments where a noisy initial guess is provided, we evaluate the initial and final errors in order to measure the improvement produced by our shape descent method. The initial errors will be noted with the superscript $^{\text{ini}}$.

Recall and mean errors

In certain cases the reconstruction procedure might fail catastrophically, especially for the first type of experiments where we only test a limited number of initializations that can all be bad approximations of the target. The objective function is highly non-convex, and if the initial guess is too far from the target, the algorithm may converge to a local minimum instead of the desired solution. The resulting errors have a disproportionately high cost on the overall mean error. We can thus proceed as in Section 2.4 and compute the mean error for the walls that have been recovered with an angular error and a wall distance error that are below set thresholds $\varepsilon_\theta = 10°$ and $\varepsilon_d = 5$ cm. We compute the recall at these thresholds, *i.e.* the proportion of walls that were accurately recovered. For reference, we also present the global mean error for each wall, even for those that were not accurately recovered.

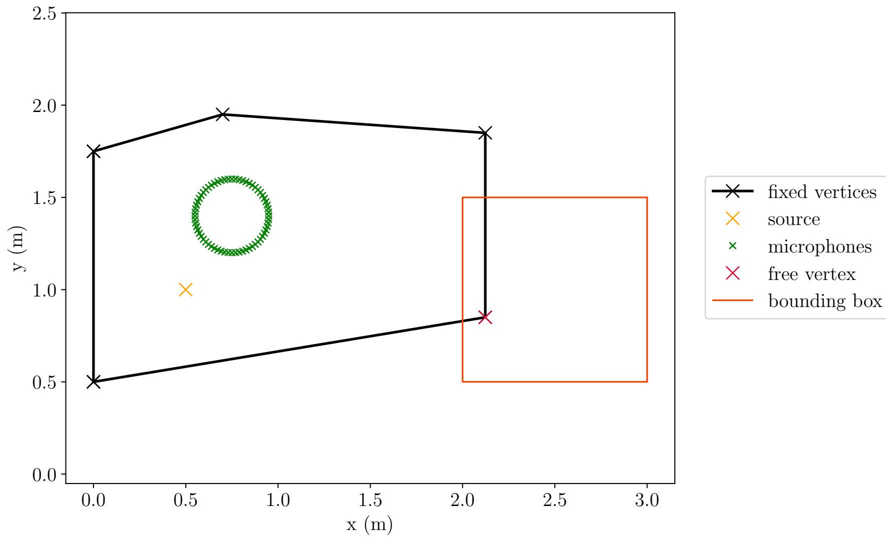

Figure 7.4: Setup for visualizing the cost function J. The free vertex is allowed to move in the bounding box, and J is evaluated for each corresponding polygon.

7.4.3 Structure of the cost function

In this section we make some observations on the cost function and the nature of its local minima. Local minima might arise from a variety of different factors. For instance, near-symmetries of the source, microphones and polygon setup can result in a local minimum. This is amplified at low frequencies when the radius of the array is small, since at low frequencies the measure points are indistinguishable. Another aspect to take into account is the presence of dominant first order reflections. As seen in Section 6.3, the early specular reflections are prominent in the time responses, and moving a wall can be seen as moving its corresponding spike in the time response in order to best match measurements. It can thus be advantageous for the algorithm to wrongly push back a wall in order to decrease the amplitude of its first order reflection if the initialization was too far from target. The occlusion of reflections can be problematic, as it can cause sharp changes in the cost function. Higher order reflections can also cause issues, especially in the case of parallel or near-parallel walls. For example, in the case of a rectangle, doubling the dimensions of the rectangle in any direction results in a local minimum. Indeed, one of the first order reflections is missing, but most of the higher order reflections are perfectly matched. The combination of all these factors causes a complex behavior, especially if we take into account the fact that the observations are band-limited. Note that providing an informative visualization of the cost function is a complex task, as it is defined on a high-dimensional space (dimension $2S$ for a polygon with S vertices). In order to visualize the objective function, we set a reference polygon, source location and microphone positions and simulate target measurements with 256 frequencies uniformly spaced between 0 and

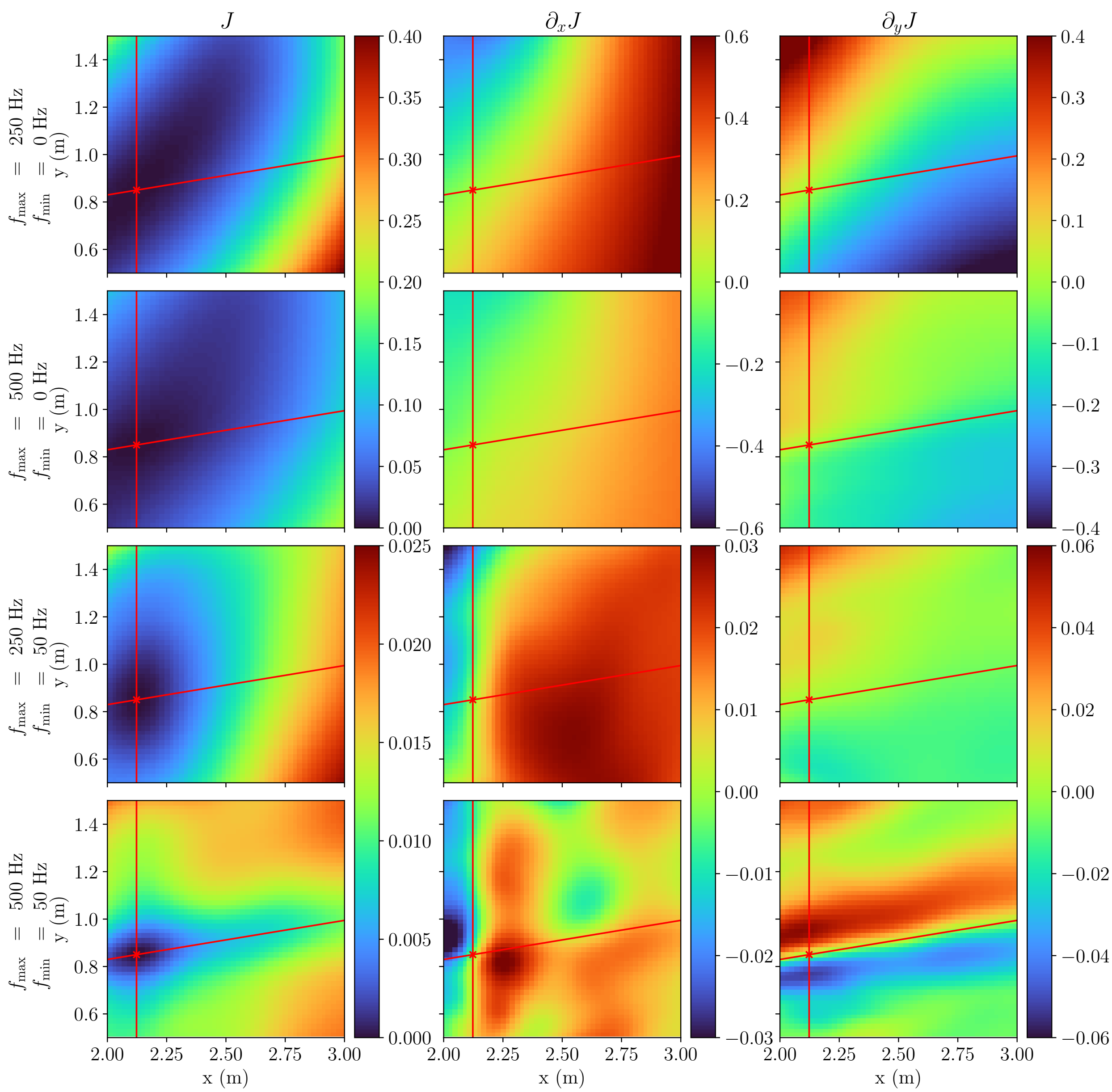

Figure 7.5: Values of the objective function J and its gradient when moving the free vertex in the bounding box, for different minimum and maximum frequencies. The red cross designates the target vertex location, and the red lines are the continuation of the target polygon's edges.

500 Hz. We designate one of the vertices to be a free vertex, according to the setup presented in Fig. 7.4. We then proceed to move the free vertex while keeping the other vertices still, and compute the value of the objective function for each corresponding polygon, taking the simulations for the reference polygon as the target measurements. The values taken by the objective function for each polygon defined by the different locations of the free vertex are plotted in Fig. 7.5. We also plot the gradient, and consider different values for the minimal and maximal frequencies to see the influence of the frequency range on the cost.

During the execution of a randomly initialized gradient descent algorithm, every vertex would be allowed to move simultaneously, and so Fig. 7.5 does not completely render the complexity of the objective function's behavior. However, we can note that the function seems well-behaved when lower frequencies are included, and even looks locally convex around the true minimum. The profile of the function seems more complex when we exclude low frequencies. The impact of the first order reflection caused by the bottom room wall is clearly visible, especially for $f_{\min} = 50$ Hz, and $f_{\max} = 500$ Hz and when looking at the y derivative. However, the right wall has a lesser impact, as the corresponding reflection path is longer and thus the corresponding wave is damped.

7.4.4 Evaluation of the algorithm

We split the evaluation of the algorithm in two parts, in order to account for the two types of experiments (full geometry inference and refinement with noisy initialization).

Random initialization

Recall that in these experiments we have no initial guess on the shape, and we test multiple random initializations before starting the full gradient descent. This can cause the algorithm to converge to a very different shape from the target, as the number of starting polygons tested is limited. Fig. 7.6 and Fig. 7.7 present two applications of the algorithm in the case where the low frequencies are retained. The evolution of the objective function is plotted on the left and the best initial shape, the target and the estimated shapes are represented on the right. For the cost plot, the extension of the frequency range is represented by a dashed line. Note that increasing the maximal frequency causes a jump in the cost function. In the first case, the algorithm converges to the correct shape, and stops after reaching the minimal number of iterations of 1000 as the cost is below the threshold, with final mean errors $\overline{e_d} = 0.085$ mm, $\overline{e_{\boldsymbol{v}}} = 2.5$ cm, $\overline{e_\theta} = 0.47°$ and an error on the volume of $5.1 \cdot 10^{-5}$ m^2. However, the cost does not plateau, and additional gradient steps might have improved results. In the second case a local minimum is quickly reached after approximately 200 iterations, and the algorithm gets stuck far from the optimal shape with the errors $\overline{e_d} = 41$ cm, $\overline{e_{\boldsymbol{v}}} = 320$ cm, $\overline{e_\theta} = 65°$. However, it is notable that the error on volume remains quite low at $e_V = 0.32$ m^2. Two of the estimated walls are a relatively close match to the target walls, which could be explained by the

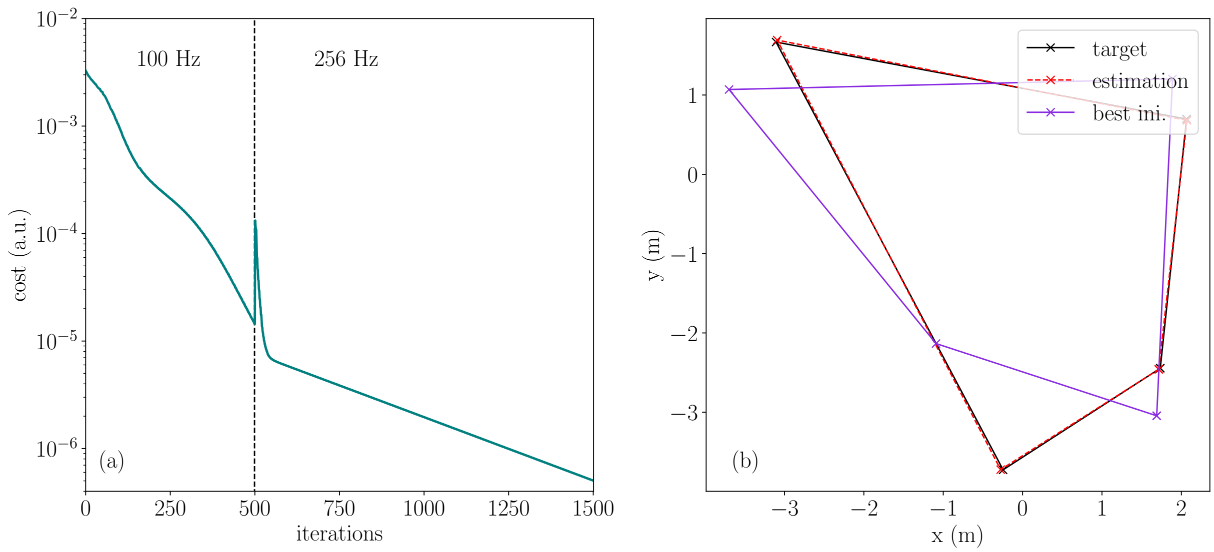

Figure 7.6: Successful shape optimization for a random room. Mean angular error: 0.47°, (a) cost as a function of iterations (b) best initial shape, target and final estimated shape after gradient descent.

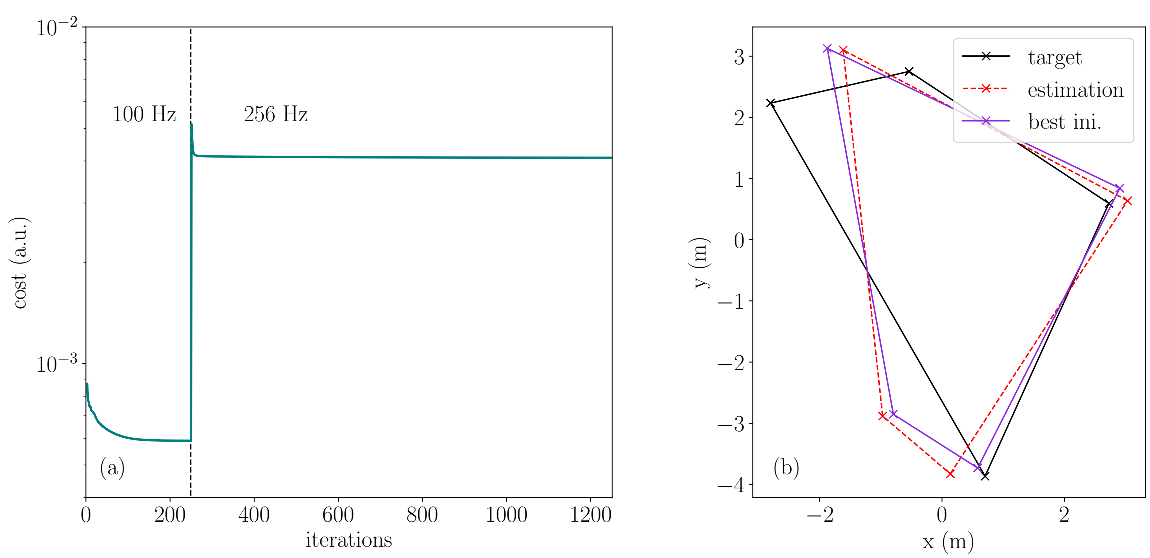

Figure 7.7: Failed shape optimization for a random room as the algorithm converges to a local minimum. (a) cost as a function of iterations (b) best initial shape, target and final estimated shape after gradient descent.

observations made in Section 7.4.3

The mean metrics obtained for the quadrilaterals and pentagons datasets are presented in Tab. 7.2. The means computed over the recovered walls only are displayed with the superscript $^{\text{rec}}$. Note that the volume error is computed over every room, including rooms that contain inaccurately recovered walls. Intriguingly, despite the presence of bad recoveries, the mean volume error remains low both for quadrilaterals and pentagons when low frequencies are available, which indicates the ability of the algorithm to recover intrinsic geometric properties of the room even when the shape itself is poorly approximated. We obtain low angular errors of 3.1° and 3.9° for the recovered walls, with negligible radial errors of 0.1 cm and 0.3 cm when using the full frequency range. In that case, the recall rates for the quadrilaterals' and pentagons' walls are respectively 90 % and 63 %. The algorithm demonstrates an ability to recover the shape, as long as the initialization is close enough to the target shape. This could be ensured by drastically increasing the number of random initializations tested, at a severe computational cost.

Whilst the mean errors for recovered walls remain quite similar when we remove the low frequencies, the recall rate drops drastically to 42 % for quadrilaterals and to 24 % for pentagons. This indicates that the algorithm is more likely to converge to a local minimum when the low frequencies are not available, and that the importance of a correct initialization is increased in that case. However, even if the recall rates are low, the algorithm still manages to recover the shape with a small error in that case when a decent initial guess is provided. The ability of the algorithm to converge to the true shape when a good initialization is provided is further illustrated in the next section. Moreover, note that the errors obtained for successfully recovered walls could be further reduced by increasing the number of gradient steps and relaxing the stopping criteria. This will also be shown in the next subsection.

Noisy initialization

We consider in this section the second type of experiments, *i.e.* a full gradient descent with an initial shape obtained by adding noise to the target shape, with measurements only available for $f \in [50 \text{ Hz}, 256 \text{ Hz}]$. The other parameters for the gradient descent are the same as those used for

$f_{\min}$ (Hz)	S	R (%)	$\overline{e_\theta}$ (°)	$\overline{e_d}$ (cm)	$\overline{e_{\boldsymbol{v}}}$ (cm)	$\overline{e_V}$ (m^2)	$\overline{e_\theta^{\text{rec}}}$ (°)	$\overline{e_d^{\text{rec}}}$ (cm)	$\overline{e_{\boldsymbol{v}}^{\text{rec}}}$ (cm)
0	4	90	5.8 ± 11	3.4 ± 18	32 ± 59	0.014 ± 0.047	3.1 ± 2.2	0.13 ± 0.14	17 ± 13
0	5	63	12 ± 16	10 ± 26	64 ± 82	0.091 ± 0.17	3.9 ± 2.1	0.27 ± 0.51	23 ± 22
50	4	42	21 ± 25	36 ± 66	130 ± 150	4.2 ± 4.5	2.8 ± 2.0	0.84 ± 1.4	32 ± 58
50	5	24	27 ± 26	49 ± 70	180 ± 150	6.9 ± 5.5	4.7 ± 2.5	1.0 ± 1.4	45 ± 51

Table 7.2: Mean angular $\overline{e_\theta}$, distance $\overline{e_d}$, vertex $\overline{e_{\boldsymbol{v}}}$, volume $\overline{e_V}$ error. Mean errors at the angular and distance thresholds $\varepsilon_\theta = 10°$ and $\varepsilon_d = 5$ cm are given by the superscript $^{\text{rec}}$, and the corresponding recall rate is denoted by R.

S	$\overline{e_\theta}$ (°)	$\overline{e_d}$ (cm)	$\overline{e_{\boldsymbol{v}}}$ (cm)	$\overline{e_\theta^{\text{ini}}}$ (°)	$\overline{e_d^{\text{ini}}}$ (cm)	$\overline{e_{\boldsymbol{v}}^{\text{ini}}}$ (cm)
4	0.257 ± 0.207	0.0133 ± 0.0206	1.41 ± 1.15	19.0 ± 18.5	7.55 ± 5.29	26.8 ± 16.6
5	1.24 ± 4.24	3.92 ± 25.2	7.08 ± 24.3	21.0 ± 15.9	7.64 ± 6.20	25.8 ± 18.1

Table 7.3: Mean angular $\overline{e_\theta}$, distance $\overline{e_d}$, vertex $\overline{e_{\boldsymbol{v}}}$. The mean initial errors are denoted by the superscript $^{\text{ini}}$, and S is the number of vertices.

previous experiments. Tab. 7.3 gives the values of the mean initial and final errors for quadrilaterals and pentagons. We observe in both cases a sharp improvement in angular error, as the mean error is approximately divided by 70 for quadrilaterals and 20 for pentagons. Similarly, wall distance errors are significantly reduced. For quadrilaterals the errors become negligible with less than 0.5° angular error and less than 1 mm wall distance error, indicating true convergence to the target polygon for every room. We can however note a difference in performance between quadrilaterals and pentagons, due in part to some failure cases in the pentagon dataset. Indeed, the recall at 10° of angular error and 5 cm wall distance error is 100 % for the walls of the quadrilaterals' dataset, and 96 % for pentagons. The algorithm thus failed to converge to the target room for several pentagons. The impact of the few failure cases can be seen by noticing the especially high standard deviations for the mean errors on pentagons. We still obtain satisfactory errors for pentagons, with 1.2° mean angular error and 3.9 cm mean wall distance error. Note that these errors decrease respectively to 0.53° and 0.36 cm if we proceed as in the last section and consider only the walls localized with lower errors than the fixed threshold, yielding errors on the same order of magnitude as those obtained for quadrilaterals.

Finally, note that the initial noise levels here are above the errors obtained for the recovered walls of last section. This indicates in particular that similar accuracy could be achieved using a limited number of random initializations by simply letting the gradient descent continue for a higher number of iterations, as the initializations used in this section are usually worse estimations of the target shape than the end results of last section's gradient descents. The errors obtained are thus in great part bounded by the stopping criteria used, which can be relaxed at the cost of greater computational requirements. This also further validates the ability of the algorithm to converge to the right shape when using random initializations, as long as a sufficient number of initializations are tested.

7.5 Conclusion

We presented a shape optimization method to recover the boundary of a polygonal room from partial frequency measurements of a multichannel room impulse response. We formally computed a boundary formulation of the shape derivative, which included non-standard terms due to the irregularity of the boundary. We then implemented a shape gradient descent algorithm, which was evaluated on a dataset consisting of random rooms. Whilst the proposed algorithm demonstrated an ability to accurately reconstruct the boundary of a room in our preliminary numerical results, the gradient descent algorithm is highly dependent on initialization, especially when limiting the access to lower frequencies. In its current state, the performance of the algorithm seems mainly limited by the computing budget allowed, as using a greater number of random initializations would ultimately yield a first guess sufficiently close to the target shape. This constitutes a first encouraging step towards the development of a shape optimization algorithm for room acoustics. Several avenues for improvement will be presented in the general conclusion.

General conclusion and perspectives

We presented two very different approaches to the problem of hearing the shape of a room, following the questions raised in the introduction.

The first approach, based on the Image Source Method, displays an impressive ability to recover the geometry of a cuboid room from a single multichannel RIR recorded at a compact microphone array. However, the proposed approach is currently not directly applicable to real measured RIRs. This is mainly because the image source localization method it relies upon is specifically designed to reverse the forward image-source model, which makes a number of simplifying assumptions that do not hold in reality. A path towards real-data applicability can nevertheless be envisioned. For this, the algorithm of Section 2.3.3 would need to be extended to take into account both angular and frequency dependencies of receiver, source, and wall responses. Even assuming the responses of the source and microphones are known, and using a physics-based model for the angular dependencies of wall responses, the number of unknowns in the problem is then significantly increased. Namely, one needs to additionally estimate the source (and image sources) orientations, as well as a frequency-dependent impedance for each wall. One could try to make the inverse problem tractable by adding physical or geometrical constraints on these unknowns. Restricting the observed frequency range could also be a first step towards applicability to real data, as the presented model can directly be translated to a frequency-domain formulation. The translation of the source localization method to general polyhedra is not obvious, as one would have to factor in image-source occlusions, *i.e.* configurations where a source is not visible from a given microphone location. The generalization of the proposed geometry recovery algorithm to arbitrary geometries is also not straightforward.

The second approach overcomes some limitations of the first by removing the restriction to cuboid geometries and adopting a more realistic physical model for sound absorption. Numerical experiments show that the method can recover the shape of a polygonal room from simulated RIRs, given sufficient computational budget. However, it still falls short of being applicable to real-world data. One major limitation is the high computational cost due to the numerous initializations needed to ensure the algorithm converges to the target shape, especially when the frequency range excludes low frequencies. One potential improvement would be to use a preprocessing algorithm, such as one based on specular reflections and the ISM, to get a rough initial guess for the walls' locations. Another possibility is to add a stochastic element, by activating either random frequencies or microphones at each iteration. Note that when using the MFS, changing the number of microphone measurements has a limited impact on computational cost, whilst limiting the number of used frequency reduces the simulation time. The influence of microphone and source positioning can also be investigated. Using multiple sources can be considered, as it reduces ambiguities in the measurements. This can be achieved either by considering simultaneous sources, which has a negligible impact on computation time, or by considering separate emission times, in which case an additional simulation per source is required. Another issue is maintaining convexity during iterations. This could be enforced by penalizing each angle of the polygon. Similarly, the length of each edge can be penalized, in order to avoid degenerate shapes. It would also be possible to compute the derivative with respect to β

and alternate gradient steps between geometry and impedance optimization, or to use a different algorithm altogether to estimate β, as the impedance is usually an unknown of the problem. A theoretical study of the shape derivative has still to be performed beyond the formal computations, and will be the subject of a future publication. The directivity of the source could be added to the simulation model, for instance by considering the multipole model described in [20]. Finally, the method could be applied to 3D room shapes. This would however require adapting the MFS, as the corner functions developed in [14] for 2D polygons do not directly generalize to 3D polyhedra.

Whilst we highlighted the limitations of the proposed methods, the first numerical results demonstrate that both approaches are promising stepping stones towards the application to real-world data.

Bibliography

[1] Lekbir Afraites, Chorouk Masnaoui, and Mourad Nachaoui. Shape optimization method for an inverse geometric source problem and stability at critical shape. *Discrete Contin. Dyn. Syst. Ser. S*, 15(1):1–21, 2022.

[2] Mark Ainsworth. Discrete dispersion relation for hp-version finite element approximation at high wave number. *SIAM Journal on Numerical Analysis*, 42(2):553–575, 2004.

[3] Mark Ainsworth and J Tinsley Oden. A posteriori error estimation in finite element analysis. *Computer methods in applied mechanics and engineering*, 142(1-2):1–88, 1997.

[4] Grégoire Allaire, Charles Dapogny, and François Jouve. Shape and topology optimization. In *Handbook of numerical analysis*, volume 22, pages 1–132. Elsevier, 2021.

[5] Jont B Allen and David A Berkley. Image method for efficiently simulating small-room acoustics. *The Journal of the Acoustical Society of America*, 65(4):943–950, 1979.

[6] Carlos JS Alves and Pedro RS Antunes. The method of fundamental solutions applied to the calculation of eigenfrequencies and eigenmodes of 2d simply connected shapes. *CMC-TECH SCIENCE PRESS-*, 2(4):251, 2005.

[7] Carlos JS Alves and Pedro RS Antunes. The method of fundamental solutions applied to some inverse eigenproblems. *SIAM Journal on Scientific Computing*, 35(3):A1689–A1708, 2013.

[8] Fabio Antonacci, Jason Filos, Mark RP Thomas, Emanuël AP Habets, Augusto Sarti, Patrick A Naylor, and Stefano Tubaro. Inference of room geometry from acoustic impulse responses. *IEEE Transactions on Audio, Speech, and Language Processing*, 20(10):2683–2695, 2012.

[9] Fabio Antonacci, Augusto Sarti, and Stefano Tubaro. Geometric reconstruction of the environment from its response to multiple acoustic emissions. In *2010 IEEE International Conference on Acoustics, Speech and Signal Processing*, pages 2822–2825. IEEE, 2010.

[10] Niccolò Antonello, Toon van Waterschoot, Marc Moonen, and Patrick A Naylor. Evaluation of a numerical method for identifying surface acoustic impedances in a reverberant room. In *Proc. of the10th European Congress and Exposition on Noise Control Engineering*, pages 1–6, 2015.

[11] Julieta António, Antonio Tadeu, and Luís Godinho. A three-dimensional acoustics model using the method of fundamental solutions. *Engineering Analysis with Boundary Elements*, 32(6):525–531, 2008.

[12] Pedro Ricardo Simão Antunes and Filippo Gazzola. Convex shape optimization for the least biharmonic steklov eigenvalue. *ESAIM: Control, Optimisation and Calculus of Variations*, 19(2):385–403, 2013.

[13] Pedro RS Antunes and Beniamin Bogosel. Parametric shape optimization using the support function. *Computational Optimization and Applications*, 82(1):107–138, 2022.

[14] Pedro RS Antunes and Svilen S Valtchev. A meshfree numerical method for acoustic wave propagation problems in planar domains with corners and cracks. *Journal of Computational and Applied Mathematics*, 234(9):2646–2662, 2010.

[15] Jean-Marc Azais, Yohann De Castro, and Fabrice Gamboa. Spike detection from inaccurate samplings. *Applied and Computational Harmonic Analysis*, 38(2):177–195, 2015.

[16] Mingsian R Bai. Application of bem (boundary element method)-based acoustic holography to radiation analysis of sound sources with arbitrarily shaped geometries. *The Journal of the Acoustical Society of America*, 92(1):533–549, 1992.

[17] Harry Bateman. *Tables of integral transforms*, volume 1. McGraw-Hill book company, 1954.

[18] Nancy Bertin, Srdjan Kitić, and Rémi Gribonval. Joint estimation of sound source location and boundary impedance with physics-driven cosparse regularization. In *IEEE international conference on acoustics, speech and signal processing (ICASSP)*, pages 6340–6344. IEEE, 2016.

[19] H Nazim Bicer, Cagdas Tuna, Andreas Walther, and Emanuël AP Habets. Data-driven joint detection and localization of acoustic reflectors. *arXiv preprint arXiv:2402.06246*, 2024.

[20] Stefan Bilbao and Brian Hamilton. Directional sources in wave-based acoustic simulation. *IEEE/ACM Transactions on Audio, Speech, and Language Processing*, 27(2):415–428, 2018.

[21] Beniamin Bogosel. Numerical shape optimization among convex sets. *Applied Mathematics & Optimization*, 87(1):1, 2023.

[22] Jeffrey Borish. Extension of the image model to arbitrary polyhedra. *The Journal of the Acoustical Society of America*, 75(6):1827–1836, 1984.

[23] Nicholas Boyd, Geoffrey Schiebinger, and Benjamin Recht. The alternating descent conditional gradient method for sparse inverse problems. *SIAM Journal on Optimization*, 27(2):616–639, 2017.

[24] Claire Boyer, Antonin Chambolle, Yohann De Castro, Vincent Duval, Frédéric De Gournay, and Pierre Weiss. On representer theorems and convex regularization. *SIAM Journal on Optimization*, 29(2):1260–1281, 2019.

[25] Kristian Bredies and Hanna Katriina Pikkarainen. Inverse problems in spaces of measures. *ESAIM: Control, Optimisation and Calculus of Variations*, 19(1):190–218, 2013.

[26] Haim Brezis and Haim Brézis. *Functional analysis, Sobolev spaces and partial differential equations*, volume 2. Springer, 2011.

[27] Michel Bruneau. *Fundamentals of acoustics*. John Wiley & Sons, 2013.

[28] Pierre-Jean Bénard, Yann Traonmilin, and Jean-Francois Aujol. Fast off-the-grid sparse recovery with over-parametrized projected gradient descent. In *30th European Signal Processing Conference (EUSIPCO)*, pages 2206–2210. IEEE, 2022.

[29] Antonio Canclini, Paolo Annibale, Fabio Antonacci, Augusto Sarti, Rudolf Rabenstein, and Stefano Tubaro. From direction of arrival estimates to localization of planar reflectors in a two dimensional geometry. In *2011 IEEE International Conference on Acoustics, Speech and Signal Processing (ICASSP)*, pages 2620–2623. IEEE, 2011.

[30] Antonio Canclini, Fabio Antonacci, Mark RP Thomas, Jason Filos, Augusto Sarti, Patrick A Naylor, and Stefano Tubaro. Exact localization of acoustic reflectors from quadratic constraints. In *2011 IEEE Workshop on Applications of Signal Processing to Audio and Acoustics (WASPAA)*, pages 17–20. IEEE, 2011.

[31] Emmanuel J Candès and Carlos Fernandez-Granda. Super-resolution from noisy data. *Journal of Fourier Analysis and Applications*, 19:1229–1254, 2013.

[32] Emmanuel J Candès and Carlos Fernandez-Granda. Towards a mathematical theory of super-resolution. *Communications on pure and applied Mathematics*, 67(6):906–956, 2014.

[33] Diego Di Carlo, Pinchas Tandeitnik, Cedric Foy, Nancy Bertin, Antoine Deleforge, and Sharon Gannot. dEchorate: a calibrated room impulse response dataset for echo-aware signal processing. *EURASIP Journal on Audio, Speech, and Music Processing*, 2021(1):1–15, 2021.

[34] Jean Céa. Conception optimale ou identification de formes, calcul rapide de la dérivée directionnelle de la fonction coût. *ESAIM: Modélisation mathématique et analyse numérique*, 20(3):371–402, 1986.

[35] SN Chandler-Wilde, S Langdon, and L Ritter. A high–wavenumber boundary–element method for an acoustic scattering problem. *Philosophical Transactions of the Royal Society of London. Series A: Mathematical, Physical and Engineering Sciences*, 362(1816):647–671, 2004.

[36] Gilles Chardon. Gridless covariance matrix fitting methods for three dimensional acoustical source localization. *Journal of Sound and Vibration*, 551:117608, 2023.

[37] Gilles Chardon and Ulysse Boureau. Gridless three-dimensional compressive beamforming with the sliding frank-wolfe algorithm. *The Journal of the Acoustical Society of America*, 150(4):3139–3148, 2021.

[38] Scott Shaobing Chen, David L Donoho, and Michael A Saunders. Atomic decomposition by basis pursuit. *SIAM review*, 43(1):129–159, 2001.

[39] Yuejie Chi, Louis L Scharf, Ali Pezeshki, and A Robert Calderbank. Sensitivity to basis mismatch in compressed sensing. *IEEE Transactions on Signal Processing*, 59(5):2182–2195, 2011.

[40] Lenaic Chizat. Sparse optimization on measures with over-parameterized gradient descent. *Mathematical Programming*, 194(1):487–532, 2022.

[41] Lenaic Chizat and Francis Bach. On the global convergence of gradient descent for over-parameterized models using optimal transport. *Advances in neural information processing systems*, 31, 2018.

[42] Robert D Ciskowski and Carlos Alberto Brebbia. *Boundary element methods in acoustics*, volume 20. Springer, 1991.

[43] A Colaço, P Alves Costa, C Mont'Alverne Parente, and A Silva Cardoso. Ground-borne noise and vibrations in buildings induced by pile driving: An integrated approach. *Applied Acoustics*, 179:108059, 2021.

[44] Laurent Condat and Akira Hirabayashi. Cadzow denoising upgraded: A new projection method for the recovery of dirac pulses from noisy linear measurements. *Sampling Theory in Signal and Image Processing*, 14(1):17–47, 2015.

[45] Marco Crocco and Alessio Del Bue. Estimation of TDOA for room reflections by iterative weighted l_1 constraint. In *IEEE International Conference on Acoustics, Speech and Signal Processing (ICASSP)*, pages 3201–3205. IEEE, 2016.

[46] Stefano Damiano, Federico Borra, Alberto Bernardini, Fabio Antonacci, and Augusto Sarti. Soundfield reconstruction in reverberant rooms based on compressive sensing and image-source models of early reflections. In *IEEE Workshop on Applications of Signal Processing to Audio and Acoustics (WASPAA)*, pages 366–370. IEEE, 2021.

[47] E Brian Davies. *Spectral theory and differential operators*, volume 42. Cambridge University Press, 1995.

[48] Yohann De Castro and Fabrice Gamboa. Exact reconstruction using beurling minimal extrapolation. *Journal of Mathematical Analysis and applications*, 395(1):336–354, 2012.

[49] Yohann De Castro, Fabrice Gamboa, Didier Henrion, and J-B Lasserre. Exact solutions to super resolution on semi-algebraic domains in higher dimensions. *IEEE Transactions on Information Theory*, 63(1):621–630, 2016.

[50] Michel C Delfour and J-P Zolésio. *Shapes and geometries: metrics, analysis, differential calculus, and optimization*. SIAM, 2011.

[51] Michel C Delfour and Jean-Paul Zolésio. Structure of shape derivatives for nonsmooth domains. *Journal of Functional Analysis*, 104(1):1–33, 1992.

[52] Quentin Denoyelle, Vincent Duval, and Gabriel Peyré. Support recovery for sparse super-resolution of positive measures. *Journal of Fourier Analysis and Applications*, 23:1153–1194, 2017.

[53] Quentin Denoyelle, Vincent Duval, Gabriel Peyré, and Emmanuel Soubies. The Sliding Frank-Wolfe Algorithm and its Application to Super-Resolution Microscopy. *Inverse Problems*, 2019.

[54] Diego Di Carlo. *Echo-aware signal processing for audio scene analysis*. PhD thesis, UNIVERSITÉ DE RENNES 1; INRIA-IRISA-PANAMA, 2020.

[55] Diego Di Carlo, Clement Elvira, Antoine Deleforge, Nancy Bertin, and Rémi Gribonval. Blaster: An off-grid method for blind and regularized acoustic echoes retrieval. In *IEEE International Conference on Acoustics, Speech and Signal Processing (ICASSP)*, pages 156–160. IEEE, 2020.

[56] Stéphane Dilungana, Antoine Deleforge, Cédric Foy, and Sylvain Faisan. Geometry-informed estimation of surface absorption profiles from room impulse responses. In *30th European Signal Processing Conference (EUSIPCO)*, pages 867–871. IEEE, 2022.

[57] Ivan Dokmanić, Yue M Lu, and Martin Vetterli. Can one hear the shape of a room: The 2-d polygonal case. In *2011 IEEE International Conference on Acoustics, Speech and Signal Processing (ICASSP)*, pages 321–324. IEEE, 2011.

[58] Ivan Dokmanić, Reza Parhizkar, Andreas Walther, Yue M Lu, and Martin Vetterli. Acoustic echoes reveal room shape. *Proceedings of the National Academy of Sciences*, 110(30):12186–12191, 2013.

[59] Ivan Dokmanić and Martin Vetterli. Room helps: Acoustic localization with finite elements. In *2012 IEEE International Conference on Acoustics, Speech and Signal Processing (ICASSP)*, pages 2617–2620. Ieee, 2012.

[60] Vincent Duval and Gabriel Peyré. Exact Support Recovery for Sparse Spikes Deconvolution. *Foundations of Computational Mathematics*, 15(5):1315–1355, 2015.

[61] Youssef El Baba, Andreas Walther, and Emanuël AP Habets. 3D room geometry inference based on room impulse response stacks. *IEEE/ACM Transactions on Audio, Speech, and Language Processing*, 26(5):857–872, 2017.

[62] Lawrence C Evans. *Partial differential equations*, volume 19. American Mathematical Society, 2022.

[63] LawrenceCraig Evans. *Measure theory and fine properties of functions*. Routledge, 2018.

[64] Charbel Farhat, Isaac Harari, and Leopoldo P Franca. The discontinuous enrichment method. *Computer methods in applied mechanics and engineering*, 190(48):6455–6479, 2001.

[65] Carlos Fernandez-Granda. Support detection in super-resolution. *arXiv preprint arXiv:1302.3921*, 2013.

[66] Jason Filos, Antonio Canclini, Fabio Antonacci, Augusto Sarti, and Patrick A Naylor. Localization of planar acoustic reflectors from the combination of linear estimates. In *2012 Proceedings of the 20th European Signal Processing Conference (EUSIPCO)*, pages 1019–1023. IEEE, 2012.

[67] Jason Filos, Emanuël AP Habets, and Patrick A Naylor. A two-step approach to blindly infer room geometries. In *Proc. Int. Workshop Acoust. Echo Noise Control (IWAENC)*. Citeseer, 2010.

[68] Marguerite Frank, Philip Wolfe, et al. An algorithm for quadratic programming. *Naval research logistics quarterly*, 3(1-2):95–110, 1956.

[69] G Fremiot. Eulerian semiderivatives of the eigenvalues for laplacian in domains with cracks. *ADVANCES IN MATHEMATICAL SCIENCES AND APPLICATIONS*, 12(1):115–134, 2002.

[70] Friedrich Gerard Friedlander. *Introduction to the Theory of Distributions*. Cambridge University Press, 1998.

[71] Florian Gerber. optimparallel - A parallel version of scipy.optimize. minimize(method='L-BFGS-B'), June 2020. https://doi.org/10.5281/ zenodo.3888570.

[72] L Godinho, P Amado Mendes, J Ramis, W Cardenas, and J Carbajo. A numerical mfs model for computational analysis of acoustic horns. *Acta Acustica united with Acustica*, 98(6):916–927, 2012.

[73] LMC Godinho, EGA Costa, ASC Pereira, and JAF Santiago. Some observations on the behavior of the method of fundamental solutions in 3d acoustic problems. *International Journal of Computational Methods*, 9(04):1250049, 2012.

[74] Loukas Grafakos et al. *Classical fourier analysis*, volume 2. Springer, 2008.

[75] Denis S Grebenkov and B-T Nguyen. Geometrical structure of laplacian eigenfunctions. *siam REVIEW*, 55(4):601–667, 2013.

[76] Pierre Grisvard. *Elliptic problems in nonsmooth domains.* SIAM, 2011.

[77] Pierre-Amaury Grumiaux, Srdan Kitić, Laurent Girin, and Alexandre Guérin. A survey of sound source localization with deep learning methods. *The Journal of the Acoustical Society of America*, 152(1):107–151, 2022.

[78] Isaac Harari and Thomas JR Hughes. Galerkin/least-squares finite element methods for the reduced wave equation with non-reflecting boundary conditions in unbounded domains. *Computer methods in applied mechanics and engineering*, 98(3):411–454, 1992.

[79] Jaroslav Haslinger and Raino AE Mäkinen. *Introduction to shape optimization: theory, approximation, and computation.* SIAM, 2003.

[80] Antoine Henrot. *Shape optimization and spectral theory.* De Gruyter Open, 2017.

[81] Antoine Henrot and Michel Pierre. *Shape variation and optimization.* European Mathematical Society, 2018.

[82] Bo Huang, Mark Bates, and Xiaowei Zhuang. Super resolution fluorescence microscopy. *Annual review of biochemistry*, 78:993, 2009.

[83] Simona Irimie and Ph Bouillard. A residual a posteriori error estimator for the finite element solution of the helmholtz equation. *Computer methods in applied mechanics and engineering*, 190(31):4027–4042, 2001.

[84] Ingmar Jager, Richard Heusdens, and Nikolay D Gaubitch. Room geometry estimation from acoustic echoes using graph-based echo labeling. In *IEEE International Conference on Acoustics, Speech and Signal Processing (ICASSP)*, pages 1–5. IEEE, 2016.

[85] Martin Jaggi. Revisiting frank-wolfe: Projection-free sparse convex optimization. In *International conference on machine learning*, pages 427–435. PMLR, 2013.

[86] Mark Kac. Can one hear the shape of a drum? *The american mathematical monthly*, 73(4P2):1–23, 1966.

[87] Andreas Karageorghis and D Lesnic. The pressure-stream function mfs formulation for the detection of an obstacle immersed in a two-dimensional stokes flow. *Adv. Appl. Math. Mech*, 2(2):183–199, 2010.

[88] Andreas Karageorghis, D Lesnic, and L Marin. The method of fundamental solutions for the identification of a scatterer with impedance boundary condition in interior inverse acoustic scattering. *Engineering analysis with boundary elements*, 92:218–224, 2018.

[89] Stephen Martin Kirkup. *The boundary element method in acoustics*. Integrated sound software, 2007.

[90] Victor A Kovtunenko and Karl Kunisch. Shape derivative for penalty-constrained nonsmooth–nonconvex optimization: cohesive crack problem. *Journal of Optimization Theory and Applications*, 194(2):597–635, 2022.

[91] Konrad Kowalczyk, Emanuël AP Habets, Walter Kellermann, and Patrick A Naylor. Blind system identification using sparse learning for TDOA estimation of room reflections. *IEEE Signal Processing Letters*, 20(7):653–656, 2013.

[92] Shoichi Koyama and Laurent Daudet. Sparse representation of a spatial sound field in a reverberant environment. *IEEE Journal of Selected Topics in Signal Processing*, 13(1):172–184, 2019.

[93] Sacha Krstulovic and Rémi Gribonval. Mptk: Matching pursuit made tractable. In *2006 IEEE International Conference on Acoustics Speech and Signal Processing Proceedings*, volume 3, pages III–III. IEEE, 2006.

[94] Stefan Kunis, Thomas Peter, Tim Römer, and Ulrich von der Ohe. A multivariate generalization of prony's method. *Linear Algebra and its Applications*, 490:31–47, 2016.

[95] Martin Kuster, Diemer de Vries, EM Hulsebos, and A Gisolf. Acoustic imaging in enclosed spaces: Analysis of room geometry modifications on the impulse response. *The Journal of the Acoustical Society of America*, 116(4):2126–2137, 2004.

[96] Heinrich Kuttruff and Eckard Mommertz. Room acoustics. In *Handbook of engineering acoustics*, pages 239–267. Springer, 2012.

[97] Ignacio Labarca and Ralf Hiptmair. Acoustic scattering problems with convolution quadrature and the method of fundamental solutions. *Commun. Comput. Phys.*, 30(4):985–1008, 2021.

[98] Thomas Lachand-Robert and Édouard Oudet. Minimizing within convex bodies using a convex hull method. *SIAM Journal on Optimization*, 16(2):368–379, 2005.

[99] Jimmy Lamboley, Arian Novruzi, and Michel Pierre. Estimates of first and second order shape derivatives in nonsmooth multidimensional domains and applications. *Journal of Functional Analysis*, 270(7):2616–2652, 2016.

[100] Jimmy Lamboley and Michel Pierre. Structure of shape derivatives around irregular domains and applications. *Journal of Convex Analysis*, 14(4):807–822, 2007.

[101] Christophe Langrenne, Manuel Melon, and Alexandre Garcia. Boundary element method for the acoustic characterization of a machine in bounded noisy environment. *The Journal of the Acoustical Society of America*, 121(5):2750–2757, 2007.

[102] Jean Bernard Lasserre. *Moments, positive polynomials and their applications*, volume 1. World Scientific, 2009.

[103] Antoine Laurain. Distributed and boundary expressions of first and second order shape derivatives in nonsmooth domains. *Journal de Mathématiques Pures et Appliquées*, 134:328–368, 2020.

[104] Antoine Laurain and Kevin Sturm. Distributed shape derivative via averaged adjoint method and applications. *ESAIM: Mathematical Modelling and Numerical Analysis*, 50(4):1241–1267, 2016.

[105] Michael Lovedee-Turner and Damian Murphy. Three-dimensional reflector localisation and room geometry estimation using a spherical microphone array. *The Journal of the Acoustical Society of America*, 146(5):3339–3352, 2019.

[106] Edwin Mabande, Konrad Kowalczyk, Haohai Sun, and Walter Kellermann. Room geometry inference based on spherical microphone array eigenbeam processing. *The Journal of the Acoustical Society of America*, 134(4):2773–2789, 2013.

[107] Steffen Marburg. Boundary element method for time-harmonic acoustic problems. *Computational Acoustics*, pages 69–158, 2018.

[108] Dejan Markovic, Fabio Antonacci, Augusto Sarti, and Stefano Tubaro. Estimation of room dimensions from a single impulse response. In *2013 IEEE Workshop on Applications of Signal Processing to Audio and Acoustics*, pages 1–4. IEEE, 2013.

[109] Dejan Markovic, Fabio Antonacci, Augusto Sarti, and Stefano Tubaro. Soundfield imaging in the ray space. *IEEE Transactions on Audio, Speech, and Language Processing*, 21(12):2493–2505, 2013.

[110] Nuno FM Martins. An iterative shape reconstruction of source functions in a potential problem using the mfs. *Inverse Problems in Science and Engineering*, 20(8):1175–1193, 2012.

[111] Nuno FM Martins and Ana L Silvestre. An iterative mfs approach for the detection of immersed obstacles. *Engineering analysis with boundary elements*, 32(6):517–524, 2008.

[112] Rudolf Mathon and Robert Laurence Johnston. The approximate solution of elliptic boundary-value problems by fundamental solutions. *SIAM Journal on Numerical Analysis*, 14(4):638–650, 1977.

[113] Yasushi Miki. Acoustical properties of porous materials-modifications of delany-bazley models. *Journal of the Acoustical Society of Japan (E)*, 11(1):19–24, 1990.

[114] Alastair H Moore, Mike Brookes, and Patrick A Naylor. Room geometry estimation from a single channel acoustic impulse response. In *21st European Signal Processing Conference (EUSIPCO 2013)*, pages 1–5. IEEE, 2013.

[115] Veniamin I Morgenshtern and Emmanuel J Candes. Super-resolution of positive sources: The discrete setup. *SIAM Journal on Imaging Sciences*, 9(1):412–444, 2016.

[116] Yusuke Naka, Assad A Oberai, and Barbara G Shinn-Cunningham. Acoustic eigenvalues of rectangular rooms with arbitrary wall impedances using the interval newton/ generalized bisection method. *The Journal of the Acoustical Society of America*, 118(6):3662–3671, 2005.

[117] E Nastasia, Fabio Antonacci, Augusto Sarti, and Stefano Tubaro. Localization of planar acoustic reflectors through emission of controlled stimuli. In *2011 19th European Signal Processing Conference*, pages 156–160. IEEE, 2011.

[118] Gabriel Pablo Nava, Yosuke Yasuda, Yoichi Sato, and Shinichi Sakamoto. On the in situ estimation of surface acoustic impedance in interiors of arbitrary shape by acoustical inverse methods. *Acoustical science and technology*, 30(2):100–109, 2009.

[119] Yukiko Okawa, Yasuaki Watanabe, Yusuke Ikeda, and Yasuhiro Oikawa. Estimation of acoustic impedances in a room using multiple sound intensities and fdtd method. In *Advances in Acoustics, Noise and Vibration-Proceedings of the 27th International Congress on Sound and Vibration, ICSV*, 2021.

[120] Fabian Pedregosa, Gaël Varoquaux, Alexandre Gramfort, Vincent Michel, Bertrand Thirion, Olivier Grisel, Mathieu Blondel, Peter Prettenhofer, Ron Weiss, Vincent Dubourg, et al. Scikit-learn: Machine learning in python. *the Journal of machine Learning research*, 12:2825–2830, 2011.

[121] Sönke Pelzer, Marc Aretz, and Michael Vorländer. Quality assessment of room acoustic simulation tools by comparing binaural measurements and simulations in an optimized test scenario. In *Proc. Forum Acusticum Aalborg*, 2011.

[122] Thomas Peter, Gerlind Plonka, and Robert Schaback. Prony's method for multivariate signals. *Pamm*, 15(1):665–666, 2015.

[123] Sebastian Pokutta. The frank-wolfe algorithm: a short introduction. *Jahresbericht der Deutschen Mathematiker-Vereinigung*, 126(1):3–35, 2024.

[124] Clarice Poon and Gabriel Peyré. Multidimensional sparse super-resolution. *SIAM Journal on Mathematical Analysis*, 51(1):1–44, 2019.

[125] Tilak Rajapaksha, Xiaojun Qiu, Eva Cheng, and Ian Burnett. Geometrical room geometry estimation from room impulse responses. In *2016 IEEE International Conference on Acoustics, Speech and Signal Processing (ICASSP)*, pages 331–335. IEEE, 2016.

[126] Luca Remaggi, Philip JB Jackson, Philip Coleman, and Wenwu Wang. Acoustic reflector localization: Novel image source reversion and direct localization methods. *IEEE/ACM Transactions on Audio, Speech, and Language Processing*, 25(2):296–309, 2016.

[127] Luca Remaggi, Philip JB Jackson, Wenwu Wang, and Jonathon A Chambers. A 3d model for room boundary estimation. In *2015 IEEE International Conference on Acoustics, Speech and Signal Processing (ICASSP)*, pages 514–518. IEEE, 2015.

[128] Luca Remaggi, Hansung Kim, Philip JB Jackson, Filippo Maria Fazi, and Adrian Hilton. Acoustic reflector localization and classification. In *IEEE International Conference on Acoustics, Speech and Signal Processing (ICASSP)*, pages 201–205. IEEE, 2018.

[129] Flavio Ribeiro, Dinei Florencio, Demba Ba, and Cha Zhang. Geometrically constrained room modeling with compact microphone arrays. *IEEE Transactions on Audio, Speech, and Language Processing*, 20(5):1449–1460, 2011.

[130] Richard Roy and Thomas Kailath. Esprit-estimation of signal parameters via rotational invariance techniques. *IEEE Transactions on acoustics, speech, and signal processing*, 37(7):984–995, 1989.

[131] Walter Rudin. *Real and complex analysis, 3rd ed.* McGraw-Hill, Inc., USA, 1987.

[132] Ralph Schmidt. Multiple emitter location and signal parameter estimation. *IEEE transactions on antennas and propagation*, 34(3):276–280, 1986.

[133] Tom Shlomo and Boaz Rafaely. Blind amplitude estimation of early room reflections using alternating least squares. In *IEEE International Conference on Acoustics, Speech and Signal Processing (ICASSP)*, pages 476–480. IEEE, 2021.

[134] Tom Shlomo and Boaz Rafaely. Blind localization of early room reflections using phase aligned spatial correlation. *IEEE transactions on signal processing*, 69:1213–1225, 2021.

[135] M Souli, JP Zolesio, and A Ouahsine. Shape optimization for non-smooth geometry in two dimensions. *Computer methods in applied mechanics and engineering*, 188(1-3):109–119, 2000.

[136] Tom Sprunck, Antoine Deleforge, Yannick Privat, and Cédric Foy. Gridless 3d recovery of image sources from room impulse responses. *IEEE Signal Processing Letters*, 29:2427–2431, 2022.

[137] Tom Sprunck, Antoine Deleforge, Yannick Privat, and Cédric Foy. Fully reversing the shoebox image source method: From impulse responses to room parameters. *arXiv preprint arXiv:2405.03385*, 2024.

[138] Prerak Srivastava. *Realism in virtually supervised learning for acoustic room characterization and sound source localization.* PhD thesis, Université de Lorraine, 2023.

[139] Haohai Sun, Edwin Mabande, Konrad Kowalczyk, and Walter Kellermann. Localization of distinct reflections in rooms using spherical microphone array eigenbeam processing. *The Journal of the Acoustical Society of America*, 131(4):2828–2840, 2012.

[140] Julius Fergy T Rabago and Hideyuki Azegami. Shape optimization approach to defect-shape identification with convective boundary condition via partial boundary measurement. *Japan Journal of Industrial and Applied Mathematics*, 36:131–176, 2019.

[141] Sakari Tervo and Teemu Korhonen. Estimation of reflective surfaces from continuous signals. In *IEEE International Conference on Acoustics, Speech and Signal Processing (ICASSP)*, pages 153–156. IEEE, 2010.

[142] Sakari Tervo and Archontis Politis. Direction of arrival estimation of reflections from room impulse responses using a spherical microphone array. *IEEE/ACM Transactions on Audio, Speech, and Language Processing*, 23(10):1539–1551, 2015.

[143] Lonny L Thompson. A review of finite-element methods for time-harmonic acoustics. *The Journal of the Acoustical Society of America*, 119(3):1315–1330, 2006.

[144] Reiji Tomiku, Toru Otsuru, and Yasuo Takahashi. Finite element sound field analysis of diffuseness in reverberation rooms. *Journal of Asian Architecture and building engineering*, 1(2):33–39, 2002.

[145] Ana M Torres, Jose J Lopez, Basilio Pueo, and Maximo Cobos. Room acoustics analysis using circular arrays: An experimental study based on sound field plane-wave decomposition. *The Journal of the Acoustical Society of America*, 133(4):2146–2156, 2013.

[146] Yann Traonmilin and Jean-François Aujol. The basins of attraction of the global minimizers of the non-convex sparse spike estimation problem. *Inverse Problems*, 36(4):045003, 2020.

[147] Yann Traonmilin, Jean-François Aujol, and Arthur Leclaire. Projected gradient descent for non-convex sparse spike estimation. *IEEE Signal Processing Letters*, 27:1110–1114, 2020.

[148] CC Tsai, DL Young, CW Chen, and CM Fan. The method of fundamental solutions for eigenproblems in domains with and without interior holes. *Proceedings of The Royal Society A: Mathematical, Physical and Engineering Sciences*, 462(2069):1443–1466, 2006.

[149] Cagdas Tuna, Altan Akat, H Nazim Bicer, Andreas Walther, and Emanuël AP Habets. Data-driven 3d room geometry inference with a linear loudspeaker array and a single microphone. In *Forum Acusticum*, 2023.

[150] Cagdas Tuna, Antonio Canclini, Federico Borra, Philipp Götz, Fabio Antonacci, Andreas Walther, Augusto Sarti, and Emanuël AP Habets. 3d room geometry inference using a linear loudspeaker array and a single microphone. *IEEE/ACM Transactions on Audio, Speech, and Language Processing*, 28:1729–1744, 2020.

[151] Michael Unser. A unifying representer theorem for inverse problems and machine learning. *Foundations of Computational Mathematics*, 21(4):941–960, 2021.

[152] DG Vasil'ev and Yu G Safarov. The asymptotic distribution of eigenvalues of differential operators. *Amer. Math. Soc. Transl.(2)*, 150:55–110, 1992.

[153] Pauli Virtanen, Ralf Gommers, Travis E. Oliphant, Matt Haberland, Tyler Reddy, David Cournapeau, Evgeni Burovski, Pearu Peterson, Warren Weckesser, Jonathan Bright, Stéfan J. van der Walt, Matthew Brett, Joshua Wilson, K. Jarrod Millman, Nikolay Mayorov, Andrew R. J. Nelson, Eric Jones, Robert Kern, Eric Larson, C J Carey, İlhan Polat, Yu Feng, Eric W. Moore, Jake VanderPlas, Denis Laxalde, Josef Perktold, Robert Cimrman, Ian Henriksen, E. A. Quintero, Charles R. Harris, Anne M. Archibald, Antônio H. Ribeiro, Fabian Pedregosa, Paul van Mulbregt, and SciPy 1.0 Contributors. SciPy 1.0: Fundamental Algorithms for Scientific Computing in Python. *Nature Methods*, 17:261–272, 2020.

[154] Mark Wagner, Yongsung Park, and Peter Gerstoft. Gridless doa estimation and root-music for non-uniform linear arrays. *IEEE transactions on signal processing*, 69:2144–2157, 2021.

[155] T.W. Wu and Martin Ochmann. Boundary element acoustics fundamentals and computer codes. *The Journal of the Acoustical Society of America*, 111(4):1507–1508, 2002.

[156] Inmo Yeon and Jung-Woo Choi. Rgi-net: 3d room geometry inference from room impulse responses in the absence of first-order echoes. *arXiv preprint arXiv:2309.01513*, 2023.

[157] Wangyang Yu and W Bastiaan Kleijn. Room acoustical parameter estimation from room impulse responses using deep neural networks. *IEEE/ACM Transactions on Audio, Speech, and Language Processing*, 29:436–447, 2020.

[158] Ladan Zamaninezhad, Paolo Annibale, and Rudolf Rabenstein. Localization of environmental reflectors from a single measured transfer function. In *2014 6th International Symposium on Communications, Control and Signal Processing (ISCCSP)*, pages 157–160. IEEE, 2014.

Peut-on entendre la forme d'une pièce ? Cette thèse aborde le problème inverse de la reconstruction de la géométrie d'une pièce à partir de mesures acoustiques. Plus précisément, nous nous concentrons sur les Réponses Impulsionnelles de Salle, qui sont des mesures ponctuelles de la réponse d'une pièce à une source sonore parfaitement impulsionnelle. L'objectif est d'exploiter la réverbération du son dans la pièce pour estimer sa géométrie. Nous développons deux approches distinctes pour résoudre ce problème. La première approche considère des pièces parallélépipédiques avec des murs réfléchissants et repose sur la méthode dite des Sources Images (Image Source Method). Nous proposons un cadre novateur basé sur l'algorithme Frank-Wolfe pour reconstruire les positions 3D des sources images sans utiliser de grille, en résolvant un problème d'optimisation convexe dans l'espace des mesures de Radon. Les positions des sources images sont ensuite utilisées dans un algorithme pour estimer tous les paramètres géométriques de la pièce, y compris l'orientation de l'antenne de microphones. La deuxième approche s'étend à des formes de pièce plus générales et intègre des conditions aux limites d'admittance pour modéliser la réflexion et l'absorption des ondes sonores par les murs. Le problème inverse est formulé comme un problème d'optimisation de forme, où la géométrie de la pièce est optimisée en minimisant les écarts entre des observations dans le domaine fréquentiel et la solution de l'équation de Helmholtz définie sur le domaine de la pièce. Une dérivée de forme est calculée, introduisant des termes tangentiels non standard en raison du manque de régularité des formes polygonales. Enfin, nous implémentons un algorithme de descente de gradient de forme pour reconstruire la géométrie de la pièce.

Can one hear the shape of a room? This thesis addresses the inverse problem of reconstructing the geometry of a room from acoustic measurements. Specifically, we focus on Room Impulse Responses, which are point measurements of a room's response to a perfectly impulsive sound source. The objective is to leverage sound reverberation within the room to estimate its geometry. We develop two distinct approaches to tackle this problem. The first approach considers cuboid rooms with reflective walls and is based on the so-called Image Source Method. We propose a novel framework, utilizing the Frank-Wolfe algorithm, to reconstruct the 3D positions of image sources in a gridless manner by solving a convex optimization problem in the space of Radon measures. These reconstructed image-source positions are subsequently used in an algorithm to estimate all geometric parameters of the room, including the orientation of the microphone array. The second approach extends to more general room shapes and incorporates admittance boundary conditions to model the reflection and absorption of sound waves at the walls. The inverse problem is formulated as a shape optimization problem, where the room geometry is refined by minimizing discrepancies between frequency-domain observations and the solution of the Helmholtz equation defined on the room domain. A shape derivative is calculated, introducing non-standard tangential terms due to the lack of regularity of polygonal shapes. Finally, we implement a shape gradient descent algorithm to reconstruct the room geometry.

INSTITUT DE RECHERCHE MATHÉMATIQUE AVANCÉE
UMR 7501
Université de Strasbourg et CNRS
7 Rue René Descartes
67 084 STRASBOURG CEDEX

Tél. 03 68 85 01 29
Fax 03 68 85 03 28

https://irma.math.unistra.fr
irma@math.unistra.fr

cnrs

Université de Strasbourg

IRMA
Institut de Recherche Mathématique Avancée

IRMA 2024/011
https://hal.science/tel-04818990

ISSN 0755-3390